

Quantum Operator Design for Lattice Baryon Spectroscopy

Adam C. Lichtl

Advisor: Colin Morningstar

Submitted in partial fulfillment of the
requirements for the degree
of Doctor of Philosophy
in the Mellon College of Science at
Carnegie Mellon University

September 7, 2006

Abstract

A previously-proposed method of constructing spatially-extended gauge-invariant three-quark operators for use in Monte Carlo lattice QCD calculations is tested, and a methodology for using these operators to extract the energies of a large number of baryon states is developed. This work is part of a long-term project undertaken by the Lattice Hadron Physics Collaboration to carry out a first-principles calculation of the low-lying spectrum of QCD.

The operators are assemblages of smeared and gauge-covariantly-displaced quark fields having a definite flavor structure. The importance of using smeared fields is dramatically demonstrated. It is found that quark field smearing greatly reduces the couplings to the unwanted high-lying short-wavelength modes, while gauge field smearing drastically reduces the statistical noise in the extended operators. Group-theoretical projections onto the irreducible representations of the symmetry group of a cubic spatial lattice are used to endow the operators with lattice spin and parity quantum numbers, facilitating the identification of the J^P quantum numbers of the corresponding continuum states.

The number of resulting operators is very large; consequently a key aspect of this work is the development of a selection method for finding a sufficient subset of operators for accurately extracting the lowest seven or eight energy levels in each symmetry channel. A procedure in which the diagonal elements of the correlation matrix of the operators are first evaluated to remove noisy operators, followed by the selection of sixteen operators whose renormalized correlation matrix at a fixed small time separation has a low condition number for both the even- and odd-parity channels, is found to work well.

These techniques are applied in the construction of nucleon operators. Correlation matrix elements between these operators are estimated using 200 configurations on a $12^3 \times 48$ anisotropic lattice in the quenched approximation with unphysically heavy u, d quark masses (the pion mass is approximately 700 MeV). After a change of basis operators using a variational method is applied, the energies of up to eight states are extracted in each symmetry channel. Although comparison with experiment is not justified, the pattern of levels obtained qualitatively agrees with the observed spectrum. A comparison with quark model predictions is also made; the quark model predicts more low-lying even-parity states than this study yields, but both the quark model and this study predict more odd-parity states near 2 GeV than currently observed in experiments.

Dedication

This work is dedicated to my family and friends for their unwavering support and love as I pursue my dreams. They are a continuing source of strength as I climb, and they are always there to catch me if I fall.

Acknowledgements

This project would not have been possible without the support of many people. Special thanks goes to my advisor Colin Morningstar who had the confidence to put me on such an important project, and who had the patience to let me learn from my mistakes. I am also grateful to Keisuke (Jimmy) Juge, Matthew Bellis, David Richards, Robert Edwards, and George Fleming who took the time to answer my questions and to show me some of the nuances of their respective specialties.

The configurations used in this work were provided by David Richards and were generated using the computing resources at Thomas Jefferson National Laboratory. The bulk of the computational work for this project was performed on the Medium Energy Group's computing cluster at Carnegie Mellon University. I am grateful to the Medium Energy Experimental Group for their flexibility concerning the allocation of computing resources, and am especially grateful to Curtis Meyer for keeping the cluster running as smoothly as possible (even on the weekends).

Contents

1	Introduction	1
1.1	The atom and nucleus	1
1.2	Hydrogen spectroscopy	3
1.3	Nucleons and the strong nuclear force	5
1.4	Particle sources, particle detectors, and the particle zoo	5
1.5	A new periodic table	9
1.6	The Standard Model	13
1.7	Quantum chromodynamics	14
1.8	Unresolved mysteries in hadronic physics	28
1.9	Goal of this work	32
1.10	Organization of this dissertation	33
2	Calculation overview	35
2.1	Spectral states and resonances	35
2.2	Euclidean space-time	37
2.3	Euclidean gauge links and gauge action	39
2.4	The Euclidean fermion lattice action	40
2.5	Tuning the lattice action	42
2.6	The spectral representation of correlation functions	44

2.7	Effective mass plots	49
2.8	Extracting excited states	51
3	The Monte Carlo method	56
3.1	The need for the Monte Carlo method	57
3.2	Integrating the quark fields	57
3.3	The Monte Carlo method of integration	60
3.4	Markov updating	62
3.5	Error analysis	64
4	Baryon operator construction	69
4.1	Operator design goals	69
4.2	Building blocks	70
4.3	Classification of states by transformation behavior	77
4.4	Spin and parity	89
5	Evaluation of baryon correlation matrices	94
5.1	Charge conjugation and backward propagating states	94
5.2	Three-quark propagators	97
6	Quark field and gauge link smearing parameter tuning	108
6.1	Criterion for judging the effectiveness of smearing	109
6.2	Contamination and noise in extended baryon operators	109
6.3	Systematic study of the smearing parameter space	111
7	Baryon operator pruning	116
7.1	Signal quality	117

7.2	Linear independence	119
8	Baryon operator results: The nucleon spectrum	129
8.1	Fixed-coefficient correlation functions	129
8.2	Fitting range	131
8.3	Fit method	134
8.4	Lattice nucleon spectrum results	136
8.5	Discussion	148
8.6	Conclusion and outlook	154
	Appendix: Final operator selection	156
	Bibliography	165

List of Figures

1.1	The baryon octet (left) and decuplet (right). The N^0 is the neutron and the N^+ is the proton.	11
1.2	The quark model view of hadrons. Left: a baryon consisting of three quarks joined by flux-tubes of glue. Right: a meson consisting of a quark-antiquark pair joined by a flux-tube of glue.	12
1.3	The quark model view of the reaction $\pi^- + p^+ \rightarrow K^0 + \Lambda^0$. Time increases from left to right. The up quark and antiquark annihilate, and a new strange quark-antiquark pair appears.	13
1.4	An example of parallel transport around a non-trivial manifold. The blue arrow ends up in a different orientation even though it made only locally parallel moves.	18
1.5	Two gauge-invariant quark-antiquark operators. The quark and antiquark fields at neighboring sites x and $x + \hat{\mu}$ may be combined by use of a gauge link at x . The gauge link $U_\mu(x)$ parallel transports a color vector from $x + \hat{\mu}$ to x and the Hermitian conjugate gauge link $U^\dagger(x)$ transports a color vector in the opposite direction. Any gauge-invariant quark-antiquark operator can be formed by connecting the fields at any two sites by a suitable product of gauge links.	25
1.6	The gauge-invariant plaquette operator $U_{\mu\nu}(x)$	26
2.1	The pion effective mass plots. The standard effective mass $a_\tau M(\tau)$ (red) fails to plateau due to backward channel contamination. This contamination is explicitly treated by the meson effective mass function $a_\tau M_{\text{cosh}}(\tau)$ (blue). A cosh fit to the correlation function yields a pion mass in lattice units of $a_\tau m_\pi = 0.1125(26)$	50

-
- 4.1 A schematic view of Gaussian quark field smearing. The quark operators are replaced by ‘fatter’ versions which better mimic the ‘fuzzy’ nature of the quark wavefunctions. 72
- 6.1 A sample effective mass plot of a single-site operator showing contamination at early times due to operator coupling with higher lying modes. 110
- 6.2 A sample effective mass plot of a triply-displaced operator showing noise due to stochastic gauge link noise. This noise remains present even after significant quark field smearing ($\sigma_s = 4.0, n_\sigma = 32$). 110
- 6.3 The effective mass $a_\tau M(4a_\tau)$ for the operators $\overline{\mathcal{O}}_{SS}, \overline{\mathcal{O}}_{SD}, \overline{\mathcal{O}}_{TDT}$ against smearing radius σ_s for $n_\sigma = 1, 2, 4, 8, 16, 32, 64$. The gauge field is smeared using $n_\rho = 16$ and $n_{\rho\rho} = 2.5$. Results are based on 50 quenched configurations on a $12^3 \times 48$ anisotropic lattice using the Wilson action with $a_s \sim 0.1$ fm and $a_s/a_\tau \sim 3.0$. The quark mass is such that the mass of the pion is approximately 700 MeV. 113
- 6.4 Leftmost plot: the effective mass $a_\tau E(0)$ for $\tau = 0$ corresponding to the static quark-antiquark potential at spatial separation $R = 5a_s \sim 0.5$ fm against $n_{\rho\rho}$ for $n_\rho = 1, 2, 4, 8, 16, 32$. Results are based on 100 configurations on a 16^4 isotropic lattice using the Wilson gauge action with $\beta = 6.0$. Right three plots: the relative jackknife error $\eta(4a_\tau)$ of effective masses $a_\tau M(4a_\tau)$ of the three nucleon operators $\overline{\mathcal{O}}_{SS}, \overline{\mathcal{O}}_{SD}, \overline{\mathcal{O}}_{TDT}$ for $n_\sigma = 32, \sigma_s = 4.0$ against $n_{\rho\rho}$ for $n_\rho = 1, 2, 4, 8, 16, 32$. Results are based on 50 quenched configurations on a $12^3 \times 48$ anisotropic lattice using the Wilson action with $a_s \sim 0.1$ fm, $a_s/a_\tau \sim 3.0$ 113
- 6.5 Effective masses $a_\tau M(\tau)$ for unsmeared (black circles) and smeared (red triangles) operators $\overline{\mathcal{O}}_{SS}, \overline{\mathcal{O}}_{SD}, \overline{\mathcal{O}}_{TDT}$. Top row: only quark field smearing $n_\sigma = 32, \sigma_s = 4.0$ is used. Middle row: only link-variable smearing $n_\rho = 16, n_{\rho\rho} = 2.5$ is applied. Bottom row: both quark and link smearing $n_\sigma = 32, \sigma_s = 4.0, n_\rho = 16, n_{\rho\rho} = 2.5$ are used, dramatically improving the signal for all three operators. Results are based on 50 quenched configurations on a $12^3 \times 48$ anisotropic lattice using the Wilson action with $a_s \sim 0.1$ fm, $a_s/a_\tau \sim 3.0$ 114
- 6.6 The effects of different values of the quark smearing radius σ_s on the excited states. Throughout, stout-link smearing is used with $n_{\rho\rho} = 2.5, n_\rho = 16$, and $n_\sigma = 32$ quark smearing interactions are used. The black circles have $\sigma_s = 4.0$, the red squares have $\sigma_s = 3.0$, and the blue triangles have $\sigma_s = 2.0$. A Gaussian radius of $\sigma_s = 3.0$ was chosen as a balance between high state contamination vs. stochastic noise in the excited states. 115

7.1	Effective mass plots for eight representative operators from the complete set of extended baryon operators in the G_{1u} channel. We chose up to ten candidate operators of each type (SD, DDI, DDL, TDT) based on the average jackknife error over the first sixteen time slices. This process helped us to identify ‘quiet’ operators (top row, in green) and remove some of the noisier operators (bottom row, in red).	118
7.2	The effective masses for the final sixteen G_{1g} operators selected by our pruning process.	123
7.3	The effective masses for the final sixteen H_g operators selected by our pruning process.	124
7.4	The effective masses for the final sixteen G_{2g} operators selected by our pruning process.	125
7.5	The effective masses for the final sixteen G_{1u} operators selected by our pruning process.	126
7.6	The effective masses for the final sixteen H_u operators selected by our pruning process.	127
7.7	The effective masses for the final sixteen G_{2u} operators selected by our pruning process.	128
8.1	The effective mass function for the trial correlation function $C(\tau) = e^{-m\tau} + e^{-m(T-\tau)}$. The number of lattice sites in the temporal direction is $N_\tau = 48$, and the lowest baryon state is taken to be $a_\tau m = 0.24$. The backward propagating state significantly contaminates the effective mass function at times greater than $\tau \approx 20a_\tau$	132
8.2	An example of an off-diagonal element of the rotated correlation matrix $\tilde{C}_{ij}(\tau) = v_i^\dagger C(\tau) v_j$ having $i = 0$ and $j = 1$. Because we are using fixed coefficients to rotate the matrix, we are unable to maintain the orthogonality of the states at all times τ . Here we see that we can safely work with the fixed-coefficient correlation functions until $\tau \approx 30a_\tau$. After that, they all relax to the lowest excited state: $\tilde{C}_{kk}(\tau) \rightarrow c_1 ^2 \exp(-E_1\tau)$	133
8.3	The lowest eight levels for the G_{1g} nucleon channel. The green circles are the fixed coefficient effective masses, and the red squares are the principal effective masses. The fits were made to the fixed coefficient correlation functions and are denoted by the blue lines.	139

-
- 8.4 The lowest eight levels for the H_g nucleon channel. The green circles are the fixed coefficient effective masses, and the red squares are the principal effective masses. The fits were made to the fixed coefficient correlation functions and are denoted by the blue lines. 140
- 8.5 The lowest eight levels for the G_{2g} nucleon channel. The green circles are the fixed coefficient effective masses, and the red squares are the principal effective masses. The fits were made to the fixed coefficient correlation functions and are denoted by the blue lines. 141
- 8.6 The lowest eight levels for the G_{1u} nucleon channel. The green circles are the fixed coefficient effective masses, and the red squares are the principal effective masses. The fits were made to the fixed coefficient correlation functions and are denoted by the blue lines. 142
- 8.7 The lowest eight levels for the H_u nucleon channel. The green circles are the fixed coefficient effective masses, and the red squares are the principal effective masses. The fits were made to the fixed coefficient correlation functions and are denoted by the blue lines. 143
- 8.8 The lowest eight levels for the G_{2u} nucleon channel. The green circles are the fixed coefficient effective masses, and the red squares are the principal effective masses. The fits were made to the fixed coefficient correlation functions and are denoted by the blue lines. 144
- 8.9 The low-lying $I=1/2$, $I_3=+1/2$ nucleon spectrum extracted from 200 quenched configurations on a $12^3 \times 48$ anisotropic lattice using the Wilson action with $a_s \sim 0.1$ fm and $a_s/a_\tau \sim 3.0$. The vertical height of each box indicates the statistical uncertainty in that estimate. Our pion mass for this study was $a_\tau M_\pi = 0.1125(26)$, or approximately 700 MeV. A different color was chosen for each level in a symmetry channel to help the reader discern among the different levels. 145
- 8.10 The $I=1/2$, $I_3=+1/2$ nucleon spectrum as determined by experiment [Y⁺06] and projected into the space of lattice spin-parity states. Black denotes a four-star state, blue denotes a three-star state, tan denotes a two-star state, and gray denotes a one-star state. 146
- 8.11 The low-lying $I=1/2$, $I_3=+1/2$ nucleon spectrum up to 2820 MeV as predicted by the relativistic quark model [CR93] and projected into the space of lattice spin-parity states. ‘Missing resonances’ are displayed in red, and observed resonances are labeled by their assigned state in the experimental spectrum. Note that the location of a labeled state is given by its predicted energy value, and the text of the label tells its experimentally measured energy value. For a labeled state black denotes a four-star state, blue denotes a three-star state, tan denotes a two-star state, and gray denotes a one-star state. 147

List of Tables

1.1	The quark flavor content of some sample hadrons. The properties of the hadrons are determined by the properties of the quarks from which they are composed.	11
1.2	The standard model of particle interactions. This model describes all matter as made up of quarks and leptons, held together by the interactions of the force-carrying mediators. The Higgs boson is the only particle of the Standard Model which has not been observed, and is not shown.	14
1.3	The lowest lying spin-1/2 nucleons. The numbers in parenthesis are the masses of the resonances in MeV, L is the orbital angular momentum of the quarks, S is the total spin of the quarks, and P is the parity of the state. The quark model treats the nucleon resonances as increasing excitations in an oscillator potential. The $N(1440)$, or Roper, is measured to be lower than predicted by the quark model.	30
4.1	The spatial arrangements of the extended three-quark baryon operators $\bar{\Phi}_{ijk}$ and Φ_{ijk} . Quark-fields are shown by solid circles, line segments indicate gauge-covariant displacements, and each hollow circle indicates the location of a Levi-Civita color coupling. For simplicity, all displacements have the same length in an operator.	76
4.2	The isospin and strangeness quantum numbers for the different baryon sectors. The isospin projection I_3 ranges from $-I$ to I by increments of 1. The charge Q of each baryon listed increases with increasing isospin projection I_3	86
4.3	Elemental three-quark baryon operators $\bar{B}_{\alpha\beta\gamma,ijk}^F$ having definite isospin I , maximal $I_3 = I$, and strangeness S in terms of the gauge-invariant extended three quark operators $\bar{\Phi}_{\alpha\beta\gamma,ijk}^{ABC}(\tau)$	89

-
- 4.4 Our choice of the representation matrices for the double-valued irreps of O_h . The G_{1u}, G_{2u}, H_u matrices for the rotations C_{4y}, C_{4z} are the same as the G_{1g}, G_{2g}, H_g matrices, respectively, given below. Each of the G_{1g}, G_{2g}, H_g matrices for spatial inversion I_s is the identity matrix, whereas each of the G_{1u}, G_{2u}, H_u matrices for I_s is -1 times the identity matrix. The matrices for all other group elements can be obtained from appropriate multiplications of the C_{4y}, C_{4z} , and I_s matrices. 92
- 4.5 The single-site N^+ operators which transform irreducibly under the symmetry group of the spatial lattice, defining $N_{\alpha\beta\gamma} = \Phi_{\alpha\beta\gamma;000}^{uud} - \Phi_{\alpha\beta\gamma;000}^{duu}$ (see Table (4.3)) and using the Dirac-Pauli representation for the Dirac gamma matrices. . . 92
- 4.6 Because O_h^D is a subgroup of the continuum spin group, the continuum states appear as degenerate states within each of the lattice irreps. This table allows us to identify the continuum spin state which corresponds to each lattice state. 93
- 5.1 To minimize the number of sources, thereby reducing the number of three-quark propagators needed, we rotate our source and sink operators such that the displaced quarks at the source are always in the same canonical positions. 98
- 5.2 The number of three-quark propagators needed for each part of the full nucleon correlation matrix. The total number of propagators needed is 671. The diagonal correlation matrix elements required only 175 propagators, which were reused for the full run. 106
- 7.1 The numbers of operators of each type which project into each row of the G_{1g}, H_g , and G_{2g} irreps for the $\Delta^{++}, \Sigma^+, N^+$, and Λ^0 baryons. The numbers for the G_{1u}, H_u , and G_{2u} irreps are the same as for the G_{1g}, H_g , and G_{2g} irreps, respectively. The Ξ^0 operators are obtained from the Σ^+ operators by making the flavor exchange $u \leftrightarrow s$. The Ω^- operators are obtained from the Δ^{++} operators by making the flavor replacement $u \rightarrow s$ 116
- 7.2 The condition numbers κ and for the 5×5 extended operator submatrices chosen. The percentages denote how much greater each condition number is than its minimum possible value. 121
- 7.3 The condition numbers κ for the 16×16 final operator submatrices chosen. The percentages denote how much greater each condition number is than its minimum possible value. The operators in each odd-parity irrep are the opposite-parity partners of the operators in the corresponding even-parity irrep. 122
- 7.4 The numbers of N^+ operators of each type which are used in each correlation matrix. The operators selected in the G_{1u}, H_u and G_{2u} irreps are the same as those selected for the G_{1g}, H_g , and G_{2g} irreps, respectively. 122

-
- 8.1 The final spectrum results for the even-parity channels. These results are based on 200 quenched configurations on a $12^3 \times 48$ anisotropic lattice using the Wilson action with $a_s \sim 0.1$ fm and $a_s/a_\tau \sim 3.0$. Our pion mass for this study was $a_\tau M_\pi = 0.1125(26)$ (see Figure 2.1), or approximately 700 MeV. 137
- 8.2 The final spectrum results for the odd-parity channels. These results are based on 200 quenched configurations on a $12^3 \times 48$ anisotropic lattice using the Wilson action with $a_s \sim 0.1$ fm and $a_s/a_\tau \sim 3.0$. Our pion mass for this study was $a_\tau M_\pi = 0.1125(26)$ (see Figure 2.1), or approximately 700 MeV. We did not find a satisfactory fit range for the eighth level in the G_{1u} channel. 138
- 8.3 The current experimental values [Y⁺06] for all known nucleon resonances. The state names are given in spectroscopic notation: $L_{2I} 2J$, where $L = S, P, D, F, \dots$ is the orbital angular momentum of an $N\pi$ system having the same J^P as the state, I is the isospin, and J is the total angular momentum. A four-star experimental status implies that existence is certain and that the properties are fairly well explored. A three-star status implies that existence ranges from very likely to certain, but further confirmation is desirable. Two stars implies that the evidence for existence is only fair, and one star implies that the evidence is poor. The number of times each state is expected to appear in each lattice O_h^D irrep (obtained from subduction) is also shown. The experimental uncertainties are at the 5% level or less. 150
- 8.4 The quark model predictions [CR93] for the excited nucleon spectrum below 2100 MeV. The proton is used to set the parameters of the model. The state names are given in spectroscopic notation: $L_{2I} 2J$, where $L = S, P, D, F, \dots$ is the orbital angular momentum of an $N\pi$ system having the same J^P as the state, I is the isospin, and J is the total angular momentum. The superscripted integer on the model state name denotes the principal quantum number in the quark model (see [CR93]). The number of times each state is expected to appear in each lattice O_h^D irrep is also shown. Dashes indicate ‘missing resonances.’ 151
- 8.5 The quark model predictions [CR93] for the excited nucleon spectrum from 2100 MeV to 2820 MeV. Dashes indicate ‘missing resonances.’ 152
- 6 The numbers of operators of each type which project into each row of the G_{1g}, H_g , and G_{2g} irreps for the N^+ baryons. The numbers for the G_{1u}, H_u , and G_{2u} irreps are the same as for the G_{1g}, H_g , and G_{2g} irreps, respectively. 156
- 7 The identification numbers for the final sixteen nucleon operators selected from the G_{1g}/G_{1u} channels. The ID number corresponds to the operator number within each type (see Table 6) as indexed in our `projection_coefficients` data files. 157

-
- 8 The identification numbers for the final sixteen nucleon operators selected from the H_g/H_u channels. The ID number corresponds to the operator number within each type (see Table 6) as indexed in our `projection_coefficients` data files. 158
- 9 The identification numbers for the final sixteen nucleon operators selected from the G_{2g}/G_{2u} channels. The ID number corresponds to the operator number within each type (see Table 6) as indexed in our `projection_coefficients` data files. 159

Chapter 1

Introduction

Particle physicists seek to identify the elementary building blocks of the universe, and the mechanisms by which these elements interact. This view, known as reductionism, is seen by many as the necessary starting point for the discovery of a unified theory which quantitatively describes all natural phenomena. If we can identify the building blocks and the rules which hold them together, then we can begin to explore which features of our universe arise from the complex interactions of these fundamental components.

1.1 The atom and nucleus

In 1803, John Dalton presented his atomic theory which stated that all compounds were composed of and reducible to collections of atoms. This sparked a great effort to use any chemical means available to separate compounds into their fundamental atoms, the so called elements. As scientists discovered new elements and observed their properties in reactions, they began to notice that entire groups of elements behaved in similar ways. In 1869, Dmitri Mendeleev [HM84] introduced his now ubiquitous periodic table of the elements, which placed elements with similar reaction properties into columns, ordered by atomic mass. Mendeleev's table classified the 63 known elements at the time, and he predicted the existence and characteristics of three elements which were later discovered: gallium, scandium, and germanium.

The similar behavior of the different elements in each column was a reassurance that there was indeed an order hidden beneath the diversity of the everyday world. Today, the 118 known elements fit neatly into the eighteen columns of the modern periodic table (there are also the lanthanoid and actinoid classifications). These elements include stable atoms such as hydrogen, carbon, nitrogen, and oxygen; and unstable atoms, such as radium and uranium which last long enough to be characterized, but which eventually break down into lighter elements through radioactive decay.

The large size and redundancy in the table were also significant hints that the atom possessed substructure. A breakthrough on this front was the identification of the electron in 1897 by J.J. Thomson [Gri87]. At this time, scientists were fascinated by the cathode ray tube, a glass chamber with a metal electrode at each end and a port for a vacuum pump. When the air was pumped out of the tube and a voltage difference was applied to the electrodes, the tube would glow with ‘rays’ emanating from the negative electrode (the cathode). This effect was later enhanced by J.B. Johnson who added a heating element to the cathode. Before 1897 scientists suspected, but were not certain, that the rays were composed of electrically charged particles.

J.J. Thomson’s cathode ray experiments built on those of his contemporaries, and involved the deflection of these rays by known electric and magnetic fields. By balancing the electric force $\vec{F}_E = q\vec{E}$ with the magnetic force $\vec{F}_B = q\vec{v} \times \vec{B}$, he determined the velocity of the particles to be roughly one tenth of the speed of light from the relation

$$v = \frac{E}{B}.$$

He then switched off the electric field, measured the radius of curvature R of the beam, and used the condition of uniform circular motion $F = mv^2/R$ to determine the charge-to-mass ratio from the relation

$$\frac{q}{m} = \frac{v}{RB}.$$

Thomson found that the charge-to-mass ratio was abnormally large when compared to the known ions. He assumed that the mass was very small (as opposed to assuming that the charge was very large), and concluded that the ray was composed of negatively charged elementary particles, and identified the particles as constituents of the atom. Later, they were named ‘electrons’¹, taken from a term coined in 1894 by electro-chemist G. Johnstone Stoney. Thomson had discovered that cathode ray electrons came from the atoms composing the cathode; these electrons were ‘boiled’ off of the cathode as it heated up.

The charge of the electron (and mass, from Thomson’s ratio) was measured in 1909 by Robert Millikan in his oil-drop experiment. He used an atomizer to spray a mist of oil droplets above two plates. The top plate had a small hole through which a few droplets could pass. Millikan would vary the electric field between the plates until he had one (charged) drop of oil suspended. Then he turned off the electric field and allowed the drop to fall until it had reached its terminal velocity v_1 . The velocity-dependent drag force on the drop was given by Stoke’s Law:

$$F_{D1} = 6\pi r\eta v_1,$$

where r is the radius of the (assumed spherical) drop and η is the viscosity of air. At terminal velocity, the drag force balanced the the ‘apparent weight’ of the oil drop

¹From the Greek *elektron*, meaning amber. Early experiments in electricity used amber rods rubbed with fur to build up a static charge.

$F_{D1} = W$, which is

$$W = (4/3)\pi r^3(\rho_{\text{oil}} - \rho_{\text{air}})g,$$

where ρ_{oil} is the density of the oil, and ρ_{air} is the density of air. His measurement of v_1 allowed him to infer r , and thus the apparent weight of the drop W . He then turned the electric field back on before the drop reached the bottom plate and measured the terminal velocity v_2 of the drop's upward motion. At this point, Millikan knew that $qE = F_{D2} + W = F_{D1}v_2/v_1 + W$ and could therefore determine the charge q on the drop:

$$q = \frac{W}{E} \left(1 + \frac{v_2}{v_1} \right).$$

After repeating the experiment for many droplets, Millikan confirmed that the quantity of charge on a drop was always a multiple of the same number, the charge on a single electron (1.602×10^{-19} Coulomb, in SI units).

Electrically neutral atoms must possess enough positive charge to compensate for the negative charge of the electrons. The modern model of the atom was born from Geiger and Marsden's [GM09] alpha scattering experiments performed under Ernest Rutherford [Rut11], a former student of Thomson's, in 1909. The goal of these experiments was to probe the positive charge distribution of the atom. Charged alpha particles (doubly ionized helium atoms) emitted from a radioactive radium source were directed at a gold foil. A zinc sulfide screen was placed at various positions to detect the scattered alpha particles. Rutherford, Geiger, and Marsden found that most of the alpha particles passed through the foil with little deflection but some deflected through large angles. This suggested that the positive charge in each atom was concentrated at the center and occupied just a fraction of the total atomic volume.

The nucleus of the lightest element (Hydrogen) was named the proton². Its charge is exactly equal to the magnitude of the electron charge, but its mass is roughly 2000 times greater. In the atomic model, a hydrogen atom consisted of a proton and electron bound together via the electromagnetic force.

1.2 Hydrogen spectroscopy

Once scientists had a model of the hydrogen atom, they were in a position to discuss the hydrogen spectrum. When an electrical current is passed through pure hydrogen gas, the atoms absorb energy and then radiate at specific discrete wavelengths, which can be observed by passing the emitted light through a prism or diffraction grating. Spectroscopy was pioneered by people such as A.J. Angstrom and was in widespread use in chemistry for the classification of elements. The first observed series of emission lines was the Balmer series, named after J.J. Balmer who in 1885 first developed the empirical relationship for

²From the Greek *proton*, meaning first.

the spacing of the lines. The relationship was generalized in 1888 by Johannes Rydberg for the complete emission line spectrum:

$$\kappa = \mathcal{R} \left(\frac{1}{n_1^2} - \frac{1}{n_2^2} \right),$$

where $\kappa = 1/\lambda$ is the discrete emission wavenumber and $\mathcal{R} = 10967757.6 \pm 1.2 m^{-1}$ is the Rydberg constant for the hydrogen spectrum [ER85]. The Balmer series lines correspond to

$$n_1 = 2 \text{ and } n_2 = 3, 4, \dots$$

A burning question was: could the atomic model reproduce the observed hydrogen spectrum?

In 1913, Niels Bohr combined the Rutherford model of the atom with Einstein's quantum theory of the photoelectric effect³ introduced in 1905 by introducing his quantization condition. Bohr's model related the electromagnetic radiation emitted by an atom to electron transitions from states of definite angular momentum:

$$L = n\hbar.$$

The quantization of atomic energy states was experimentally verified in 1914 by Frank and Hertz who accelerated electrons through a potential difference in a tube filled with mercury vapor [ER85]. They measured the current as a function of applied voltage, which was an indicator of the number of electrons which passed unimpeded through the gas. When the kinetic energy of the electrons reached a threshold level, the current abruptly dropped. Frank and Hertz interpreted this to mean that the electrons were exciting the mercury atoms and being scattered. As the voltage was increased, the current would increase until successive thresholds were reached. This showed that the mercury atoms possessed discrete energy levels. The mercury atoms would only absorb energy from the electrons by transitioning from one energy level to another.

The urge to understand the underpinnings of Bohr's (and in 1916 Sommerfeld and Wilson's) quantization conditions sparked the rapid development of an entirely new field of physics: quantum mechanics. Two notable contributions were Werner Heisenberg's 1925 matrix mechanics paper, and Erwin Schrödinger's 1926 paper on quantization as an eigenvalue problem (which introduced 'Schrödinger's equation'). Quantum mechanics succeeded not only in accurately describing atomic spectra, but also led to revolutionary technological advances such as the semiconductor used in computers and nuclear magnetic resonance (NMR) used in medical imaging.

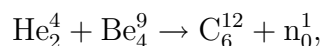
The hydrogen spectrum not only provided a test of the atomic model, it also led to refinements in our understanding of the atom and opened up an entirely new branch of physics. The importance of spectroscopy cannot be overstated.

³Einstein proposed that radiant energy comes in quanta known as photons with the energy frequency relation $E = h\nu$.

1.3 Nucleons and the strong nuclear force

The neutron, the electrically neutral partner of the proton in the nucleus, was identified in 1932 by James Chadwick [Cha32] from previous experiments in which a polonium source was used to bombard beryllium with alpha particles.

In modern notation [CG89], the nuclear reaction was:



where the subscript denotes the atomic number (number of protons), and the superscript denotes the atomic weight (number of protons+neutrons).

The observation that every atom contains a nucleus in which protons and neutrons are confined within 0.01% of the volume of the atom raises the question: what keeps the protons from flying apart from electrostatic repulsion? Physicists inferred the existence of a new force which could overpower the electromagnetic force, but which had a range on the order of the nuclear radius. In 1934, Hideki Yukawa worked out the quantization of the strong nuclear force field and predicted a new particle, the pion [Gri87]. In Yukawa's theory, nucleons interact with each other via the pion field. When the field is quantized according to the formalism of quantum field theory, the potential felt by the nucleons goes as

$$\frac{1}{r} \exp \left\{ -\frac{m_\pi r}{\hbar c} \right\},$$

where r is the inter-nucleon separation, and m_π is the mass of the pion, the quantum which mediates the strong nuclear force⁴. To get a force with a range of 1 fm, the order of the typical nuclear radius

$$m_\pi \approx \frac{\hbar c}{1 \text{ fm}} \approx 200 \text{ MeV}.$$

It was then up to particle physicists to use all of the tools at their disposal to confirm the existence of the pion and complete the atomic model.

1.4 Particle sources, particle detectors, and the particle zoo

1.4.1 Sources of subatomic particles

We have already discussed the cathode ray tube, a source of electrons when the cathode is heated enough to boil them off of the metal. A wide variety of experiments were performed which involved accelerating the electrons through a potential difference.

⁴Note that the electromagnetic force is mediated by the massless photon, giving the usual $1/r$ Coulomb potential.

In 1895, Henri Becquerel discovered that uranium was radioactive from the darkening of photographic film [CG89]. The radioactive decay of heavy elements such as polonium produced light nuclei such as that of helium (two protons and two neutrons), the so called alpha radiation. When a neutron decays into a proton, it emits an electron, the so called beta radiation. Electromagnetic radiation is called gamma radiation. Sources of radiation would be placed in front of collimators, which would only let through thin beams of the particles. These beams could then be directed onto various targets and the reactions observed.

In 1912, Victor Hess used a hot air balloon to take measurements of ionizing radiation at varying altitudes. He discovered that the rate of ionization was roughly four times greater at an altitude of 5,300 meters than it was at ground level, thus showing that the radiation which ionizes the atmosphere is cosmic in origin. The discovery of these so called cosmic rays led to the discovery of a wide range of subatomic particles.

Particle accelerators ('atom smashers') use electromagnetic fields to accelerate beams of charged particles to velocities comparable with the speed of light. Accelerators may be linear or circular⁵. Circular colliders use magnetic fields to curve the paths of particles as they are accelerated around the ring. These high energy beams of particles can be directed upon stationary targets or made to collide with other beams of particles. Particles of one type could also be directed onto targets, producing particles of a different type which can themselves be collimated into a beam and focused with magnets.

1.4.2 Detectors of subatomic particles

A conspicuous signature of a charged cosmic ray is the ion trail left behind as electrons are stripped off of atoms in the ray's path. Some particle detectors turn these ion trails into visible paths, but this is not the only way to detect a subatomic particle. Here is a brief description of some of the tools experimentalists use to detect subatomic particles.

Nuclear emulsions are a special mixture of gelatin and silver bromide salts and work under the same principles as chemical photography. The track of a charged particle creates sites of silver atoms on the salt grains. Photographic development chemicals reduce the silver bromide salts to silver, but are most effective when there are already silver atoms present. Early cosmic ray researchers would stack plates of nuclear emulsions, and then develop them into pictures of subatomic paths.

Cloud chambers, also called Wilson chambers after their inventor C.T.R. Wilson, contain a supersaturated vapor (such as isopropyl alcohol) that forms droplets along the trail of ionization. The trails are illuminated with a bright light source and photographed.

Bubble chambers work under the same principle as cloud chambers, but use a

⁵The Large Hadron Collider (LHC) is a proton-proton collider with a ring 27 km in circumference.

superheated transparent liquid (such as liquid hydrogen). When a charged particle passes through the liquid, it interacts with the molecules and deposits enough energy to boil the liquid around the interaction points. The result is the formation of a string of small bubbles along the particle's path which can then be illuminated and photographed.

Drift chambers are described by [Col02]:

Charged particles passing through the chambers ionize the gas in the chambers (DME or an argon/ethane mixture), and the resulting ionization is collected by wires maintained at high voltage relative to the surrounding "field" wires. The electrical signals from these wires are amplified, digitized, and fed into a computer which reconstructs the path of the original particle from the wire positions and signal delay times.

Silicon detectors operate under the same principle as drift chambers but utilize a semiconducting material instead of a gas. This allows for much a higher energy resolution and a much higher spatial resolution. However, they are more expensive and more sensitive to the degrading effects of radiation than drift chambers.

Scintillators are compounds which absorb energy from interactions with charged particles, and then re-emit that energy in the form of electromagnetic radiation at a longer wavelength (fluorescence). Scintillators have short decay times and are optically transparent to the flashes. Thus, particle tracks register as a series of rapid flashes within the material which can be seen by light detectors (such as photomultiplier tubes).

Calorimeters measure the energy content of the particle shower which occurs when a subatomic particle strikes a dense barrier in the detector. Often calorimeters are segmented into different chambers, and the energy deposited by the particle showers in each chamber is used to infer the particle's identity and direction of travel. Calorimeters can be designed to detect either electromagnetic showers or hadron showers, which occur when a subatomic particle interacts with the barrier.

1.4.3 The particle zoo

Particle physicists use detectors to examine the contents of cosmic rays and the products of beam-target and beam-beam scattering experiments. They measure the trajectories either directly in the detector, or through reconstruction via the principle of conservation of mass and momentum. A particularly useful quantity measured is the *differential cross section*, the reaction rate per unit incident flux as a function of angle, energy, and any other parameters of interest [Per00]. Other properties of the particles such as mass, spin, parity, form factors (describing the structure of the particle), life-time, and branching ratios (describing the relative likelihood of decay into each of several final states), can then be deduced from interaction cross section data.

There are three classes of outcomes when two subatomic particles A and B approach each other:

1. Nothing happens: the particles pass right by each other without interacting
2. Elastic scattering ($A + B \rightarrow A + B$): the particles interact through the exchange of a ‘messenger’ particle. The outgoing particles are of the same type as the incoming particles, but may have a different energy and trajectory.
3. Inelastic scattering ($A + B \rightarrow C + D + \dots$): Einstein’s mass-energy relation⁶ $E = \gamma mc^2$ allows for the transmutation the combined energy and mass of the input particles into a completely different set of output particles, subject to quantum transition rules and kinematic constraints.

It was expected that the above sources and detectors of particles would lead to the discovery of Yukawa’s pion, and the completion of the atomic model. Some scientists anticipated that the proton, neutron, electron, photon, and pion would constitute the fundamental building blocks of all matter. It was a great surprise, then, when detailed observations of cosmic rays and scattering experiments uncovered a plethora of subatomic particles. One of the early cosmic ray candidates for the pion ended up being the muon, a more massive relative of the electron. I.I. Rabi put it best when he said ”Who ordered that?” [CG89]

The pion was experimentally confirmed in 1947 when D.H. Perkins [Per47] observed the explosion of a nucleus after capturing a cosmic-ray pion. He saw the ion trails created by the incoming pion and outgoing nuclear debris in a photographic emulsion. Nuclear disintegration by pion capture had been predicted in 1940 by Tomonaga and Araki.

Modern estimates [H⁺02] of the mass of the charged and neutral pions are:

Pion	Mass (MeV)
π^\pm	139.57018(35)
π^0	134.9766(6)

which is close to the very rough estimate of 200 MeV made by Yukawa.

The muon, now identified as a distinct particle from the pion, was only the beginning of a long revolutionary series of discoveries. Positrons, kaons, antiprotons, tau leptons, neutrinos, and more took their place with the proton, neutron, and electron in the rapidly expanding ‘particle zoo.’

Most of these particles were unstable resonances. In analogy with radioactive elements in the periodic table which decay into simpler elements, a resonance is defined as an object of

⁶Einstein’s original formulation of special relativity made a distinction between the mass of a body at rest and the perceived mass of a body in motion. Modern convention takes mass to be a characteristic of an object (e.g. on equal footing with charge), and explicitly includes the relativistic dilatation factor $\gamma \equiv 1/\sqrt{1 - v^2/c^2}$.

mass M with a lifetime τ much longer than the period associated with its ‘characteristic frequency’ $\nu = M/h$:

$$\tau \gg h/M.$$

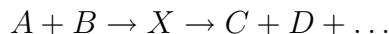
For very massive resonances, this lifetime can be very short and is quoted in terms of the decay width $\Gamma = \hbar/\tau$, a natural spread in the energy of the decaying state induced by the uncertainty principle [Per00]. Resonances are then defined by the property (neglecting factors of 2π and working in energy units)

$$\Gamma \ll M.$$

For example the Z^0 resonance, discovered in 1983 at CERN, has a mass of approximately 91 GeV [H⁺02] and a decay width of approximately 2.5 GeV, which corresponds to a lifetime of roughly 2.6×10^{-25} seconds, enough time for light to travel about one-tenth of a Fermi, much less than the spatial extent of a proton. Such resonances cannot, therefore, be observed directly in particle detectors. Rather, resonances in the elastic channel,⁷



show up as enhancements in the differential and total cross sections compared to what would be expected from simple kinematics alone. Resonances in the inelastic channel



can be identified from trajectory reconstruction and decay products.

The overwhelming number of subatomic particles discovered (including resonances) lead Wolfgang Pauli to exclaim in the 1950s “Had I foreseen this, I would have gone into botany.”

1.5 A new periodic table

1.5.1 Classification of particles

As new particles were discovered, they were classified by their values of conserved quantities, such as mass and electric charge. The existence of ‘forbidden’ reactions, which were never observed, led to the introduction of two more conserved quantum numbers: lepton number and baryon number. Leptons (such as the electron and muon) have lepton number = 1, baryon number = 0, and do not participate in any strong interactions. Hadrons have lepton number = 0, participate in strong interactions, and either have baryon number = 1 for baryons (such as the proton and neutron), or baryon number = 0

⁷A *channel* refers to the way a reaction can proceed. The channel concept is also applied to initial, intermediate, or final states in a reaction, e.g. the ‘nucleon channel’ contribution for a process has a nucleon resonance as an intermediate state, and the Δ^{++} can be created in the $p\pi$ channel.

for mesons⁸ (such as the pion). Because an antiparticle annihilates its corresponding particle, it must have the opposite quantum numbers (except for mass, which is always positive and which is conserved in the radiation emitted from an annihilation reaction).

The discovery of kaons, unstable mesons which were created easily via the strong interaction but which decayed slowly via a different process (the weak interaction, which also governs radioactive beta decay), led to the introduction of ‘strangeness’, a new quantum number. The strong interaction conserves strangeness, but the weak interaction violates it. The time-scale over which the strong interaction acts is very short, thus giving rapid creation and decay rates. On the other hand, weak interactions have long time-scales which cause strangeness-changing reactions to proceed slowly. For example, a kaon (meson with strangeness = +1) and lambda (baryon with strangeness = -1) can be produced easily by the strong reaction:

$$\pi^- + p^+ \rightarrow K^0 + \Lambda^0, \quad |\Delta S| = 0,$$

but must decay separately via the much slower weak reactions

$$\begin{aligned} K^0 &\rightarrow \pi^+\pi^-, & |\Delta S| &= 1, \\ \Lambda^0 &\rightarrow p^+\pi^-, & |\Delta S| &= 1. \end{aligned}$$

In the tradition of Mendeleev, the discovered hadrons were placed into tables according to their masses and reaction properties (quantum numbers) independently by Murray Gell-Mann and Yuval Ne’eman in 1961 [GMN00]. In this arrangement scheme, dubbed the ‘Eightfold Way’ by Gell-Mann, particles with similar masses were placed into hexagonal and triangular arrays which were labeled by strangeness S and electric charge Q . Two examples of these tables are shown in Figure 1.1.

Just as Mendeleev had predicted the existence and properties of gallium, scandium, and germanium from holes in his periodic table, so also did Murray Gell-Mann predict the existence, mass, and quantum numbers of a new particle, the Ω^- , a strangeness = -3 heavy baryon, which was later discovered at Brookhaven National Laboratory in 1964 [B+64].

The existence of such a large number of hadrons along with their classification according to a comparably small number of quantum numbers hinted, once again, that there was substructure yet to be discovered. What was needed was a model of nucleon substructure which could explain the patterns in Gell-Mann and Ne’eman’s tables.

1.5.2 The constituent quark model

The constituent quark model describes hadrons as being built up from combinations of point-like particles. This model was proposed independently in 1964 by Gell-Mann and Zweig, and Gell-Mann named the constituents ‘quarks’⁹.

⁸From the Greek *mesos*, meaning middle. Mesons are so named because the first mesons had masses between that of the electron (0.5 MeV) and the proton (938 MeV).

⁹From James Joyce’s *Finnigan’s Wake*, referring to the sound a seagull makes.

Quarks are spin-1/2 objects (fermions) with baryon number = 1/3 and come in different flavors. Originally three flavors were introduced: ‘up’, ‘down’, and ‘strange’:

	Charge	Strangeness
u	+2/3	0
d	-1/3	0
s	-1/3	-1

The quarks combine into baryon and meson multiplets following the well-established rules of addition of angular momenta. According to the quark model, baryons are three-quark states, and mesons are quark-antiquark states. All of the hadrons known in 1964 (and most discovered since) could be described using this model. Figure 1.2 shows baryons and mesons as viewed in the quark model, and figure 1.3 shows pictorially the reaction

$$\pi^- + p^+ \rightarrow K^0 + \Lambda^0.$$

Hadron	Quark Content	Baryon Number	Charge	Strangeness
p^+	uud	1	+1	0
n^0	udd	1	0	0
Λ^0	uds	1	0	-1
Ω^-	sss	1	-1	-3
π^+	$u\bar{d}$	0	+1	0
π^-	$d\bar{u}$	0	-1	0
π^0	$\frac{1}{\sqrt{2}}(u\bar{u} + d\bar{d})$	0	0	0
K^0	$d\bar{s}$	0	0	+1

Table 1.1: The quark flavor content of some sample hadrons. The properties of the hadrons are determined by the properties of the quarks from which they are composed.

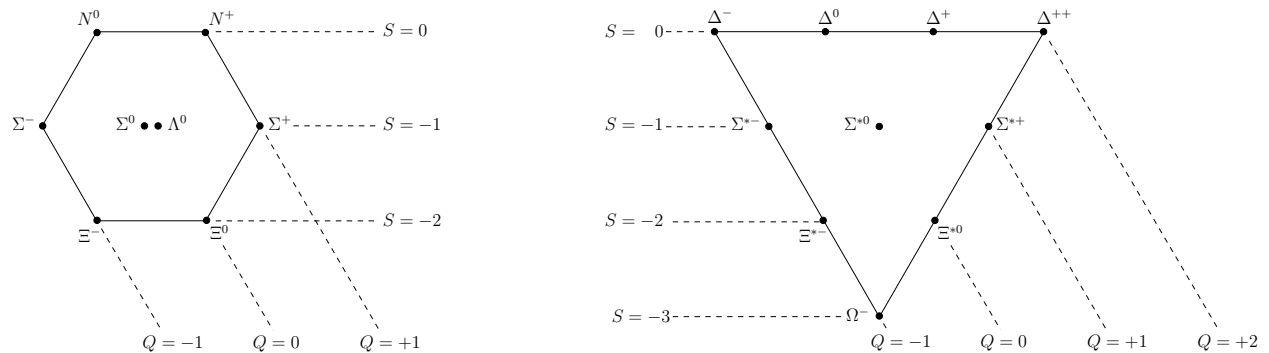


Figure 1.1: The baryon octet (left) and decuplet (right). The N^0 is the neutron and the N^+ is the proton.



Figure 1.2: The quark model view of hadrons. Left: a baryon consisting of three quarks joined by flux-tubes of glue. Right: a meson consisting of a quark-antiquark pair joined by a flux-tube of glue.

The quark model correctly described the baryon octet and baryon decuplet. It also predicted that the light meson octet and singlet would mix, forming a meson nonet. This corrected the Eightfold Way which had treated a newly discovered meson, the η' , as a singlet with no relation to the existing meson octet.

Observed states such as the $\Delta^{++}(uuu)$ produced from

$$\pi^+ + p^+ \rightarrow \Delta^{++},$$

and the $\Omega^-(sss)$ appeared to violate the Pauli exclusion principle, because all three fermions were in a symmetric spin-flavor-spatial wavefunction. This led Greenberg to postulate the existence of a new quantum number in 1964 [Gre64] which could take on one of three values. This additional quantum number later evolved into the concept of ‘color,’ the charge associated with the force holding the quarks together. Thus, every flavor of quark comes in three ‘colors’: ‘red’, ‘green’, or ‘blue.’ The color hypothesis holds that all hadrons are colorless states (combinations of all three colors in the case of baryons, or a color-anticolor combination in the case of mesons). A profound and disturbing prediction is that the fundamental building blocks themselves, the quarks, could never be observed in isolation. This phenomenon is known as ‘color confinement.’

Experimental verification for quarks came from the SLAC (Stanford Linear Accelerator Center) experiments performed under “Pief” Panofsky [CG89] in the late 1960s using a beam of electrons directed onto a hydrogen target. The goal of the experiments was to repeat the Rutherford experiment, but at energies high enough (up to about 18 GeV) to probe the structure of the proton by deep inelastic scattering. They found that the proton did indeed contain concentrations of charge which were ‘point-like’ in comparison to its spatial extent. High energy electrons were unable to knock isolated quarks out of hadrons as expected from the color confinement hypothesis. On the other hand, it appeared that quarks behaved as free particles within the hadrons. This vanishing of the color force at high scattering energies (short distance resolution) is known as *asymptotic freedom*.

In 1974, the J/Ψ , a meson containing a new heavier flavor of quark dubbed the ‘charm’ was discovered independently at Brookhaven and SLAC. Currently, a total of six quark flavors has been identified.

Other experiments measured the ratio of cross sections

$$\frac{\sigma(e^+e^- \rightarrow \text{hadrons})}{\sigma(e^+e^- \rightarrow \mu^+\mu^-)},$$

as a function of center of mass energy. At lower energies, only $u\bar{u}$ and $d\bar{d}$ quark pairs can be created¹⁰. However, as the center of mass energy increases, it reaches the threshold where the more massive $s\bar{s}$ pairs can be produced, then $c\bar{c}$ pairs and so on. Because each quark comes in one of three colors, there is an overall factor of three in the reaction rate. These experiments provided an impressive confirmation of the existence of exactly three colors [PRSZ99].

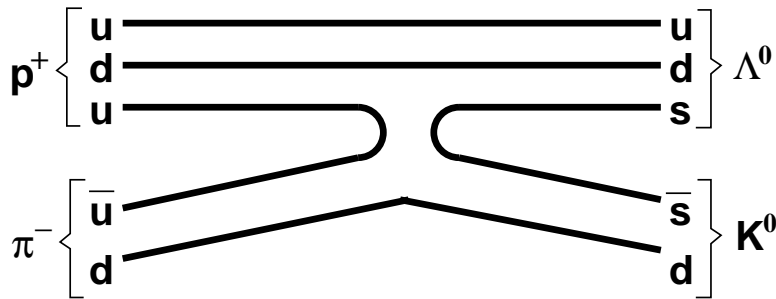


Figure 1.3: The quark model view of the reaction $\pi^- + p^+ \rightarrow K^0 + \Lambda^0$. Time increases from left to right. The up quark and antiquark annihilate, and a new strange quark-antiquark pair appears.

1.6 The Standard Model

Currently, the interactions among objects can be understood in terms of three basic forces: the force of gravity, the electroweak force, and the strong nuclear force.

The electroweak and strong interactions are treated in a theoretical framework known as the Standard Model, which successfully predicts virtually all observed phenomena in particle physics. In the Standard Model, matter consists of quarks and leptons (and associated antiparticles), which are described by quantum field theories possessing a local gauge symmetry. This local gauge symmetry gives rise to the interactions among the quarks and leptons mediated by ‘gauge bosons.’ The electroweak gauge bosons are the massless γ (photon), and the massive W^\pm and Z^0 which acquire their mass (it is believed¹¹) from the Higgs boson H via the ‘Higgs mechanism.’ The strong gauge bosons are the massless gluons (see Table 1.2).

It is widely recognized that this model is incomplete (most conspicuously, it fails to cleanly integrate gravity with the other forces), and there is active research into extensions and

¹⁰The dynamics of the strong interaction is independent of quark flavor, but the kinematics does in general depend on the masses of the different quark flavors.

¹¹The Higgs boson has not yet been observed experimentally.

revisions. For this work, we will focus on extracting predictions from quantum chromodynamics, that component of the Standard Model which defines the dynamics of the quarks and which gives rise to the strong nuclear force.

Generation	Leptons	Quarks
I	e, ν_e	d, u
II	μ, ν_μ	s, c
III	τ, ν_τ	b, t

Gauge Bosons
$(\gamma, W^\pm, Z^0), g$

Table 1.2: The standard model of particle interactions. This model describes all matter as made up of quarks and leptons, held together by the interactions of the force-carrying mediators. The Higgs boson is the only particle of the Standard Model which has not been observed, and is not shown.

1.7 Quantum chromodynamics

1.7.1 Quantum field theory

Quantum field theory (QFT) is the extension of quantum mechanics to relativistic systems, allowing for a unified description of matter and radiation fields. The first foundations of QFT were laid by Dirac in his 1927 paper [Dir27] which treated the emission and absorption of electromagnetic radiation by atoms.

A quantum field theory is based on a Hilbert space of possible physical states of the system. The fundamental degrees of freedom are fields of operators which act on the Hilbert space and which are defined over a space-time manifold.

Natural units are used in which $\hbar = c = 1$. In Minkowski (flat) space-time, points are labeled by $(x^0, x^1, x^2, x^3) \equiv (t, \vec{x})$ with respect to some basis with associated metric $\eta_{\mu\nu} = \text{diag}(1, -1, -1, -1)$. Quantities of the form¹²

$$\eta_{\mu\nu}(x^\mu - y^\mu)(x^\nu - y^\nu) \equiv (x^\mu - y^\mu)(x_\mu - y_\mu) = (x^0 - y^0)^2 - (\vec{x} - \vec{y}) \cdot (\vec{x} - \vec{y})$$

are invariant under the Poincaré group of translations, rotations, and relativistic boosts. The fields in QFT may have indices which label different components, and usually these components are required to transform irreducibly under the Poincaré group [Ram90]. This means that an arbitrary Poincaré transformation R (e.g. a rotation) transforms the field Φ_a as:

$$\Phi_a(x) \rightarrow \Phi'_a(x) = \Phi_b(R^{-1}x)D_{ba}(R),$$

¹²Summation over repeated indices is implied unless noted otherwise.

where $D(R)$ is an irreducible¹³ representation matrix representing the effect of R on the components of the field. In general, there are many different irreducible representations allowing for the definition of a different type of field for each.

The Poincaré group has ten generators. Two operators which commute with all of the generators of the Poincaré group are called Casimir operators and consist of the mass and the relativistic spin. Thus, we label the different types of fields by their mass and spin.

In the Heisenberg operator picture, we single out the time direction and treat the degrees of freedom at a given time as operators with eigenvectors and associated eigenvalues:

$$\Phi(\vec{x}; t)|\phi; t\rangle = \phi(\vec{x}; t)|\phi; t\rangle.$$

For fixed t , all of the spatial points \vec{x} are space-like separated, which allows us to define $|\phi; t\rangle$, the simultaneous eigenstate for all of the operators at different spatial locations at time t . The eigenvectors represent the possible states of the field at time t and form a complete (Hilbert) space:

$$\begin{aligned} \langle\phi; t|\phi'; t\rangle &= \delta(\phi - \phi') \\ \int d\phi |\phi; t\rangle\langle\phi; t| &= 1 \end{aligned}$$

with the appropriate definition of the inner product and integration measure. A general state of the system at time t is specified by the state-vector $|\psi; t\rangle$, and the probability amplitude¹⁴ of the system to be in state $|\psi'; t'\rangle$ if it was known that it was in the state $|\psi; t\rangle$ at $t < t'$ is given by the inner product

$$\langle\psi'; t'|\psi; t\rangle.$$

A field at a spatial location \vec{x} evolves in time via the Heisenberg time-evolution equation:

$$\Phi(\vec{x}; t') = e^{iH(t'-t)}\Phi(\vec{x}; t)e^{-iH(t'-t)}$$

where H is the Hermitian Hamiltonian operator, the Poincaré generator of temporal translations. The Hamiltonian operator governs the dynamics of the theory, and its spectrum consists of the steady states of the theory, including all stable single- and multi-particle energy states. In order for the particle content of the field theory to be well-defined, the Hamiltonian must be bounded from below. Subtracting a suitable constant from H , we may define the ‘vacuum’ state $|\Omega\rangle$, the time-independent state of lowest energy:

$$H|\Omega\rangle = 0$$

¹³A representation of a group is a set of matrices $\{D\}$ which satisfies $D(R)D(R') = D(RR')$ for all R and R' in the group. The representation is irreducible if there is no invariant subspace which only mixes with itself under the group operations, i.e. if the representation matrices cannot all be simultaneously block diagonalized.

¹⁴In quantum theory, the probability of a particular observed outcome is given by the absolute square of the sum of the probability amplitudes for all of the ways that outcome could occur. The fields may not be directly observable, but we may always speak of the probability *amplitude* for a particular configuration’s contribution to a process.

By the action of a suitable operator, any state may be excited from the vacuum:

$$|\phi; t\rangle = \mathcal{O}_\phi(t)|\Omega\rangle$$

Because all operators of interest can be expressed as analytic functions of the fundamental degrees of freedom of the theory, all of the information about the properties and dynamics of the theory is contained in the so called Green's functions, the vacuum expectation values of products of fields, such as:

$$\langle\Omega|T[\Phi(\vec{x}_b; t_b)\Phi(\vec{x}_a; t_a)]|\Omega\rangle,$$

where $T[\dots]$ is the right-to-left time ordering operator which arranges the fields in time order from earliest on the right to latest on the left.

Inspired by the work of Dirac, Richard Feynman developed the path integral approach to quantum mechanics in 1948 [Fey48], which was quickly extended to quantum field theory. His work made possible the evaluation of vacuum expectation values (VEVs) by use of the Feynman functional integral [PS95]:

$$\begin{aligned} \langle\Omega|T[\Phi(\vec{x}_b; t_b)\Phi(\vec{x}_a; t_a)]|\Omega\rangle &= \lim_{\epsilon\rightarrow 0} \lim_{T\rightarrow\infty(1+i\epsilon)} \frac{\int \mathcal{D}\phi \phi(\vec{x}_b; t_b)\phi(\vec{x}_a; t_a) \exp\{iS[\phi]\}}{\int \mathcal{D}\phi \exp\{iS[\phi]\}} \\ &= \lim_{\epsilon\rightarrow 0} \lim_{T\rightarrow\infty(1+i\epsilon)} \frac{1}{Z[0]} \frac{\delta}{\delta J(\vec{x}_b; t_b)} \frac{\delta}{\delta J(\vec{x}_a; t_a)} Z[J] \Big|_{J=0} \end{aligned}$$

where

$$Z[J] \equiv \int \mathcal{D}\phi \exp\{iS[\phi] + iJ\phi\}$$

is a generating functional of the fields, and

$$S[\phi] \equiv \int_{-T/2}^{T/2} dt \int_V d^3x \mathcal{L}(\phi, \partial\phi)$$

is the *action* functional, the space-time integral of the Lagrangian density \mathcal{L} which determines the dynamics of the theory.¹⁵

In practice, the infinite-dimensional functional integral over field configurations ϕ is ill-defined. In order to calculate quantities in quantum field theory, we work in a finite box and introduce a regulator which makes the integrals convergent. The regulator is then removed by using the method of renormalization, which allows the 'bare' parameters in the

¹⁵ When the magnitude of the action is large (in units of \hbar), then the theory becomes classical and the expectation values are dominated by values of the field around which the phase remains stationary. This principle of stationary phase (often referred to as the 'principle of least action') gives the Euler-Lagrange equations which govern all of classical mechanics:

$$\frac{\delta S}{\delta\phi} = 0 \rightarrow \partial_\mu \left(\frac{\delta\mathcal{L}}{\delta(\partial_\mu\phi)} \right) - \frac{\delta\mathcal{L}}{\delta\phi} = 0$$

original Lagrangian (such as mass, coupling, and field normalization) to vary as functions of the regulator parameter. These bare parameters are not observable, and can be used to absorb the divergences encountered in the theory. It is not always possible to do this; in non-renormalizable theories the divergences cannot all be absorbed into the small number of original bare parameters.

1.7.2 Reference frame covariance

The concept of reference frame covariance [Mor83, Sch85] was developed in Einstein's Special and General Theories of Relativity and states simply that coordinate systems at different space-time points may have different orientations. A physical quantity represented by a vector v can always be written as a linear combination of some basis vectors $\{\hat{\eta}_{(a)}\}$ with coefficients v^a :

$$v = v^a \hat{\eta}_{(a)}$$

where summation over repeated indices is implied. The basis vectors are abstract entities which define some reference frame, and the components are simply numbers which express the orientation of the vector within that reference frame. The vector v is an abstract entity and is independent of the choice of reference frame. A different reference frame corresponds to a different set of basis vectors $\{\hat{\eta}'_{(a)}\}$ and coefficients $\{v'^a\}$, but the vector v remains unchanged:

$$v = v'^a \hat{\eta}'_{(a)}$$

General relativity postulates that a reference frame can only be defined locally. If we want to make meaningful comparisons of the components of a vector field $\{v^a(x)\}$ at two different points, we need a way to specify the relative orientations of the basis vectors at those points. Manifolds are locally flat, which means that we can define vectors connecting the points in a small neighborhood of x using a basis $\{\hat{e}_{(\mu)}\}$. Because the neighborhood is flat, we can always write the basis vectors at $x + \epsilon \hat{e}_{(\mu)}$ as linear combinations of the basis vectors at x :

$$\hat{\eta}_{(a)}(x + \epsilon \hat{e}_{(\mu)}) = \hat{\eta}_{(a)}(x) + ig \epsilon \hat{\eta}_{(b)}(x) A_{\mu ba}(x) + O(\epsilon^2)$$

which gives the correct behavior as $\epsilon \rightarrow 0$. We have pulled out a factor of ig for later convenience and have not yet specified the form of the *connection* $A_{\mu ab}(x)$. We now have a way of expressing the components of a vector at $x + \epsilon \hat{e}_{(\mu)}$ on the same basis as the components of a vector at x :

$$\begin{aligned} v(x + \epsilon \hat{e}_{(\mu)}) &= v^a(x + \epsilon \hat{e}_{(\mu)}) \hat{\eta}_{(a)}(x + \epsilon \hat{e}_{(\mu)}) \\ &= v^a(x + \epsilon \hat{e}_{(\mu)}) (\hat{\eta}_{(a)}(x) + ig \epsilon \hat{\eta}_{(b)}(x) A_{\mu ba}(x) + O(\epsilon^2)) \\ &= [(\delta_{ab} + ig \epsilon A_{\mu ab}(x)) v^b(x + \epsilon \hat{e}_{(\mu)})] \hat{\eta}_{(a)}(x) + O(\epsilon^2) \\ &\equiv [U_{ab}(x, x + \epsilon \hat{e}_{(\mu)}) v^b(x + \epsilon \hat{e}_{(\mu)})] \hat{\eta}_{(a)}(x), \end{aligned}$$

where we have introduced the infinitesimal linear *parallel transporter*

$$U(x, x + \epsilon \hat{e}_{(\mu)}) = 1 + ig \epsilon A_{\mu}(x) + O(\epsilon^2)$$

which expresses the components of a vector at $x + \hat{e}_{(\mu)}$ with respect to the basis at x . Alternatively, we may say that the parallel transporter moves a vector from $x + \epsilon \hat{e}_{(\mu)}$ to x while keeping it (locally) parallel to its original orientation.

$$U(x, x + \epsilon \hat{e}_{(\mu)}) : \quad (x) \leftarrow (x + \epsilon \hat{e}_{(\mu)}).$$

We may build up a finite parallel transporter along a directed curve \mathcal{C}_{yx} from x to y by repeated application of the above. Break \mathcal{C}_{yx} up into an $N + 1$ point mesh $\{z_0, z_1, \dots, z_N\}$ where $z_0 = x$, $z_N = y$, and the distance between z_k and z_{k-1} is ϵ . Letting $dz_k = z_k - z_{k-1}$ we may define the left-to-right *path ordered exponential* by [Rot97]:

$$\begin{aligned} U(\mathcal{C}_{yx}) &= \mathcal{P} \exp \left\{ ig \int_{\mathcal{C}_{yx}} dz^\mu A_\mu(z) \right\} \\ &\equiv \lim_{\epsilon \rightarrow 0} (1 + ig dz_1^\mu A_\mu(z_0)) (1 + ig dz_2^\mu A_\mu(z_1)) \cdots (1 + ig dz_N^\mu A_\mu(z_{N-1})) \end{aligned}$$

We may also define the covariant derivative D_μ , which takes into account both the spatial change and basis change of $v^a(x)$ under an infinitesimal displacement ϵ in the μ^{th} direction $\hat{e}_{(\mu)}$

$$\begin{aligned} D_\mu v^a(x) &\equiv \lim_{\epsilon \rightarrow 0} \frac{U_{ab}(x, x + \epsilon \hat{e}_{(\mu)}) v^b(x + \epsilon \hat{e}_{(\mu)}) - v^a(x)}{\epsilon} \\ &= \lim_{\epsilon \rightarrow 0} \frac{(\delta_{ab} + ig \epsilon A_{\mu ab}(x)) v^b(x + \epsilon \hat{e}_{(\mu)}) - v^a(x)}{\epsilon} \\ &= (\delta_{ab} \partial_\mu + ig A_{\mu ab}(x)) v^b(x) \end{aligned}$$

The significance of this approach is two-fold. First, the quantity $(D_\mu v^a(x)) \hat{\eta}_{(a)}$ is a proper abstract vector; the components transform ‘covariantly’ under operators on the vector space. Second, the connection $A(x)$ encapsulates any non-trivial topological properties of the space of different coordinate systems on which the vector is defined. For example, the surface of a sphere is locally flat, but has a path-dependent parallel transporter $U(\mathcal{C})$ as can be seen in figure 1.4.

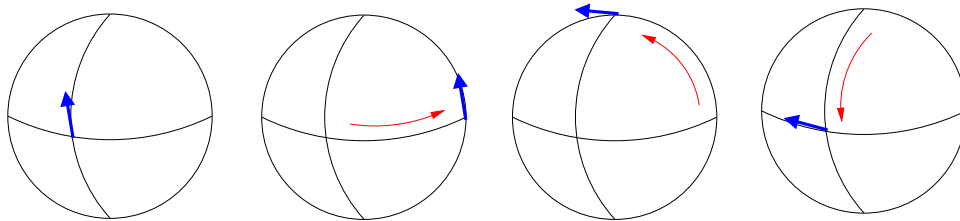


Figure 1.4: An example of parallel transport around a non-trivial manifold. The blue arrow ends up in a different orientation even though it made only locally parallel moves.

1.7.3 Quantum electrodynamics

Hermann Weyl had attempted to apply the concept of local gauge symmetry to electrodynamics in 1919. He suggested that one could choose a different scale, or gauge, at each point in space, but this idea was quickly proven incorrect (e.g. the atom had an observable characteristic scale). He succeeded, however, in the late 1920's along with Fock and London to identify the the ‘coordinate system’ of relevance in electrodynamics. An electron’s quantum mechanical wavefunction $\psi(x)$ can be rotated by a global phase without changing the dynamics of the theory. They postulated that the phase of an electron’s wavefunction was a local quantity and required that comparisons of the phase at two different points x and y required the use of the parallel transporter

$$U(\mathcal{C}_{yx}) = \mathcal{P} \exp \left\{ ig \int_{\mathcal{C}_{yx}} dz^\mu A_\mu(z) \right\}$$

where the *gauge* field $A_\mu(x)$ is a real-valued field.

Dirac had already found a quantum field theory describing a free electron when he sought to write a relativistic form of Schrödinger equation (which is first order in the time derivative) by factoring the relativistic energy-momentum expression [Gri87]:

$$(p^\mu p_\mu - m^2) = (\gamma^\mu p_\mu + m)(\gamma^\nu p_\nu - m)$$

where the four Dirac matrices γ^μ must satisfy

$$\{\gamma^\mu, \gamma^\nu\} = \gamma^\mu \gamma^\nu + \gamma^\nu \gamma^\mu = 2g^{\mu\nu} \quad (1.1)$$

The Dirac equation of motion $(i\gamma^\mu \partial_\mu - m)\psi = 0$ comes from the classical limit of the quantum field theory described by the Dirac Lagrangian [PS95]:

$$\mathcal{L}_{\text{Dirac}} = \bar{\psi}(i\gamma^\mu \partial_\mu - m)\psi$$

where $\psi(x)$ is the electron field and $\bar{\psi}(x) \equiv \psi^\dagger(x)\gamma^0$. In order to have a real action (leading to a Hermitian Hamiltonian), we must have $(\gamma^0 \gamma^\mu)^\dagger = (\gamma^0 \gamma^\mu)$ and $\gamma^{0\dagger} = \gamma^0$, or equivalently:

$$\gamma^{0\dagger} = \gamma^0, \quad \gamma^{j\dagger} = -\gamma^j \quad (1.2)$$

Replacing the regular derivative in $\mathcal{L}_{\text{Dirac}}$ with a covariant derivative gives rise to an electromagnetic interaction term:

$$\begin{aligned} \bar{\psi}(x)(i\gamma^\mu \partial_\mu - m)\psi(x) &\rightarrow \bar{\psi}(x)(i\gamma^\mu D_\mu - m)\psi(x) \\ &= \bar{\psi}(x)(i\gamma^\mu \partial_\mu - m)\psi - gA_\mu(x)\bar{\psi}(x)\gamma^\mu\psi(x) \\ &= \mathcal{L}_{\text{Dirac}} + \mathcal{L}_{\text{Int}} \end{aligned}$$

Where we see that the gauge field $A_\mu(x)$ is to be identified with the electromagnetic potential, $\bar{\psi}\gamma^\mu\psi$ is the electron probability ‘current’ (which transforms as a Poincaré

4-vector), and $g = -|e|$ is the electron charge, the coupling constant for the electromagnetic interaction between the electron field ψ and electromagnetic field A .

This theory possesses an important symmetry: local gauge invariance. The Lagrangian is unchanged under local gauge transformations (picking a new phase at each space-time point, and updating the connection accordingly):

$$\begin{aligned}\psi(x) &\rightarrow e^{i\alpha(x)}\psi(x) \\ \bar{\psi}(x) &\rightarrow \bar{\psi}(x)e^{-i\alpha(x)} \\ A_\mu(x) &\rightarrow A_\mu(x) - \frac{1}{g}\partial_\mu\alpha(x).\end{aligned}$$

Quantum field theories which are based on a local gauge symmetry are known as *gauge* theories. In 1971, Gerard 'tHooft [tH71] showed that all gauge theories were renormalizable. This was a critical success for gauge theory, because it means that calculations are guaranteed to give finite results for physical processes as the regulator is removed.

In analogy with General Relativity and figure 1.4, the field strength tensor is associated with the curvature of the gauge field, the amount the phase changes around an infinitesimal square loop [Sch85, MM94] in the $\mu - \nu$ plane:

$$F_{\mu\nu} \equiv \frac{1}{ig}[D_\mu, D_\nu]$$

Considering first

$$\begin{aligned}D_\mu D_\nu &= \frac{1}{ig}(\partial_\mu + igA_\mu(x))(\partial_\nu + igA_\nu(x)) \\ &= \frac{1}{ig}\partial_\mu\partial_\nu + \partial_\mu A_\nu(x) + A_\nu(x)\partial_\mu A_\mu(x)\partial_\nu + ig^2 A_\mu A_\nu\end{aligned}$$

we see that

$$\begin{aligned}F_{\mu\nu} \equiv \frac{1}{ig}[D_\mu, D_\nu] &= \partial_\mu A_\nu - \partial_\nu A_\mu + ig[A_\mu, A_\nu] \\ &= D_\mu A_\nu - D_\nu A_\mu\end{aligned}\tag{1.3}$$

The gauge group of electrodynamics is the group of all unimodular complex phases $U(1)$. Because $U(1)$ is Abelian (commutative), the commutator in 1.3 vanishes and we are left with the familiar expression

$$F_{\mu\nu} = \partial_\mu A_\nu - \partial_\nu A_\mu$$

The kinetic term in quantum electrodynamics gives Maxwell's equations in the classical limit, and is obtained by considering the simplest gauge-invariant quantity involving the field strength tensor:

$$\mathcal{L}_{\text{Maxwell}} = -\frac{1}{4}F_{\mu\nu}F^{\mu\nu}.$$

Putting it all together gives the Lagrangian describing quantum electrodynamics (QED), one of the most successful theories in the history of physics:

$$\begin{aligned}
 \mathcal{L}_{\text{QED}} &= \mathcal{L}_{\text{Dirac}} + \mathcal{L}_{\text{Int}} + \mathcal{L}_{\text{Maxwell}} \\
 &= \bar{\psi}(i\gamma^\mu D_\mu - m)\psi - \frac{1}{4}F_{\mu\nu}F^{\mu\nu} \\
 D_\mu &\equiv \partial_\mu + igA_\mu \\
 F_{\mu\nu} &\equiv D_\mu A_\nu - D_\nu A_\mu = \partial_\mu A_\nu - \partial_\nu A_\mu
 \end{aligned}$$

QED is formulated on a flat space-time manifold, but may have curvature in ‘phase space’ described by $A_\mu(x)$. If the phase space is flat, then the parallel transporter will be path independent, meaning that A is a total derivative of some function. In such a case, we can perform a local gauge transformation which eliminates the electromagnetic field: $A \rightarrow 0$. Thus we see that if we treat the electron phase as an internal degree of freedom, it can give rise to electromagnetic interactions as a result of curvature in this internal coordinate space.

The gauge field can be quantized to give the mediating boson of the gauge force. $U(1)$ has only one parameter $A_\mu(x)$, and thus there is only one gauge boson of the quantized theory, the photon.

1.7.4 From pions to the Standard Model

In 1936, Breit [BCP36] discovered that the strong nuclear force was blind to electric charge. That is, the strong nuclear force between two protons was the same as the strong nuclear force between a proton and neutron, or between two neutrons. Heisenberg suggested that the proton and neutron were two states in the ‘isospin’ doublet:

$$N = \begin{pmatrix} p \\ n \end{pmatrix}.$$

Yang and Mills promoted isospin to a local gauge symmetry by introducing a connection based on the $SU(2)$ gauge group, the set of all complex 2×2 matrices with unit determinant. This allowed for the identity of the proton and neutron to vary as a function of position. The Yang-Mills $SU(2)$ gauge field was shown to describe the pion in the same way that the $U(1)$ field describes the photon. In the case of $SU(2)$, there are three generators yielding three gauge bosons, the π^- , π^0 , and π^+ .

Physicists then searched for the ‘correct’ gauge theories describing the interactions of the standard model. Work on the electroweak Lagrangian describing the interactions of leptons and quarks via the W^\pm , Z^0 , and γ gauge bosons was started in 1961 by Glashow [Gla61], completed in 1967 by Weinberg [Wei67] and Salam [Sal68], and is based on the $SU(2) \times U(1)$ gauge group.

1.7.5 Quantum Chromodynamics

Quantum chromodynamics (QCD) is the gauge theory describing the interactions of quarks and is the primary focus of this dissertation. Fritzsche and Gell-Mann [FGM72, FGML73] identified the quark color as the fundamental charge associated with QCD. Quark fields come in six flavors, possess four spin components (which transform irreducibly under Poincaré transformations), and have three color components. Let the quark field be denoted by $\psi_{\alpha a}^A(x)$, where A is the flavor index, α is the spin index, and a is the color index. In this section we will focus on the behavior of the color index, and will suppress indices where possible for simplicity of notation.

The color reference frame (defining the directions of ‘red’, ‘green’, and ‘blue’) is defined locally. The infinitesimal linear parallel transporter defining the covariant derivative is now an $SU(3)$ matrix instead of a $U(1)$ phase:

$$U_{ab}(x, x + \epsilon \hat{e}_{(\mu)}) = \exp(ig\epsilon A_{\nu}^c(x) \frac{\lambda^c}{2})_{ab}$$

where the λ^a are the eight 3×3 traceless Hermitian Gell-Mann matrices which generate the $SU(3)$ group. $SU(3)$ is the non-Abelian (non-commutative) group of 3×3 complex unitary matrices with unit determinant.

We get the covariant derivative $D_{\mu} = \partial_{\mu} + igA_{\mu}$ by defining

$$A_{\mu}(x) \equiv \frac{1}{2} A_{\mu}^a(x) \lambda^a.$$

This gives us eight real gauge fields $A_{\mu}^a(x)$ which transform as vectors under Poincaré transformations. They represent eight spin-1 gluons, the gauge bosons which mediate the QCD interactions among quarks. The spin-1/2 quarks are represented by Grassmann (anticommuting) fields which transform as Dirac spinors under Poincaré transformations. In a hypothetical free field theory where $A = 0$ (all the links are unity), the quantum operator $\bar{\Psi}$ creates a quark state and annihilates an anti-quark state while Ψ annihilates a quark and creates an anti-quark. In the general interacting theory ($A \neq 0$), we will still refer to $\bar{\Psi}$ as a *quark source* and Ψ as a *quark sink*.

The gluon field strength tensor is given again by the curvature of the gauge field, this time with a non-vanishing gauge field commutator $[A_{\mu}, A_{\nu}]$:

$$\begin{aligned} F_{\mu\nu} \equiv \frac{1}{ig} [D_{\mu}, D_{\nu}] &= D_{\mu} A_{\nu} - D_{\nu} A_{\mu} \\ &= \partial_{\mu} A_{\nu} - \partial_{\nu} A_{\mu} + ig[A_{\mu}, A_{\nu}], \end{aligned}$$

The new commutator term can be expressed in terms of the gluon fields by using the fact that the Gell-Mann matrices $\{\lambda_a\}$ obey the $SU(3)$ Lie Algebra

$$[\lambda_a, \lambda_b] = i2f_{abc}\lambda_c,$$

where the f_{abc} are the completely antisymmetric $SU(3)$ structure constants defining the group.

$$\begin{aligned} ig[A_\mu, A_\nu] &= \frac{ig}{4} A_\mu^a A_\nu^b [\lambda^a, \lambda^b] \\ &= -\frac{g}{2} f_{abc} A_\mu^a A_\nu^b \lambda^c = -\frac{g}{2} f_{abc} A_\mu^b A_\nu^c \lambda^a \end{aligned}$$

Therefore

$$\begin{aligned} F_{\mu\nu} &= \frac{1}{2} F_{\mu\nu}^a \lambda^a, \\ F_{\mu\nu}^a &\equiv \partial_\mu A_\nu^a - \partial_\nu A_\mu^a - gf_{abc} A^b A^c \end{aligned}$$

Using the fact that $\text{Tr}(\lambda^a \lambda^b) = 2\delta^{ab}$, we may put these gauge-invariant pieces together to define the QCD Lagrangian density, the functional defining the dynamics of the interaction of quarks and gluons:

$$\begin{aligned} \mathcal{L}_{\text{QCD}} &\equiv \bar{\psi}(i\gamma^\mu D_\mu - M)\psi - \frac{1}{2}\text{Tr}(F_{\mu\nu}F^{\mu\nu}), \\ D_\mu &\equiv \partial_\mu + igA_\mu, \\ A_\mu &\equiv \frac{1}{2}A_\mu^a \lambda^a \\ F_{\mu\nu} &\equiv \frac{1}{2}F_{\mu\nu}^a \lambda^a, \\ F_{\mu\nu}^a &\equiv \partial_\mu A_\nu^a - \partial_\nu A_\mu^a - gf_{abc}A^b A^c \\ M &\equiv \text{diag}(m_d, m_u, m_s, m_c, m_b, m_t). \end{aligned}$$

In the above, M in a 6×6 matrix in flavor space, γ^μ is a 4×4 matrix in spin space, and λ^a is a 3×3 matrix in color space. In other spaces, the matrices appear as the identity (e.g. γ^μ acts as the identity in color space). The trace is taken with respect to color. The non-Abelian nature of QCD introduces three- and four gluon interactions through the kinetic term $-\text{Tr}(F_{\mu\nu}F^{\mu\nu})/2$. These gauge field self-interaction terms are believed to reproduce the desirable properties of asymptotic freedom and color confinement. Also, the strong nuclear force binding nucleons together in the nucleus is seen to be a van der Waals-type residual interaction among the quarks in different nucleons.

1.7.6 Calculating in quantum chromodynamics

The Lagrangian density \mathcal{L}_{QCD} completely determines the dynamics and properties of quantum chromodynamics. However, theorists still need to calculate complicated integrals of the form¹⁶

$$\frac{1}{Z} \int \mathcal{D}\bar{\psi} \mathcal{D}\psi \mathcal{D}A f(\bar{\psi}, \psi, A) \exp \{iS[\bar{\psi}, \psi, A]\},$$

¹⁶The exact integrals we will need will be discussed in the next chapter.

where

$$Z = \int \mathcal{D}\bar{\psi}\mathcal{D}\psi\mathcal{D}A \exp \{iS[\bar{\psi}, \psi, A]\}.$$

At high energies, asymptotic freedom tells us the interactions among quarks are weak, and can thus be described using perturbation theory. Perturbative QCD treats the exponential as a power series expansion in the strong coupling constant g . At high energies, or equivalently short length scales (such as those probed in deep inelastic scattering experiments), the renormalized coupling constant becomes small and the power series is convergent. By calculating the ‘tree level’ and the first few ‘correction’ terms for various processes, theorists have shown that the predictions of QCD are in striking agreement with the results of high-energy experiments [Mut98].

At lower energies (e.g. below 2 GeV in e+p scattering, where Bjorken scaling is violated), we enter the domain of ‘nonperturbative phenomena,’ such as color confinement (hadronization). At these energies, the renormalized coupling constant becomes large, and perturbation expansions diverge badly.

1.7.7 The lattice regulator

In 1974, Kenneth Wilson introduced a regularization method [Wil74b] which made rigorous low-energy calculations in QCD possible for the first time. Wilson defined an action on a discrete space-time lattice with spacing a . This serves two purposes: first, if the lattice is introduced in a finite volume, the number of integration variables becomes finite and the integrals become well defined. Second, the lattice regulator introduces an ultraviolet cutoff at the scale of the inverse lattice spacing $1/a$, thus controlling divergences. The introduction of a regulator necessarily breaks symmetries of the theory, and it is hoped that these symmetries will be recovered in the continuum limit. For instance, the lattice regulator explicitly breaks Poincaré invariance.

Let the elementary lattice vectors which give the minimal displacement in each direction be denoted as:

$$\hat{\mu} \equiv a\hat{e}_{(\mu)}.$$

The *quark fields* are defined at each site as

$$\psi_{\alpha a}^A(x),$$

where x denotes the discrete site on the lattice, A is the flavor index, α is the Dirac spin index, and a is the color index. Rather than simply replacing the derivatives in the continuum action with finite differences, Wilson preserved local gauge invariance by working directly with *gauge links*, the $SU(3)$ parallel transporters defined on the elementary links between neighboring sites:

$$U_{\mu ab}(x) \equiv U_{ab}(x, x + \hat{\mu})$$

where a and b are color indices. For simplicity of notation, we will continue to suppress indices where possible. $SU(3)$ matrices U and Ω will always act on the color degrees of freedom, Dirac gamma matrices γ^μ will always act on the spin degrees of freedom, and the mass matrix M will always be $\text{diag}(m_d, m_u, \dots)$ and will act on the flavor degrees of freedom.

Under a local gauge transformation represented by $SU(3)$ matrices $\Omega(x)$ at each site, the quark fields and gauge links transform as:

$$\begin{aligned}\psi(x) &\rightarrow \Omega(x)\psi(x) \\ \bar{\psi}(x) &\rightarrow \bar{\psi}(x)\Omega^\dagger(x) \\ U_\mu(x) &\rightarrow \Omega(x)U_\mu(x)\Omega^\dagger(x + \hat{\mu}) \\ U_\mu^\dagger(x) &\rightarrow \Omega(x + \hat{\mu})U_\mu(x)\Omega^\dagger(x)\end{aligned}$$

This formulation allowed Wilson to form gauge-invariant expressions such as

$$\bar{\psi}(x)U_\mu(x)\psi(x + \hat{\mu})$$

and

$$\bar{\psi}(x + \hat{\mu})U_\mu^\dagger(x)\psi(x)$$

denoted pictorially in Figure 1.5.



Figure 1.5: Two gauge-invariant quark-antiquark operators. The quark and antiquark fields at neighboring sites x and $x + \hat{\mu}$ may be combined by use of a gauge link at x . The gauge link $U_\mu(x)$ parallel transports a color vector from $x + \hat{\mu}$ to x and the Hermitian conjugate gauge link $U^\dagger(x)$ transports a color vector in the opposite direction. Any gauge-invariant quark-antiquark operator can be formed by connecting the fields at any two sites by a suitable product of gauge links.

If we replace $D_\mu\psi(x)$ with the symmetric difference

$$\frac{1}{a}\nabla_\mu\psi(x) \equiv \frac{1}{2a} (U_\mu(x)\psi(x + \hat{\mu}) - U_\mu^\dagger(x - \hat{\mu})\psi(x - \hat{\mu}))$$

we get the fermion part of the action (in Minkowski space-time):

$$S_F^M \equiv \sum_x a^4 \bar{\psi}(x) (i\gamma^\mu \frac{1}{a} \nabla_\mu - M) \psi(x)$$

The exact form of fermion action we will use will be discussed in chapter 2. It differs from the above because we will work in Euclidean (not Minkowski) space-time, use an anisotropic lattice, absorb the factors of a to work in ‘lattice units,’ and add the ‘Wilson’ term which fixes a discretization problem (the ‘fermion doubling’ lattice artifact).

Another gauge-invariant quantity involving just the links is the *plaquette*, the trace (with respect to color) of a product of links around an elementary loop on the lattice:

$$U_{\mu\nu} \equiv \text{Tr}(U_\mu(x)U_\nu(x + \hat{\mu})U_\mu^\dagger(x + \nu)U^\dagger(x)),$$

denoted in figure 1.6.

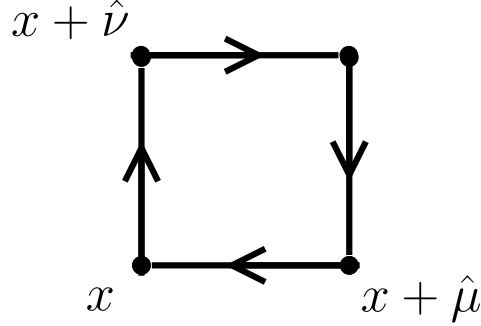


Figure 1.6: The gauge-invariant plaquette operator $U_{\mu\nu}(x)$.

The plaquette is the trace of the parallel transporter around an elementary loop. It is reasonable to expect that the plaquette is related to the field strength tensor, and this can be verified by writing $U_{\mu\nu}(x)$ in terms of the A fields using the Campbell-Baker-Hausdorff formula:

$$\exp(A)\exp(B) = \exp\left(A + B + \frac{1}{2}[A, B] + (\text{terms higher in A and B})\right).$$

Because we are interested in the continuum limit where $a \rightarrow 0$, we may write

$$U_\mu(x) \xrightarrow{a \rightarrow 0} \exp(igaA_\mu(x))$$

Then expanding the exponentials and keeping terms only up to order a^2 gives:

$$\begin{aligned} U_{\mu\nu}(x) &\equiv U_\mu(x)U_\nu(x + \hat{\mu})U_\mu^\dagger(x + \nu)U^\dagger(x) \\ &= \exp(igaA_\mu(x))\exp(igaA_\nu(x + \hat{\mu}))\exp(-igaA_\mu(x + \hat{\nu}))\exp(-igaA_\nu(x)) \\ &= \exp\left(iga^2(\nabla_\mu^f A_\nu(x) - \nabla_\nu^f A_\mu(x) + ig[A_\mu(x), A_\nu(x)]) + O(a^3)\right) \\ &\xrightarrow{a \rightarrow 0} \exp\left(iga^2F_{\mu\nu}(x) + O(a^3)\right) \end{aligned}$$

where

$$\nabla_\mu^f A_\nu(x) \equiv \frac{1}{a}(A_\nu(x + \hat{\mu}) - A_\nu(x)) \xrightarrow{a \rightarrow 0} \partial_\mu A_\nu(x)$$

is the forward lattice difference when applied to gauge fields, and we have evaluated all of the commutator terms at x , for example:

$$-\frac{g^2a^2}{2}[A_\mu(x), A_\nu(x + \hat{\mu})] = -\frac{g^2a^2}{2}[A_\mu(x), A_\nu(x)] + O(a^3)$$

Thus

$$\begin{aligned}
\text{Re Tr}(U_{\mu\nu}) &= \frac{1}{2}(\text{Tr}(U_{\mu\nu}) + \text{Tr}(U_{\mu\nu}^\dagger)) \\
&= \frac{1}{2}(\text{Tr}(U_{\mu\nu}) + \text{Tr}(U_{\nu\mu})) \\
&= \text{Tr}(1) - g^2 a^4 \frac{1}{2} \text{Tr}(F_{\mu\nu} F^{\mu\nu}) + O(a^5) \quad (\text{no sum})
\end{aligned}$$

because $F_{\nu\mu} = -F_{\mu\nu}$ (also because $\text{Tr}(F_{\mu\nu}) = 0$ for $SU(3)$). In the gauge action, we will write $N \equiv \text{Tr}(1)$.

The pure gauge (also called *Yang-Mills*) part of the lattice action (in Minkowski space-time) is thus given by [MM94]:

$$\begin{aligned}
S_G^M &\equiv -\frac{\beta}{N} \sum_x \sum_{\mu < \nu} \text{Re Tr}(1 - U_{\mu\nu}(x)), \quad \beta \equiv \frac{2N}{g^2}, \\
&= -\frac{2}{g^2} \sum_x \sum_{\mu < \nu} \{N - \text{Re Tr}(U_{\mu\nu})\}, \\
&= -2 \sum_x \sum_{\mu < \nu} a^4 \frac{1}{2} \text{Tr}(F_{\mu\nu} F^{\mu\nu}) + O(a^5). \\
&= -\sum_x \sum_{\mu, \nu} a^4 \frac{1}{2} \text{Tr}(F_{\mu\nu} F^{\mu\nu}) + O(a^5).
\end{aligned}$$

For $SU(3)$, $\beta = \frac{6}{g^2}$. In the case of Abelian gauge groups, the expression for β is divided by two in order to reproduce the continuum action to leading order in a [MM94].

1.7.8 Renormalization and integration

Wilson's lattice regulator breaks Poincaré invariance, but it maintains local gauge invariance which is crucial to ensuring that the regularized theory is renormalizable. In the continuum limit ($\lim a \rightarrow 0$), it is easy to see that Poincaré invariance is restored. Any quantity calculated using the lattice regulator will equal the continuum quantity plus an infinite number of $O(a)$ terms. There is no way to guarantee that the total effect of these terms will vanish as $a \rightarrow 0$ (a series of terms may combine to give an $O(1/a)$ contribution which will remain in the continuum limit). Thus it is critical to make a theory which is renormalizable at finite a .

Another advantage is that the Wilson action is a functional of the gauge links $U_\mu(x)$, which are compact gauge fields. This means that the parameter space we must integrate over is closed. In contrast, the underlying gauge fields $A_\mu^a(x)$ may take any value in the open set $(-\infty, \infty)$. There are an infinite number of values of $A_\mu^a(x)$, related by gauge transformations, that correspond to a single value of the gauge link $U_\mu(x)$. This gauge

freedom implies that gauge fixing must be used in integrals over the A fields to avoid divergences. No gauge fixing is required when integrating over the gauge links directly [Wil74b].

The coupling constant g is renormalized by tuning $\beta = 6/g^2$ and calculating some physical quantity to get a . In this way, we may send a to zero by increasing β . When all ratios become independent of a , then we have reached the *scaling regime*. Similarly, we may renormalize the quark masses by tuning the bare quark masses while measuring the pion mass m_π and watching the ratios of different calculated masses. It is hoped that these parameters will ‘flow’ to a critical point where the theory will reproduce the predictions of continuum QCD.

The appearance of the *inverse* power of the coupling constant in $\beta = 6/g^2$ allowed Wilson to calculate some, but not all, non-perturbative quantities using the so called strong coupling expansion. For instance, he showed that the static quark-antiquark potential increases linearly with separation in the Yang-Mills (pure gauge) $SU(3)$ theory, which is evidence that *QCD* may be confining in the continuum limit.

The lattice regulator is also perfectly suited for calculation on a computer. The framework of calculating QCD quantities using a lattice regulator on a computer is called *lattice QCD*. Starting from the work of Michael Creutz [CJR79] and others in 1979, lattice gauge theorists have applied the techniques of Monte Carlo integration discussed in chapter 3 to calculate increasingly ambitious quantities. This work is a contribution to one such effort: quantum operator design for the low-lying baryon spectrum.

1.8 Unresolved mysteries in hadronic physics

The high energy predictions of QCD obtained from perturbation theory do a spectacular job of describing the measurements of high-energy physics experiments. On the other hand, the low-energy behavior of QCD has not been thoroughly tested. This is due to the fact, mentioned above, that such calculations are nonperturbative with respect to the coupling constant of the theory. Fortunately, theoretical methods and computational power have now evolved to the point where the extraction of low-energy predictions from QCD has become feasible.

Predictions from lattice QCD will come at an opportune time; there are several ‘mysteries’ concerning the hadron spectrum which the constituent quark model, along with other QCD inspired models, have failed to resolve in a definitive manner.

1.8.1 Dynamics in the constituent quark model

The constituent quark model is able to predict the masses of many observed low-energy hadron resonances. It does this by treating the hadron states as either a quark-antiquark state (for mesons) or as a three-quark state (for baryons). The quark interactions lead to predictions of the total energy and quantum numbers of the state. Different quark models specify different interaction mechanism, but most consist of non-relativistic dynamics of the form (adapted from [H⁺02]):

1. A confining interaction, which is generally spin-independent.
2. A spin-dependent interaction, modeled after the effects of gluon exchange in QCD. For example, in the S-wave states, there is a spin-spin hyperfine interaction of the form

$$H_{HF} = -gM \sum_{i>j} (\vec{\sigma}\lambda_a)_i (\vec{\sigma}\lambda_a)_j$$

where M is a constant with units of energy. Spin-orbit interactions, although allowed, seem to be small. This may be due to relativistic QCD-inspired corrections such as a Thomas precession term [CI86].

3. A strange quark mass somewhat larger than the up and down quark masses, in order to split the $SU(3)$ flavor multiplets.
4. In the case of isoscalar mesons, an interaction for mixing $q\bar{q}$ configurations of different flavors (e.g. $u\bar{u} \leftrightarrow d\bar{d} \leftrightarrow s\bar{s}$), in a manner which is generally chosen to be flavor independent.

1.8.2 Missing baryon resonances

The constituent quark model predicts many more baryon resonances than have been observed experimentally. Because most of the observed baryon resonances have been produced from electron beams (electroproduction) or photon beams (photoproduction), it is possible that these ‘missing resonances’ are created in channels which have not yet been sufficiently examined. Experiments are currently underway using different types of beams (such as linearly polarized photons) to excite resonances through different processes.

An alternative explanation suggests that the missing resonances are due to an excess of degrees of freedom in the quark model. One proposed fix is to reduce the degrees of freedom by ‘locking’ two of the quarks of a baryon together in a di-quark configuration. In this picture, the higher resonances would be various single-quark excitations of the three-quark bound state.

Direct QCD calculations are needed to determine the properties of these missing resonances. Lattice QCD is in a position to identify the relevant degrees of freedom in a

Name	L	S	P	Oscillator Band
$N(939)$	0	1/2	+	0
$N(1440)$	0	1/2	+	2
$N(1535)$	1	1/2	-	1
$N(1650)$	1	3/2	-	1
$N(1710)$	0	1/2	+	2

Table 1.3: The lowest lying spin-1/2 nucleons. The numbers in parenthesis are the masses of the resonances in MeV, L is the orbital angular momentum of the quarks, S is the total spin of the quarks, and P is the parity of the state. The quark model treats the nucleon resonances as increasing excitations in an oscillator potential. The $N(1440)$, or Roper, is measured to be lower than predicted by the quark model.

baryon. Simulations can probe the spatial structure of the fields which compose the baryon state thus leading to a better understanding.

1.8.3 The Roper resonance

The simplest confining interaction in the quark model is the linear oscillator potential. If that potential is used, then the baryon spectrum can be divided into *oscillator bands*, which correspond to increasing excitations of the spatial wavefunctions with alternating parity. Within each band, the levels split according to spin-spin and spin-orbit interactions. Consider the five lowest known spin-1/2 nucleons ($J=1/2$, $I=1/2$) and their corresponding levels in the oscillator approximation [H⁺02] shown in table 1.8.3.

The $N(1440)$, known as the ‘Roper’ resonance, is the first excited even-parity nucleon state, but it is *below* the lowest odd-parity spin-1/2 nucleon state, the $N(1535)$. This is surprising [MCD⁺05], because most quark models treat the Roper as a radially-excited ‘breathing mode’ of the $N(939)$, which belongs to the second oscillator band having two nodes in the spatial wavefunction. On the other hand, the odd-parity state $N(1535)$ is modeled as an orbitally excited state in which the quarks have orbital angular momentum $L = 1$ with only one node in the spatial wavefunction.

Alternative models have proposed that the Roper resonance is a $qqqg$ hybrid state with excited glue or that it is a $qqqq\bar{q}$ five-quark molecular state. The mystery is complicated by the facts that the Roper has a wide width and has only been detected from phase shift analysis, never directly as an enhancement in the cross section.

1.8.4 The $\Lambda(1405)$

The $\Lambda(1405)$ having $I(J^P) = 0(\frac{1}{2}^-)$ is another puzzle in baryon spectroscopy [NNMS04]. In the quark model, the Λ series of resonances are described as different excitations of a three-quark uds flavor singlet system. Because the Λ contains a strange quark, the first odd-parity state would be expected to be above the first odd-parity nucleon, which contains only the lighter up and down quarks. However we see from table 1.8.3 that the $\Lambda(1405)$ is below the $N(1535)$, the first negative-parity nucleon. It has been proposed that the $\Lambda(1405)$ is a linear combination the three-quark uds state with two baryon-meson bound states $N\bar{K}$ and $\pi\Sigma$, where the Σ baryons have even parity, strangeness=-1, and $I(J^P) = 1(\frac{1}{2}^+)$.

Because the molecular states will mix with the three-quark state, lattice calculations are needed to determine the amount $qqqq\bar{q}$ contribution vs the amount of qqq contribution in the $\Lambda(1405)$. Understanding molecular hadronic states will lead to a better understanding of hadron structure and hadron reactions.

1.8.5 Exotic hadron states

The quark model treats hadron resonances as excitations of quarks in a confining potential with inter-quark interactions. It does not have anything to say about excitations of the gluon field. Laboratories are dedicating significant resources to the exploration of these ‘hybrid’ states of quarks bound by excited glue. QCD predicts that the gluon field can carry quantum numbers such as angular momentum, resulting in the possibility of *exotic* states, with quantum numbers inexplicable within the quark model. If such a state was found, it would be a significant low-energy validation of QCD. Two exotic $J^{PC} = 1^{-+}$ hybrid meson candidates have been tentatively identified at 1.6 GeV and 1.4 GeV in the $\rho\pi$ and $\eta\pi$ channels respectively by the E852 collaboration at BNL [A⁺98, C⁺99].

Lattice QCD theorists are assisting in this effort by calculating the properties of exotic mesons and baryons. Understanding hybrid states will lead to a better understanding of when and how the gluonic degrees of freedom play a role in the baryon spectrum.

1.8.6 Current experimental efforts

The spectrum is a fundamental quantity of QCD, yet remains incompletely understood by experimentalists and theorists alike. There are a number of high-precision baryon spectroscopy initiatives at laboratories including Jefferson Laboratory (JLab), BNL, Mainz, Graal, and BES.

CLEO-c at Cornell is committed to exploring heavy quark systems [Col01], Hall B at JLab is dedicated to mapping out the low-lying baryon spectrum, and the planned Hall D at JLab will search for exotic hadrons [Man05]. Each one of these efforts will rely on lattice

QCD calculations for valuable theoretical input. Such calculations will tell the experimentalists the quantum numbers of the states they may find, and will help them decide on the optimal energy ranges to explore.

1.9 Goal of this work

The need has never been greater for a systematic exploration of the hadron spectrum using the best theory we have, quantum chromodynamics. Unfortunately, low-energy features of QCD cannot be treated by perturbation expansions in the coupling constant. As the world's experimental dataset grows, so does the number of resonances which cannot be adequately described by QCD-inspired phenomenological models. The lattice approach allows us to numerically solve QCD, not just model it, and is currently the best tool for low-energy QCD calculations available.

The Lattice Hadron Physics Collaboration (LHPC) was formed in 2000, with the stated goal of using lattice QCD to understand the structure and interactions of hadrons [I⁺00]. One major goal of the collaboration is to calculate a significant portion of the low-lying spectrum of baryon resonances in QCD by developing and using the best possible methods in lattice QCD.

Spectrum calculations serve four main purposes. First, such calculations help answer the question: can QCD reproduce the observed hadron spectrum? Second, predictions of the energy and quantum numbers of new states will help the experimental community as they plan and design the next generation of experiments. Third, spectrum calculations help identify the important degrees of freedom in the theory. Specifically, theorists hope to identify subsets of configurations which dominate the functional integral. In thermodynamics, systems with an unmanageably large number of degrees of freedom can be described in terms of a few bulk properties such as pressure and specific heat. Similarly, lattice QCD may find a way to describe systems in quantum field theory in terms of a few dominant subsets of configurations. Such a description would facilitate the construction of simpler models and calculation schemes which would serve as an analytical complement to a fundamentally numerical approach. Among other things, such models may help us better understand the process of hadron formation in the early universe. Fourth, just as hydrogen spectroscopy led to the rapid development of quantum mechanics, so too may hadron spectroscopy lead to new theoretical breakthroughs.

This work presents the operator design, tuning, and pruning techniques developed during the course of my research. These methods have been used to achieve unprecedented signals for spectral states in the nucleon channel, and are readily extended to the other baryon channels (Δ , Λ , Σ , Ξ , \dots). This work describes both the methodology used in the operator design and the computational steps involved in tuning and pruning the operators. Specific operators are presented which can be used to extract the low-lying nucleon spectrum in future high-statistics, low-quark mass calculations. Preliminary heavy-quark quenched

spectrum results are given which, while unsuitable for comparison with experiment, do show the signal quality achieved by the operators. It is expected that these operators will play a valuable role in the LHPC's ongoing high-precision baryon spectrum calculations.

1.10 Organization of this dissertation

The formalism of extracting the spectrum of a quantum field theory is reviewed in chapter 2. We describe how QCD is formulated on a computer, how the Monte Carlo method is used to calculate expectation values of correlation functions of quantum operators, and what these functions can tell us about the spectrum of QCD. We discuss the role of Euclidean space-time correlation functions, a method for reliably extracting multiple excited states, and the importance of the lattice symmetry group in identifying the spin of the created states.

In chapter 3, we introduce the lattice-regulated formulation of QCD, and review the Monte Carlo method for evaluating functional integrals. We also discuss our error analysis methodology which uses bootstrap and jackknife resampling.

In chapter 4, we discuss construction of nucleon operators from the building blocks we have at our disposal on the lattice. We introduce smeared quark- and gauge-fields which provide a closer link between our operators and phenomenological models. Covariant displacement is discussed as a natural way to build up radial structure. We treat in detail the classification of our quantum operators based on their behavior under groups of symmetry transformations, and how this behavior relates to the continuum spin values of the states created by our operators.

In chapter 5, we discuss the combination of our operators into correlation matrices. We integrate out the quark degrees of freedom and reduce the problem to that of evaluating three-quark propagators. We then provide a detailed walk-through of the computational steps performed on the Carnegie Mellon University Medium Energy Physics computer cluster which allowed us to tune and select the best quantum operators for extracting the low-lying QCD spectrum.

The tuning of the operators is discussed in chapter 6, where stout-link gauge-field smearing is shown to reduce the noise of extended baryon operators, while Laplacian quark field smearing is shown to reduce the contamination in our baryon operators due to high-frequency modes. The systematic approach we developed to tune the smearing parameters is presented, and the optimal smearing parameter values are reported.

The construction of nucleon operators utilizing the symmetries of the lattice discussed in chapter 4 leads to a unmanageably large number of operators for our correlation matrices. Chapter 7 discusses the systematic approach we developed to prune these operators down to an optimal linear combination of sixteen operators.

These sixteen operators are then used to extract the low-lying nucleon spectrum on 200 quenched configurations. In chapter 8 the methodology and analysis code written for this task are discussed, and fit results are presented. Although the configurations are quenched, in a small volume, and have an unrealistic quark mass, we still get reasonable results for the nucleon spectrum. The spectrum extracted in this work is discussed in comparison to the experimentally measured nucleon excitation spectrum, and the predictions of the relativistic constituent quark model. We conclude by summarizing the main results of this work, and by discussing the ongoing efforts of the Lattice Hadron Physics Collaboration.

Chapter 2

Calculation overview

2.1 Spectral states and resonances

2.1.1 Hilbert spaces

In quantum field theory, all physical states of a system are represented by rays in a Hilbert space \mathcal{H} . A ray is an equivalence class of vectors differing only by a non-zero scale factor. Thus $|\phi\rangle$ and $\alpha|\phi\rangle$ ($\alpha \neq 0$) represent the same state of the system.

A Hilbert space is defined as a normed (or metric) space in which all Cauchy sequences are convergent. The norm $\|\cdot\|$ is defined for any vector $|\phi\rangle$ as

$$\| |\phi\rangle \| \equiv \sqrt{\langle \phi | \phi \rangle}.$$

A sequence of vectors $\{|\phi_n\rangle\}$ is a Cauchy sequence if for every real number $\epsilon > 0$ there is a non-negative integer N such that

$$\| |\phi_n\rangle - |\phi_m\rangle \| < \epsilon \quad \forall m, n > N.$$

A normed space is a Hilbert space if all Cauchy sequences in the space converge to an element in the space. This property is essential to justify many assumptions we will make about the convergence of integrals over elements in this space.

2.1.2 The Hamiltonian

Allowed transformations on the system are represented by unitary operators which map Hilbert space states to Hilbert space states. Examples of transformations include Poincaré transformations (space-time translations, rotations, and boosts), reflections, and charge

conjugation. Continuous transformations can be written as the exponentiation of Hermitian operators, known as generators. For example, spatial translations are generated by the momentum operator \vec{p} :

$$\begin{aligned} f(\vec{x}) \rightarrow f'(\vec{x}) &= f(\vec{x} - \vec{a}) \\ &= \exp(-a^j \partial_j) f(\vec{x}) \\ &\equiv \exp(ia^j p_j) f(\vec{x}), \quad p_j \equiv i\partial_j \end{aligned}$$

temporal translations are generated by the Hamiltonian, and rotations are generated by the angular momentum operator.

The spectrum of a theory consists of those states $|k\rangle$ in the Hilbert space which are eigenstates of the Hermitian generator of temporal translations H , the Hamiltonian operator:

$$H|k\rangle = E_k|k\rangle.$$

These are the *steady-states* of the theory which remain stable if allowed to freely propagate. Because the Hamiltonian operator is Hermitian, the eigenvalues E_k are real and represent the energy of the states $|k\rangle$. States which are eigenvectors of any Hermitian generator which commute with the Hamiltonian (such as linear and angular momentum) may also be labeled by their associated eigenvalue. Thus, it is possible to speak of a state having a particular value of both energy and momentum.

An additional constraint placed on a quantum field theory is that the Hamiltonian must be bounded from below. This means that there is a stable state of minimum energy, the vacuum $|\Omega\rangle$. By adding a suitable constant to the Hamiltonian (which does not change the spectrum), we may require that

$$H|\Omega\rangle = 0.$$

The existence of a state of minimum energy is essential in a quantum field theory to ensure that the field degrees of freedom in a finite spatial region don't radiate away an infinite amount of energy as they drop to lower and lower energy states.

The stable energy states $|k\rangle$ form a complete basis for the Hilbert space:

$$\sum_k |k\rangle\langle k| = 1,$$

where the sum is over both discrete and continuous states (with the appropriate measure).

2.1.3 Resonances

In a scattering experiment, a resonance is characterized by a dramatic increase in cross-section with a corresponding sudden variation in the scattering phase shift. A resonance observed in the scattering of hadrons can often be interpreted as an unstable particle lasting long enough to be recognized as having a particular set of quantum

numbers. Such a state is not an eigenstate of the Hamiltonian, but has a large overlap onto a single eigenstate. Note that if the quark mass is taken to be large in the simulation, then it may happen that a normally unstable state would be kinematically forbidden to decay due to energy conservation. Because its would-be decay products are too heavy, such a resonance would appear as a stable state in the spectrum.

Finite spatial volumes provide a second way to infer the existence and properties of resonances. A method of using the lattice approach to probe resonances is presented in Refs. [Lus86, Lus91b, Lus91a]. In this method, the dependence of a two-particle spectrum on the spatial box size is used to determine elastic scattering phase shifts, which are in turn related to the energies and widths of any resonances in that channel. For this work, we will extract the spectrum in a single volume. Future studies will be needed to determine the single and multi-particle content of the spectrum we find.

2.2 Euclidean space-time

Having the Lagrangian describing QCD, our next step is to find a method to extract the spectrum. In ordinary quantum mechanics, we would simply solve the Schrödinger equation for the stationary states in time: $i\partial_t\psi = E\psi$. Unfortunately, it is extremely difficult to work directly with the QCD Schrödinger equation due to the number of variables and the self-interaction terms. It is more practical to extract the energy levels of the theory from correlation functions of fields in Euclidean space-time.

The following discussion will deal with the theory of a single real scalar field ϕ . Afterward, we will discuss subtleties that arise when applying the results to the case of quark fields and gauge links.

The Hilbert space and the original field can be reconstructed from the Green's functions. Osterwalder and Schrader [OS73a, OS75] showed that under general conditions, we may analytically continue the Minkowski Green's functions to imaginary time. Doing so will make the integrals explicitly convergent and will allow us to use the computational tools of statistical mechanics to calculate quantities in this system. We will summarize the main features of this approach in the following. A more detailed treatment is presented in [MM94]. For the rest of this work, we will work in Euclidean space-time, and will denote Minkowski space-time quantities with a subscript or superscript M .

The points on the Euclidean space-time manifold are related to those on the Minkowski space-time manifold as:

$$x^4 = x_4 = ix_M^0 = ix_0^M, \quad x^j = x_j = x_M^j = -x_j^M, \quad (2.1)$$

$$\partial_4 = \partial^4 = -i\partial_0^M = -i\partial_M^0, \quad \partial_j = \partial^j = \partial_j^M = -\partial_M^j. \quad (2.2)$$

With these definitions, the new metric therefore becomes Euclidean:

$\delta_{\mu\nu} = \text{diag}(+1, +1, +1, +1)$, and there is no distinction between covariant (lower) and

contravariant (upper) indices. Summation over repeated indices will be assumed unless specified otherwise.

Making the above replacements, the continuum fermionic action becomes:

$$iS_F^M = i \int dx_M^0 d^3x_M \bar{\psi}_M(x_M) (i\gamma_M^0 \partial_0 + i\gamma_M^j \partial_j^M - m) \psi_M(x_M) \quad (2.3)$$

$$\rightarrow \int dx_4 d^3x \bar{\psi}(x) (-\gamma_M^0 \partial_4 + i\gamma_M^j \partial_j - m) \psi(x) \quad (2.4)$$

If we define the Euclidean space-time Dirac γ matrices as

$$\gamma^4 = \gamma_4 = \gamma_M^0, \quad \gamma_k = \gamma^k = -i\gamma_M^k \quad (2.5)$$

then we have:

$$iS_F^M \rightarrow - \int d^4x \bar{\psi}(x) (\gamma_\mu \partial_\mu + m) \psi(x) \quad (2.6)$$

$$\equiv -S_F. \quad (2.7)$$

Using Eqn. 1.1 and Eqn. 1.2, we see that the Euclidean space-time Dirac γ matrices defined in 2.5 satisfy:

$$\{\gamma_\mu, \gamma_\nu\} = 2\delta_{\mu\nu}, \quad \gamma_\mu^\dagger = \gamma_\mu \quad (2.8)$$

We will use the standard Dirac-Pauli representation for the γ matrices:

$$\gamma_4 = \begin{pmatrix} I & 0 \\ 0 & -I \end{pmatrix}, \quad \gamma_j = \begin{pmatrix} 0 & -i\sigma_j \\ i\sigma_j & 0 \end{pmatrix}, \quad (2.9)$$

where I is the 2×2 identity matrix and the Pauli spin matrices are

$$\sigma_1 = \begin{pmatrix} 0 & 1 \\ 1 & 0 \end{pmatrix}, \quad \sigma_2 = \begin{pmatrix} 0 & -i \\ i & 0 \end{pmatrix}, \quad \sigma_3 = \begin{pmatrix} 1 & 0 \\ 0 & -1 \end{pmatrix}. \quad (2.10)$$

The fermion fields $\psi(x)$ and $\bar{\psi}(x)$ transform irreducibly under $SO(4)$ rotations in Euclidean space-time, and represent the Minkowski fields analytically continued to imaginary time. Unlike in Minkowski space-time, ψ and $\bar{\psi}$ must be treated as independent fields: $\bar{\psi} \neq \psi^\dagger \gamma_4$. This is required to simultaneously satisfy Euclidean covariance of the fields, the canonical anticommutation relations of the fermion fields, and the equality of the Euclidean two-point function with the relativistic Feynman propagator continued to imaginary times [OS73b, Wil74a].

2.3 Euclidean gauge links and gauge action

The fermion action may now be discretized as before, using gauge links which are now defined between neighboring quark field sites on the Euclidean manifold.

$$\begin{aligned} U_\mu^M(x) &= \mathcal{P} \exp \left\{ ig \int_x^{x+\hat{\mu}} dz_M^\nu A_\nu^M(z) \right\} \\ &\rightarrow \mathcal{P} \exp \left\{ ig \int_x^{x+\hat{\mu}} dz_\nu A_\nu(z) \right\} \\ &\equiv U_\mu(x) \end{aligned}$$

with the Euclidean gauge field defined by

$$A_4 = A^4 = -iA_0^M = -iA_M^0, \quad A_j = A^j = A_j^M = -A_M^j. \quad (2.11)$$

This gives

$$F_{44} = -F_M^{00} = -F_{00}^M, \quad F_{4j} = iF_M^{0j} = -iF_{0j}^M, \quad F^{jk} = F_M^{jk} = F_{jk}^M.$$

In order to find the Euclidean gauge action, we must keep track of the temporal vs spatial directions. Consider the anisotropic Minkowski lattice spacings defined by:

$$a_t^M \equiv \int_x^{x+\hat{0}} dz_M^0, \quad a_s^M = \int_x^{x+\hat{j}} dz_M^j, \quad \xi_0^M \equiv a_s^M / a_t^M + O(a)$$

where ξ_0^M is the bare anisotropy¹ of the lattice. The corresponding Euclidean lattice spacings are given by:

$$a_\tau = ia_t^M, \quad a_s = a_s^M, \quad \xi_0 = -i\xi_0^M.$$

The anisotropic gauge action becomes

$$\begin{aligned} iS_G^M &= -i \frac{\beta}{N} \sum_x \left[\sum_{j<k} \frac{1}{\xi_0^M} \text{Re Tr}(1 - U_{jk}^M(x)) + \sum_j \xi_0^M \text{Re Tr}(1 - U_{j4}^M(x)) \right], \\ &= -i \sum_x \sum_{\mu,\nu} a_t^M (a_s^M)^3 \frac{1}{2} \text{Tr}(F_{\mu\nu}^M F_M^{\mu\nu}) + O(a^5) \\ &\rightarrow - \sum_x \sum_{\mu,\nu} a_s^3 a_\tau \frac{1}{2} \text{Tr}(F_{\mu\nu} F_{\mu\nu}) + O(a^5) \\ &= -S_G \end{aligned}$$

where the anisotropic Euclidean gauge action is given by [Kla98a]:

$$S_G = \frac{\beta}{N} \sum_x \left[\sum_{j<k} \frac{1}{\xi_0} \text{Re Tr}(1 - U_{jk}(x)) + \sum_j \xi_0 \text{Re Tr}(1 - U_{j4}(x)) \right]. \quad (2.12)$$

¹The bare anisotropy parameter ξ_0^M in the action is note the same as a_s/a_τ due to quantum corrections.

2.4 The Euclidean fermion lattice action

For clarity, we will show all sums explicitly in this section and begin by describing the fermion action on an isotropic lattice. On the lattice, we will replace first and second covariant derivatives by symmetric differences using gauge links as parallel transporters:

$$\begin{aligned}\partial_\mu &\rightarrow \frac{1}{a}(\nabla_\mu)_{x,y} \equiv \frac{1}{2a} (U_\mu(x)\delta_{x+\hat{\mu},y} - U^\dagger(x-\hat{\mu})\delta_{x-\hat{\mu},y}) \\ \partial_\mu\partial_\mu &\rightarrow \frac{1}{a^2}(\Delta_\mu)_{x,y} \equiv \frac{1}{a^2} (U_\mu(x)\delta_{x+\hat{\mu},y} + U_\mu^\dagger(x-\hat{\mu})\delta_{x-\hat{\mu},y} - 2\delta_{x,y})\end{aligned}$$

We use symmetric differences in the action in order to guarantee a Hamiltonian which satisfies *reflection positivity*:

$$H \xrightarrow{\tau \rightarrow -\tau} H.$$

Minkowski time evolution $e^{iHt}\mathcal{O}(0)e^{-iHt}$ requires $H^\dagger = H$, but Euclidean time evolution $e^{H\tau}\mathcal{O}(0)e^{-H\tau}$ requires reflection positivity.

Making the appropriate replacements, we may write the fermionic part of the lattice action as

$$\begin{aligned}S_F &= \int d^4x \bar{\psi}(x) \left(\sum_\mu \gamma_\mu \partial_\mu + m \right) \psi(x), \\ &\rightarrow \sum_{x,y} a^4 \bar{\psi}(x) \left(\sum_\mu \gamma_\mu \frac{1}{a} (\nabla_\mu)_{x,y} + m \delta_{x,y} \right) \psi(y), \\ &= \sum_{x,y} (a^{3/2} \bar{\psi}(x)) \left(\sum_\mu \gamma_\mu (\nabla_\mu)_{x,y} + (am) \delta_{x,y} \right) (a^{3/2} \psi(y)), \\ &\equiv \sum_{x,y} \bar{\psi}_x \left(\sum_\mu \gamma_\mu (\nabla_\mu)_{x,y} + am \delta_{x,y} \right) \psi_y, \\ &\equiv \bar{\psi} \left(\sum_\mu \gamma_\mu \nabla_\mu + am \right) \psi,\end{aligned}$$

where we have defined the dimensionless quark fields $\bar{\psi}_x \equiv a^{3/2} \bar{\psi}(x)$ and $\psi_x \equiv a^{3/2} \psi(x)$ and have grouped a factor of the lattice spacing a with the bare mass m to make the dimensionless quantity am .

2.4.1 The Wilson term

The naïve replacement of the derivative by the symmetric difference in the above leads to a serious lattice artifact known as *fermion doubling* [Rot97] in which there are 15 additional massless fermion ‘doublers’ which contribute to the calculations. These doublers can be

made harmless by introducing the *Wilson term*, an $O(a)$ term (irrelevant in the naïve continuum limit) into the action which gives the doublers a mass of $1/a$:

$$\begin{aligned}
S_F &\rightarrow S_F - a \frac{1}{2} \sum_{x,y,\mu} a^4 \psi(x) \partial_\mu \partial_\mu \psi(y) \\
&= \bar{\psi} \left(\sum_\mu \gamma_\mu \nabla_\mu + am \right) \psi - \frac{1}{2} \sum_\mu \bar{\psi} \Delta_\mu \psi \\
&\equiv \bar{\psi} Q \psi \\
Q &\equiv am + \sum_\mu (\gamma_\mu \nabla_\mu - \frac{1}{2} \Delta_\mu) \\
Q_{x,y} &\equiv (am + 4) \delta_{x,y} - \frac{1}{2} \sum_\mu \left[(1 - \gamma_\mu) U_\mu(x) \delta_{x+\hat{\mu},y} + (1 + \gamma_\mu) U_\mu^\dagger(x - \hat{\mu}) \delta_{x-\hat{\mu},y} \right]
\end{aligned}$$

2.4.2 Anisotropic lattices

We would like to use large spatial volumes in order to mitigate finite volume effects in our calculations. This requires a coarse spatial mesh in order to have a manageable number of spatial lattice sites. On the other hand, our temporal correlation functions decay exponentially with the baryon mass, motivating us to work with a fine mesh in the temporal direction. Accordingly, we will work with an anisotropic lattice [Kla98a, MP99, Kla99] with spatial lattice spacing a_s , and temporal lattice spacing a_τ . The anisotropic gauge action is given by Eqn. 2.12. Repeating the derivation above for an anisotropic fermionic lattice action is straightforward if we introduce the elementary lattice vector $a_\mu = (a_s, a_s, a_s, a_\tau)$. We now absorb factors of $a_s^{3/2}$ into $\bar{\psi}$ and ψ , and associate a factor of a_τ with m . In addition, we put in an explicit factor of the bare speed of light ν which takes into account the fermion anisotropy effects. This gives us

$$\begin{aligned}
S_F &= \bar{\psi} Q \psi \\
Q &= a_\tau m + \frac{\nu}{\xi_0} \sum_j (\gamma_j \nabla_j - \frac{1}{2} \Delta_j) + (\gamma_4 \nabla_4 - \frac{1}{2} \Delta_4) \\
Q_{x,y} &= (a_\tau m + \frac{3\nu}{\xi_0} + 1) \delta_{x,y} \\
&\quad - \frac{\nu}{2\xi_0} \sum_j \left[(1 - \gamma_j) U_j(x) \delta_{x+\hat{j},y} + (1 + \gamma_j) U_j^\dagger(x - \hat{j}) \delta_{x-\hat{j},y} \right] \\
&\quad - \frac{1}{2} \left[(1 - \gamma_4) U_4(x) \delta_{x+\hat{4},y} + (1 + \gamma_4) U_4^\dagger(x - \hat{4}) \delta_{x-\hat{4},y} \right]
\end{aligned} \tag{2.13}$$

2.4.3 Setting the scale

In order to get back to energy units (i.e. MeV and fm) from lattice units ($a_\tau = 1$), we will relate a measured quantity such as the heavy quarkonium string tension (which is not very sensitive to mass tuning) to an experimentally measured quantity.

The heavy quark string tension for large separation R is given experimentally by:

$$V(R) \approx V_0 + \sigma R,$$

where $\sigma \approx (465 \text{ MeV})^2$. On the lattice, we can measure the static quark-antiquark potential and fit to the dimensionless form:

$$\begin{aligned} a_\tau V(R/a_s) &= (a_\tau V_0) + (a_\tau a_s \sigma)(R/a_s) \\ &= (a_\tau V_0) + (\xi a_\tau^2 \sigma)(R/a_s) \\ &= (a_\tau V_0) + \left(\frac{a_s^2}{\xi}\sigma\right)(R/a_s). \end{aligned}$$

The anisotropy can be determined by comparing the behavior of the static quark-antiquark potential as a function of both spatial separation (regular) and temporal separation (sideways).

Once the anisotropy has been determined, the string tension can be used to find the temporal (or spatial) lattice spacing in units of MeV^{-1} . This fixes the energy scale of all quantities in the simulation [EHK98a, LM93].

2.5 Tuning the lattice action

The general steps involved in tuning the lattice parameters typically involve:

- Tune the bare anisotropy ξ_0 and compare the regular and sideways static quark potential to determine the renormalized anisotropy $\xi = a_s/a_\tau$ [Kla98a].
- Tune the bare coupling β and use the string tension ($\sqrt{\sigma} = 465 \text{ MeV}$) to determine the temporal lattice spacing a_τ or spatial lattice spacing a_s [EHK98a].
- Tune the bare fermion anisotropy ν (the ‘bare velocity of light’) and measure the pion dispersion relation, which will converge to $E^2 = m^2 + p^2$ as the fermion anisotropy approaches ξ [Kla99, SLLL06].
- Tune the quark masses and measure the spectrum. As quark masses decrease, spectral quantities should scale according to chiral perturbation theory.

For the current work, we use unrealistically high quark masses in order to have rapid convergence of our propagator inversions. The pion mass can be estimated by a back-of-the-envelope calculation:

$$\begin{aligned}
 \xi &\equiv \frac{a_s}{a_\tau} \approx 3.0 && \text{(from sideways potential tuning)} \\
 a_s &\approx 0.1 \text{ fm} && \text{(from string tension)} \\
 a_\tau m_\pi &= 0.1125(26) && \text{(from pion effective mass)} \\
 m_\pi &= \frac{\xi a_\tau m_\mu}{a_s} \approx 700 \text{ MeV} && (\hbar c \approx 200 \text{ MeV}\cdot\text{fm})
 \end{aligned}$$

where we have rounded to the most significant digit due to the crudeness of our estimate.

2.5.1 Lattice parameters for this study

Our study uses the anisotropic Wilson action with the following parameters.

- Lattice size: $N_s = 12$, $N_\tau = 48$
- $\xi_0 = 2.464 \leftrightarrow \xi \approx 3.0$
- $\beta = 6.1 \leftrightarrow a_s \approx 0.1 \text{ fm}$
- $a_\tau m_{ud} = -0.305 \leftrightarrow m_\pi \approx 700 \text{ MeV}$
- $\nu = 0.902$

The configurations used for this work were quenched (discussed in the next chapter) and the spatial volume considered was relatively small ($\approx 1.2 \text{ fm}$). This was acceptable because the purpose of the present work was to develop and test a new operator design methodology, specifically with the goal of designing and tuning good nucleon operators to be used in later ‘production’ runs to extract the low-lying baryon spectrum in the nucleon sector. It is expected that the operator design methodology described in this work will remain relevant as we work to larger spatial volumes, lower quark masses, and finer lattice spacings. Production runs will use the anisotropic Wilson action with dynamical u , d , and s quarks and a clover improvement term [ADL⁺95, AKL97, Kla98b, EHR03].

2.6 The spectral representation of correlation functions

The Euclidean formulation of a quantum field theory provides a simple way to calculate vacuum expectation values $\langle \Omega | A | \Omega \rangle$ [MM94]. Consider

$$\begin{aligned} \frac{\text{Tr}(e^{-H\tau} A)}{\text{Tr}(e^{-H\tau})} &= \frac{\sum_{k=0}^{\infty} \langle k | e^{-H\tau} A | k \rangle}{\sum_{l=0}^{\infty} \langle l | e^{-H\tau} | l \rangle} \\ &= \frac{\sum_{k=0}^{\infty} \langle k | A | k \rangle e^{-E_k \tau}}{\sum_{l=0}^{\infty} e^{-E_l \tau}} \\ &\xrightarrow{\tau \rightarrow \infty} \langle \Omega | A | \Omega \rangle \end{aligned}$$

To see how this Hamiltonian approach connects to the functional integral approach with a lattice regulator, we will use a complete set of field eigenstates $\{|\phi\rangle\}$ in the trace, rather than the complete set of energy eigenstates $\{|k\rangle\}$. For clarity we will consider the case of a complex scalar field operator Φ for the rest of this section. Let the integration measure over field configurations be denoted by $d\mu(\phi)$. Then for a fixed time slice we have:

$$\begin{aligned} \Phi|\phi\rangle &= \phi|\phi\rangle, \\ \langle\phi|\Phi^\dagger &= \langle\phi|\phi^*, \\ \int d\mu(\phi) |\phi\rangle\langle\phi| &= \int d\phi^* d\phi e^{-\phi^*\phi} |\phi\rangle\langle\phi|, \\ &= 1. \end{aligned}$$

where the factor of $e^{-\phi^*\phi}$ arises due to the definition of the field eigenstates. This will be illustrated in the case of fermions in Subsection 2.6.1. A rigorous treatment for both bosons and fermions is given in [Bro92]. Consider the following partition function with the trace taken with respect to a complete basis of field configurations:

$$\begin{aligned} Z &\equiv \text{Tr}(e^{-HT}), \\ &= \int d\mu(\phi_0) \langle\phi_0|e^{-HT}|\phi_0\rangle, \\ &\quad (\text{inserting } N_\tau - 1 \text{ complete sets of states, with } T = N_\tau a_\tau), \\ &= \int d\mu(\phi_{N_\tau-1}) d\mu(\phi_{N_\tau-2}) \cdots d\mu(\phi_0) \langle\phi_0|e^{-Ha_\tau}|\phi_{N_\tau-1}\rangle \langle\phi_{N_\tau-1}|e^{-Ha_\tau}|\phi_{N_\tau-2}\rangle \cdots \langle\phi_1|e^{-Ha_\tau}|\phi_0\rangle, \\ &= \int_{\phi_{N_\tau}=\phi_0} d\mu(\phi_{N_\tau-1}) \cdots d\mu(\phi_0) \langle\phi_{N_\tau}|e^{-Ha_\tau}|\phi_{N_\tau-1}\rangle \cdots \langle\phi_1|e^{-Ha_\tau}|\phi_0\rangle. \end{aligned}$$

It can be shown [Bro92] that:

$$\langle \phi_{\tau+1} | e^{-Ha_\tau} | \phi_\tau \rangle \equiv \exp\{\phi_{\tau+1}^*(\vec{x})\phi_{\tau+1}(\vec{x}) - a_\tau L(\phi_{\tau+1}(\vec{x}), \phi_\tau(\vec{x}))\}. \quad (2.14)$$

The quantity on the left is the matrix element of the *transfer* operator e^{-Ha_τ} between two states in the Hilbert space. The quantity on the right is a function of two different field configurations $\phi_{\tau+1}(\vec{x})$ and $\phi_\tau(\vec{x})$. We have shown the spatial indices as a reminder that we are dealing with the field degrees of freedom defined over all of space (the Hamiltonian is time-independent). If we regularize the individual integrals over the ϕ_τ by placing the system in a finite spatial volume with periodic boundary conditions and by discretizing the spatial coordinates we have:

$$\begin{aligned} \int_{\phi_{N_\tau}=\phi_0} \prod_{\tau} d\mu(\phi_\tau) &= \int \prod_{\tau} \prod_{\vec{x}} d\mu(\phi_\tau(\vec{x})), \\ &= \int_{\text{p.b.c.}} \prod_{\tau} \prod_{\vec{x}} d\phi_\tau^*(\vec{x}) d\phi_\tau(\vec{x}) e^{-\phi_\tau^*(\vec{x})\phi_\tau(\vec{x})}, \\ &\equiv \int_{\text{p.b.c.}} \mathcal{D}\phi e^{-\phi^*\phi}. \end{aligned}$$

The choice of periodic boundary conditions (p.b.c.) for the spatial volume eliminates edge effects, but does not eliminate finite volume effects due to images. The periodic boundary conditions in the ‘temporal’ direction (τ) arise naturally as a consequence of the trace. It is not necessary to use a trace to extract the spectrum, but the trace has the useful property of temporal translation invariance. The anti-periodic temporal fermion boundary conditions to be used with the trace method are discussed in Subsection 2.6.1.

If we identify the lattice action $S[\phi] = \sum_{\tau} a_\tau L(\phi_{\tau+1}, \phi_\tau)$, we arrive at the fundamental relation between the trace of the operator e^{-HT} and the (well-defined) functional integral over field configurations $\phi_\tau(\vec{x}) \equiv \phi(x)$ on our Euclidean space-time lattice (identifying $x_4 \equiv \tau$):

$$Z = \text{Tr}(e^{-HT}) = \int_{\text{p.b.c.}} \mathcal{D}\phi e^{-S[\phi]} \quad (2.15)$$

For finite lattice spacings a_τ, a_s and a given lattice action S , the lattice Hamiltonian H defined via Eqn. 2.15 will differ from the continuum Hamiltonian of the theory by terms of order a_τ and a_s . The goal of action improvement programs is to reduce these discretization errors by adding offsetting $O(a)$ terms to the lattice action S .

We can access the spectrum of the theory by inserting an arbitrary creation operator $\bar{\mathcal{O}}$ at ‘time slice’ 0 and an arbitrary annihilation operator \mathcal{O} at ‘time slice’ τ into the functional

integral expression for Z :

$$\langle \mathcal{O}(\tau) \bar{\mathcal{O}}(0) \rangle \equiv \frac{1}{Z} \int_{\text{p.b.c.}} \mathcal{D}\phi \mathcal{O}(\tau) \bar{\mathcal{O}}(0) e^{-S[\phi]} \quad (2.16)$$

$$\begin{aligned} &= \frac{\text{Tr} (e^{-H(T-\tau)} \mathcal{O} e^{-H\tau} \bar{\mathcal{O}})}{\text{Tr} (e^{-HT})} \\ &= \frac{\sum_n \langle n | e^{-H(T-\tau)} \mathcal{O} e^{-H\tau} \bar{\mathcal{O}} | n \rangle}{\sum_m \langle m | e^{-HT} | m \rangle} \\ &= \frac{\sum_n e^{-E_n T} \langle n | e^{+H\tau} \mathcal{O} e^{-H\tau} \bar{\mathcal{O}} | n \rangle}{\sum_m e^{-E_m T}} \\ &\xrightarrow{T \rightarrow \infty} \langle \Omega | e^{+H\tau} \mathcal{O} e^{-H\tau} \bar{\mathcal{O}} | \Omega \rangle \quad (2.17) \end{aligned}$$

$$\begin{aligned} &= \sum_{k=0}^{\infty} \langle \Omega | \mathcal{O} e^{-H\tau} | k \rangle \langle k | \bar{\mathcal{O}} | \Omega \rangle \\ &= \sum_{k=1}^{\infty} |\langle k | \bar{\mathcal{O}} | \Omega \rangle|^2 e^{-E_k \tau} \quad (2.18) \end{aligned}$$

where in 2.17 we have taken the limit $T \rightarrow \infty$ (large temporal extent of our lattice). If we require our creation operators $\bar{\mathcal{O}}$ to have a vacuum expectation value of zero ($\langle \Omega | \bar{\mathcal{O}} | \Omega \rangle = 0$), then we can extract the first (non-zero) energy state of the theory by fitting to the asymptotic form of Eqn. 2.18.

The form of 2.17 looks like a Heisenberg time-evolution equation if we replace $t \rightarrow -i\tau$ (giving diffusion dynamics, not wave dynamics). This was to be expected because we constructed our Euclidean theory such that the correlation functions would be related to the Minkowski Green's functions analytically continued to imaginary time.

2.6.1 Temporal boundary conditions for fermions

There is some subtlety involved with taking the trace using eigenstates of fermion fields due to their Fermi-Dirac statistics [Bro92]. For clarity in this section, we consider the mathematics of a single fermion field carrying no indices.

The fermion fields in the functional integral are Grassmann (anticommuting) numbers, not c-numbers (which commute). Consider the case of two independent Grassmann variables: z and z^* (not related by complex conjugation). These objects satisfy:

$$zz^* = -z^*z, \quad z^2 = z^{*2} = 0.$$

Consequently, any polynomial in these variables has a finite (exact) power series expansion:

$$P(z, z^*) = p_0 + p_1 z + p_2 z^* + p_{12} z z^*.$$

Specifically:

$$e^z \equiv 1 + z.$$

We can define integration over Grassmann variables formally by

$$\int dz = 0 \quad \int dz z = 1 \quad \int dz^* = 0 \quad \int dz^* z^* = 1$$

with the requirement that $\int dz^* dz = -\int dz dz^*$ for consistency. Note that the above definition defines a translationally invariant integral

$$\int dz (z + d) = \int dz z$$

where d is any c-number or Grassmann number.

The pair of fermionic field operators Ψ and Ψ^\dagger satisfy the fermion anticommutation relations:

$$\Psi^2 = \Psi^{\dagger 2} = 0 \quad \Psi\Psi^\dagger + \Psi^\dagger\Psi = 1.$$

These relations are sufficient to show that these operators act upon a two-dimensional Hilbert space spanned by the states $|0\rangle$ and $|1\rangle$. The behavior of the operators Ψ and Ψ^\dagger on this space is completely specified by

$$\begin{aligned} \Psi|0\rangle &= \langle 0|\Psi^\dagger = 0, \\ \Psi^\dagger|1\rangle &= \langle 1|\Psi = 0, \\ \langle 0|0\rangle &= \langle 1|1\rangle = 1, \\ \langle 0|1\rangle &= \langle 1|0\rangle = 0 \end{aligned}$$

and

$$\begin{aligned} \Psi^\dagger|0\rangle &= |1\rangle, & \langle 0|\Psi &= \langle 1|, \\ \Psi|1\rangle &= |0\rangle, & \langle 1|\Psi^\dagger &= \langle 0|. \end{aligned}$$

In order to take a trace over field configurations, we will need the eigenstates of the field operators. These are given by:

$$|z\rangle = e^{\Psi^\dagger z}|0\rangle \quad \langle z| = \langle 0|e^{z^*\Psi}$$

where the Grassmann numbers z and z^* anticommute with the operators Ψ and Ψ^\dagger

$$\begin{aligned} \Psi z &= -z\Psi, & z\Psi^\dagger &= -\Psi^\dagger z, \\ \Psi z^* &= -z^*\Psi, & z^*\Psi^\dagger &= -\Psi^\dagger z^*. \end{aligned}$$

Using the rules we have just defined, we can verify that

$$\Psi|z\rangle = z|z\rangle, \quad \langle z|\Psi^\dagger = \langle z|z^*.$$

Notice that (by construction) this *looks* like complex conjugation. To define the measure over the set of field eigenstates, we need

$$\begin{aligned}
\langle z_1 | z_2 \rangle &= \langle 0 | e^{z_1^* \Psi} e^{\Psi^\dagger z_2} | 0 \rangle \\
&= \langle 0 | (1 + z_1^* \Psi) (1 + \Psi^\dagger z_2) | 0 \rangle \\
&= \langle 0 | (1 + z_1^* \Psi + \Psi^\dagger z_2 + z_1^* \Psi \Psi^\dagger z_2) | 0 \rangle \\
&= \langle 0 | 0 \rangle + z_1^* \langle 0 | \Psi | 0 \rangle + \langle 0 | \Psi^\dagger | 0 \rangle + z_1^* z_2 \langle 0 | \Psi \Psi^\dagger | 0 \rangle \\
&= 1 + z_1^* z_2 = e^{z_1^* z_2}
\end{aligned}$$

If we define the measure over coherent states $d\mu(z)$ by

$$d\mu(z) = dz^* dz e^{-z^* z}$$

then we have the resolution of the identity in terms of a complete set of coherent field states:

$$\int d\mu(z) |z\rangle \langle z| = 1.$$

Checking this:

$$\begin{aligned}
\int d\mu(z) \langle z_1 | z \rangle \langle z | z_2 \rangle &= \int dz^* dz e^{-z^* z} e^{z_1^* z} e^{z z_2}, \\
&= \int dz^* dz (1 - z^* z) (1 + z_1^* z) (1 + z z_2), \\
&= \int dz^* z^* dz z (1 + z_1^* z_2), \\
&= e^{z_1^* z_2} = \langle z_1 | z_2 \rangle.
\end{aligned}$$

Alternatively:

$$\begin{aligned}
\int d\mu(z) |z\rangle \langle z| &= \int dz^* dz e^{-z^* z} (1 + \psi^\dagger z) |0\rangle \langle 0| (1 + z^* \psi) \\
&= |0\rangle \langle 0| + |1\rangle \langle 1|.
\end{aligned}$$

Let $F(\Psi, \Psi^\dagger)$ be an analytic function of an even number of fermion operators Ψ^\dagger and an even number of antifermion operators Ψ . The trace of F is:

$$\begin{aligned}
\text{Tr}(F) &= \int d\mu(z) \langle -z | F | z \rangle \\
&= \int dz^* dz (1 - z^* z) \langle 0 | (1 - z^* \Psi) F (1 + \Psi^\dagger z) | 0 \rangle \\
&= \langle 0 | F | 0 \rangle + \langle 1 | F | 1 \rangle
\end{aligned}$$

Notice that the trace must be taken between $\langle -z | \cdots | z \rangle$, not $\langle z | \cdots | z \rangle$. In the functional integral, this translates to using periodic temporal (x_4) boundary conditions for the bosonic fields (i.e. gauge links) but *anti-periodic* temporal boundary conditions for the fermionic fields (i.e. quark fields). We use periodic spatial boundary conditions for both bosonic and fermionic fields. These boundary conditions will be implied when we write ‘p.b.c.’ on our functional integrals.

2.7 Effective mass plots

Returning to the spectral representation of the Euclidean correlation function:

$$C(\tau) = \langle \mathcal{O}(\tau) \overline{\mathcal{O}}(0) \rangle \xrightarrow{T \rightarrow \infty} \sum_{k=1}^{\infty} |c_k|^2 e^{-E_k \tau}, \quad c_k \equiv \langle k | \overline{\mathcal{O}} | \Omega \rangle, \quad (2.19)$$

we can get an idea of how well the temporal extent of our lattice is approximating the $T \rightarrow \infty$ limit by examining how calculated physical quantities vary with the number of lattice sites in the temporal direction for a fixed temporal lattice spacing a_τ .

We wish to extract as many of the energy levels E_k as possible from the exponentially decaying signal in Eqn. 2.19. It will be a recurring theme in this work to examine plots of *effective mass functions* to judge the quality of our signals and to tune our parameters. The effective mass function is defined by:

$$a_\tau M(\tau) = \ln(C(\tau)/C(\tau + a_\tau)). \quad (2.20)$$

This definition of the effective mass is not unique, but it is one of the simplest, involving the value of the correlation function at only two neighboring values of time.

For large values of τ in the $T \rightarrow \infty$ limit, the effective mass may be expanded as:

$$\begin{aligned} a_\tau M(\tau) &\equiv \ln \left[\frac{C(\tau)}{C(\tau + a_\tau)} \right] \\ &= \ln \left[\frac{|c_1|^2 e^{-E_1 \tau} + |c_2|^2 e^{-E_2 \tau} + \dots}{|c_1|^2 e^{-E_1(\tau + a_\tau)} + |c_2|^2 e^{-E_2(\tau + a_\tau)} + \dots} \right] \\ &= a_\tau E_1 \left(1 + O(|c_2|^2/|c_1|^2 e^{-(E_2 - E_1)\tau/a_\tau}) \right) \end{aligned}$$

and thus $a_\tau M(\tau)$ approaches a plateau of $a_\tau E_1$ for sufficiently large τ/a_τ . We emphasize that effective mass plots are simply visualization tools; final fits are best made to the correlation matrix elements directly.

Because the lattice is periodic (anti-periodic) in the temporal direction for bosons (fermions), we can expect significant contamination from the *backward propagating* states for large correlation lengths τ . In the case of meson operators, the backward propagating state contamination comes from a time-reversed mirror image of the meson itself. We can explicitly take this contamination into account by defining the effective mass $a_\tau M_{\text{cosh}}(\tau)$ as the solution to:

$$\ln[\cosh((a_\tau M_{\text{cosh}})(\tau/a_\tau))] = \ln[\cosh((a_\tau M_{\text{cosh}})(\tau/a_\tau))] + \text{const.}$$

An example of both types of effective mass plot is given in Figure 2.1, which gives the pion effective mass as measured on our configurations.

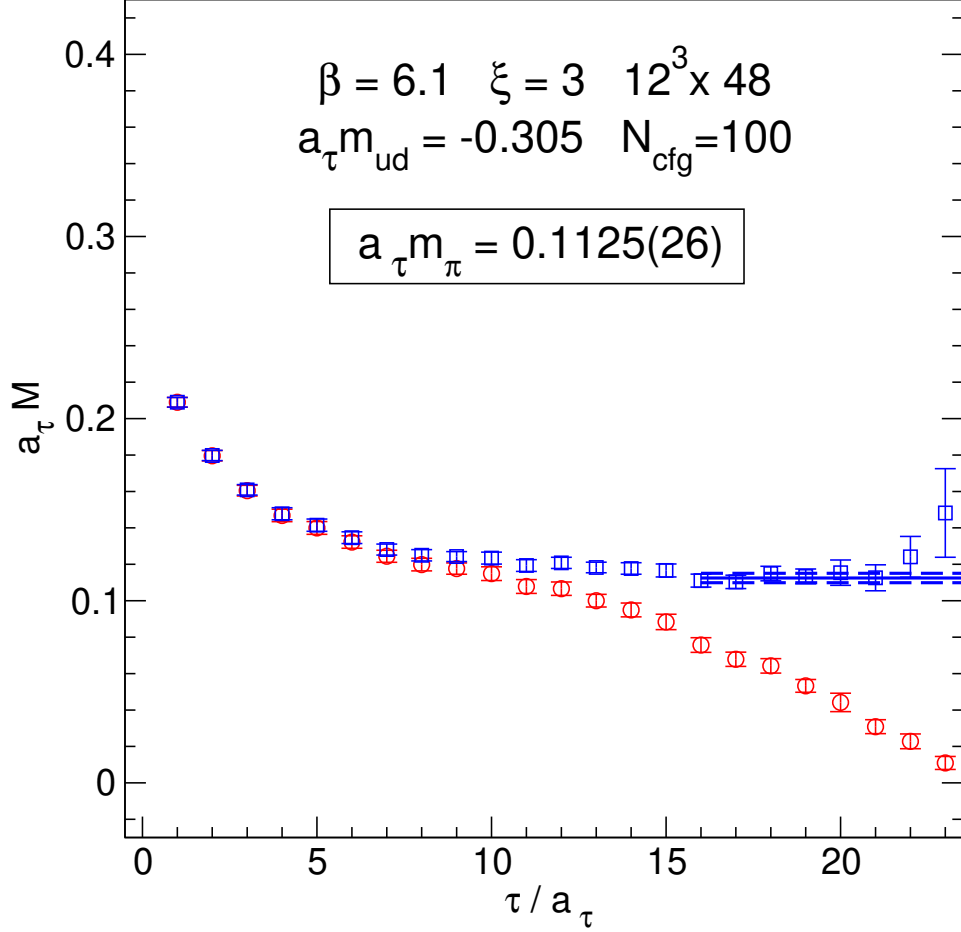


Figure 2.1: The pion effective mass plots. The standard effective mass $a_\tau M(\tau)$ (red) fails to plateau due to backward channel contamination. This contamination is explicitly treated by the meson effective mass function $a_\tau M_{\text{cosh}}(\tau)$ (blue). A cosh fit to the correlation function yields a pion mass in lattice units of $a_\tau m_\pi = 0.1125(26)$.

In the case of baryon operators, the backward propagating state contamination comes from states in the opposite-parity channel, which will generally have different masses due to spontaneous chiral symmetry breaking. As a result, we are unable to model the correlation function using a simple cosh form. In this work, we do not correct for this contamination, but limit our effective mass plots to the first or twenty values of τ/a_τ (we are working on a lattice with $N_\tau = 48$). Because our baryon states are much heavier than mesons, the backward propagating states decay significantly by the time their signal reaches early values of τ/a_τ . This is treated in detail in Chapters 5 and 8.

2.8 Extracting excited states

In order to extract higher states, we may try to fit multiple exponentials to the decaying correlation function. In practice, the correlation function is estimated using numerical techniques (c.f. Chapter 3), which results in an uncertainty associated with each data point. The method of fitting many exponentials to a numerically estimated correlation function is ineffective due to the rapid decay of the signal to noise ratio.

We introduce a method for extracting multiple excited states which is based on the approach of Lüscher and Wolff [LW90]. In this approach we utilize a set of n ‘candidate’ operators $\{\overline{\mathcal{O}}_1, \overline{\mathcal{O}}_2, \dots, \overline{\mathcal{O}}_n\}$ and construct linear combinations

$$\overline{\Theta}_i = \sum_{a=1}^n \overline{\mathcal{O}}_a v_{ai},$$

with associated correlation functions:

$$\begin{aligned} C_i(\tau) &= \langle \Theta_i(\tau) \overline{\Theta}_i(0) \rangle, \\ &= \sum_{a,b} v_{ia}^* \langle \mathcal{O}_a(\tau) \overline{\mathcal{O}}_b(0) \rangle v_{bi}, \\ &\equiv v_i^\dagger C(\tau) v_i, \end{aligned}$$

where we have introduced the correlation matrix $C_{ab}(\tau) \equiv \langle \mathcal{O}_a(\tau) \overline{\mathcal{O}}_b(0) \rangle$ and the fixed coefficient vector v_i . $C(\tau)$ consists of correlation functions between every possible pair of candidate operators in our original set, and therefore contains more information about the spectrum than the correlation function of a single operator. Note that all of the $C_i(\tau)$ and $C_{aa}(\tau)$ (diagonal elements) are real and positive for all $\tau \neq 0$. Our task is to extract as much information as possible about the spectrum from the correlation matrix $C(\tau)$ by finding suitable coefficient vectors $\{v_i\}$.

2.8.1 The variational method

Let the state $|v_i\rangle$ be defined by:

$$\begin{aligned} |v_i\rangle &\equiv e^{-H\tau_0/2} \overline{\Theta}_i |\Omega\rangle = e^{-H\tau_0/2} \sum_a \overline{\mathcal{O}}_a |\Omega\rangle v_{ai} \\ \langle v_i| &\equiv \langle \Omega | \Theta_i e^{-H\tau_0/2} = \sum_a v_{ai}^* \langle \Omega | \mathcal{O}_a e^{-H\tau_0/2} \end{aligned}$$

for some reference time $\tau_0 > 0$. Inclusion of a reference time in the normalization of $|v_i\rangle$ is necessary to ensure that we never have to evaluate a correlation function at zero time separation:

$$\begin{aligned} \langle v_i | v_i \rangle &= \langle \Omega | \Theta_i e^{-H\tau_0} \overline{\Theta}_i |\Omega\rangle \\ &= C_i(\tau_0) \\ &= v_i^\dagger C(\tau_0) v_i \end{aligned}$$

$C(0)$ will generally involve products of multiple fields evaluated at a single space-time point. Such expressions lead to subtle difficulties which arise during the regularization process [Wei95]. Specifically, $C(0)$ will often receive nonzero contributions from ‘Schwinger terms’ [Sch59].

In the space of all possible states $\{|v_i\rangle\}$ parameterized by the vectors v_i , we would like to find states which are as close to the stationary states $\{|k\rangle\}$ as possible. The variational method [CT77] is a powerful technique that is used to diagonalize some Hermitian operator F within some subspace spanned by a set of parameterized trial states $\{|v\rangle\}$. To illustrate this method, let $f(v)$ be the expectation value of F in the state $|v\rangle$:

$$\begin{aligned} f(v) &\equiv \frac{\langle v|F|v\rangle}{\langle v|v\rangle}, \\ \langle v|F|v\rangle &= f(v)\langle v|v\rangle. \end{aligned}$$

Taking the first-order variation with respect to the parameter v gives

$$\begin{aligned} \langle \delta v|F|v\rangle + \langle v|F|\delta v\rangle &= (\delta f(v))\langle v|v\rangle + f(v)\langle \delta v|v\rangle + f(v)\langle v|\delta v\rangle \\ \langle \delta v|(F - f(v))|v\rangle + \langle v|(F^\dagger - f^*(v))|\delta v\rangle &= (\delta f(v))\langle v|v\rangle \end{aligned}$$

where we have used the Hermitian property $F^\dagger = F$. As long as $\langle v|v\rangle \neq 0$, we see that

$$\delta f(v) = 0 \quad \leftrightarrow \quad F|v\rangle = f(v)|v\rangle.$$

The variational method diagonalizes the operator F *restricted* to the subspace spanned by the $\{|v\rangle\}$. If any eigenstates of the unrestricted operator F are within the subspace, this method will find them. Otherwise, the method will produce the ‘closest states’ to the eigenstates of the full operator F it can find in the subspace.

For our purposes, we will vary the parameters v_i until the following expression is at an extremum:

$$\frac{\langle v_i|e^{-H(\tau-\tau_0)}|v_i\rangle}{\langle v_i|v_i\rangle} = \frac{v_i^\dagger C(\tau)v_i}{v_i^\dagger C(\tau_0)v_i}.$$

The infinitesimal change

$$v_i \rightarrow v_i + \delta v_i$$

gives

$$\begin{aligned} \delta \left[\frac{v_i^\dagger C(\tau)v_i}{v_i^\dagger C(\tau_0)v_i} \right] &= \frac{(v_i + \delta v_i)^\dagger C(\tau)(v_i + \delta v_i)}{(v_i + \delta v_i)^\dagger C(\tau_0)(v_i + \delta v_i)} - \frac{v_i^\dagger C(\tau)v_i}{v_i^\dagger C(\tau_0)v_i} = 0, \\ (v_i + \delta v_i)^\dagger C(\tau)(v_i + \delta v_i) - \left(\frac{v_i^\dagger C(\tau)v_i}{v_i^\dagger C(\tau_0)v_i} \right) (v_i + \delta v_i)^\dagger C(\tau_0)(v_i + \delta v_i) &= 0, \\ \delta v_i^\dagger \left[C(\tau)v_i - \left(\frac{v_i^\dagger C(\tau)v_i}{v_i^\dagger C(\tau_0)v_i} \right) C(\tau_0)v_i \right] + (\text{c.c.}) + O(\delta v_i^2) &= 0, \quad (2.21) \end{aligned}$$

where (c.c.) stands for the complex conjugate of the first term, and we have used the fact that $C^\dagger(\tau) = C(\tau)$.

Equation (2.21) is satisfied for all infinitesimal variations δv_i if:

$$C(\tau)v_i = \lambda_i(\tau, \tau_0)C(\tau_0)v_i \quad (2.22)$$

The eigenvalues $\lambda_i(\tau, \tau_0)$ (ordered by increasing value at each τ) of this generalized eigenvalue problem are called the *principal correlation functions*.

To find the asymptotic behavior of the principal correlation functions expressed in terms of the desired energies E_k , consider the quantity $v_i^\dagger C(\tau)v_j$. From the orthogonality property of the generalized Hermitian eigenvalue problem, we can always normalize our eigenvectors v_i such that:

$$v_i^\dagger C(\tau_0)v_j = \langle v_i | v_j \rangle = \delta_{ij},$$

which gives:

$$\begin{aligned} v_i^\dagger C(\tau)v_j &= \lambda_j(\tau, \tau_0)v_i^\dagger C(\tau_0)v_j, \\ \langle v_i | e^{-H(\tau-\tau_0)} | v_j \rangle &= 0 \quad i \neq j. \end{aligned}$$

We can write any state in the Hilbert space as a linear combination of the energy basis states

$$|v_j\rangle = \sum_k |k\rangle \alpha_{kj},$$

with the associated time evolution (or *relaxation*) given by

$$e^{-H(\tau-\tau_0)}|v_j\rangle = \sum_k |k\rangle \alpha_{kj} e^{-E_k(\tau-\tau_0)}.$$

Here we see that $|v_j\rangle$ evolves to a state which is orthogonal to $|v_i\rangle$. Because $|v_i\rangle$ has no overlap with the large-time relaxation state of $|v_j\rangle$, it is forced to relax to a *different* excited state. Thus, the n principal correlation functions $\lambda_i(\tau)$ behave as:

$$\lim_{\tau \rightarrow \infty} \lambda_k(\tau, \tau_0) = e^{-E_k(\tau-\tau_0)}(1 + O(e^{-\Delta_k(\tau-\tau_0)})) \quad (2.23)$$

$$\Delta_k \equiv \min_{l \neq k} |E_l - E_k|$$

where the E_k are the energies of the first n states accessible from the vacuum by the action of our creation operators $\overline{\mathcal{O}}$. An energy state $|k\rangle$ is accessible if there exists some $a \in 1, \dots, n$ such that

$$\langle k | \overline{\mathcal{O}}_a | \Omega \rangle \neq 0.$$

The contamination Δ_k arises due to the fact we are restricted to the subspace of states spanned by $\{\overline{\mathcal{O}}_a | \Omega \rangle\}$.

Looking at Eqn. 2.23, we may define the *principal effective mass functions*:

$$\begin{aligned} a_\tau M_k(\tau) &\equiv \ln \left[\frac{\lambda_k(\tau, \tau_0)}{\lambda_k(\tau + a_\tau, \tau_0)} \right] \\ \lim_{\tau \rightarrow \infty} a_\tau M_k(\tau) &\rightarrow a_\tau E_k \end{aligned}$$

We may turn the generalized Hermitian eigenvalue problem (2.22) into a regular Hermitian eigenvalue problem:

$$\begin{aligned} C(\tau)v_i &= \lambda_i(\tau, \tau_0)C(\tau_0)v_i, \\ C(\tau)C^{-1/2}(\tau_0)C^{+1/2}(\tau_0)v_i &= \lambda_i(\tau, \tau_0)C(\tau_0)v_i, \\ C^{-1/2}(\tau_0)C(\tau)C^{-1/2}(\tau_0)C^{+1/2}(\tau_0)v_i &= \lambda_i(\tau, \tau_0)C^{+1/2}(\tau_0)v_i, \\ [C^{-1/2}(\tau_0)C(\tau)C^{-1/2}(\tau_0)]u_i(\tau, \tau_0) &= \lambda_i(\tau, \tau_0)u_i(\tau, \tau_0), \end{aligned} \quad (2.24)$$

where we assume a positive-definite correlation matrix at $\tau = \tau_0$ and have added an explicit τ dependence to the eigenvector solutions $u_i(\tau, \tau_0)$ to remind the reader that fluctuations in the Monte Carlo estimates of the correlation matrix elements at different values of τ will result in corresponding fluctuations in the solution of Eqn. 2.24.

In practice, degeneracies or near-degeneracies in the energy levels combine with numerical uncertainties to introduce ambiguities into the estimate of a consistent set of fixed-coefficient vectors v_i and the consistent ordering of the principal correlation functions λ_i across different values of τ . In order to avoid these ambiguities and to fix a basis in degenerate subspaces, we will adopt the approach of solving for the fixed coefficient vectors v_i at a single time τ^* :

$$v_i = C^{-1/2}(\tau_0)u(\tau^*, \tau_0),$$

where τ^* is chosen to be as small as possible (to avoid noise) but large enough to ensure that the estimates of the v_i have stabilized. The diagonal elements of the *rotated* correlation matrix $\tilde{C}(\tau)$ are called *fixed-coefficient* correlation functions, and are defined by

$$\tilde{C}_{kk}(\tau) \equiv v_k^\dagger C(\tau)v_k,$$

and can be used to define *fixed-coefficient* effective mass functions:

$$a_\tau M_k(\tau) \equiv \ln \left[\frac{\tilde{C}_{kk}(\tau)}{\tilde{C}_{kk}(\tau + a_\tau)} \right] = \ln \left[\frac{v_k^\dagger C(\tau)v_k}{v_k^\dagger C(\tau + a_\tau)v_k} \right].$$

The fixed-coefficient correlation functions $\tilde{C}_{kk}(\tau)$ differ from the principal correlation functions $\lambda_k(\tau, \tau_0)$ because we are only solving the eigenvalue problem once, at τ^* . Thus we are only guaranteed orthogonality at τ^* :

$$\tilde{C}_{ij}(\tau^*) = 0 \quad i \neq j.$$

The lack of orthogonality for $\tau > \tau^*$, no matter how small, means that our fixed-coefficient correlation functions will eventually relax to the lowest excited state

$$\tilde{C}_{kk}(\tau) \xrightarrow{\tau \gg \tau^*} |c_1|^2 \exp(-E_1\tau).$$

In Chapter 8, we will seek (and find) a range of τ values over which orthogonality holds to good approximation. This will allow us to extract the values of the excited states using exponential fits to the fixed-coefficient correlation functions.

2.8.2 Discussion

The variational method allows the physics to tell us which combination of the candidate operators best interpolates for the stationary states of the Hamiltonian. Because the coefficients $\{v_{ai}\}$ are time-independent, we may use them to infer something about the physical structure of the state $|k\rangle$ from the way in which the operators $\overline{\mathcal{O}}_a$ combine to form $\overline{\Theta}_k$.

Our need to perform the inversion and square root in Eqn. 2.24 underscores the importance of choosing candidate operators which give a correlation matrix with a good condition number. We will keep this in mind in Chapter 7 when we prune our large operator set down to manageable size.

Our task is to construct a ‘good’ set of candidate operators $\overline{\mathcal{O}}_a$ which we believe capture a representative set of features of the baryon spectrum we seek (in order to construct a ‘good’ trial subspace for the variational method).

Chapter 3

The Monte Carlo method

Our goal is to compute the low-lying spectrum of lattice QCD. We do this by calculating the elements of Euclidean space-time correlation matrices, each of which is a ratio of functional integrals:

$$C_{ab}(\tau) = \langle \mathcal{O}_a(\tau) \overline{\mathcal{O}}_b(0) \rangle, \quad (3.1)$$

$$= \frac{1}{Z} \int_{\text{p.b.c.}} \mathcal{D}U \mathcal{D}\overline{\psi} \mathcal{D}\psi \mathcal{O}_a(\tau) \overline{\mathcal{O}}_b(0) e^{-S_F[\overline{\psi}, \psi, U] - S_G[U]}, \quad (3.2)$$

where

$$Z = \int_{\text{p.b.c.}} \mathcal{D}U \mathcal{D}\overline{\psi} \mathcal{D}\psi e^{-S_F[\overline{\psi}, \psi, U] - S_G[U]}, \quad (3.3)$$

$$S_F[\overline{\psi}, \psi, U] = \overline{\psi} Q[U] \psi, \quad (3.4)$$

$$Q_{x,y}[U] = (a_\tau m + \frac{3\nu}{\xi_0} + 1) \delta_{x,y} \quad (3.5)$$

$$- \frac{\nu}{2\xi_0} \sum_j \left[(1 - \gamma_j) U_j(x) \delta_{x+\hat{j},y} + (1 + \gamma_j) U_j^\dagger(x - \hat{j}) \delta_{x-\hat{j},y} \right]$$

$$- \frac{1}{2} \left[(1 - \gamma_4) U_4(x) \delta_{x+\hat{4},y} + (1 + \gamma_4) U_4^\dagger(x - \hat{4}) \delta_{x-\hat{4},y} \right], \quad (3.6)$$

$$S_G[U] = \frac{\beta}{N} \sum_x \left[\sum_{j < k} \frac{1}{\xi_0} \text{Re Tr}(1 - U_{jk}(x)) + \sum_j \xi^0 \text{Re Tr}(1 - U_{j4}(x)) \right]. \quad (3.7)$$

Before we turn to the design of the operators $\overline{\mathcal{O}}_a$, we briefly discuss how we will evaluate the ratio of functional integrals defined by Eqns. 3.2 and 3.3.

3.1 The need for the Monte Carlo method

These integrals are regularized by the space-time lattice, but still consist of an unmanageable number of integration variables. The Feynman diagram method is not applicable to QCD functional integrals because expansions parameterized by the coupling constant do not converge at the energy scales in which we are interested.

We turn instead to the Monte Carlo method, a powerful technique which requires us to formulate the problem on a computer. Our quark fields satisfy Fermi-Dirac statistics, and are therefore represented by anticommuting Grassmann variables which are not suitable for direct numerical integration on a computer. Fortunately, the quark fields appear quadratically in the action and in the operator pairs $\mathcal{O}(\tau)\overline{\mathcal{O}}(0)$, which means that the Gaussian integral over the fermion fields is symbolically integrable. Therefore, we will integrate out the Grassmann fields by hand before we translate the functional integral to computer language.

3.2 Integrating the quark fields

We wish to perform integrals of the form

$$\begin{aligned} & \frac{1}{Z_F} \int_{\text{p.b.c.}} \mathcal{D}\bar{\psi} \mathcal{D}\psi \psi_{x_1} \bar{\psi}_{x_2} \cdots \psi_{x_{n-1}} \bar{\psi}_{x_n} \exp\left(-\sum_{x,y} \bar{\psi}_x Q_{x,y}[U] \psi_y\right) \\ &= \frac{\delta}{\delta J_{x_2}} \frac{\delta}{\delta \bar{J}_{x_1}} \cdots \frac{\delta}{\delta J_{x_n}} \frac{\delta}{\delta \bar{J}_{x_{n-1}}} \ln(Z_F[\bar{J}, J])|_{\bar{J}, J=0} \end{aligned} \quad (3.8)$$

where we have introduced the fermion generating functional $Z_F[\bar{J}, J]$:

$$Z_F[\bar{J}, J] \equiv \int_{\text{p.b.c.}} \mathcal{D}\bar{\psi} \mathcal{D}\psi \exp\left(-\sum_{x,y} \bar{\psi}_x Q_{x,y}[U] \psi_y + \sum_x [\bar{J}_x \psi_x + \bar{\psi}_x J_x]\right), \quad (3.9)$$

which will allow us to insert arbitrary factors of $\psi_x \bar{\psi}_y$ into the functional integral by taking functional derivatives of $Z_F[\bar{J}, J]$ with respect to the source fields J_y and \bar{J}_x and then setting $J_y = 0$, $\bar{J}_x = 0$, which eliminates the source terms and gives $Z_F = Z_F[0, 0]$.

The sources \bar{J}_x , J_x and the functional derivatives $\frac{\delta}{\delta \bar{J}_x}$, $\frac{\delta}{\delta J_x}$ obey the Grassmann algebra just like the quark variables $\bar{\psi}_x$ and ψ_x , and satisfy:

$$\frac{\delta}{\delta \bar{J}_x} \bar{J}_y = \delta_{x,y} \quad \frac{\delta}{\delta \bar{J}_x} J_y = 0 \quad \frac{\delta}{\delta J_x} J_y = \delta_{x,y} \quad \frac{\delta}{\delta J_x} \bar{J}_y = 0$$

We can integrate $Z_F[\bar{J}, J]$ by shifting the quark field variables to complete the square in

the exponent:

$$\begin{aligned}\bar{\psi}'_x &\equiv \bar{\psi}_x - \bar{J}_y Q_{y,x}^{-1}[U] \\ \psi'_x &\equiv \psi_x - Q_{x,y}^{-1}[U] J_y\end{aligned}$$

$$\begin{aligned}Z_F[\bar{J}, J] &= \int_{\text{p.b.c.}} \mathcal{D}\bar{\psi}' \mathcal{D}\psi' \exp\left(-\sum_{x,y} \bar{\psi}'_x Q_{x,y}[U] \psi'_y + \sum_{x,y} \bar{J}_x Q_{x,y}^{-1}[U] J_y\right), \\ &= \int \prod_{x'} d\bar{\psi}_{x'} d\psi_{x'} \exp\left(-\sum_{x,y} \bar{\psi}_x Q_{x,y}[U] \psi_y\right) \exp\left(\sum_{x,y} \bar{J}_x Q_{x,y}^{-1}[U] J_y\right)\end{aligned}\quad (3.10)$$

where we have dropped the primes, written the integration measure explicitly, and have used the fact that the product of two Grassmann numbers behaves as a c-number. The product of integrations extends over all lattice sites x' , and the fermionic boundary conditions are applied to expressions such as $\delta_{x,x+\hat{\mu}}$ within the quark matrix $Q[U]$ and inverse quark matrix $Q^{-1}[U]$.

The Gaussian integral over Grassmann variables in Eqn. 3.10 can be evaluated [MM94] by expanding the integral and keeping only terms which do not vanish when integrated:

$$\int \prod_{x'} d\bar{\psi}_{x'} d\psi_{x'} \exp\left(-\sum_{x,y} \bar{\psi}_x Q_{x,y}[U] \psi_y\right) = \det(Q[U]) \int \prod_{x'} (d\bar{\psi}_{x'} \bar{\psi}_{x'}) (d\psi_{x'} \psi_{x'}) = \det(Q[U])$$

Thus

$$Z_F[\bar{J}, J] = \det(Q[U]) \exp\left(\sum_{x,y} \bar{J}_x Q_{x,y}^{-1}[U] J_y\right)$$

At this point it is essential to address the correct treatment of the suppressed color, flavor, and Dirac indices. The matrix $Q[U]$ carries those indices, as do the variables $\bar{\psi}$, ψ , \bar{J} and J . The quark matrix $Q[U]$ can be thought of as a tensor product of matrices acting in position space, color space, flavor space, and spin space:

- $\delta_{x,x+\hat{\mu}}$ acts in position space
- $(U_\mu)_{ab}(x)$ acts in color space
- $Q[U]$ is diagonal in flavor space (QCD conserves flavor)
- $(\gamma_\mu)_{\alpha\beta}$ acts in spin space

Consequently, when we take a matrix determinant or inversion, we must do so with respect to all indices.

We can use the fermion generating functional to define the full generating functional $Z[\bar{J}, J]$:

$$Z[\bar{J}, J] \equiv \int_{\text{p.b.c.}} \mathcal{D}U \det(Q[U]) e^{-S_G[U] + \bar{J}Q^{-1}[U]J} \quad (3.11)$$

where now the functional integral is only over gauge links, with the fermionic boundary conditions applied to $Q[U]$, $Q^{-1}[U]$, and the bosonic boundary conditions applied to $S_G[U]$.

Any correlation matrix element of the form in Eqn. 3.2 can be evaluated with the use of the generating functional in Eqn. 3.11. For every fermion pair $\psi_x \bar{\psi}_y$, we apply $\frac{\delta}{\delta J_y} \frac{\delta}{\delta \bar{J}_x}$ to $\ln(Z[\bar{J}, J])$. Any gauge link factors are left as they are. We then set the Grassmann source fields \bar{J} and J to zero, and evaluate the remaining regularized and well-defined integral over the gauge links U .

For example, the single quark propagator is:

$$\begin{aligned} \langle \psi_x \bar{\psi}_y \rangle &= \frac{1}{Z} \int_{\text{p.b.c.}} \mathcal{D}U Q_{x,y}^{-1}[U] \det(Q[U]) e^{-S_G[U]} \\ Z &= \int_{\text{p.b.c.}} \mathcal{D}U \det(Q[U]) e^{-S_G[U]}. \end{aligned}$$

In the case of two quark/antiquark fields, an additional term is generated by the derivatives:

$$\langle \psi_{x_1} \bar{\psi}_{x_2} \psi_{x_3} \bar{\psi}_{x_4} \rangle = \frac{1}{Z} \int_{\text{p.b.c.}} \mathcal{D}U (Q_{x_1, x_2}^{-1} Q_{x_3, x_4}^{-1} - Q_{x_1, x_4}^{-1} Q_{x_3, x_2}^{-1}) \det(Q) e^{-S_G}$$

The general way to evaluate correlation functions of arbitrary numbers of quark-antiquark field pairs is to add up all possible permutations the fields which are in alternating ψ - $\bar{\psi}$ form (this can be done graphically using Wick's theorem [Bro92]). For each term we can read off the inverse quark matrix indices from the indices of the fields, and include a minus sign if we performed an odd number of anticommutations to get the quark fields into their final ordering.

In Chapter 5, we will need correlation matrix elements of the form

$$\langle \psi_{x_1} \psi_{x_2} \psi_{x_3} \bar{\psi}_{x_4} \bar{\psi}_{x_5} \bar{\psi}_{x_6} \rangle$$

The six relevant permutations and signs are given by:

Permutation	Sign
14 25 36	-
14 26 35	+
15 24 36	+
15 26 34	-
16 24 35	-
16 25 34	+

Thus

$$\begin{aligned}
\langle \psi_{x_1} \psi_{x_2} \psi_{x_3} \bar{\psi}_{x_4} \bar{\psi}_{x_5} \bar{\psi}_{x_6} \rangle &= \frac{1}{Z} \int_{\text{p.b.c.}} \mathcal{D}U \left(\begin{aligned}
&- Q_{x_1, x_4}^{-1} Q_{x_2, x_5}^{-1} Q_{x_3, x_6}^{-1} \\
&+ Q_{x_1, x_4}^{-1} Q_{x_2, x_6}^{-1} Q_{x_3, x_5}^{-1} \\
&+ Q_{x_1, x_5}^{-1} Q_{x_2, x_4}^{-1} Q_{x_3, x_6}^{-1} \\
&- Q_{x_1, x_5}^{-1} Q_{x_2, x_6}^{-1} Q_{x_3, x_4}^{-1} \\
&- Q_{x_1, x_6}^{-1} Q_{x_2, x_4}^{-1} Q_{x_3, x_5}^{-1} \\
&+ Q_{x_1, x_6}^{-1} Q_{x_2, x_5}^{-1} Q_{x_3, x_4}^{-1}
\end{aligned} \right) \det(Q) e^{-S_G} \quad (3.12)
\end{aligned}$$

The integrand now contains only pure functions of the gauge link variables: $Q[U]$, $Q^{-1}[U]$, and $S_G[U]$.

3.3 The Monte Carlo method of integration

Now that we have a well defined integral and have integrated out the quark degrees of freedom, we would like to evaluate expressions such as:

$$\begin{aligned}
\langle f[U] \rangle &\equiv \frac{1}{Z} \int_{\text{p.b.c.}} \mathcal{D}U f[U] \det(Q[U]) e^{-S_G[U]} \\
&= \frac{\int \prod_{x, \mu} dU_\mu(x) f[U] \det(Q[U]) e^{-S_G[U]}}{\int \prod_{x, \mu} dU_\mu(x) \det(Q[U]) e^{-S_G[U]}} \quad (3.13)
\end{aligned}$$

where each $dU_\mu(x)$ is the appropriate Haar measure over the $SU(3)$ group [Cre85]. There are $(2 \times N_s^3 \times N_\tau \times 4)$ $SU(3)$ integration variables, where N_s and N_τ are the number of lattice sites in the spatial and temporal directions, respectively. $SU(3)$ has eight generators, so a brute force integration over our small $12^3 \times 48$ lattice would consist of a $2 \times 12^3 \times 48 \times 4 \times 8 = 5,308,416$ dimensional real integral over a compact domain.

The Monte Carlo method was specifically developed to estimate integrals over a large number of degrees of freedom [PFTV92]:

$$\frac{1}{V} \int_V d\mu(x) f(x),$$

where

$$V \equiv \int_V d\mu(x).$$

The Monte Carlo method uses the normalized integration measure $d\mu(x)/V$ at each point in the integration domain to define the measure $p_F(x)dx$ over a probability space F . An

ensemble of N configurations $\{x_1, x_2, \dots, x_n\}$ is generated according to the probability measure over F , and the integral is estimated by:

$$\frac{1}{V} \int_V d\mu(x) f(x) \approx \frac{1}{N} \sum_{n=1}^N f(x_n) \equiv \bar{f}$$

The expectation value of the ensemble average \bar{f} over F is the same as the expectation value of the function evaluated on any single member of the ensemble x_i , and equals the desired integral:

$$E_F[\bar{f}] = \frac{1}{N} \sum_{n=1}^N E_F[f(x_n)] = E_F[f(x)] \quad (3.14)$$

$$= \int_V p(x) d\mu(x) f(x) \quad (3.15)$$

$$= \frac{1}{V} \int_V d\mu(x) f(x) \quad (3.16)$$

From the central limit theorem [Bil86] we know that if N is sufficiently large¹, then \bar{f} will be normally distributed with:

$$\text{Var}_F[\bar{f}] \propto \frac{1}{N} \quad (3.17)$$

The variance of the estimate $\text{Var}_F[\bar{f}]$ is a measure of the uncertainty, or expected error, caused by using a finite number N of configurations in the Monte Carlo estimate of the integral. We will return to the task of estimating $\text{Var}_F[\bar{f}]$ in Section 3.5.

3.3.1 Importance sampling

For our present purposes, we would like to perform high-dimensional integrals of the form in Eqn. 3.13. Because the Euclidean gauge action $S_G[U]$ is real and bounded from below, we can absorb the exponential damping term $\exp(-S_G[U])$ into our definition of the measure. Weighting the probability of generating a configuration with the Boltzmann-type factor $\exp(-S_G[U])$ greatly reduces the variance of our estimates by suppressing configurations which give exponentially small contributions to the functional integral. The fermion determinant $\det(Q[U])$ is not real for all configurations because we treat $\bar{\psi}$ and ψ as independent variables in the functional integral. This unfortunate situation, known as the *fermion sign problem*, makes it difficult to include the fermion determinant into our definition of the measure.

After absorbing the exponential factor into the measure, we can estimate the functional integral in Eqn. 3.13 by first generating an ensemble of lattice-wide gauge link configurations

¹Finite ensemble error analysis involves subtle issues and is treated in detail in section 3.5.

$\{\{U_\mu(x)\}_1, \dots, \{U_\mu(x)\}_N\} \equiv \{U^{(1)}, \dots, U^{(N)}\}$ according to the joint probability density:

$$p(U^{(n)}) = \frac{e^{-S_G[U^{(n)}]}}{\int \prod_{x,\mu} dU_\mu(x) \det(Q[U]) e^{-S_G[U]}}$$

and then approximating:

$$\langle f[U] \rangle \approx \frac{\frac{1}{N} \sum_{n=1}^N f[U^{(n)}] \det(Q[U^{(n)}])}{\frac{1}{N} \sum_{m=1}^N \det(Q[U^{(m)}])}. \quad (3.18)$$

3.4 Markov updating

We now turn to the task of generating the gauge configurations $U^{(n)}$. Given some configuration, we may generate a new configuration by cycling through the lattice and proposing random (valid) changes to the individual link variables. The new proposed change is accepted or rejected based on some probabilistic rule which considers the Boltzmann factor of the configuration that would result if the link change was accepted. The process is repeated for several sweeps through the entire lattice in order to produce an updated configuration. This is an example of a *Markov chain*, a class of processes in which the current state depends probabilistically on the previous state. We require our Markov chains to be *ergodic*: any state in the configuration space can be reached from any other state in a finite number of updating steps. This is necessary to ensure that we are adequately exploring the integration domain during our Monte Carlo integration.

A Markov chain is initialized to some initial state $U^{(0)}$. It is then updated until it ‘thermalizes.’ At this point, all of the statistical properties of the states being generated in the chain have stabilized. For example, one can plot a moving average of the plaquette value to determine when the Markov chain has thermalized. The plot will drift rapidly at first, and then fluctuate around some average value. If the configuration at which this begins to happen is denoted $U^{(m)}$, then we take the configurations from $U^{(m+1)}$ to $U^{(m+N)}$ for our ensemble. $U^{(0)} \rightarrow U^{(1)} \rightarrow U^{(2)} \rightarrow \dots \rightarrow U^{(m)} \rightarrow \underbrace{U^{(m+1)} \rightarrow \dots \rightarrow U^{(m+N)}}_{\text{keep}}$

Examining the moving average of the plaquette is just a heuristic; in practice thermalization is a subtle issue requiring careful treatment. Whenever possible, it is preferred to initialize a Markov chain with a thermalized configuration from a previous instance of the Markov chain.

3.4.1 Quenching

Because the fermion determinant $\det(Q[U])$ is a complex quantity, it is an extremely difficult quantity to estimate numerically due to cancellations. There exist tricks, such as

the Weingarten pseudo-fermion method [Wei85], which enable us to include the fermion determinant in the updating algorithm as part of the integration measure. Such methods are computationally expensive because they involve the inversion of a matrix having space-time, color, and spin indices. The inversion of such matrices is currently the single largest bottleneck in Lattice QCD calculations.

For this work, we will work in the *quenched* ‘*approximation*’ where we simply set the fermion determinant in Eqn. 3.18 to one:

$$\det(Q[U]) \rightarrow 1.$$

This is an unparameterized ‘*approximation*’ which breaks the unitarity of the theory. Nonetheless, it is expected to be mostly harmless for tuning studies with unphysically heavy quark masses (such as this work) because quenching is expected to affect the levels of the spectrum, but not the coupling of the operators to the spectral states. The fermion determinant is a highly non-local object containing the complete contribution to the action of the fermionic degrees of freedom. From the (non-convergent) Feynman diagram point of view, quenching is equivalent to removing all diagrams containing sea-quark loop contributions.

3.4.2 Configurations used in this work

Although updating is an important and subtle topic, it is not the focus of this work. We briefly describe the method used to generate our gauge configurations.

The fact that Wilson’s formulation of lattice QCD uses compact gauge links removes the need for gauge fixing (see the discussion in section 1.7.8). Thus, it is possible to update the gauge links freely according only to the probability distribution $\exp(-S_G[U])$. There is no need to require that the new configuration adhere to any fixed gauge prescription.

The gauge configurations used in this work were generated using the Chroma QCD library developed at JLab, and use the parameters reported in Subsection 2.5.1. That code used the Cabibbo-Marinari heatbath algorithm [CM82, KP85] in conjunction with Creutz’s overrelaxation technique [Cre87] to update the gauge configurations.

Because the configurations are quenched, the quark masses did not play a role in the updating. However, they are used in the propagator calculations, which involve factors of inverse quark matrix elements such as $Q_{x,y}^{-1}[U]$. The operators presented in this work act on the nucleon sector, thus only the bare light quark mass $a_\tau m_u = a_\tau m_d = -0.305$ was reported in Subsection 2.5.1.

Quenching will not be used in the production runs, and it will be assumed here that our operator choices and tuning parameters will not be significantly affected by quenching. In this study, we find that our quenched configurations still yield a useful spectrum. Rather,

they serve as an indication of the quality of the operators to be used in this ongoing research effort.

3.5 Error analysis

Monte Carlo integration is a statistical procedure. It only provides stochastic estimates of quantities subject to statistical uncertainty. The use of a Markov chain to generate the configurations in our ensemble introduces autocorrelations (discussed below). Additionally, we will be transforming our data in a complicated manner (e.g. $C^{-1/2}(\tau_0)$) and need to quantify the statistical uncertainty for such quantities.

3.5.1 Estimate variance in the presence of autocorrelation

We have an ensemble of N (thermalized) configurations $\{x_i\}$ which looks as though it was drawn from some probability distribution F but was actually produced in sequential order by a Markov chain. The Markov process introduces serial autocorrelations [Ken06] into the ensemble which increases the true variance of the estimate $\text{Var}_F[\bar{f}]$. This implies that estimates² $\widehat{\text{Var}}[\bar{f}]$ of the variance of \bar{f} will *underestimate* the true variance $\text{Var}_F[\bar{f}]$ of \bar{f} . In other words, our error bars will be too small if our data is autocorrelated.

To reduce clutter in the following, we define

$$\begin{aligned} g(x) &= f(x) - E_F[f(x)], \\ \bar{g} &\equiv \frac{1}{N} \sum_{n=1}^N g(x_n) = \bar{f} - E_F[\bar{f}], \end{aligned}$$

which has the properties

$$\begin{aligned} E_F[g(x)] &= 0, \\ E_F[g(x)^2] &= \text{Var}[f(x)], \\ E_F[\bar{g}^2] &= \text{Var}[\bar{f}]. \end{aligned}$$

²In this chapter, we will denote sample estimates of statistics with a hat. For example, if we use the sample mean of some quantity x to estimate x , then we may write $\hat{x} = \bar{x}$.

The variance of the ensemble average is

$$\begin{aligned}
\text{Var}_F[\bar{f}] &= E_F[\bar{g}^2], \\
&= \frac{1}{N^2} \sum_{n=1}^N \sum_{m=1}^N E_F[g(x_m)g(x_n)], \\
&= \frac{1}{N^2} \sum_{n=1}^N E_F[g(x_n)^2] + \frac{2}{N^2} \sum_{n=1}^{N-1} \sum_{m=n+1}^N E_F[g(x_m)g(x_n)], \\
&= \frac{1}{N} E_F[g(x)^2] \left(1 + \frac{2}{N} \sum_{n=1}^{N-1} \sum_{m=n+1}^N \frac{E_F[g(x_m)g(x_n)]}{E_F[g(x)^2]} \right) \tag{3.19}
\end{aligned}$$

We can define the *autocorrelation function* $C_k[f(x)]$ for a function $f(x)$ evaluated on an ordered series of observations $\{x_1, x_2, \dots, x_N\}$ by

$$\begin{aligned}
C_k[f(x)] &= \frac{E_F[(f(x_{n+k}) - E_F[f(x_{n+k}]))(f(x_n) - E_F[f(x_n)])]}{\sqrt{E_F[(f(x_{n+k}) - E_F[f(x_{n+k}]])^2]E_F[(f(x_n) - E_F[f(x_n)])^2]}} \\
&= \frac{E_F[(f(x_{n+k}) - E_F[f(x_{n+k}]))(f(x_n) - E_F[f(x_n)])]}{E_F[(f(x) - E_F[f(x)])^2]} \tag{3.20}
\end{aligned}$$

There is no n index on the left hand side of Eqn. 3.20 because we assume that the process generating the configurations has reached a stationary state (i.e. the statistical properties of the sequence are invariant under translations in n).

We may rewrite equation (3.19) in terms of $C_k[f(x)]$:

$$\begin{aligned}
\text{Var}_F[\bar{f}] &= \frac{1}{N} \text{Var}_F[f(x)] \left(1 + \frac{2}{N} \sum_{n=1}^{N-1} \sum_{m=n+1}^N C_{m-n}[f(x)] \right), \\
&= \frac{1}{N} \text{Var}_F[f(x)] \left(1 + \frac{2}{N} \sum_{k=1}^{N-1} (N-k) C_k[f(x)] \right), \\
&= \frac{1}{N} \text{Var}_F[f(x)] \left(1 + 2 \sum_{k=1}^{N-1} C_k - \frac{2}{N} \sum_{k=1}^{N-1} k C_k[f(x)] \right),
\end{aligned}$$

where we remind the reader that $\text{Var}_F[\bar{f}]$ is the *true* variance of \bar{f} . In the case of a Markov chain, $C_k[f(x)]$ falls exponentially with k , and for sufficiently large N we have [BMK73]

$$\text{Var}_F[\bar{f}] \rightarrow \frac{1}{N} \text{Var}_F[f(x)] (1 + 2A[f(x)]). \tag{3.21}$$

where

$$A[f(x)] = \sum_{k=1}^{\infty} C_k[f(x)]$$

is the ‘integrated’ autocorrelation of the function f . Thus we see that in the presence of autocorrelation, the simple estimate of variance:

$$\widehat{Var}[\bar{f}] = \frac{1}{N} \text{Var}_F[f(x)]$$

understates the true variance $\text{Var}_F[\bar{f}]$.

A simple unbiased estimate of $\text{Var}_F[f(x)]$ on an ensemble $\{x_1, x_2, \dots, x_N\}$ is

$$\widehat{Var}[f(x)] \equiv \frac{1}{N-1} \sum_{n=1}^N (f(x_n) - \bar{f})^2 \quad (3.22)$$

with a similar expression for \widehat{C}_k . In practice, the Markov chain updating method is tuned to reduce the autocorrelation in the data to negligible levels.

3.5.2 The Jackknife estimate of variance

The variance estimate in Eqn. 3.22 is applicable to functions f evaluated separately on each ensemble member. As the ensemble member fluctuates, so does $f(x)$. Eqn. 3.22 is not generally applicable to more complicated functions f which involve multiple members of the ensemble simultaneously.

In the following, each x_n denotes a collection of simple quantities (such as correlation matrix elements) evaluated on the n^{th} gauge link configuration generated by the Markov chain. We are interested in a special class of functions f which depend on the all of the ensemble members x_i simultaneously through the ensemble average \bar{x} :

$$f(\bar{x}), \quad \bar{x} \equiv \frac{1}{N} \sum_{n=1}^N x_n.$$

In this work, the \bar{x} correspond to Monte Carlo estimates of correlation functions, and the f correspond to the analysis methods applied to these estimates. Consequently, f will typically be a complicated function of the ensemble average \bar{x} , e.g. taking the inverse square root of a matrix or solving a Hermitian eigenvalue problem. We would like to know how $f(\bar{x})$ varies across ensembles, not across the members of the ensembles.

The typical variance estimate in Eqn. 3.22 is not generally applicable to functions of the *mean* of an ensemble: $f(\bar{x})$. Using estimates $f(x_i)$ on individual ensemble members in an attempt to estimate the variance of $f(\bar{x})$ is often a poor approach because the function may only be well defined for certain values of its argument. The individual members of the ensemble x_i fluctuate far more than does the ensemble average \bar{x} , and these larger fluctuations may result in an undefined $f(x_n)$. For example, if $f(\bar{x}) = \ln(\bar{x})$, then $f(x_n)$ will be undefined any time $x_n \leq 0$, even if $\bar{x} > 0$.

The *jackknife* estimate of the variance [Efr82] is a non-parametric alternative that uses re-sampling to numerically estimate the expected squared fluctuation of f across ensembles. The jackknife method is applicable to virtually any function f , but we will specialize it here to functions of ensemble averages $f(\bar{x})$.

Let $\bar{x}_{(n)}$ be the ensemble average excluding the n^{th} ensemble member x_n :

$$\bar{x}_{(n)} \equiv \frac{1}{N-1} \sum_{\substack{m=1 \\ m \neq n}}^N x_m = \frac{N\bar{x} - x_n}{N-1} = \bar{x} - \left(\frac{x_n - \bar{x}}{N-1} \right)$$

Accordingly, we can define the n^{th} *jackknife replicate* $f_{(n)}$ by:

$$f_{(n)} \equiv f(\bar{x}_{(n)}).$$

In contrast to $f(x_n)$ which relies on the information in *only* the n^{th} ensemble member, the jackknife replicate $f_{(n)}$ is supported by the information in all ensemble members *except* the n^{th} . The power of this technique is that we can usually choose N large enough to ensure that both $f(\bar{x})$ and $f(\bar{x}_{(n)})$ are well defined.

The N jackknife replicates $f_{(n)}$ are highly correlated, but it is reasonable to expect that their mean squared fluctuations are proportional to the mean squared fluctuations of $f(\bar{x})$. The jackknife estimate of the variance of f across ensembles is:

$$\begin{aligned} \widehat{\text{Var}}_{\text{jack}}[f(\bar{x})] &\equiv \left(\frac{N-1}{N} \right) \sum_{n=1}^N (f_{(n)} - f_{(\cdot)})^2, \\ f_{(\cdot)} &\equiv \frac{1}{N} \sum_{n=1}^N f_{(n)}. \end{aligned} \quad (3.23)$$

The *jackknife error* is defined as the square root of the jackknife estimate of the variance.

We can verify the constant of proportionality $(N-1)/N$ in Eqn. 3.23 by considering the known case $f(\bar{x}) = \bar{x}$:

$$\begin{aligned} \widehat{\text{Var}}_{\text{jack}}[\bar{x}] &= \left(\frac{N-1}{N} \right) \sum_{n=1}^N (\bar{x}_{(n)} - \bar{x}_{(\cdot)})^2, \\ &= \left(\frac{N-1}{N} \right) \sum_{n=1}^N \left(\bar{x} - \left(\frac{x_n - \bar{x}}{N-1} \right) - \bar{x} \right)^2 \\ &= \left(\frac{1}{N(N-1)} \right) \sum_{n=1}^N (x_n - \bar{x})^2, \\ &= \frac{1}{N} \widehat{\text{Var}}[f(x)] \end{aligned}$$

which is the expected expression for the (uncorrelated) estimate of the variance of \bar{x} . We also emphasize that we use $f(\bar{x})$, not $f(\cdot)$, to estimate $f(x)$:

$$\hat{f} = f(\bar{x}).$$

A generalization of the jackknife is the *bootstrap*, in which a large number N_B (typically $O(1024)$) of bootstrap ensembles are each created by selecting N members (with replacement) from the original ensemble. f is then evaluated on the bootstrap ensembles to yield N_B bootstrap replicates $f_{[b]}$. The bootstrap estimate of the variance of f across ensembles is given by:

$$\widehat{\text{Var}}_{\text{boot}}[f(\bar{x})] = \left(\frac{1}{N_B - 1} \right) \sum_{b=1}^{N_B} (f_{[b]} - f_{[.]})^2$$

$$f_{[.]} \equiv \frac{1}{N_B} \sum_{b=1}^{N_B} f_{[b]}$$

We use the simple jackknife method to estimate the errors on our effective mass plots and the more thorough bootstrap method to estimate the uncertainties in our final fit parameter estimates.

Chapter 4

Baryon operator construction

4.1 Operator design goals

The spectrum is calculated by evaluating correlation matrix elements of quantum operators:

$$C_{ab}(\tau) = \langle \mathcal{O}_a(\tau) \overline{\mathcal{O}}_b(0) \rangle = \sum_{k=1}^{\infty} |c_k|^2 e^{-E_k \tau}, \quad c_k \equiv \langle k | \overline{\mathcal{O}} | \Omega \rangle, \quad (4.1)$$

assuming a large temporal extent T of the lattice and that the lattice action satisfies reflection positivity [OS73a, OS75].

This chapter describes the design of operators which excite the low-lying baryon spectral states. We seek to find operators such that c_k in Eqn. 4.1 is as large as possible for the low-lying states of interest while being as small as possible for higher-lying contaminating states. Because we are using the Monte Carlo method to estimate Eqn. 4.1, we also need to improve our operators to reduce the variance in the estimates of $C_{ab}(\tau)$. With these issues in mind, our goal is to design a set of operators which

- are gauge-invariant,
- have the correct flavor content,
- facilitate continuum spin identification,
- rapidly plateau in the effective mass,
- have minimal noise in the effective mass,
- are linearly independent, and
- compose a set of manageable size.

This chapter is based on the operator design approach developed by the LHPC and described in [BEF⁺05a, BEF⁺05b, LMB⁺06]. We begin by introducing the basic building blocks of our operators: smeared and covariantly-displaced quark fields, and smeared gauge links which are combined into gauge-invariant three-quark operators. Next, we discuss the group theoretic approach adopted by the LHPC. The gauge-invariant three-quark operators are then endowed with the appropriate flavor structure to make our three-quark elemental operators. These elemental operators are then combined into full baryon operators which transform irreducibly under spatial lattice symmetry operations (rotations and reflections). The chapter concludes by showing how the states excited by these operators are connected to the continuum J^P baryon states.

4.2 Building blocks

On the lattice, we have quark sources $\bar{\psi}_{a\alpha}^A(x)$, quark sinks $\psi_{a\alpha}^A(x)$, and gauge links $U_{\mu ab}(x)$, where A is a flavor index, a, b are color indices, and α is a Dirac spin index. We have returned to writing the space-time index x in parenthesis in order to avoid clutter. Note that we are still working with the unitless fields defined previously.

4.2.1 Spatial inversion

Under spatial inversion I , the field operators transform as:

$$U_I \bar{\psi}_\alpha(\vec{x}, \tau) U_I^\dagger = \bar{\psi}_\beta(-\vec{x}, \tau) \bar{I}_{\beta\alpha} \quad U_I \psi_\alpha(\vec{x}, \tau) U_I^\dagger = \psi_\beta(-\vec{x}, \tau) I_{\beta\alpha}$$

where the 4×4 parity matrices \bar{I} and I keep track of how the spin components of the fields change under spatial inversion. Summation over repeated indices is implied. To find the form of \bar{I} and I , we consider how the fermion terms in the continuum Euclidean action transform under the action of spatial inversion:

$$\begin{aligned} \int d^4x \bar{\psi}_\alpha(\vec{x}, \tau) \psi_\alpha(\vec{x}, \tau) &\rightarrow \int d^4x \bar{\psi}_\beta(-\vec{x}, \tau) \psi_\gamma(-\vec{x}, \tau) \bar{I}_{\beta\alpha} I_{\gamma\alpha} \\ &= \int d^4x \bar{\psi}_\beta(\vec{x}, \tau) \psi_\gamma(\vec{x}, \tau) \bar{I}_{\beta\alpha} I_{\gamma\alpha}, \\ \int d^4x \bar{\psi}_\alpha(\vec{x}, \tau) \gamma_{j\alpha\beta} \partial_j \psi_\beta(\vec{x}, \tau) &\rightarrow \int d^4x \bar{\psi}_\lambda(-\vec{x}, \tau) \gamma_{j\alpha\beta} \partial_j \psi_\sigma(-\vec{x}, \tau) \bar{I}_{\lambda\alpha} I_{\sigma\beta} \\ &= - \int d^4x \bar{\psi}_\lambda(\vec{x}, \tau) \bar{I}_{\lambda\alpha} \gamma_{j\alpha\beta} I_{\sigma\beta} \partial_j(\vec{x}, \tau) \psi_\sigma \\ \int d^4x \bar{\psi}_\alpha(\vec{x}, \tau) \gamma_{4\alpha\beta} \partial_4 \psi_\beta(\vec{x}, \tau) &\rightarrow \int d^4x \bar{\psi}_\lambda(-\vec{x}, \tau) \gamma_{4\alpha\beta} \partial_\tau \psi_\sigma(-\vec{x}, \tau) \bar{I}_{\lambda\alpha} I_{\sigma\beta} \\ &= \int d^4x \bar{\psi}_\lambda(\vec{x}, \tau) \bar{I}_{\lambda\alpha} \gamma_{4\alpha\beta} I_{\sigma\beta} \partial_\tau \psi_\sigma(\vec{x}, \tau) \end{aligned}$$

To maintain the covariant derivative, we see that:

$$\begin{aligned} A_j(x) &\rightarrow -A_j(-x), & U_\mu(x) &\rightarrow U_\mu^*(-x), \\ A_4(x) &\rightarrow +A_4(-x), & U_\mu(x) &\rightarrow U_\mu(-x). \end{aligned}$$

In order for the action to be invariant under spatial inversion, we must have

$$\bar{I}I^T = 1, \quad \bar{I}\gamma_j I^T = -\gamma_j, \quad \bar{I}\gamma_4 I^T = \gamma_4$$

Using the definitions of the Euclidean Dirac gamma matrices given in Chapter 2, we see that $\bar{I} = I = \gamma_4$, and that the fields transform as:

$$\bar{\psi}(\vec{x}, \tau) \rightarrow \bar{\psi}(-\vec{x}, \tau)\gamma_4, \quad \psi(\vec{x}, \tau) \rightarrow \psi(-\vec{x}, \tau)\gamma_4.$$

4.2.2 Gauge invariance

We require our hadron operators to be gauge-invariant; all operators must transform as scalars under local $SU(3)$ color transformations. We may combine three quark sources (or sinks) into a color singlet by contracting the free color indices with the totally antisymmetric Levi-Civita tensor:

$$\epsilon_{abc} = \begin{cases} +1 & abc = 123, 231, 312 \\ -1 & abc = 132, 213, 321 \\ 0 & \text{otherwise.} \end{cases}$$

As an example, consider the behavior of the local (single-site) operator under a local gauge transformation $\Omega(x) \in SU(3)$:

$$\begin{aligned} \epsilon_{abc} \bar{\psi}_a(x) \bar{\psi}_b(x) \bar{\psi}_c(x) &\rightarrow \epsilon_{abc} \bar{\psi}_{a'}(x) \bar{\psi}_{b'}(x) \bar{\psi}_{c'}(x) \Omega_{a'a}^\dagger(x) \Omega_{b'b}^\dagger(x) \Omega_{c'c}^\dagger(x) \\ &= \det(\Omega^\dagger(x)) \bar{\psi}_{a'}(x) \bar{\psi}_{b'}(x) \bar{\psi}_{c'}(x) \epsilon_{a'b'c'} \\ &= \bar{\psi}_{a'}(x) \bar{\psi}_{b'}(x) \bar{\psi}_{c'}(x) \epsilon_{a'b'c'} \end{aligned}$$

We will always contract our operators with the Levi-Civita tensor, with summation over repeated color indices implied.

4.2.3 Gaussian quark field smearing

To successfully extract the spectrum, operators which couple strongly to the low-lying states of interest and weakly to the high-lying states must be used. Effective phenomenological models tell us that we can improve our operators by associating

wavefunctions with the valence quarks, rather than working with point quark sources. This translates to the use of spatial quark field *smearing* in our functional integrals.

Damping out couplings to the short-wavelength, high-momentum modes is the crucial feature which any effective smearing prescription[GLM⁺89, ASB⁺93] must have. Gaussian suppression of the high-momentum modes is perhaps the simplest method one can use. Since a Gaussian in momentum space remains a Gaussian in coordinate space, we decided to employ a gauge-covariant smearing scheme[AKL96] in which the smeared quark field is defined at a given site as a Gaussian-weighted average of the surrounding sites on the same time slice (see Figure 4.1).

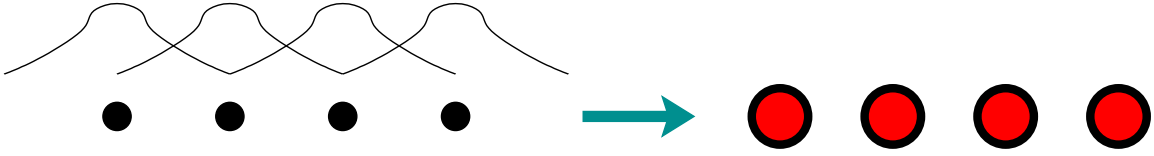


Figure 4.1: A schematic view of Gaussian quark field smearing. The quark operators are replaced by ‘fatter’ versions which better mimic the ‘fuzzy’ nature of the quark wavefunctions.

The smeared quark operators are ‘fatter’, consisting of weighted contributions from nearby values with a (real) Gaussian radius of σ . We expect that baryon operators using smeared quark fields will better represent the spatial structure of the low-lying QCD baryon states, and will therefore interpolate better for those resonances.

On a given time slice, the smeared continuum quark fields are defined as the integral transform of the unsmeared fields using the real, rotationally invariant, Gaussian kernel $\mathcal{Q}(r^2)$:

$$\tilde{\psi}(\vec{x}) \equiv \int d^3r \mathcal{Q}(r^2) \psi(\vec{x} + \vec{r}), \quad \mathcal{Q}(r^2) \equiv \frac{1}{(\sqrt{2\pi}\sigma^2)^3} e^{-r^2/(2\sigma^2)},$$

where $r^2 \equiv (\vec{r} \cdot \vec{r})$. The first three moments of the real Gaussian kernel are

$$\int d^3r \mathcal{Q}(r^2) = 1, \quad \int d^3r \mathcal{Q}(r^2) \vec{r} = 0, \quad \int d^3r \mathcal{Q}(r^2) r^2 = \sigma^2.$$

We can transform the integral equation into a multiplicative operator equation by applying the Euclidean spatial Fourier transform relations:

$$\psi(\vec{x}) = \int \frac{d^3k}{(2\pi)^3} e^{-i\vec{k}\cdot\vec{x}} \psi(\vec{k}), \quad \psi(\vec{k}) \equiv \int d^3x e^{+i\vec{k}\cdot\vec{x}} \psi(\vec{x})$$

to the expression for the smeared quark field:

$$\begin{aligned}
\tilde{\psi}(\vec{x}) &= \frac{1}{(\sqrt{2\pi\sigma^2})^3} \int d^3r e^{-r^2/(2\sigma^2)} \psi(\vec{x} + \vec{r}) \\
&= \frac{1}{(\sqrt{2\pi\sigma^2})^3} \int d^3r e^{-r^2/(2\sigma^2)} \int \frac{d^3k}{(2\pi)^3} e^{-i\vec{k}\cdot(\vec{x}+\vec{r})} \psi(\vec{k}) \\
&= \frac{1}{(\sqrt{2\pi\sigma^2})^3} \int d^3r \int \frac{d^3k}{(2\pi)^3} e^{-(r^2/\sigma^2 + 2i\vec{k}\cdot\vec{r})/2} e^{-i\vec{k}\cdot\vec{x}} \psi(\vec{k}) \\
&\quad (\text{Letting } \vec{z} \equiv \vec{r}/\sigma + i\sigma\vec{k}) \\
&= \left(\frac{1}{(\sqrt{2\pi})^3} \int d^3z e^{-z^2/2} \right) \int \frac{d^3k}{(2\pi)^3} e^{-\sigma^2 k^2/2} e^{-i\vec{k}\cdot\vec{x}} f(\vec{k}), \quad k^2 \equiv \vec{k} \cdot \vec{k} \\
&= e^{\sigma^2 \nabla^2/2} \int \frac{d^3k}{(2\pi)^3} e^{-i\vec{k}\cdot\vec{x}} \psi(\vec{k}) \\
\tilde{\psi}(\vec{x}) &= e^{\sigma^2 \nabla^2/2} \psi(\vec{x}) \tag{4.2}
\end{aligned}$$

Using the relation

$$e^x = \lim_{n \rightarrow \infty} \left(1 + \frac{x}{n} \right)^n$$

Eqn. 4.2 may be approximated on the lattice by introducing the quark smearing matrix S :

$$\tilde{\psi}_x \equiv \sum_y S_{x,y} \psi_y, \quad S(\sigma, n_\sigma) \equiv \left(1 + \frac{\sigma^2}{2n_\sigma} \Delta \right)^{n_\sigma} \tag{4.3}$$

where

$$\begin{aligned}
\Delta_{x,y} &\equiv \sum_{k=1}^3 \left(U_k(x) \delta_{x+\hat{k},y} + U_k^\dagger(x - \hat{k}) \delta_{x-\hat{k},y} - 2\delta_{x,y} \right) \\
&= \sum_{k=\pm 1, \pm 2, \pm 3} \left(U_k(x) \delta_{x+\hat{k},y} - \delta_{x,y} \right), \quad U_{-k}(x) \equiv U_k^\dagger(x - \hat{k})
\end{aligned}$$

is the three-dimensional gauge-covariant Laplace operator¹. It is simple to check that the analogous expression for $\bar{\psi}$ in the continuum

$$\bar{\tilde{\psi}}(\vec{x}) = e^{\sigma^2 \nabla^2/2} \bar{\psi}(\vec{x})$$

is approximated on the lattice by:

$$\bar{\tilde{\psi}} \equiv \bar{\psi} S^{m_\sigma \dagger}(\sigma).$$

There are two quark field smearing parameters in Eqn. 4.3 that we will tune in Chapter 6: the real (dimensionless) Gaussian radius σ and the integer number of iterations in the approximation of the exponential n_σ .

The smeared quark fields at each site are linear combinations of the original lattice quark fields; we note that the smeared quark fields obey the same transformation laws and Grassmann algebra as the unsmeared fields.

¹We have defined Δ and σ to be dimensionless. The smearing radius in MeV^{-1} or fm is given by σa_s .

4.2.4 Gauge link smearing

We can improve our operators further by replacing the gauge links in our quark smearing matrix S with smeared gauge links $\tilde{U}_\mu(x)$.

Let $C_k(x)$ denote the sum of perpendicular spatial *staples* which begin at lattice site x and terminate at the neighboring site $x + \hat{\mu}$:

$$C_k(x) \equiv \sum_{j \neq k} \left(U_j(x) U_k(x + \hat{j}) U_j^\dagger(x + \hat{k}) + U_j^\dagger(x - \hat{j}) U_k(x - \hat{j}) U_j(x - \hat{j} + \hat{k}) \right).$$

We incorporate the spatial information contained in the staple sums $\{C_k\}$ with the original links $U^{[0]} \equiv \{U_k\}$ in some manner to produce a smeared gauge link configuration $U^{[1]}$ (the superscript refers to the smearing iteration, and has nothing to do with the Markov chain). This process is then iterated n_ρ times to produce the final spatially smeared link configuration \tilde{U} :

$$U^{[0]} \rightarrow U^{[1]} \rightarrow U^{[2]} \rightarrow \dots \rightarrow U^{[n_\rho]} \equiv \tilde{U}$$

The APE smearing[A⁺87] iteration rule is commonly used:

$$U_k^{[n+1]} = \mathcal{P}_{SU(3)} \left(U_k^{[n]}(x) + \rho C_k^{[n]}(x) \right)$$

where ρ is some real weight, and $\mathcal{P}_{SU(3)}$ is a projection operator into the gauge group. The projection is needed because the sum of two $SU(3)$ matrices is not necessarily an $SU(3)$ matrix.

To avoid the abrupt projection back into the gauge group needed by this prescription, we decided instead to use the analytic and computationally efficient gauge link smearing scheme known as *stout-link*² smearing [MP04] defined by

$$U_k^{[n+1]}(x) = \exp(i\rho\Theta_\mu^{[n]}(x)) U_k^{[n]}(x), \quad (4.4)$$

$$\Theta_k(x) = \frac{i}{2} \left(\Omega_k^\dagger(x) - \Omega_k(x) \right) - \frac{i}{2N} \text{Tr} \left(\Omega_k^\dagger(x) - \Omega_k(x) \right) \quad (4.5)$$

$$\Omega_k(x) = C_k(x) U_k^\dagger(x) \quad (\text{no summation over } k) \quad (4.6)$$

where $N = 3$ for $SU(3)$. The two parameters to tune in this smearing procedure are the real staple weight ρ and the integer number of iterations n_ρ .

To make use of stout links, we replace the quark smearing matrix S in Eqn. 4.3 with the complete smearing matrix \tilde{S} :

$$\tilde{\psi}_x \equiv \sum_y \tilde{S}_{x,y} \psi_y, \quad \tilde{S}(\sigma, n_\sigma, \rho, n_\rho) \equiv \left(1 + \frac{\sigma^2}{2n_\sigma} \tilde{\Delta} \right)^{n_\sigma} \quad (4.7)$$

²The term ‘stout-link’ was coined by Morningstar and Peardon in a Dublin pub as a nod to Guinness beer. Officially, ‘stout’ refers to “their thick-bodied nature from the large brew of paths used in their formulation” [MP04]

where

$$\tilde{\Delta}_{x,y} \equiv \sum_{k=\pm 1, \pm 2, \pm 3} \left(\tilde{U}_k(x) \delta_{x+\hat{k},y} - \delta_{x,y} \right)$$

The quark field and gauge link smearing schemes preserve the gauge invariance of hadron operators. In Chapter 6, we systematically tune the smearing parameters $\sigma, n_\sigma, \rho,$ and n_ρ to give an optimal effective mass signal for our operators.

4.2.5 Radial structure through covariant displacement

The need for extended three-quark operators to capture both the radial and orbital structure of baryons has been emphasized and described in Ref. [BEF⁺05a] and Ref. [BEF⁺05b]. We may add radial structure to our operators without breaking gauge invariance by using the covariant displacement operators $\tilde{D}_j^{(p)}(x)$ which consist of p smeared parallel transporters in the j^{th} spatial direction which ‘carry the color’ back to the reference site x from the displaced site $x + p\hat{j}$:

$$\tilde{D}_j^{(p)}(x) \equiv \tilde{U}_j(x) \tilde{U}_j(x + \hat{j}) \cdots \tilde{U}_j(x + (p-1)\hat{j}), \quad j = \pm 1, \pm 2, \pm 3.$$

For economy of notation in the upcoming expressions, we also define the additional zero-displacement operator:

$$\tilde{D}_0^{(p)}(x) \equiv 1$$

A quark sink displaced from x to $x + p\hat{j}$ is represented by

$$\tilde{D}_j^{(p)}(x) \tilde{\psi}(x + p\hat{j}) \equiv [\tilde{D}_j^{(p)} \tilde{\psi}](x),$$

and a quark source displaced from x to $x + p\hat{j}$ is represented by

$$\tilde{\bar{\psi}}(x + p\hat{j}) \tilde{D}_j^{(p)\dagger}(x) \equiv [\tilde{\bar{\psi}} \tilde{D}_j^{(p)\dagger}](x)$$

For simplicity, the displaced quarks in a baryon operator will always be displaced by an equal amount p . In general, operators corresponding to different values of p may be combined (via the variational method) to capture more complex radial structure. In this work, we restrict our consideration to a single displacement length p of three links for our operators.

At this point, we can combine the smeared quark fields and gauge links into gauge-invariant *extended three-quark operators* containing the desired color and radial structure:

$$\overline{\Phi}_{\alpha\beta\gamma,ijk}^{ABC}(x) = \epsilon_{abc} [\tilde{\bar{\psi}} D_i^{(3)\dagger} \gamma_4]_{a\alpha}^A(x) [\tilde{\bar{\psi}} D_j^{(3)\dagger} \gamma_4]_{b\beta}^B(x) [\tilde{\bar{\psi}} D_k^{(3)\dagger} \gamma_4]_{c\gamma}^C(x) \quad (4.8)$$

$$\Phi_{\alpha\beta\gamma,ijk}^{ABC}(x) = \epsilon_{abc} [\tilde{D}_i^{(3)} \tilde{\psi}]_{Aa\alpha}(x) [\tilde{D}_j^{(3)} \tilde{\psi}]_{Bb\beta}(x) [\tilde{D}_k^{(3)} \tilde{\psi}]_{Cc\gamma}(x) \quad (4.9)$$





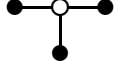
Operator type	Displacement indices
 Single-Site	$i = j = k = 0$
 Singly-Displaced	$i = j = 0, k \neq 0$
 Doubly-Displaced-I	$i = 0, j = -k, k \neq 0$
 Doubly-Displaced-L	$i = 0, j \neq k , jk \neq 0$
 Triply-Displaced-T	$i = -j, j \neq k , jk \neq 0$

Table 4.1: The spatial arrangements of the extended three-quark baryon operators $\bar{\Phi}_{ijk}$ and Φ_{ijk} . Quark-fields are shown by solid circles, line segments indicate gauge-covariant displacements, and each hollow circle indicates the location of a Levi-Civita color coupling. For simplicity, all displacements have the same length in an operator.

where a specific displacement length of $p = 3$ has been used. An explicit factor of γ_4 is included in the creation operator $\bar{\Phi}_{\alpha\beta\gamma,ijk}^{ABC}(x)$ to ensure that our correlation matrices are Hermitian.

The displacement direction indices $i, j, k = 0, \pm 1, \pm 2, \pm 3$ define the radial structure of the operator. The types of displacements for the three-quark operators considered in this work are illustrated in Table 4.1. In particular, comparing the effectiveness of the doubly-displaced-L vs. the triply-displaced-T operators can shed some light on the much discussed issue of Y-flux/ Δ -flux formation of the gluon field in three-quark systems (the Δ is actually a quantum superposition of three V-flux forms).

A sixth possible configuration in which the quarks are displaced in three orthogonal directions (triply-displaced-O) was not considered because the connecting gauge links for such an operator do not lie in the plane of the quarks. It is expected that such an operator would couple to the higher-lying contaminating states much more than the similar triply-displaced-T operator.

4.3 Classification of states by transformation behavior

So far, we have constructed gauge-invariant extended three-quark operators $\overline{\Phi}_{\alpha\beta\gamma,ijk}^{ABC}(x)$ and $\Phi_{\alpha\beta\gamma,ijk}^{ABC}(x)$ from smeared gauge links, and smeared and covariantly-displaced quark fields. Our goal is to use these extended operators to construct full baryon operators which possess good quantum numbers on our lattice.

Quantum numbers tell us how an object transforms under some symmetry operation. As an example, consider the spherical harmonics $Y_l^m(\theta, \phi)$, functions which appear frequently in the description of systems possessing spherical symmetry (e.g. the multi-pole expansions of classical electrodynamics, or the orbital wavefunction solutions of the hydrogen atom in quantum mechanics). The spherical harmonics $Y_l^m(\theta, \phi)$ transform under spatial rotations in specific l -dependent ways. The spherical harmonic Y_0^0 is a rotationally invariant function. The three spherical harmonics Y_1^{-1} , Y_1^0 , Y_1^1 transform as a vector v having components:

$$v_x = \frac{1}{\sqrt{2}}(Y_1^{-1} - Y_1^1), \quad v_y = \frac{i}{\sqrt{2}}(Y_1^{-1} + Y_1^1), \quad v_z = Y_1^0.$$

These different transformation behaviors can be used to label the state of the system (in the example of the hydrogen atom, l is the orbital quantum number).

We turn now to the task of combining our three-quark operators into baryon operators which transform irreducibly according to the symmetries of the lattice.

4.3.1 Irreducible representations of groups

Briefly, we define and summarize the key ideas from group theory we will need for the remainder of this chapter. Summation will be denoted explicitly (summation over repeated indices is not implied).

A group \mathcal{G} is a set of elements $\{R\}$ along with multiplication law which satisfies the following properties:

1. *Closure*: $RR' \in \mathcal{G} \quad \forall R, R' \in \mathcal{G}$
2. *Associativity*: $R_1(R_2R_3) = (R_1R_2)R_3 \quad \forall R_1, R_2, R_3 \in \mathcal{G}$
3. *Identity*: $\exists E \in \mathcal{G} \text{ s.t. } ER = RE = R \quad \forall R \in \mathcal{G}$
4. *Inverse*: $\exists R^{-1} \in \mathcal{G} \text{ s.t. } RR^{-1} = R^{-1}R = E \quad \forall R \in \mathcal{G}$

If the multiplication operation is commutative, then the group is Abelian, otherwise, it is non-Abelian. A *representation* of a group is any set of matrices $\{D(R)\}$ which satisfies the

group multiplication rule

$$D(R)D(R') = D(RR') \quad \forall R, R' \in \mathcal{G}.$$

In the following, we will denote our extended three-quark operators on each time slice τ using a single index:

$$\overline{B}_\sigma(\tau) \equiv \overline{\phi}_{\alpha\beta\gamma,ijk}^{ABC}(\vec{x}, \tau), \quad B_\sigma \equiv \overline{\phi}_{\alpha\beta\gamma,ijk}^{ABC}(\vec{x}, \tau),$$

where the master index σ stands for the values of $A, B, C, \alpha, \beta, \gamma, i, j, k$, and \vec{x} .

Under a color, flavor, or spatial transformation $R \in \mathcal{G}$ represented by the Hilbert space operator U_R , our operators will transform into one another as

$$\begin{aligned} \overline{B}_\alpha &\rightarrow U_R \overline{B}_\alpha U_R^\dagger = \sum_{\beta=1}^d \overline{B}_\beta W_{\beta\alpha}(R), \\ B_\alpha &\rightarrow U_R B_\alpha U_R^\dagger = \sum_{\beta=1}^d \overline{B}_\beta W_{\beta\alpha}^{-1}(R), \end{aligned} \quad (4.10)$$

where d is the dimension of the (not necessarily unitary) representation matrices $\{W(R)\}$.

For example, lattice rotations through the angles of $0, \pi/2, \pi$, and $3\pi/2$ about the axis $O\hat{j}$ transform the different orientations of a triply-displaced-T operator into each other (taking $O\hat{j}$ to be perpendicular to the plane containing the quarks). Performing the same operations on a single-site operator yields only one distinct operator.

We will restrict our discussion to these types of transformations. Other types of transformations, such as the charge conjugation operation considered in Chapter 5, do not transform baryon operators into baryon operators.

If the collection of transformations $\{R\}$ being considered composes a group \mathcal{G} , then the coefficient matrices $\{W(R)\}$ are a representation for \mathcal{G} defined on the basis $\{\overline{B}_\alpha\}$.

$$\begin{aligned} U_{R'} U_R \overline{B}_\alpha U_R^\dagger U_{R'}^\dagger &= \sum_{\beta=1}^d U_{R'} \overline{B}_\beta U_{R'}^\dagger W_{\beta\alpha}(R), \\ &= \sum_{\gamma=1}^d \sum_{\beta=1}^d \overline{B}_\gamma W_{\gamma\beta}(R') W_{\beta\alpha}(R), \\ U_{R'R} \overline{B}_\alpha U_{R'R}^\dagger &= \sum_{\gamma=1}^d \overline{B}_\gamma W_{\gamma\alpha}(R'R). \end{aligned}$$

If the representation is *reducible*, then we can define $d' < d$ operators

$$\overline{B}'_\alpha \equiv \sum_{\beta=1}^d \overline{B}_\beta A_{\beta\alpha}, \quad \alpha = 1, \dots, d', d' < d,$$

which transform only among themselves:

$$\overline{B}'_{\alpha} \rightarrow U_R \overline{B}'_{\alpha} U_R^{\dagger} = \sum_{\beta=1}^{d'} \overline{B}'_{\beta} W'_{\beta\alpha}(R),$$

where the representation matrices $\{W'(R)\}$ have a smaller dimension than the original representation matrices $\{W(R)\}$. A representation which is not reducible is called an *irreducible representation*, or an *irrep*, and is labeled by a superscript in parenthesis. Such representations are significant because they can be used to label the different sectors of our Hilbert space.

Let $\{D^{(\Lambda)}(R)\}$ denote a set of n_{Λ} -dimensional unitary³ matrices forming an irreducible representation of \mathcal{G} labeled by Λ . If we consider all nonequivalent⁴ irreducible unitary representations of a finite group \mathcal{G} of order⁵ g , then the quantities $D_{ij}^{(\mu)}(R)$ for *fixed* μ, i, j , form a vector in a g -dimensional space, such that:

$$\sum_R D_{il}^{(\mu)}(R) D_{jm}^{(\nu)*}(R) = \frac{g}{n_{\mu}} \delta_{\mu\nu} \delta_{ij} \delta_{lm} \quad (4.11)$$

Eqn. 4.11 forms the backbone of our operator construction effort, and is proven in [Ham62] as a corollary of Schur's Lemma. The fundamental theme which will guide the operator construction is that of constructing operators which transform irreducibly under symmetry transformations.

4.3.2 Symmetry operations

When constructing our baryon operators, we will consider symmetry groups of the Hamiltonian. Consider a finite group \mathcal{G} of g unitary operators U_R which act on the Hilbert space of the system ($U_R^{\dagger} U_R = 1$). \mathcal{G} is a symmetry group of the Hamiltonian if each element commutes with the Hamiltonian:

$$[U_R, H] = 0.$$

Symmetry operations may be applied to operators at different times without disrupting the time evolution relation:

$$\begin{aligned} U_R \overline{B}_{\alpha}(\tau_2) U_R^{\dagger} &= U_R e^{H(\tau_2 - \tau_1)} \overline{B}_{\alpha}(\tau_1) e^{-H(\tau_2 - \tau_1)} U_R^{\dagger} \\ &= e^{H(\tau_2 - \tau_1)} \left(U_R \overline{B}_{\alpha}(\tau_1) U_R^{\dagger} \right) e^{-H(\tau_2 - \tau_1)}. \end{aligned}$$

We would like to find linear combinations of these operators which transform irreducibly

³We will be dealing with unitary representation matrices ($D^{\dagger}(R)D(R) = 1$) unless specified otherwise. In particular, *all* finite groups possess unitary representations.

⁴Two representations are equivalent if they are related by a change of basis.

⁵The order g of a finite group \mathcal{G} is simply the number of elements in \mathcal{G} .

under \mathcal{G} :

$$\overline{B}_{i,a,\alpha}^\Lambda \equiv \sum_S c_{iaS}^\Lambda U_S \overline{B}_\alpha U_S^\dagger \quad U_R \overline{B}_{i,a,\alpha}^\Lambda U_R^\dagger = \sum_j \overline{B}_{j,a,\alpha}^\Lambda D_{ji}^{(\Lambda)}(R) \quad (4.12)$$

$$B_{i,a,\alpha}^\Lambda \equiv \sum_S c_{iaS}^{\Lambda*} U_S B_\alpha U_S^\dagger \quad U_R B_{i,a,\alpha}^\Lambda U_R^\dagger = \sum_j B_{j,a,\alpha}^\Lambda D_{ji}^{(\Lambda)*}(R) \quad (4.13)$$

where Λ labels the irrep, i labels the row of the irrep, a labels the instance of the irrep⁶, and α denotes all other operator information (e.g. displacement values).

The power of this approach may be seen by considering a general correlation function between two operators:

$$\begin{aligned} C_{ij\alpha\beta}^{\Lambda\Gamma ab}(t) &\equiv \langle B_{i,a,\alpha}^\Lambda(t) \overline{B}_{j,b,\beta}^\Gamma(0) \rangle = \text{Tr} \left(B_{i,a,\alpha}^\Lambda(t) \overline{B}_{j,b,\beta}^\Gamma(0) \right) \\ &= \frac{1}{g} \sum_R \text{Tr} \left(U_R^\dagger U_R B_{i,a,\alpha}^\Lambda(t) U_R^\dagger U_R \overline{B}_{j,b,\beta}^\Gamma(0) U_R^\dagger U_R \right) \\ &= \frac{1}{g} \sum_R \text{Tr} \left(U_R B_{i,a,\alpha}^\Lambda(t) U_R^\dagger U_R \overline{B}_{j,b,\beta}^\Gamma(0) U_R^\dagger \right) \end{aligned} \quad (4.14)$$

$$\begin{aligned} &= \sum_{k,l} \left(\frac{1}{g} \sum_R D_{ki}^{(\Lambda)*}(R) D_{lj}^{(\Gamma)}(R) \right) \text{Tr} \left(B_{k,a,\alpha}^\Lambda(t) \overline{B}_{l,b,\beta}^\Gamma(0) \right) \\ &= \delta_{\Lambda\Gamma} \delta_{ij} \frac{1}{n_\Lambda} \sum_k \langle B_{k,a,\alpha}^\Lambda(t) \overline{B}_{k,b,\beta}^\Lambda(0) \rangle \end{aligned} \quad (4.15)$$

where the last line came from using the orthogonality relation in Eqn. 4.11.

It is important to notice four things:

1. The irrep and the row must be the same for the correlation function not to vanish.
2. To get 4.14, we invoked the cyclic property of the trace. Thus the operators are not orthogonal on a configuration-by-configuration basis because equation 4.15 is an expectation value relation. Anticipating orthogonality by calculating only non-vanishing correlation functions, we are effectively reducing the noise in our Monte Carlo estimates.
3. The value of the correlation function is independent of the row. Thus we can get better statistics by correlating operators by row, and then averaging over the rows.
4. Different instances of an irrep may mix. Because the value of the instance label does not affect the transformation properties of the operator, we may group the instance label with the auxiliary index α . Let the resulting operators be denoted $\overline{B}_{i,j}^\Lambda$, where Λ is the irrep, i is the row, and j represents the value of a and α .

⁶There may be more than one linear combination of the $U_R \overline{B}_\alpha U_R^\dagger$ which transforms according to a particular irreducible transformation.

Given a set of elementary operators $\{\overline{B}_\alpha\}$, we will construct the correlation matrix in a given irrep Λ as

$$C_{ij}^\Lambda(\tau) \equiv \frac{1}{n_\Lambda} \sum_{m=1}^{n_\Lambda} \langle B_{m,i}^\Lambda(\tau) \overline{B}_{m,j}^\Lambda(0) \rangle.$$

4.3.3 Projection onto irreducible representations of finite groups

For any operators \overline{B}_α and B_α , we construct operators which transform irreducibly under transformations $R \in \mathcal{G}$ by applying the following *projection operations*:

$$\begin{aligned} \overline{B}_{i,a,\alpha}^\Lambda &\equiv \mathcal{O}_{i,a}^\Lambda \overline{B}_\alpha &\equiv \frac{n_\Lambda}{g} \sum_R D_{ia}^{(\Lambda)*}(R) U_R \overline{B}_\alpha U_R^\dagger, \\ B_{i,a,\alpha}^\Lambda &\equiv \mathcal{O}_{i,a}^\Lambda B_\alpha &\equiv \frac{n_\Lambda}{g} \sum_R D_{ia}^{(\Lambda)}(R) U_R B_\alpha U_R^\dagger. \end{aligned} \quad (4.16)$$

The required transformation behavior is easily verified:

$$\begin{aligned} U_R \overline{B}_{i,a,\alpha}^\Lambda U_R^\dagger &= \frac{n_\Lambda}{g} \sum_S D_{ia}^{(\Lambda)*}(S) U_{RS} \overline{B}_\alpha U_{RS}^\dagger \\ &= \frac{n_\Lambda}{g} \sum_S D_{ia}^{(\Lambda)*}(R^{-1}S) U_S \overline{B}_\alpha U_S^\dagger \\ &= \sum_j \left(\frac{n_\Lambda}{g} \sum_S D_{ja}^{(\Lambda)*}(S) U_S \overline{B}_\alpha U_S^\dagger \right) D_{ji}^{(\Lambda)}(R) \\ &= \sum_j \overline{B}_{j,a,\alpha}^\Lambda D_{ji}^{(\Lambda)}(R) \end{aligned}$$

$\mathcal{O}_{i,a}^\Lambda$ acting on an \overline{B}_α produces an object which transforms according to the i^{th} row of the irreducible representation labeled by Λ . Consider the effect of two such operations:

$$\begin{aligned} \mathcal{O}_{i,a}^\Lambda \mathcal{O}_{j,b}^\Gamma \overline{B}_\alpha &= \frac{n_\Lambda n_\Gamma}{g^2} \sum_{R,S} D_{ia}^{(\Lambda)*}(R) D_{jb}^{(\Gamma)*}(S) U_{RS} \overline{B}_\alpha U_{RS}^\dagger \\ &= \frac{n_\Lambda n_\Gamma}{g^2} \sum_{R,S} D_{ia}^{(\Lambda)*}(R) D_{jb}^{(\Gamma)*}(R^{-1}S) U_S \overline{B}_\alpha U_S^\dagger \\ &= \sum_k \left(\frac{n_\Gamma}{g} \sum_R D_{ia}^{(\Lambda)*}(R) D_{kj}^{(\Gamma)}(R) \right) \frac{n_\Lambda}{g} \sum_S D_{kb}^{(\Gamma)*}(S) U_S \overline{B}_\alpha U_S^\dagger \\ &= \delta_{\Lambda\Gamma} \delta_{aj} \mathcal{O}_{i,b}^\Lambda \overline{B}_\alpha. \end{aligned}$$

In particular, if we define $P_i^\Lambda \equiv \mathcal{O}_{i,i}^\Lambda$, we have

$$P_i^\Lambda P_j^\Gamma \overline{B}_\alpha = \delta_{\Lambda\Gamma} \delta_{ij} P_i^\Lambda \overline{B}_\alpha$$

The P_i^Λ are therefore projection operators.

$$\begin{aligned} \sum_{\Lambda,i} P_i^\Lambda \bar{B}_\alpha &= \sum_{\Lambda,i} \frac{n_\Lambda}{g} \sum_S D_{ii}^{(\Lambda)*}(S) U_S \bar{B}_\alpha U_S^\dagger \\ &= \sum_S \left(\frac{1}{g} \sum_\Lambda \chi^{(\Lambda)*}(S) n_\Lambda \right) U_S \bar{B}_\alpha U_S^\dagger \\ &= \bar{B}_\alpha \end{aligned}$$

where the $\chi^{(\Lambda)}(R) = \text{Tr}(D^{(\Lambda)})$ are the characters of the group irrep, and we have used the character orthogonality relation [Ham62]:

$$\frac{1}{g} \sum_\Lambda \chi^{(\Lambda)*}(R) \chi^{(\Lambda)}(E) = \delta_{RE}.$$

The identity element⁷ $D(E) = 1$ in any representation, and thus $\chi^{(\Lambda)}(E) = n_\Lambda$.

We can use Eqn. 4.10 to define projection matrices $P_{i,\alpha\beta}^\Lambda$:

$$\begin{aligned} P_i^\Lambda \bar{B}_\alpha &= \frac{n_\Lambda}{g} \sum_R D_{ii}^{(\Lambda)*}(R) \sum_{\beta=1}^d \bar{B}_\beta W_{\beta\alpha}(R), \\ &\equiv \sum_{\beta=1}^d P_{i,\alpha\beta}^\Lambda \bar{B}_\beta \end{aligned} \tag{4.17}$$

$$P_{i,\alpha\beta}^\Lambda \equiv \frac{n_\Lambda}{g} \sum_R D_{ii}^{(\Lambda)*}(R) W_{\beta\alpha}(R) \tag{4.18}$$

In the case that the $\{W(R)\}$ are not unitary, we may define the Hermitian metric matrix M :

$$M_{\alpha\beta} = \frac{1}{g} \sum_R \sum_{\gamma=1}^d W_{\gamma\alpha}^*(R) W_{\gamma\beta}(R).$$

We then compute the projection matrix for row $i = 1$:

$$P_{1,\alpha\beta}^\Lambda = \frac{n_\Lambda}{g} \sum_R D_{11}^{(\Lambda)*}(R) W_{\beta\alpha}(R).$$

From the rows of this projection matrix, r linearly-independent operators are obtained:

$$\bar{B}_{1,\alpha}^\Lambda = \sum_{\beta=1}^d c_{1,\alpha\beta}^\Lambda \bar{B}_\beta,$$

⁷The identity element is denoted by E , from the German *einheit*, meaning *unit*.

where r is the rank of the projection matrix and the superposition coefficients $c_{1,\alpha\beta}^\Lambda$ for each operator are a linear combination of the rows of the projection matrix such that these coefficients satisfy

$$\sum_{\gamma,\sigma=1}^d c_{1,\alpha\gamma}^{\Lambda*} M_{\gamma\sigma} c_{1,\beta\sigma}^\Lambda = \delta_{\alpha\beta}, \quad \alpha = 1, \dots, r.$$

In practice, these linear combinations are obtained using the well-known Gram-Schmidt procedure, but with a modified inner product to incorporate the metric matrix M . The choice of these operators is not unique. For each of the r operators $B_{1,\alpha}^\Lambda$ in the first row $i = 1$, we obtain the partner operators in all other rows $j > 1$ using:

$$c_{j,\alpha\beta}^\Lambda = \frac{n_\Lambda}{g} \sum_{\gamma=1}^d \sum_R D_{j1}^{(\Lambda)*}(R) W_{\beta\gamma}(R) c_{1,\alpha\gamma}^\Lambda$$

4.3.4 Symmetries of the lattice Hamiltonian

We will construct baryon operators which transform irreducibly according to the symmetry groups of the Hamiltonian on each time slice:

- The $SU(3)$ gauge group (color)
- The $Z_N \otimes Z_N \otimes Z_N$ cyclic translation group (momentum)
- The $SU(2)$ isospin group (flavor) (assumes $m_u = m_d$)
- The O_h^D crystal point group (spin and parity)

4.3.5 Color

By requiring our operators to be gauge-invariant, we have already ensured that the operators transform irreducibly as color singlets. The irreducible representation of the color group by which the operators transform is the trivial representation where

$$D(R) = 1 \quad \forall R \in SU(3).$$

An the projection operation for this representation acts on the color indices only, and results in the Levi-Civita coupling ϵ_{abc} .

4.3.6 Momentum

The next index we consider for projection is the spatial reference site \vec{x} . Spatial translations form an Abelian group (the product of two translations is a translation, each translation possesses an inverse, et cetera). The displacement operator acting on Euclidean space-time functions is given by

$$\begin{aligned} D(a) &= e^{ia_j P_j}, & P_j &\equiv i\partial_j \\ D(a)f(x) &= f(x - a). \end{aligned}$$

Here $D(a)$ is an operator, not a representation matrix. However, this abuse of notation will not lead to trouble because the irreps $D^{(k)}(a)$ of the group of translations are all one-dimensional and given by:

$$D^{(k)}(a) = e^{ik_j a_j},$$

where k_j is the irrep label (the momentum).

Functions which transform irreducibly under translations are labeled by their momentum k :

$$\begin{aligned} f^{(k)}(x) &= ce^{-ik_j x_j} \\ D(a)f^{(k)}(x) &= f^{(k)}(x - a) = f^{(k)}(x)D^{(k)}(a) && \text{(no sum on } k) \\ P_\mu f^{(k)}(x) &= k_\mu f^{(k)}(x) \end{aligned}$$

For our operators, we have a finite number N_j of discrete spatial lattice sites in each direction \hat{j} with periodic boundary conditions:

$$D^{(k)}(N_j a_s) = D^{(k)}(0)$$

where a_s is the spatial lattice spacing. Thus, our group of spatial translations is a direct product of three cyclic groups $Z_{N_j} = \{z_0, z_1, \dots, z_{N_j}\}$, where

- z_0 is the identity element
- z_1 corresponds to a translation from x to $x + \hat{j}$
- $z_n = z_1^n$
- $z_1^{N_j} = z_0$

The unique allowed momenta on the lattice are given by the irrep labels of Z_{N_j} :

$$k_j = \frac{2\pi}{N_j a_s} n_j, \quad \text{(no sum on } j), \quad n_j = 0, 1, \dots, N_j - 1, .$$

Some researchers shift the range of n_j to allow negative momentum values. Because we are interested in the mass spectrum, we will work in the zero-momentum sector

$k_1 = k_2 = k_3 = 0$. Applying the projection operation (Eqn. 4.16) with the trivial representation gives the average over all spatial sites. Therefore, our zero-momentum extended three-quark operators are translationally invariant and given by:

$$\bar{\Phi}_{\alpha\beta\gamma,ijk}^{ABC}(\tau) = \frac{1}{N_1 N_2 N_3} \sum_{\vec{x}} \epsilon_{abc} [\tilde{\psi} D_i^{(3)\dagger}]_{a\alpha}^A(\vec{x}, \tau) [\tilde{\psi} D_j^{(3)\dagger}]_{b\beta}^B(\vec{x}, \tau) [\tilde{\psi} D_k^{(3)\dagger}]_{c\gamma}^C(\vec{x}, \tau) \gamma_4 \quad (4.19)$$

$$\Phi_{\alpha\beta\gamma,ijk}^{ABC}(\tau) = \frac{1}{N_1 N_2 N_3} \sum_{\vec{x}} \epsilon_{abc} [\tilde{D}_i^{(3)} \tilde{\psi}]_{Aa\alpha}(\vec{x}, \tau) [\tilde{D}_j^{(3)} \tilde{\psi}]_{Bb\beta}(\vec{x}, \tau) [\tilde{D}_k^{(3)} \tilde{\psi}]_{Cc\gamma}(\vec{x}, \tau) \quad (4.20)$$

4.3.7 Flavor

For this work we will work with ‘light baryons,’ containing u , d , and s valence quarks only. Correspondingly, our flavor indices A , B , and C , can only take on the values u , d , s . In addition to conserving flavor, our Hamiltonian possesses an $SU(2)$ isospin symmetry in which the u and d quarks are assigned the same mass ($m_u = m_d$) and are treated as components of an isospin doublet:

$$l = \begin{pmatrix} u \\ d \end{pmatrix}$$

where l stands for *light* quark. The group of transformations on the isospin doublet is $SU(2)$, the continuous group of all 2×2 unitary matrices with determinant = +1.

In nature isospin symmetry is broken by a small u - d mass splitting which arises due to electromagnetic interactions and other effects, but this splitting is less than 1% mass of the lightest baryon, the proton. It is therefore reasonable to treat $SU(2)$ isospin symmetry as exact in lattice QCD simulations at present levels of precisions. We will require our operators to transform irreducibly under isospin transformations.

On the other hand, the action explicitly breaks $SU(3)$ flavor symmetry ($m_u = m_d = m_s$) by the designation of a heavier strange quark mass. In nature, the strange quark - light quark splitting is about 15 – 30% of the proton mass. Although $SU(3)$ flavor symmetry is not exact, we may design our operators to transform according to $SU(3)$ flavor irreps in addition to $SU(3)$ isospin irreps, but must expect such operators to mix.

The underlying mechanism causing the different $SU(3)$ irreps to mix is illustrated by considering the effect of using the projection operation (Eqn. 4.16) for a group which is not a symmetry of the Hamiltonian:

$$\begin{aligned} \bar{B}_{i,\alpha}^{\Lambda,a}(\tau) &= \frac{n_\Lambda}{g} \sum_S D_{ia}^{(\Lambda)*}(S) U_S \bar{B}_\alpha(\tau) U_S^\dagger \\ &= \frac{n_\Lambda}{g} \sum_S D_{ia}^{(\Lambda)*}(S) U_S e^{+H\tau} \bar{B}_\alpha(0) e^{-H\tau} U_S^\dagger \end{aligned}$$

If $[U_R, H] \neq 0$, then

$$\bar{B}_{i,\alpha}^{\Lambda,a}(\tau) \neq e^{+H\tau} \bar{B}_{i,\alpha}^{\Lambda,a}(0) e^{-H\tau}$$

and the orthogonality relation 4.15 does not hold. If we require our baryon operators to transform according to the $SU(3)$ flavor group, then the explicit symmetry breaking ($m_s \neq m_u, m_d$) in the Hamiltonian will cause the operators in different symmetry sectors to mix. This mixing will occur among baryon operators with equal isospin I , isospin projection I_3 , and quark flavor content (e.g. strangeness). Some different baryon sectors labeled by the good quantum numbers I and S are illustrated in Table 4.2.

I	S	Baryon Sector
$\frac{1}{2}$	0	N^0, N^+
$\frac{3}{2}$	0	$\Delta^-, \Delta^0, \Delta^+, \Delta^{++}$
0	-1	Λ^0
1	-1	$\Sigma^-, \Sigma^0, \Sigma^+$
$\frac{1}{2}$	-2	Ξ^-, Ξ^0
0	-3	Ω^-

Table 4.2: The isospin and strangeness quantum numbers for the different baryon sectors. The isospin projection I_3 ranges from $-I$ to I by increments of 1. The charge Q of each baryon listed increases with increasing isospin projection I_3 .

$SU(2)$ isospin is a subgroup of $SU(3)$ flavor, and consists of the set of $SU(3)$ flavor elements which leave the s quarks invariant. Given an irreducible representation of $SU(3)$ flavor (which is not necessarily three-dimensional), the subset of irrep matrices corresponding to the $SU(2)$ subgroup elements forms a representation of the $SU(2)$ isospin group. This representation will generally be reducible, which implies that we can find a basis in the $SU(3)$ irrep such that the $SU(2)$ representation (which is not two-dimensional) can be reduced to block diagonal form. In this basis, we will have states which transform irreducibly under both $SU(3)$ flavor and $SU(2)$ isospin. We will return to this theme in section 4.4.4 when we apply this *method of subduced representations* by restricting the continuum spin group $O(3)$ to the finite lattice rotation group.

4.3.8 Flavor irreps

The finite group projection operation (Eqn. 4.16) is readily extended to compact continuous groups⁸ such as $SU(2)$, but it is simpler to use Lie algebra methods to construct operators which transform irreducibly. We will write out sums explicitly in this section (summation over repeated indices is not implied).

⁸Elements of a continuous group, such as the group of three dimensional rotations, are characterized by a set of real parameters. If there exists a closed set which covers the complete range of the parameters, then the group is said to be *compact*. Elements of $U(1)$ may be written as $\exp(i\theta)$, where the parameter $\theta \in [0, 2\pi) \subset [0, 2\pi]$. Thus $U(1)$ is a compact continuous group.

An element R of $SU(2)$ can be written as

$$R = \exp\left(i \sum_{j=1}^3 a_j(R) \tau_j\right), \quad \tau_j \equiv \frac{\sigma_j}{2}$$

where the σ_j are the traceless Hermitian Pauli spin matrices as defined in Eqn 2.10. The $SU(2)$ group structure is determined by the commutation relations among the generators:

$$[\tau_i, \tau_j] = i \sum_k \epsilon_{ijk} \tau_k$$

We can construct a Casimir operator which commutes with all of the group generators:

$$\tau^2 \equiv \tau_1^2 + \tau_2^2 + \tau_3^2, \quad [\tau^2, \tau_i] = 0 \quad (i = 1, 2, 3).$$

By Schur's Lemma, we know that τ^2 is proportional to the identity matrix and can thus be used to label the different irreps. We may also choose the basis of Hilbert space states in each irrep such that τ_3 is diagonal. By introducing the ladder operators

$$\tau_{\pm} \equiv \tau_1 \pm i\tau_2$$

which satisfy

$$[\tau_3, \tau_{\pm}] = \pm \tau_{\pm}, \quad \tau_3^2 + \frac{1}{2}\tau_+\tau_- + \frac{1}{2}\tau_-\tau_+ = \tau^2,$$

it can be shown (c.f. [Mer98]) that

$$\begin{aligned} \tau_{\pm}|I, I_3\rangle &= \sqrt{I(I+1) - I_3(I_3 \pm 1)}|I, I_3 \pm 1\rangle \\ &= \sqrt{(I \mp I_3)(I \pm I_3 + 1)}|I, I_3 \pm 1\rangle \\ \tau_3|I, I_3\rangle &= I_3|I, I_3\rangle \\ \tau^2|I, I_3\rangle &= I(I+1)|I, I_3\rangle \end{aligned}$$

where the different irreps are labeled by I and the row is labeled by I_3 .

By definition, the irreducible representation matrices $\{D^{(I)}\}$ (also known as *Wigner rotation matrices* in this context) are the matrix elements of the $SU(2)$ operators between different irrep basis states in the Hilbert space:

$$\begin{aligned} U_R|I, I_3\rangle &= \sum_{I'_3} |I, I'_3\rangle D_{I'_3 I_3}^{(I)}(R) \\ D_{I'_3 I_3}^{(I)}(R) &= \langle I, I'_3|U_R|I, I_3\rangle. \end{aligned}$$

We would like our baryon operators to transform irreducibly under $SU(2)$ isospin transformations:

$$\begin{aligned} U_R \bar{B}_{I_3}^I U_R^\dagger &= \sum_{I'_3} \bar{B}_{I'_3}^I D_{I'_3 I_3}^{(I)}(R) \\ &= \sum_{I'_3} \bar{B}_{I'_3}^I \langle I, I'_3|U_R|I, I_3\rangle \end{aligned}$$

where we have suppressed all indices except the flavor irrep and row. Considering an infinitesimal transformation $a_i \rightarrow 0$ ($i = 1, 2, 3$) and keeping terms up to first order in a_i at each step gives:

$$\begin{aligned} (1 + i \sum_j a_j \tau_j) \bar{B}_{I_3}^I (1 - i \sum_k a_k \tau_k) &= \sum_{I'_3} \bar{B}_{I'_3}^I \langle I, I_3 | (1 + i \sum_l a_l \tau_l) | I, I_3 \rangle \\ \bar{B}_{I_3}^I + i \sum_j a_j [\tau_j, \bar{B}_{I_3}^I] &= \bar{B}_{I_3}^I + i \sum_j a_j \sum_{I'_3} \bar{B}_{I'_3}^I \langle I, I_3 | \tau_j | I, I_3 \rangle \\ [\tau_j, \bar{B}_{I_3}^I] &= \sum_{I'_3} \bar{B}_{I'_3}^I \langle I, I_3 | \tau_j | I, I_3 \rangle \end{aligned}$$

where in the last step we used the fact that the infinitesimal a_i parameters are arbitrary. Our baryon operators will transform under isospin according to the irreducible representation labeled I if and only if

$$\begin{aligned} [\tau_3, \bar{B}_{I_3}^I] &= I_3 \bar{B}_{I_3}^I, \\ [\tau_+, \bar{B}_{I_3}^I] &= \sqrt{(I - I_3)(I + I_3 + 1)} \bar{B}_{I_3+1}^I, \\ [\tau_-, \bar{B}_{I_3}^I] &= \sqrt{(I + I_3)(I - I_3 + 1)} \bar{B}_{I_3-1}^I. \end{aligned}$$

From these relations, we see that the analog of the Casimir operator is:

$$[\tau_3, [\tau_3, \bar{B}_{I_3}^I]] + \frac{1}{2} [\tau_+, [\tau_-, \bar{B}_{I_3}^I]] + \frac{1}{2} [\tau_-, [\tau_+, \bar{B}_{I_3}^I]] = I(I + 1) \bar{B}_{I_3}^I.$$

We may now proceed to construct baryon operators from the individual quark fields. The light quarks are represented by $\bar{u} \equiv \tilde{\bar{\psi}}^u$ and $\bar{d} \equiv \tilde{\bar{\psi}}^d$ smeared source operators having $I = 1$ and $I_3 = +1/2, -1/2$ respectively. The strange quark is represented the $\bar{s} \equiv \tilde{\bar{\psi}}^s$ smeared source operator having $I = 0, I_3 = 0$. These operators therefore satisfy

$$\begin{aligned} [\tau_3, \bar{u}] &= \frac{1}{2} \bar{u}, & [\tau_3, \bar{d}] &= -\frac{1}{2} \bar{d}, & [\tau_3, \bar{s}] &= 0, \\ [\tau_+, \bar{u}] &= 0, & [\tau_+, \bar{d}] &= \bar{u}, & [\tau_+, \bar{s}] &= 0, \\ [\tau_-, \bar{u}] &= \bar{d}, & [\tau_-, \bar{d}] &= 0, & [\tau_-, \bar{s}] &= 0. \end{aligned}$$

Due to isospin symmetry in the Hamiltonian, our particle masses will not depend on the irrep row I_3 . We will therefore construct only one operator in each isospin I , strangeness S sector, the operator corresponding to maximal isospin projection $I_3 = I$. We now have *three-quark elemental operators* having definite isospin I , maximal $I_3 = I$, and strangeness S :

$$\bar{B}_{\alpha\beta\gamma,ijk}^F \equiv \sum_{A,B,C} \bar{\Phi}_{\alpha\beta\gamma,ijk}^{ABC}(\tau) \phi_{ABC}^{(F)},$$

where $\phi_{ABC}^{(F)}$ are the coefficients for the flavor channel F . The three-quark elemental baryon operators are given explicitly in terms of the extended three-quark operators in Table 4.3.

Baryon	$I = I_3$	S	Operators
Δ^{++}	$\frac{3}{2}$	0	$\overline{\Phi}_{\alpha\beta\gamma,ijk}^{uuu}$
Σ^+	1	-1	$\overline{\Phi}_{\alpha\beta\gamma,ijk}^{uus}$
N^+	$\frac{1}{2}$	0	$\overline{\Phi}_{\alpha\beta\gamma,ijk}^{uud} - \overline{\Phi}_{\alpha\beta\gamma,ijk}^{duu}$
Ξ^0	$\frac{1}{2}$	-2	$\overline{\Phi}_{\alpha\beta\gamma,ijk}^{ssu}$
Λ^0	0	-1	$\overline{\Phi}_{\alpha\beta\gamma,ijk}^{uds} - \overline{\Phi}_{\alpha\beta\gamma,ijk}^{dus}$
Ω^-	0	-3	$\overline{\Phi}_{\alpha\beta\gamma,ijk}^{sss}$

Table 4.3: Elemental three-quark baryon operators $\overline{B}_{\alpha\beta\gamma,ijk}^F$ having definite isospin I , maximal $I_3 = I$, and strangeness S in terms of the gauge-invariant extended three quark operators $\overline{\Phi}_{\alpha\beta\gamma,ijk}^{ABC}(\tau)$

4.4 Spin and parity

At this point, we have used smeared quark fields and gauge links to construct three-quark elemental operators \overline{B}_i^F and B_i^F , which have the desired momentum, color, flavor, and radial structure. The superscript F denotes the flavor structure, and can take on the values (Δ) , (Σ) , (N) , (Ξ) , (Λ) , or (Ω) . The index i now consists of only the Dirac spin indices $\alpha\beta\gamma$ and the displacement direction indices ijk . Our final task in constructing our operators is to project our operators onto states of definite spin and parity.

4.4.1 Baryon spin in the continuum

In the continuum, we could construct our baryon operators using the irreducible representations of the continuous spin group $SU(2)$, the spinorial double cover of the rotation group $SO(3)$. The irreps of $SU(2)$ are labeled by the spin quantum number $J = \frac{1}{2}, \frac{3}{2}, \frac{5}{2}, \dots$.

For example, we can construct a single-site spin-1/2 nucleon baryon operator by taking

$$\overline{B}_\alpha^{(N)}(\tau) = \sum_{\beta\gamma} B_{\alpha\beta\gamma,i=j=k=0}^{(N)}(\tau) \Gamma_{\beta\gamma}$$

where Γ is some 4×4 matrix of constants.

By combining two of the quarks into a Lorentz scalar or pseudoscalar, the resulting three-quark operator transforms like a spin-1/2 Dirac field under Lorentz transformations. If two of the quarks are combined into a four-vector (or axial four vector), then the resulting interpolating three-quark operators produce both spin-3/2 and spin-1/2 states.

Although this method of building up baryon operators is in widespread use, it becomes

extremely cumbersome when constructing higher spin states or complicated extended operators. The difficulty is compounded by the fact that the lattice regulator explicitly breaks Lorentz covariance.

4.4.2 Baryon spin on the lattice

The discretization of space onto a lattice breaks the rotational symmetry of the system. Thus, different continuum spin states will mix, making the identification of those states problematic. We may mitigate this difficulty, however, by designing our operators to transform under the lattice symmetry group O_h^D , the double-valued (spinorial) octahedral crystallographic point group. The states excited by our operators will have well-defined lattice spin and parity labels, and will not mix with each other.

Applying the projection operation (Eqn. 4.16) gives the full baryon operators:

$$\begin{aligned}\overline{B}_i^{\Lambda\lambda F}(\tau) &\equiv \overline{B}_{\alpha\beta\gamma,jkl}^F c_{\alpha\beta\gamma,jkl}^{(\Lambda\lambda i)}, \\ B_i^{\Lambda\lambda F}(\tau) &\equiv B_{\alpha\beta\gamma,jkl}^F c_{\alpha\beta\gamma,jkl}^{(\Lambda\lambda i)*},\end{aligned}\tag{4.21}$$

where Λ is the O_h^D irrep and λ is the row. The coefficients $c_{\alpha\beta\gamma,jkl}^{(\Lambda\lambda i)}$ can be determined using the methods of Subsection 4.3.3 once we have the irreducible representation matrices for O_h^D .

The exposition below is adapted from [BEF⁺05b] and [MEF⁺04].

4.4.3 Irreducible representation matrices for O_h^D

The basic building blocks used to assemble our baryon operators transform under the allowed spatial rotations and reflections of the point group O_h^D according to

$$U_R \left(\tilde{\psi}(x) \tilde{D}_j^{(p)\dagger} \right)_{a\alpha}^A U_R^\dagger = \left(\tilde{\psi}(Rx) \tilde{D}_{Rj}^{(p)\dagger} \right)_{a\beta}^A S_{\beta\alpha}(R),\tag{4.22}$$

$$U_R \left(\tilde{D}_j^{(p)} \tilde{\psi}(x) \right)_{a\alpha}^A U_R^\dagger = S(R)_{\alpha\beta}^{-1} \left(\tilde{D}_{Rj}^{(p)} \tilde{\psi}(Rx) \right)_{a\beta}^A,\tag{4.23}$$

where the transformation matrices for spatial inversion I_s and proper rotations C_{nj} through angle $2\pi/n$ about axis $O\hat{j}$ are given by

$$S(C_{nj}) = \exp\left(\frac{1}{8}\omega_{\mu\nu}[\gamma_\mu, \gamma_\nu]\right),\tag{4.24}$$

$$S(I_s) = \gamma_4,\tag{4.25}$$

with $\omega_{kl} = -2\pi\varepsilon_{jkl}/n$ and $\omega_{4k} = \omega_{k4} = 0$ ($\omega_{\mu\nu}$ is an antisymmetric tensor which parameterizes rotations and boosts). A rotation by $\pi/2$ about the y -axis is conventionally

denoted by C_{4y} , and C_{4z} denotes a rotation by $\pi/2$ about the z -axis. These particular group elements are given by

$$S(C_{4y}) = \frac{1}{\sqrt{2}}(1 + \gamma_1\gamma_3), \quad S(C_{4z}) = \frac{1}{\sqrt{2}}(1 + \gamma_2\gamma_1). \quad (4.26)$$

The allowed rotations on a three-dimensional spatially-isotropic cubic lattice form the octahedral group O which has 24 elements. Inclusion of spatial inversion yields the point group O_h which has 48 elements occurring in ten conjugacy classes. All elements of O_h can be generated from appropriate products of only C_{4y} , C_{4z} , and I_s .

Operators which transform according to the irreducible representations of O_h can then be constructed using the group-theoretical projections given in Eqn. (4.21). Orthogonality relations and hence, projection techniques, in group theory apply only to single-valued irreducible representations. However, the fermionic representations are double-valued representations of O_h . The commonly-used trick to circumvent this difficulty is to exploit the equivalence of the double-valued irreps of O_h with the extra single-valued irreps of the so-called *double point group* O_h^D . This group is formed by introducing a new element \bar{E} which represents a rotation by an angle 2π about any axis, such that $\bar{E}^2 = E$ (the identity). By including such an element, the total number of elements in O_h^D is double the number of elements in O_h . The 96 elements of O_h^D occur in sixteen conjugacy classes.

Since baryons are fermions, we need only be concerned with the six double-valued irreps of O_h . There are four two-dimensional irreps G_{1g} , G_{1u} , G_{2g} , and G_{2u} , and two four-dimensional irreps H_g and H_u . The subscript g refers to even-parity states, whereas the subscript u refers to odd-parity states⁹. The irreps G_{1g} and G_{1u} contain the spin-1/2 states, spin-3/2 states reside in the H_g and H_u , and two of the spin projections of the spin-5/2 states occur in the G_{2g} and G_{2u} irreps, while the remaining four projections reside in the H_g and H_u irreps. The spin content of each O_h irrep in the continuum limit is summarized in Table 4.6. This table lists the number of times that each of the O_h irreps occurs in the $J = \frac{1}{2}, \frac{3}{2}, \frac{5}{2}, \dots$ representations of $SU(2)$ subduced to O_h .

To carry out the projections in Eqn. (4.21), explicit representation matrices are needed. Our choice of representation matrices is summarized in Table 4.4. Matrices for only the group elements C_{4y} , C_{4z} , and I_s are given in Table 4.4 since the representation matrices for all other group elements can be obtained by suitable multiplications of the matrices for the three generating elements. For baryons, the representation matrix for \bar{E} in each of the O_h^D extra irreps is -1 times the identity matrix.

To give an example of this method, the single-site N^+ (nucleon) operators which transform irreducibly under the symmetry group of the spatial lattice are given in Table 4.5.

⁹From the German *gerade* meaning ‘even,’ and *ungerade* meaning ‘odd’

Λ	$\Gamma^{(\Lambda)}(C_{4y})$	$\Gamma^{(\Lambda)}(C_{4z})$
G_{1g}	$\frac{1}{\sqrt{2}} \begin{bmatrix} 1 & -1 \\ 1 & 1 \end{bmatrix}$	$\frac{1}{\sqrt{2}} \begin{bmatrix} 1-i & 0 \\ 0 & 1+i \end{bmatrix}$
G_{2g}	$\frac{-1}{\sqrt{2}} \begin{bmatrix} 1 & -1 \\ 1 & 1 \end{bmatrix}$	$\frac{-1}{\sqrt{2}} \begin{bmatrix} 1-i & 0 \\ 0 & 1+i \end{bmatrix}$
H_g	$\frac{1}{2\sqrt{2}} \begin{bmatrix} 1 & -\sqrt{3} & \sqrt{3} & -1 \\ \sqrt{3} & -1 & -1 & \sqrt{3} \\ \sqrt{3} & 1 & -1 & -\sqrt{3} \\ 1 & \sqrt{3} & \sqrt{3} & 1 \end{bmatrix}$	$\frac{1}{\sqrt{2}} \begin{bmatrix} -1-i & 0 & 0 & 0 \\ 0 & 1-i & 0 & 0 \\ 0 & 0 & 1+i & 0 \\ 0 & 0 & 0 & -1+i \end{bmatrix}$

Table 4.4: Our choice of the representation matrices for the double-valued irreps of O_h . The G_{1u}, G_{2u}, H_u matrices for the rotations C_{4y}, C_{4z} are the same as the G_{1g}, G_{2g}, H_g matrices, respectively, given below. Each of the G_{1g}, G_{2g}, H_g matrices for spatial inversion I_s is the identity matrix, whereas each of the G_{1u}, G_{2u}, H_u matrices for I_s is -1 times the identity matrix. The matrices for all other group elements can be obtained from appropriate multiplications of the C_{4y}, C_{4z} , and I_s matrices.

Irrep	Row	Operator	Row	Operator
G_{1g}	1	N_{211}	2	N_{221}
G_{1g}	1	N_{413}	2	N_{423}
G_{1g}	1	$2N_{332} + N_{413} - 2N_{431}$	2	$2N_{432} - 2N_{441} - N_{423}$
G_{1u}	1	N_{433}	2	N_{443}
G_{1u}	1	$N_{321} - N_{312}$	2	$N_{421} - N_{412}$
G_{1u}	1	$N_{312} + N_{321} - 2N_{411}$	2	$2N_{322} - N_{412} - N_{421}$
H_g	1	$\sqrt{3} N_{331}$	2	$N_{332} - N_{413} + 2N_{431}$
H_g	3	$2N_{432} + N_{441} - N_{423}$	4	$\sqrt{3} N_{442}$
H_u	1	$-\sqrt{3} N_{311}$	2	$-N_{312} - N_{321} - N_{411}$
H_u	3	$-N_{322} - N_{412} - N_{421}$	4	$-\sqrt{3} N_{422}$

Table 4.5: The single-site N^+ operators which transform irreducibly under the symmetry group of the spatial lattice, defining $N_{\alpha\beta\gamma} = \Phi_{\alpha\beta\gamma;000}^{uud} - \Phi_{\alpha\beta\gamma;000}^{duu}$ (see Table (4.3)) and using the Dirac-Pauli representation for the Dirac gamma matrices.

4.4.4 Continuum spin identification

Once we have the lattice spectrum, we may use the method of subduced representations to identify the continuum spin values of the extracted states. Because O_h^D is a subgroup of the continuum rotation group for spinors (with inversion), the continuum states appear as degenerate states within each of the lattice irreps. Table 4.6 denotes the number of times a continuum-limit spin J state will appear in each irreducible representation of the lattice. Thus, Table 4.6 allows us to identify the continuum-limit spin J corresponding to the

masses extracted in our Monte Carlo calculations. For example, to identify an even-parity baryon as having $J = 1/2$, a level must be observed in the G_{1g} channel, and there must be no degenerate partners in either of the G_{2g} or H_g . A level observed in the H_g channel with no degenerate partners in the G_{1g} and G_{2g} channels (in the continuum limit) is a $J = 3/2$ state. Degenerate partners observed in the G_{2g} and H_g channels with no partner in the G_{1g} channel indicates a $J = 5/2$ baryon. In other words, Table 4.6 details the patterns of continuum-limit degeneracies corresponding to each half-integral J value.

J	$n_{G_1}^J$	n_H^J	$n_{G_2}^J$
$\frac{1}{2}$	1	0	0
$\frac{3}{2}$	0	1	0
$\frac{5}{2}$	0	1	1
$\frac{7}{2}$	1	1	1
$\frac{9}{2}$	1	2	0
$\frac{11}{2}$	1	2	1
$\frac{13}{2}$	1	2	2
$\frac{15}{2}$	1	3	1
$\frac{17}{2}$	2	3	1

Table 4.6: Because O_h^D is a subgroup of the continuum spin group, the continuum states appear as degenerate states within each of the lattice irreps. This table allows us to identify the continuum spin state which corresponds to each lattice state.

Chapter 5

Evaluation of baryon correlation matrices

5.1 Charge conjugation and backward propagating states

5.1.1 Charge conjugation

As discussed in chapter 2, the Euclidean $\bar{\psi}$ and ψ operators are the analytic continuations of $\bar{\psi}_M$ and ψ_M , respectively, and must be treated as independent fields:

$$\bar{\psi} \neq \psi^\dagger \gamma_4.$$

However, we can define a *charge conjugation* operator U_C on the Hilbert space which exchanges quarks and antiquarks. This introduces a relation between the operators $\bar{\psi}$ and ψ :

$$U_C \bar{\psi}_\alpha(x) U_C^\dagger = \psi_\beta \bar{C}_{\beta\alpha}, \quad U_C \psi_\alpha(x) U_C^\dagger = \bar{\psi}_\beta C_{\beta\alpha},$$

where the 4×4 charge conjugation matrices C and \bar{C} keep track of how the spin components of the fields change under charge conjugation and summation over repeated indices is implied. To find the form of C and \bar{C} , we consider how the fermion terms in the continuum Euclidean action transform under the action of charge conjugation:

$$\begin{aligned} \bar{\psi}_\alpha \psi_\alpha &\rightarrow \psi_\beta \bar{\psi}_\gamma \bar{C}_{\beta\alpha} C_{\gamma\alpha}, \\ &= -\bar{\psi}_\gamma \psi_\beta, \bar{C}_{\beta\alpha} C_{\gamma\alpha}, \\ \int d^4x \bar{\psi}_\alpha \gamma_{\mu\alpha\beta} \partial_\mu \psi_\beta &\rightarrow \int d^4x \psi_\lambda \gamma_{\mu\alpha\beta} \partial_\mu \bar{\psi}_\sigma \bar{C}_{\lambda\alpha} C_{\sigma\beta}, \\ &= \int d^4x \bar{\psi}_\sigma \bar{C}_{\lambda\alpha} \gamma_{\mu\alpha\beta} C_{\sigma\beta} \partial_\mu \psi_\lambda, \end{aligned}$$

where we anticommutated the Grassmann variables, integrated by parts, and discarded the surface term. In order for the action to be invariant under charge conjugation, we must have

$$\begin{aligned}\bar{C}C^T &= -1, & \bar{C}\gamma_\mu C^T &= \gamma_\mu^T, \\ A_\mu(x) &\rightarrow -A_\mu^T(x), & U_\mu(x) &\rightarrow U_\mu^\dagger(x).\end{aligned}$$

A common choice for the charge conjugation matrix in the Dirac-Pauli basis (c.f. Chapter 2) is:

$$\bar{C} = C = \gamma_4\gamma_2,$$

and the fields transform as:

$$\bar{\psi} \rightarrow \psi\gamma_4\gamma_2, \quad \psi \rightarrow \bar{\psi}\gamma_4\gamma_2.$$

As an example, consider the charge conjugation behavior of the simple bilinear form $\psi\gamma_\mu\bar{\psi}$ (which can be used to interpolate for vector mesons):

$$\begin{aligned}\psi\gamma_\mu\bar{\psi} &\rightarrow \bar{\psi}\gamma_4\gamma_2\gamma_\mu(\gamma_4\gamma_2)^T\psi, \\ &= \bar{\psi}\gamma_4\gamma_2\gamma_\mu\gamma_2\gamma_4\psi, \\ &= -\bar{\psi}\gamma_\mu^T\psi, \\ &= \psi\gamma_\mu\bar{\psi}.\end{aligned}$$

5.1.2 Backward propagating states

Our operators are constructed using fermion fields $\bar{\psi}(x)$ which create a quark and annihilate an antiquark. Hence, each of our baryon operators creates a three-quark system of a given parity P and annihilates a three-antiquark system of the *same* parity P . This means that in the baryon propagator, a baryon of parity P propagates forward in time while an antibaryon of parity P propagates backwards in time. If we apply charge conjugation to our baryon operators, we arrive at the ‘backward propagating’ partners mentioned in Chapter 2.

Unlike boson fields, a fermion and its antifermion have opposite intrinsic parities, so that the antibaryon propagating backwards in time is the antiparticle of the *parity partner* of the baryon propagating forwards in time. Since chiral symmetry (vanishing quark mass) is spontaneously broken in QCD, the masses of opposite-parity partners may differ. The forward propagating baryon will have a mass different from that of the antibaryon propagating backwards in time. If the even- and odd-parity baryon operators are carefully designed with respect to one another, it is possible to arrange a definite relationship between the correlation matrix elements of one parity for $\tau > 0$ and the opposite-parity matrix elements for $\tau < 0$, allowing us to increase our statistics.

We can get a useful relation between the correlation matrix elements $C_{ab}(\tau)$ and $C_{ab}(T - \tau)$ if we utilize the projection procedure in Chapter 4 for our *even*-parity operators, and utilize charge conjugation to construct our *odd*-parity operators. Consider the correlation matrix element of two even-parity operators for $\tau \geq 0$. Suppressing irrep, displacement, and flavor indices, one sees that invariance under charge conjugation implies that

$$\begin{aligned}
C_{ab}(\tau) &= c_{\alpha\beta\gamma}^{(i)*} c_{\bar{\alpha}\bar{\beta}\bar{\gamma}}^{(j)} \langle 0 | B_{\alpha\beta\gamma}(\tau) \bar{B}_{\bar{\alpha}\bar{\beta}\bar{\gamma}}(0) | 0 \rangle, \\
&= c_{\alpha\beta\gamma}^{(i)*} c_{\bar{\alpha}\bar{\beta}\bar{\gamma}}^{(j)} \langle 0 | \mathcal{C}^\dagger \mathcal{C} B_{\alpha\beta\gamma}(\tau) \mathcal{C}^\dagger \mathcal{C} \bar{B}_{\bar{\alpha}\bar{\beta}\bar{\gamma}}(0) \mathcal{C}^\dagger \mathcal{C} | 0 \rangle, \\
&= c_{\alpha\beta\gamma}^{(i)*} c_{\bar{\alpha}\bar{\beta}\bar{\gamma}}^{(j)} \langle 0 | \bar{B}_{\alpha'\beta'\gamma'}(\tau) B_{\bar{\alpha}'\bar{\beta}'\bar{\gamma}'}(0) | 0 \rangle \\
&\quad \times \gamma_{\alpha'\alpha}^2 \gamma_{\beta'\beta}^2 \gamma_{\gamma'\gamma}^2 \gamma_{\bar{\alpha}'\bar{\alpha}}^2 \gamma_{\bar{\beta}'\bar{\beta}}^2 \gamma_{\bar{\gamma}'\bar{\gamma}}^2, \\
&= c_{\alpha\beta\gamma}^{(i)*} c_{\bar{\alpha}\bar{\beta}\bar{\gamma}}^{(j)} \langle 0 | \bar{B}_{\alpha'\beta'\gamma'}(0) B_{\bar{\alpha}'\bar{\beta}'\bar{\gamma}'}(-\tau) | 0 \rangle \\
&\quad \times \gamma_{\alpha'\alpha}^2 \gamma_{\beta'\beta}^2 \gamma_{\gamma'\gamma}^2 \gamma_{\bar{\alpha}'\bar{\alpha}}^2 \gamma_{\bar{\beta}'\bar{\beta}}^2 \gamma_{\bar{\gamma}'\bar{\gamma}}^2,
\end{aligned}$$

using invariance under time translations of the above expectation value and invariance of the vacuum under charge conjugation. The last line above represents the correlation of odd-parity operators propagating temporally backwards. Hence, for a given even-parity operator $\bar{B}_i^g(t)$, we can define an odd-parity operator $\bar{B}_i^u(t)$ by rotating the three Dirac indices using the γ_2 matrix and replacing the expansion coefficients by their complex conjugates such that the correlation matrices of the even- and odd-parity operators are related by

$$\begin{aligned}
C_{ab}^{G1g}(\tau) &= -C_{ab}^{G1u}(-\tau)^*, \\
C_{ab}^{Hg}(\tau) &= -C_{ab}^{Hu}(-\tau)^*, \\
C_{ab}^{G2g}(\tau) &= -C_{ab}^{G2u}(-\tau)^*.
\end{aligned}$$

For a lattice of time-extent T with anti-periodic temporal boundary conditions, this means that

$$C_{ab}^{(g)}(\tau) = C_{ba}^{(u)}(T - \tau), \quad (5.1)$$

and similarly for the other irreps. This allows us to appropriately average over forward and backward temporal propagations for increased statistics.

5.1.3 Improved estimators

In the absence of any external applied fields, the energies of the baryons do not depend on the row λ of a given irrep Λ , so we can increase statistics by averaging over all rows:

$$C_{ab}^{\Lambda F} \equiv \frac{1}{n_\Lambda} \sum_{\lambda=1}^{n_\Lambda} \langle B_a^{\Lambda\lambda F}(\tau) \bar{B}_b^{\Lambda\lambda F}(0) \rangle.$$

Because ψ and $\bar{\psi}$ are independent fields in the functional integral, the correlation matrix for a single configuration will not be Hermitian due to statistical fluctuations inherent in

the Monte Carlo estimate. Thus, we can increase our statistics by taking the average:

$$C_{ab}^{(g)}(\tau) \rightarrow \frac{1}{2}(C_{ab}^{(g)}(\tau) + C_{ba}^{(g)*}(\tau)).$$

In addition, we can use the backward propagating states in our correlation matrix to improve the statistics of the opposite-parity correlation matrix by exploiting the relation

$$C_{ab}^{(g)}(\tau) = C_{ba}^{(u)}(T - \tau).$$

Putting it together gives us the improved estimator for our correlation matrix elements:

$$C_{ab}^{(g)}(\tau) \rightarrow \frac{1}{4} \left[C_{ab}^{(g)}(\tau) + C_{ba}^{(u)}(T - \tau) + C_{ba}^{(g)*}(\tau) + C_{ab}^{(u)*}(T - \tau) \right], \quad (5.2)$$

$$C_{ab}^{(u)}(\tau) \rightarrow \frac{1}{4} \left[C_{ab}^{(u)}(\tau) + C_{ba}^{(g)}(T - \tau) + C_{ba}^{(u)*}(\tau) + C_{ab}^{(g)*}(T - \tau) \right]. \quad (5.3)$$

It is important to note that although we have increased the precision of our estimates by averaging, we have not increased the number of configurations produced by the Monte Carlo method. Thus, when estimating the jackknife errors according to the method presented in Chapter 3, we must form our n^{th} jackknife sample *before* calculating the improved estimators. Specifically, we do *not* treat the different terms in the improved estimator (Eqn. 5.3) as additional configurations which can be excluded to form a jackknife sample.

5.2 Three-quark propagators

Having constructed our baryon operators, we now have correlation matrix elements which look like:

$$\begin{aligned} C_{ab}^{\Lambda F}(\tau) &= \frac{1}{n_\Lambda} \sum_{\lambda=1}^{n_\Lambda} \langle B_a^{\Lambda\lambda F}(\tau) \bar{B}_b^{\Lambda\lambda F}(0) \rangle \\ &= \frac{1}{n_\Lambda} \sum_{\lambda=1}^{n_\Lambda} \sum_{k,l=1}^{M_B} c_{ak}^{\Lambda\lambda F*} c_{bl}^{\Lambda\lambda F} \langle B_k^F(\tau) \bar{B}_l^F(0) \rangle. \end{aligned}$$

where the indices a, b, k, l range from $1, \dots, M_B$, and encapsulate all of the information about the type of operator (single-site, singly-displaced, doubly-displaced-L, doubly-displaced-I, or triply-displaced-T), and the particular linear combination over Dirac indices used to make an operator which transforms irreducibly according to row λ of the Λ irrep ($G_{1g}, H_g, G_{2g}, G_{1u}, H_u,$ or G_{2u}) in the flavor channel F ($\Delta, \Sigma, N, \Xi, \Lambda,$ or Ω).

Since the number of elemental operators is large and the quark propagators are rather expensive to compute, it is very important to use symmetry to reduce the number of

Operator Type	Displaced Quark Direction(s)
Singly-Displaced	$+z$
Doubly-Displaced-I	$+z, -z$
Doubly-Displaced-L	$+y, +z$
Triply-Displaced-T	$+z, +y, -z$

Table 5.1: To minimize the number of sources, thereby reducing the number of three-quark propagators needed, we rotate our source and sink operators such that the displaced quarks at the source are always in the same canonical positions.

quark-propagator sources. Given the cyclic property of the trace and the unitarity of the symmetry transformation operators, we know that

$$\begin{aligned}
\langle B_k^F(\tau) \overline{B}_l^F(0) \rangle &= \langle U_R B_k^F(\tau) U_R^\dagger U_R \overline{B}_l^F(0) U_R^\dagger \rangle, \\
&= \sum_{k', l'=1}^{M_B} W_{k'k}(R) W_{l'l}(R)^* \langle B_{k'}^F(\tau) \overline{B}_{l'}^F(0) \rangle,
\end{aligned}$$

for any group element R of O_h . Hence, for each source $\overline{B}_l^F(0)$, we can choose a group element R_l such that we minimize the total number of source elemental operators which must be considered. For example, consider the singly-displaced operators. We can choose an R_l such that the displaced quark in the source is always displaced in the $+z$ direction. Similarly, a group element R_l can always be chosen to rotate each of the other types of operators into a specific orientation. The canonical source orientations for each type of operator are given in Table 5.1

To make zero momentum operators, we averaged over all spatial reference sites \vec{x} at both the sink and the source. However, we know that correlation functions of operators having different momenta will vanish (as expectation values), and thus we need only perform the spatial average at the sink. The source operator, evaluated at only one reference site, will no longer be translationally invariant, but the zero momentum contribution will be the only one which gives a non-canceling contribution to the correlation function. This increases the noise in our Monte Carlo estimates, but dramatically reduces the number of quark propagators needed.

The coefficients $c_{ij}^{\Lambda\Lambda F}$ in the baryon operators involve only the, Dirac spin components and the quark displacement directions and are independent of the color indices and spatial sites. Thus, in calculating the baryon correlation functions, it is convenient to first calculate gauge-invariant three-quark propagators in which all summations over color indices and spatial sites have been done. A three-quark propagator is defined by

$$\begin{aligned}
&\tilde{G}_{(\alpha i | \bar{\alpha} \bar{i})(\beta j | \bar{\beta} \bar{j})(\gamma k | \bar{\gamma} \bar{k})}^{(ABC)(p\bar{p})}(t) \\
&= \sum_{\vec{x}} \varepsilon_{abc} \varepsilon_{\bar{a}\bar{b}\bar{c}} \tilde{G}_{a\alpha i p | \bar{a}\bar{\alpha} \bar{i} \bar{p}}^{(A)}(\vec{x}, t | \vec{x}_0, 0) \\
&\times \tilde{G}_{b\beta j p | \bar{b}\bar{\beta} \bar{j} \bar{p}}^{(B)}(\vec{x}, t | \vec{x}_0, 0) \tilde{G}_{c\gamma k p | \bar{c}\bar{\gamma} \bar{k} \bar{p}}^{(C)}(\vec{x}, t | \vec{x}_0, 0),
\end{aligned} \tag{5.4}$$

where $\tilde{G}_{a\alpha ip|\bar{a}\bar{\alpha}\bar{i}\bar{p}}^{(A)}(\vec{x}, t|\vec{x}_0, 0)$ denotes the propagator for a single smeared quark field of flavor A from source site \vec{x}_0 at time $t = 0$ to sink site \vec{x} at time t . At the sink, a denotes color, α is the Dirac spin index, i is the displacement direction, and p is the displacement length, and similarly at the source for $\bar{a}, \bar{\alpha}, \bar{i}$, and \bar{p} , respectively. Notice that the three-quark propagator is symmetric under interchange of all indices associated with the same flavor. As usual, translation invariance is invoked at the source so that summation over spatial sites is done only at the sink. These three-quark propagators are computed for all possible values of the six Dirac spin indices.

Each baryon correlation function is simply a linear superposition of elements of the three-quark propagators. These superposition coefficients are calculated as follows: first, the baryon operators at the source and sink are expressed in terms of the elemental operators; next, Wick's theorem is applied to express the correlation function as a large sum of three-quark propagator components; finally, symmetry operations are applied to minimize the number of source orientations, and the results are averaged over the rows of the representations. C++ code was written by Colin Morningstar to perform these computations, and the resulting superposition coefficients are stored in computer files which are subsequently used as input to the Monte Carlo runs.

Wick's theorem is an important part of expressing the baryon correlation functions in terms of the three-quark propagators. To simplify the notation in the following, let the indices μ, ν, τ each represent a Dirac spin index and a displacement direction, and suppress the displacement lengths. Define $\bar{c}_{\mu\nu\tau}^{(i)} = c_{\mu'\nu'\tau'}^{(i)*} \gamma_{\mu\mu'}^4 \gamma_{\nu\nu'}^4 \gamma_{\tau\tau'}^4$, then the elements of the baryon correlation matrix in the Δ^{++} channel are given in terms of three-quark propagator components (before source-minimizing rotations) by

$$\begin{aligned}
C_{ij}^{(\Delta)}(t) &= c_{\mu\nu\tau}^{(i)} \bar{c}_{\mu\nu\tau}^{(j)} \left\{ \tilde{G}_{(\tau|\bar{\mu})(\nu|\bar{\nu})(\mu|\bar{\tau})}^{(uuu)}(t) \right. \\
&+ \tilde{G}_{(\tau|\bar{\mu})(\nu|\bar{\tau})(\mu|\bar{\nu})}^{(uuu)}(t) + \tilde{G}_{(\tau|\bar{\nu})(\nu|\bar{\mu})(\mu|\bar{\tau})}^{(uuu)}(t) \\
&+ \tilde{G}_{(\tau|\bar{\nu})(\nu|\bar{\tau})(\mu|\bar{\mu})}^{(uuu)}(t) + \tilde{G}_{(\tau|\bar{\tau})(\nu|\bar{\nu})(\mu|\bar{\mu})}^{(uuu)}(t) \\
&\left. + \tilde{G}_{(\tau|\bar{\tau})(\nu|\bar{\mu})(\mu|\bar{\nu})}^{(uuu)}(t) \right\}. \tag{5.5}
\end{aligned}$$

The N^+ correlation functions are expressed in terms of components of three-quark propagators by

$$\begin{aligned}
C_{ij}^{(N)}(t) &= c_{\mu\nu\tau}^{(i)} \bar{c}_{\mu\nu\tau}^{(j)} \left\{ \tilde{G}_{(\mu|\bar{\mu})(\nu|\bar{\nu})(\tau|\bar{\tau})}^{(uud)} \right. \\
&+ \tilde{G}_{(\mu|\bar{\nu})(\nu|\bar{\mu})(\tau|\bar{\tau})}^{(uud)} - \tilde{G}_{(\mu|\bar{\tau})(\nu|\bar{\nu})(\tau|\bar{\mu})}^{(uud)} \\
&- \tilde{G}_{(\mu|\bar{\tau})(\nu|\bar{\tau})(\tau|\bar{\mu})}^{(uud)} - \tilde{G}_{(\nu|\bar{\nu})(\tau|\bar{\mu})(\mu|\bar{\tau})}^{(uud)} \\
&- \tilde{G}_{(\nu|\bar{\mu})(\tau|\bar{\nu})(\mu|\bar{\tau})}^{(uud)} + \tilde{G}_{(\tau|\bar{\tau})(\nu|\bar{\nu})(\mu|\bar{\mu})}^{(uud)} \\
&\left. + \tilde{G}_{(\tau|\bar{\nu})(\nu|\bar{\tau})(\mu|\bar{\mu})}^{(uud)} \right\}, \tag{5.6}
\end{aligned}$$

and for the Σ^+ and Λ^0 channels, one finds

$$C_{ij}^{(\Sigma)}(t) = c_{\mu\nu\tau}^{(i)} \bar{c}_{\bar{\mu}\bar{\nu}\bar{\tau}}^{(j)} \left\{ \tilde{G}_{(\mu|\bar{\mu})(\nu|\bar{\nu})(\tau|\bar{\tau})}^{(uus)}(t) + \tilde{G}_{(\mu|\bar{\mu})(\nu|\bar{\nu})(\tau|\bar{\tau})}^{(uus)}(t) \right\}, \quad (5.7)$$

$$C_{ij}^{(\Lambda)}(t) = c_{\mu\nu\tau}^{(i)} \bar{c}_{\bar{\mu}\bar{\nu}\bar{\tau}}^{(j)} \left\{ \tilde{G}_{(\mu|\bar{\mu})(\nu|\bar{\nu})(\tau|\bar{\tau})}^{(uds)} - \tilde{G}_{(\mu|\bar{\mu})(\nu|\bar{\nu})(\tau|\bar{\tau})}^{(uds)} - \tilde{G}_{(\nu|\bar{\nu})(\mu|\bar{\mu})(\tau|\bar{\tau})}^{(uds)} + \tilde{G}_{(\nu|\bar{\nu})(\mu|\bar{\mu})(\tau|\bar{\tau})}^{(uds)} \right\}. \quad (5.8)$$

5.2.1 Smearing, covariantly-displaced quark propagators

We are now ready to compute the quark propagators for smeared and displaced sinks and sources. Recall that we are computing expectation values via path integrals, such as

$$\begin{aligned} \langle 0 | T f(\bar{\psi}, \psi, U) | 0 \rangle &= \frac{\int \mathcal{D}(\bar{\psi}, \psi, U) f(\bar{\psi}, \psi, U) \exp(-\bar{\psi}Q[U]\psi - S_G[U])}{\int \mathcal{D}(\bar{\psi}, \psi, U) \exp(-\bar{\psi}Q[U]\psi - S_G[U])} \\ &= \frac{\int \mathcal{D}U h(\bar{\psi}, \psi, U) \det Q[U] \exp(-S_G[U])}{\int \mathcal{D}U \det Q[U] \exp(-S_G[U])} \end{aligned}$$

where U represents the gluon field (link variables) and $S_G[U]$ is the pure gauge action. The remaining path integration over the link variables is carried out by the Monte Carlo method. Results in the so-called *quenched approximation* are obtained if $\det Q[U]$ is ignored in the updating and measurement process. Full QCD simulations require the incorporation of the computationally-expensive fermion determinant $\det Q[U]$ in the updating.

Now define

$$\begin{aligned} &\int \mathcal{D}(\bar{\psi}, \psi) (\tilde{D}_i^{(p)} \tilde{\psi})_{A\alpha\alpha}(\vec{x}, t) (\overleftarrow{\tilde{\psi} \tilde{D}_i^{(p)}})_{\bar{A}\bar{\alpha}\bar{\alpha}}(\vec{x}_0, 0) \exp(-\bar{\psi}Q[U]\psi) \\ &\equiv \det Q[U] \delta_{A\bar{A}} \tilde{G}_{a\alpha ip|\bar{a}\bar{\alpha}\bar{i}\bar{p}}^{(A)}(\vec{x}, t|\vec{x}_0, 0). \end{aligned}$$

To see how to compute the quark propagator $\tilde{G}_{a\alpha ip|\bar{a}\bar{\alpha}\bar{i}\bar{p}}^{(A)}(\vec{x}, t|\vec{x}_0, 0)$, let us proceed in steps of increasing complexity. First, we shall focus on the application of the three-dimensional Laplacian. If we can understand how to compute the quark propagators with the three-dimensional covariant Laplacian acting on both the source and sink fields, then it is straightforward to understand how to compute the smeared-smeared propagator. Finally, the p -link displacements will be included.

First, consider the application of a single Laplacian on both the source and sink fields:

$$(\Delta\psi)_a(x) = \sum_{j=\pm 1, \pm 2, \pm 3} \left\{ U_j^{ab}(x) \psi_b(x+\hat{j}) - \psi_a(x) \right\}, \quad (5.9)$$

$$\left(\overleftarrow{\psi}\overleftarrow{\Delta}\right)_a(x) = \sum_{j=\pm 1, \pm 2, \pm 3} \left\{ \overleftarrow{\psi}_b(x+\hat{j}) U_j^{\dagger ba}(x) - \overleftarrow{\psi}_a(x) \right\}, \quad (5.10)$$

where the indices a, b are color indices. To simplify the notation, both flavor and spin indices are omitted, as well as the gauge-field smearing tildes. Our goal now is to compute

$$\int \mathcal{D}(\overleftarrow{\psi}, \psi) (\Delta\psi)_a(x) \left(\overleftarrow{\psi}\overleftarrow{\Delta}\right)_b(y) \exp(-\overleftarrow{\psi} Q[U] \psi). \quad (5.11)$$

First, write the Laplacian operators in matrix form:

$$\begin{aligned} \Delta_{ab}(x|y) &= \sum_{j=\pm 1, \pm 2, \pm 3} \left\{ U_j^{ab}(x) \delta(x+\hat{j}, y) - \delta^{ab} \delta(x, y) \right\}, \\ &= \sum_{j=1}^3 \left\{ U_j^{ab}(x) \delta(x+\hat{j}, y) + U_j^{\dagger ab}(x-\hat{j}) \delta(x-\hat{j}, y) - 2\delta^{ab} \delta(x, y) \right\}, \\ &= \sum_{j=1}^3 \left\{ U_j^{ab}(x) \delta(x+\hat{j}, y) + U_j^{ba}(y)^* \delta(x-\hat{j}, y) - 2\delta^{ab} \delta(x, y) \right\}, \end{aligned} \quad (5.12)$$

$$\begin{aligned} \overleftarrow{\Delta}_{ab}(x|y) &= \sum_{j=\pm 1, \pm 2, \pm 3} \left\{ U_j^{\dagger ab}(y) \delta(x, y+\hat{j}) - \delta^{ab} \delta(x, y) \right\}, \\ &= \sum_{j=1}^3 \left\{ U_j^{\dagger ab}(y) \delta(x, y+\hat{j}) + U_j^{ab}(y-\hat{j}) \delta(x, y-\hat{j}) - 2\delta^{ab} \delta(x, y) \right\}, \\ &= \sum_{j=1}^3 \left\{ U_j^{ba}(y)^* \delta(x-\hat{j}, y) + U_j^{ab}(x) \delta(x+\hat{j}, y) - 2\delta^{ab} \delta(x, y) \right\}, \\ &= \Delta_{ab}(x|y). \end{aligned} \quad (5.13)$$

Grassmann integration quickly gives us the quark propagator:

$$\int \mathcal{D}(\overleftarrow{\psi}, \psi) (\Delta\psi)_a(x) \left(\overleftarrow{\psi}\overleftarrow{\Delta}\right)_b(y) \exp(-\overleftarrow{\psi} Q[U] \psi) \quad (5.14)$$

$$= \int \mathcal{D}(\overleftarrow{\psi}, \psi) \Delta_{ac}(x|z) \psi_c(z) \overleftarrow{\psi}_d(w) \Delta_{db}(w|y) \exp(-\overleftarrow{\psi} Q[U] \psi) \quad (5.15)$$

$$= \det Q[U] \Delta_{ac}(x|z) Q_{cd}^{-1}(z|w) \Delta_{db}(w|y). \quad (5.16)$$

A straightforward application of the above formula would require the computation of the inverse of the Dirac matrix Q for several local sources d . For higher powers of the Laplacian which may arise in usual quark smearings, the number of values of d needed may be quite large. Due to the computational expense of this inversion, it is better to proceed

as follows. The inverse of the fermion Dirac matrix is computed by solving the linear system of equations

$$Q_{fc}(v|z) Q_{cd}^{-1}(z|w) = \delta_{fd}\delta(v, w). \quad (5.17)$$

Apply $\overleftarrow{\Delta}$ from the right onto both sides of this equation to obtain:

$$Q_{fc}(v|z) Q_{cd}^{-1}(z|w) \Delta_{ab}(w|y) = \delta_{fd}\delta(v, w) \Delta_{ab}(w|y). \quad (5.18)$$

Write

$$P_{cb}(z|y) = Q_{cd}^{-1}(z|w) \Delta_{ab}(w|y), \quad (5.19)$$

$$R_{fb}(v|y) = \delta_{fd}\delta(v, w) \Delta_{ab}(w|y), \quad (5.20)$$

then the above equation becomes

$$Q_{fc}(v|z) P_{cb}(z|y) = R_{fb}(v|y). \quad (5.21)$$

This is a linear system of equations. We can solve for $P_{cb}(z|y)$ for a single fixed value of b and y by some variant of the conjugate gradient method. This is then repeated for the different colors b and Dirac spin components α , but usually only one site y is involved. The final propagator is obtained using

$$G_{ab}(x|y) = \Delta_{ac}(x|z) P_{cb}(z|y). \quad (5.22)$$

Eq. (5.20) tells us how we must apply the Laplacian for the source, and Eq. (5.22) tells us how we must apply the Laplacian for the sink.

The generalization of these results to higher powers of the Laplacian is straightforward. One starts at the source by forming the right-hand side

$$\begin{aligned} R_{ab}(x|y) &= \delta_{ac_1}\delta(x, z_1) \Delta_{c_1c_2}(z_1|z_2) \Delta_{c_2c_3}(z_2|z_3) \dots \Delta_{c_nb}(z_n|y), \\ &= \Delta_{ac_n}(x|z_n) \dots \Delta_{c_3c_2}(z_3|z_2) \Delta_{c_2c_1}(z_2|z_1) \delta_{c_1b}\delta(z_1, y), \end{aligned} \quad (5.23)$$

solves the linear system of equations

$$Q_{ac}(x|z) P_{cb}(z|y) = R_{ab}(x|y), \quad (5.24)$$

then applies the Laplacians at the sink to the result:

$$G_{ab}(x|y) = \Delta_{ac_n}(x|z_n) \dots \Delta_{c_3c_2}(z_3|z_2) \Delta_{c_2c_1}(z_2|z_1) P_{c_1b}(z_1|y). \quad (5.25)$$

Using Eq. (5.12), the application of the Laplacians at the sink in Eq. (5.25) is straightforward. For fixed b, y , $P_{c_1b}(z_1|y)$ can be viewed as a known vector (since it is a column of a matrix), then the applications of the Laplacians are equivalent to successive matrix-vector multiplications. Similarly, using Eq. (5.13) in Eq. (5.23) at the source is straightforward, too.

The computation of the propagator for smeared fields

$$\int \mathcal{D}(\bar{\psi}, \psi) \tilde{\psi}_a(x) \tilde{\psi}_b(y) \exp(-\bar{\psi} Q[U] \psi) \quad (5.26)$$

is now obvious. Let the smearing kernel be

$$F_{ab}(x|y) = \delta_{ab}\delta(x, y) + \xi \tilde{\Delta}_{ab}(x|y), \quad (5.27)$$

$$= (1 - 6\xi)\delta^{ab}\delta(x, y) + \xi \sum_{j=1}^3 \left\{ \tilde{U}_j^{ab}(x) \delta(x + \hat{j}, y) + \tilde{U}_j^{ba}(y)^* \delta(x - \hat{j}, y) \right\}. \quad (5.28)$$

One first forms the source field using

$$R_{ab}(x|y) = F_{ac}^{n\xi}(x|z) \delta_{cb}\delta(z, y), \quad (5.29)$$

$$= F_{acn_\xi}(x|zn_\xi) \dots F_{c_3c_2}(z_3|z_2) F_{c_2c_1}(z_2|z_1) \delta_{c_1b}\delta(z_1, y), \quad (5.30)$$

solves the linear system of equations

$$Q_{ac}(x|z) P_{cb}(z|y) = R_{ab}(x|y), \quad (5.31)$$

then applies the smearing at the sink to the result:

$$G_{ab}(x|y) = F_{ac}^{n\xi}(x|z) P_{cb}(z|y), \quad (5.32)$$

$$= F_{acn_\xi}(x|zn_\xi) \dots F_{c_3c_2}(z_3|z_2) F_{c_2c_1}(z_2|z_1) P_{c_1b}(z_1|y). \quad (5.33)$$

Lastly, we need to include the p -link covariant displacement operators:

$$\int \mathcal{D}(\bar{\psi}, \psi) \left(\tilde{D}_j^{(p)} \tilde{\psi} \right)_a(x) \left(\overleftarrow{\tilde{D}_k^{(p)}} \right)_b(y) \exp(-\bar{\psi} Q[U] \psi). \quad (5.34)$$

In matrix form, these operators are given by

$$\left(\tilde{D}_j^{(p)} \right)_{ab}(x|y) = \tilde{U}_j^{ac_2}(x) \tilde{U}_j^{c_2c_3}(x + \hat{j}) \dots \tilde{U}_j^{c_p b}(x + (p-1)\hat{j}) \delta(x + p\hat{j}, y), \quad (5.35)$$

$$\left(\overleftarrow{\tilde{D}_j^{(p)}} \right)_{ab}(x|y) = \tilde{U}_j^{\dagger ac_p}(y + (p-1)\hat{j}) \dots \tilde{U}_j^{\dagger c_3c_2}(y + \hat{j}) \tilde{U}_j^{\dagger c_2 b}(y) \delta(x, y + p\hat{j}), \quad (5.36)$$

$$\begin{aligned} &= \left(\tilde{U}_j^{bc_2}(y) \tilde{U}_j^{c_2c_3}(y + \hat{j}) \dots \tilde{U}_j^{c_p a}(y + (p-1)\hat{j}) \delta(y + p\hat{j}, x) \right)^* \\ &= \left(\tilde{D}_j^{(p)} \right)_{ba}(y|x)^*. \end{aligned} \quad (5.37)$$

Unlike the Laplacian, this is *not* a Hermitian operator. The source function is now given by

$$R_{ab}(x|y) = F_{ac}^{n\xi}(x|z) \left(\overleftarrow{\tilde{D}_k^{(p)}} \right)_{cd}(z|w) \delta_{db}\delta(w, y). \quad (5.38)$$

Since the $\overleftarrow{\tilde{\Delta}}$ matrix may also be written as

$$\begin{aligned} \left(\overleftarrow{\tilde{D}_j^{(p)}} \right)_{ab}(x|y) &= \tilde{U}_j^{\dagger ac_p}(y + (p-1)\hat{j}) \dots \tilde{U}_j^{\dagger c_3c_2}(y + \hat{j}) \tilde{U}_j^{\dagger c_2 b}(y) \delta(x, y + p\hat{j}), \\ &= \tilde{U}_{-j}^{ac_p}(y + p\hat{j}) \dots \tilde{U}_{-j}^{c_3c_2}(y + 2\hat{j}) \tilde{U}_{-j}^{c_2 b}(y + \hat{j}) \delta(x, y + p\hat{j}), \\ &= \tilde{U}_{-j}^{ac_p}(x) \dots \tilde{U}_{-j}^{c_2 b}(x - (p-1)\hat{j}) \delta(x - p\hat{j}, y), \\ &= \left(\tilde{D}_{-j}^{(p)} \right)_{ab}(x|y), \end{aligned} \quad (5.39)$$

the source function may be better expressed as

$$R_{ab}(x|y) = F_{ac}^{n\xi}(x|z) \left(\tilde{D}_{-k}^{(p)} \right)_{cd} (z|w) \delta_{db} \delta(w, y). \quad (5.40)$$

The two key points to note about Eq. (5.40) are that (a) the displacement is applied *first* to the δ -function, and then the smearing is applied, and (b) a displacement in the $-\hat{k}$ direction must be made.

In summary, to compute

$$\int \mathcal{D}(\bar{\psi}, \psi) \left(\tilde{D}_j^{(p)} \tilde{\psi} \right)_a (x) \left(\overleftarrow{\tilde{\psi} D_k^{(p)}} \right)_b (y) \exp(-\bar{\psi} Q[U] \psi) = G_{ab}(x|y) \det Q[U], \quad (5.41)$$

one first forms the following source field

$$R_{ab}(x|y) = F_{ac}^{n\xi}(x|z) \left(\tilde{D}_{-k}^{(p)} \right)_{cd} (z|w) \delta_{db} \delta(w, y), \quad (5.42)$$

$$= F_{ac_{n\xi}}(x|z_{n\xi}) \dots F_{c_3 c_2}(z_3|z_2) F_{c_2 c_1}(z_2|z_1) \left(\tilde{D}_{-k}^{(p)} \right)_{c_1 d} (z_1|w) \delta_{db} \delta(w, y) \quad (5.43)$$

solves the linear system of equations

$$Q_{ac}(x|z) P_{cb}(z|y) = R_{ab}(x|y), \quad (5.44)$$

then applies the smearing and displacement at the sink to the result:

$$G_{ab}(x|y) = \left(\tilde{D}_j^{(p)} \right)_{ad} (x|w) F_{dc}^{n\xi}(w|z) P_{cb}(z|y), \quad (5.45)$$

$$= \left(\tilde{D}_j^{(p)} \right)_{ad} (x|w) F_{dc_{n\xi}}(w|z_{n\xi}) \dots F_{c_3 c_2}(z_3|z_2) F_{c_2 c_1}(z_2|z_1) P_{c_1 b}(z_1|y), \quad (5.46)$$

where the smearing kernel is

$$F_{ab}(x|y) = \delta_{ab} \delta(x, y) + \xi \tilde{\Delta}_{ab}(x|y), \quad (5.47)$$

$$= (1 - 6\xi) \delta^{ab} \delta(x, y) + \xi \sum_{j=1}^3 \left\{ \tilde{U}_j^{ab}(x) \delta(x + \hat{j}, y) + \tilde{U}_j^{ba}(y)^* \delta(x - \hat{j}, y) \right\}. \quad (5.48)$$

In short,

- at the sink: smear then displace in desired direction,
- at the source: start with point source, displace in *opposite* direction, then smear.

5.2.2 Chroma walk-through

Our generalized three-quark propagators were generated using the Chroma QCD library developed at JLab [Edw05]. We first used Chroma to make four smeared, covariantly-displaced single-quark sources:

1. no displacement
2. $+y$ -direction displacement
3. $-z$ -direction displacement
4. $+z$ -direction displacement

Each source object was then propagated to all sink sites on the lattice, resulting in a smeared, covariantly-displaced source and an unsmeared, undisplaced sink.

It is in this step that the computationally expensive quark matrix inversion Q^{-1} is performed. This is done using the bi-conjugate gradient algorithm [GL89]. The resulting ‘one-to-all’ propagators take the form of $Q_{x,0}^{-1}$, requiring the inversion of only a single column of the quark matrix $Q[U]$.

The sinks were then smeared and covariantly-displaced. For each of the four input propagators, there were seven output propagators, one for each of the types of displacement: no displacement, $\pm x$, $\pm y$, $\pm z$. These 28 single-quark propagators were then combined, three at a time, to make all of the needed generalized three-quark propagators. These propagators were saved to disk for later use.

Combining the indices of the single quark propagators to form the three-quark propagators was one of the most computationally intensive steps. This is because the 28 single-quark propagators combine into a rich variety of three quark propagators. At the source, there can be one of five three-quark elemental operators, one for each type (remembering that we have fixed a canonical orientation). At the sink, the number of orientations depends on the symmetry of the elemental three-quark operator:

- single-site (SD): 1 orientation,
- singly-displaced (SD): 6 orientations,
- doubly-displaced-I (DDI): 3 orientations,
- doubly-displaced-L (DDL): 12 orientations,
- triply-displaced-T (TDT): 12 orientations.

In addition, we must choose which source quark propagators to each sink quark, and take into account that the up and down quarks are indistinguishable (isospin symmetry: $m_u = m_d$).

For the correlation matrix involving a singly-displaced operator at the source (\overline{SD}) and a singly-displaced operator at the sink, there is only one orientation for the quarks at the source (by convention), there are six ways to orient the sink quarks, and there are two ways

	\overline{SS}	\overline{SD}	\overline{DDI}	\overline{DDL}	\overline{TDT}
SS	1	1	1	1	1
SD	6	12	18	18	18
DDI	3	9	18	18	18
DDL	12	36	72	72	72
TDT	12	36	72	72	72

Table 5.2: The number of three-quark propagators needed for each part of the full nucleon correlation matrix. The total number of propagators needed is 671. The diagonal correlation matrix elements required only 175 propagators, which were reused for the full run.

to propagate the displaced source quark: either to the displaced sink quark, or to one of the (indistinguishable) undisplaced quarks.

For example: the number of three-quark propagators required for a full correlation matrix run including only single-site and singly-displaced nucleon operators can be calculated as follows:

- $SS - \overline{SS} = 1 \times 1$ possibility +
- $SS - \overline{SD} = 1 \times 1$ possibility +
- $SD - \overline{SS} = 1 \times 6$ possibilities +
- $SD - \overline{SD} = 1 \times 6 \times 2$ possibilities = 20 three-quark propagators

We restricted the scope of this project to the N^+ (nucleon) channel. Our final correlation matrix run used all five types of operators at the source and sink and required 671 three-quark propagators (see Table 5.2.2). These three-quark propagators were stored on disk, each file containing one three-quark propagator measured on one configuration. We were able to reuse 175 of those three-quark propagators from our diagonal runs.

5.2.3 Correlation matrix elements

The C++ program we wrote to tie the three quark propagators together into correlation matrix elements was based on the JLab `ttt` program¹.

The program would first read in the pre-calculated coefficients. For each configuration, or *bin*, the program would read in the three-quark propagator files for that configuration and combine them into the desired correlation matrix elements.

¹The program name `ttt` stands for ‘tie them together.’

We designed the program to process multiple irreps and to generate only the user-selected elements of a correlation matrix. Early in the operator tuning and selection process, we were only interested in the diagonal elements of the correlation matrices (for effective mass functions). Later, we utilized the off-diagonal elements of our correlation matrices to extract excited states.

Chapter 6

Quark field and gauge link smearing parameter tuning

The smearing method we use to smear our quark fields and gauge links was developed in Chapter 4 and is summarized here:

$$\tilde{\psi} \equiv \tilde{S}\psi, \quad \tilde{\bar{\psi}} \equiv \tilde{S}^\dagger \bar{\psi} \quad (6.1)$$

where

$$\tilde{S}(\sigma, n_\sigma, \rho, n_\rho) \equiv \left(1 + \frac{\sigma^2}{2n_\sigma} \tilde{\Delta}\right)^{n_\sigma} \quad (6.2)$$

$$\tilde{\Delta}_{x,y} \equiv \sum_{k=\pm 1, \pm 2, \pm 3} \left(\tilde{U}_k(x) \delta_{x+\hat{k},y} - \delta_{x,y}\right) \quad (6.3)$$

$$\tilde{U}_k \equiv U_k^{[n_\rho]} \quad (6.4)$$

$$U_k^{[n+1]}(x) = \exp(i\rho\Theta_\mu^{[n]}(x)) U_k^{[n]}(x), \quad (6.5)$$

$$\Theta_k(x) = \frac{i}{2} \left(\Omega_k^\dagger(x) - \Omega_k(x)\right) - \frac{i}{6} \text{Tr} \left(\Omega_k^\dagger(x) - \Omega_k(x)\right) \quad (6.6)$$

$$\Omega_k(x) = C_k(x) U_k^\dagger(x) \quad (\text{no summation over } k) \quad (6.7)$$

$$C_k(x) \equiv \sum_{j \neq k} \left(U_j(x) U_k(x + \hat{j}) U_j^\dagger(x + \hat{k}) \right) \quad (6.8)$$

$$+ U_j^\dagger(x - \hat{j}) U_k(x - \hat{j}) U_j(x - \hat{j} + \hat{k}). \quad (6.9)$$

The four parameters to tune in this smearing procedure are the real (dimensionless) Gaussian radius σ and staple weight ρ , and the integer quark field and gauge link smearing iterations n_σ and n_ρ . Due to Chroma conventions, the Gaussian radius values reported here will be denoted by σ_s and related to the σ in our equations by

$$\sigma_s \equiv \sqrt{2}\sigma.$$

6.1 Criterion for judging the effectiveness of smearing

Recalling our definition of the effective mass function from chapter 2, a good measure of the signal of an operator $\overline{\mathcal{O}}_i$ is the effective mass associated with the correlation function

$$C_{ii}(\tau) = \langle \Omega | \mathcal{O}_i(\tau) \overline{\mathcal{O}}_i(0) | \Omega \rangle,$$

given by

$$\begin{aligned} a_\tau M(\tau) &\equiv \ln \left[\frac{C_{ii}(\tau)}{C_{ii}(\tau + a_\tau)} \right], \\ &= \ln \left[\frac{|c_{i,1}|^2 e^{-E_1 \tau} + |c_{i,2}|^2 e^{-E_2 \tau} + \dots}{|c_{i,1}|^2 e^{-E_1(\tau+a_\tau)} + |c_{i,2}|^2 e^{-E_2(\tau+a_\tau)} + \dots} \right], \quad c_{i,k} \equiv \langle k | \overline{\mathcal{O}}_a | \Omega \rangle, \\ &= a_\tau E_1 \left(1 + O(|c_{i,2}|^2 / |c_{i,1}|^2 e^{-(E_2-E_1)\tau}) \right). \end{aligned}$$

A reasonable way to proceed is to tune our operators to reduce $|c_{i,k}|^2 / |c_{i,1}|^2$ for large k , because an objective measure of the quality of an operator is the time τ at which its effective mass function reaches its plateau. In addition, we would like to reduce the variance of the Monte Carlo estimate. We define the *noise* of the effective mass function at each time as the absolute ratio of the signal to jackknife error.

To compare the effectiveness of different values of the quark field smearing parameters, we compared the effective mass $a_\tau M(\tau = 4a_\tau)$ for each of the three operators at a particular temporal separation $\tau = 4a_\tau$. Results using 50 quenched configurations on a $12^3 \times 48$ anisotropic lattice using the Wilson action with $a_s \sim 0.1$ fm and $a_s/a_\tau \sim 3.0$ are shown in Figure 6.3.

6.2 Contamination and noise in extended baryon operators

For single-site (local) hadron operators, it is well known that the use of spatially-smearred quark fields is crucial. For extended baryon operators, one expects quark field smearing to be equally important, but the relevance and interplay of link-field smearing is less well known. Thus, we decided that a systematic study of both quark field and link-variable smearing was warranted.

From our smearing parameter tuning studies [LMB⁺06] we found that Gaussian quark field smearing substantially reduces contributions from the short wavelength modes of the theory, while stout gauge link smearing significantly reduces the noise from the stochastic evaluations. The use of gauge link smearing is shown to be crucial for baryon operators constructed of covariantly-displaced quark fields.

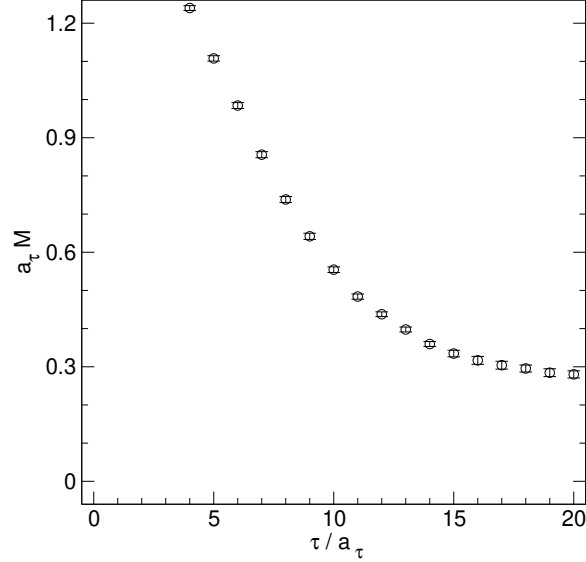


Figure 6.1: A sample effective mass plot of a single-site operator showing contamination at early times due to operator coupling with higher lying modes.

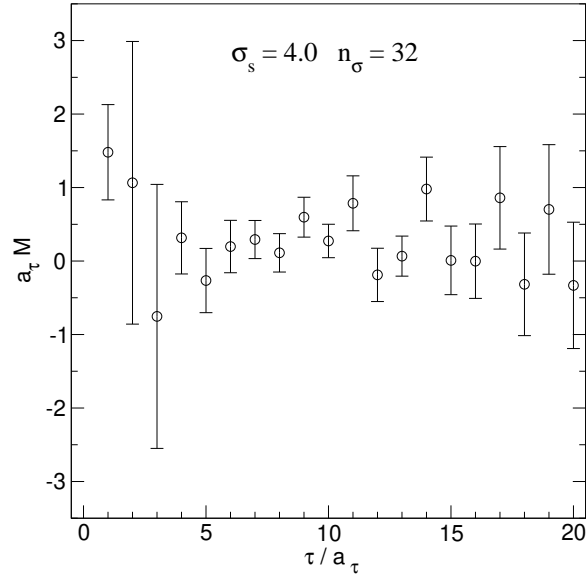


Figure 6.2: A sample effective mass plot of a triply-displaced operator showing noise due to stochastic gauge link noise. This noise remains present even after significant quark field smearing ($\sigma_s = 4.0$, $n_\sigma = 32$).

Also, the order of approximation of the exponential operator n_σ determines the maximum value of σ we can use before the approximation breaks down (see Figure 6.3). Once σ becomes too large, the smearing operator behaves as $(1 + \frac{\sigma^2}{2n_\sigma}\Delta)^{n_\sigma} \rightarrow \sim \sigma^{2n_\sigma}\Delta^{n_\sigma}$, which is simply a momentum weighting. Thus, high momentum modes rapidly start to contribute even more than in the unsmearred case.

6.3 Systematic study of the smearing parameter space

6.3.1 Trial operators

Each choice of smearing parameter values necessitates the generation of a new set of generalized three-quark propagators. In order to maximize the number of different smearing parameter values we could examine, we constructed our three trial operators out of three nucleon three-quark propagators having the same operator type at the source and sink (single-site, singly-displaced, and triply-displaced-T, see Figure 4.1). Our first trial operator was a single-site operator $\overline{\mathcal{O}}_{SS}$ projected into the G_{1g} irreducible representation of the cubic point group. Because we did not have different orientations at the sink, we chose a particular choice of the Dirac indices for the singly-displaced operator $\overline{\mathcal{O}}_{SD}$ and triply-displaced-T operator $\overline{\mathcal{O}}_{TDT}$. In later runs, we found that the choice of smearing parameters was insensitive to the type of extended baryon operator used.

6.3.2 Quark field smearing

Without gauge link smearing, the displaced operators were found to be excessively noisy, making a meaningful comparison impossible. For this reason, we first tuned the link smearing parameters to minimize the noise of the effective mass at the fourth time slice, using unsmearred quark fields. We then fixed the gauge link smearing parameters, and varied the quark field smearing parameters. These results are shown in Figure 6.3 and include gauge-field smearing with $n_\rho = 16$ and $n_\rho\rho = 2.5$. One sees that $a_\tau M(\tau = 4a_\tau)$ is independent of n_σ for sufficiently small σ_s . For each value of n_σ , $a_\tau M(\tau = 4a_\tau)$ first decreases as σ_s is increased, until the approximation to a Gaussian eventually breaks down, signaled by a sudden rapid rise in $a_\tau M(\tau = 4a_\tau)$. This rapid rise occurs at larger values of σ_s for larger values of n_σ .

6.3.3 Gauge link smearing

Next, we fixed the quark field smearing parameters and studied the effect of changing the gauge-field smearing parameters. Before tuning the trial operators, we examined the the effective mass $a_\tau E(0)$ associated with the static quark-antiquark potential at a spatial separation $R = 5a_s \sim 0.5$ fm and at a particular temporal separation $\tau = 0$ to get an idea of the effectiveness of different values of ρ and n_ρ . The results are shown in the leftmost plot in Figure 6.4. The behavior is qualitatively similar to that observed when we tuned the gauge link smearing parameters for our trial operators, shown in Figure 6.3. One sees that the $\tau = 0$ effective mass is independent of the product $n_\rho\rho$ for sufficiently small values of $n_\rho\rho$. For each value of n_ρ , $a_\tau E(0)$ decreases as $n_\rho\rho$ increases, until a minimum is reached and a rapid rise occurs. The onset of the rise occurs at larger values of $n_\rho\rho$ as n_ρ increases.

Note that $a_\tau E(0)$ does not decrease appreciably as $n_\rho \rho$ increases above 2.5. Hence, $n_\rho \rho = 2.5$ with $n_\rho = 16$ are our preferred values for the link smearing at lattice spacing $a_s \sim 0.1$ fm, based on the static quark-antiquark potential.

Somewhat surprisingly, we found that changing the link-smearing parameters did not appreciably affect the mean values of the effective masses of our three nucleon operators. However, the effect on the variances of the effective masses was dramatic. The relative jackknife error $\eta(4a_\tau)$ of $a_\tau M(4a_\tau)$ is shown against $n_\rho \rho$ in the right three plots in Figure 6.4, and amazingly, this error shows the same qualitative behavior as in Figure 6.3 and the leftmost plot in Figure 6.4. One key point learned here is that the preferred link-smearing parameters determined from the static quark-antiquark potential produce the smallest error in the extended baryon operators.

The effective masses shown in Figure 6.5 also illustrate these findings. The top row shows that applying only quark field smearing to the three selected nucleon operators significantly reduces couplings to higher-lying states, but the displaced operators remain excessively noisy. The second row illustrates that including only link-field smearing substantially reduces the noise, but does not appreciably alter the effective masses themselves. The bottom row shows dramatic improvement from reduced couplings to excited states and dramatically reduced noise when both quark field and link-field smearing is applied, especially for the extended operators.

6.3.4 Excited state considerations

Incorporating both quark field and link-variable smearing is crucial for extracting the baryon spectrum using gauge-invariant extended three-quark operators. Gaussian quark field smearing dramatically diminishes couplings to the short wavelength modes of the theory, whereas stout-link smearing drastically reduces the noise in operators with displaced quarks. Preferred smearing parameters $\sigma_s = 4.0$, $n_\sigma = 32$, $n_\rho \rho = 2.5$, $n_\rho = 16$ were found for a lattice spacing $a_s \sim 0.1$ fm and were independent of the baryon operators chosen. After examining the behavior of the excited state signal (using the principal effective mass method), we decided to reduce the quark smearing in order to decrease the noise in the excited states (see Figure 6.6).

The final values of smearing parameters we selected were:

- Gaussian smearing: $\sigma_s = 3.0$, $n_\sigma = 32$ iterations,
- Stout-link smearing: $n_\rho \rho = 2.5$, $n_\rho = 16$ iterations.

An issue which remains to be addressed in future work is the dependence of the preferred smearing parameters on the quark mass.

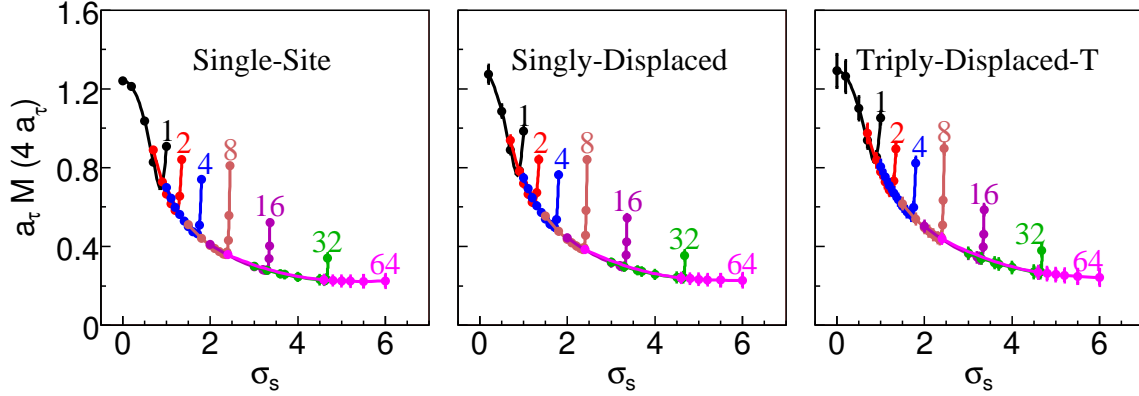


Figure 6.3: The effective mass $a_\tau M(4a_\tau)$ for the operators $\overline{\mathcal{O}}_{SS}$, $\overline{\mathcal{O}}_{SD}$, $\overline{\mathcal{O}}_{TDT}$ against smearing radius σ_s for $n_\sigma = 1, 2, 4, 8, 16, 32, 64$. The gauge field is smeared using $n_\rho = 16$ and $n_\rho \rho = 2.5$. Results are based on 50 quenched configurations on a $12^3 \times 48$ anisotropic lattice using the Wilson action with $a_s \sim 0.1$ fm and $a_s/a_\tau \sim 3.0$. The quark mass is such that the mass of the pion is approximately 700 MeV.

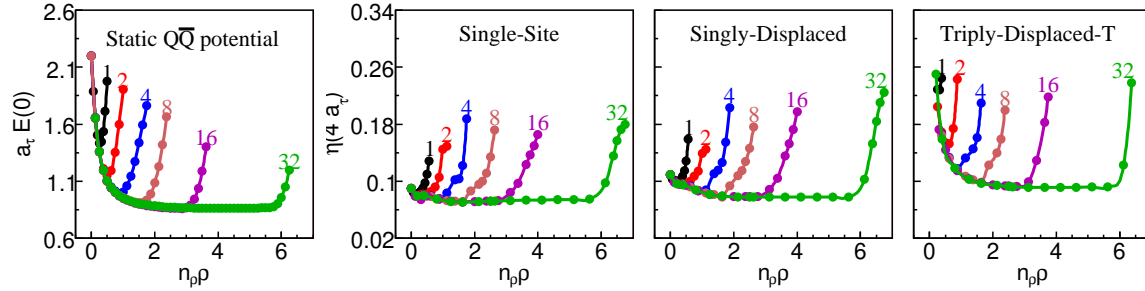


Figure 6.4: Leftmost plot: the effective mass $a_\tau E(0)$ for $\tau = 0$ corresponding to the static quark-antiquark potential at spatial separation $R = 5a_s \sim 0.5$ fm against $n_\rho \rho$ for $n_\rho = 1, 2, 4, 8, 16, 32$. Results are based on 100 configurations on a 16^4 isotropic lattice using the Wilson gauge action with $\beta = 6.0$. Right three plots: the relative jackknife error $\eta(4a_\tau)$ of effective masses $a_\tau M(4a_\tau)$ of the three nucleon operators $\overline{\mathcal{O}}_{SS}$, $\overline{\mathcal{O}}_{SD}$, $\overline{\mathcal{O}}_{TDT}$ for $n_\sigma = 32$, $\sigma_s = 4.0$ against $n_\rho \rho$ for $n_\rho = 1, 2, 4, 8, 16, 32$. Results are based on 50 quenched configurations on a $12^3 \times 48$ anisotropic lattice using the Wilson action with $a_s \sim 0.1$ fm, $a_s/a_\tau \sim 3.0$.

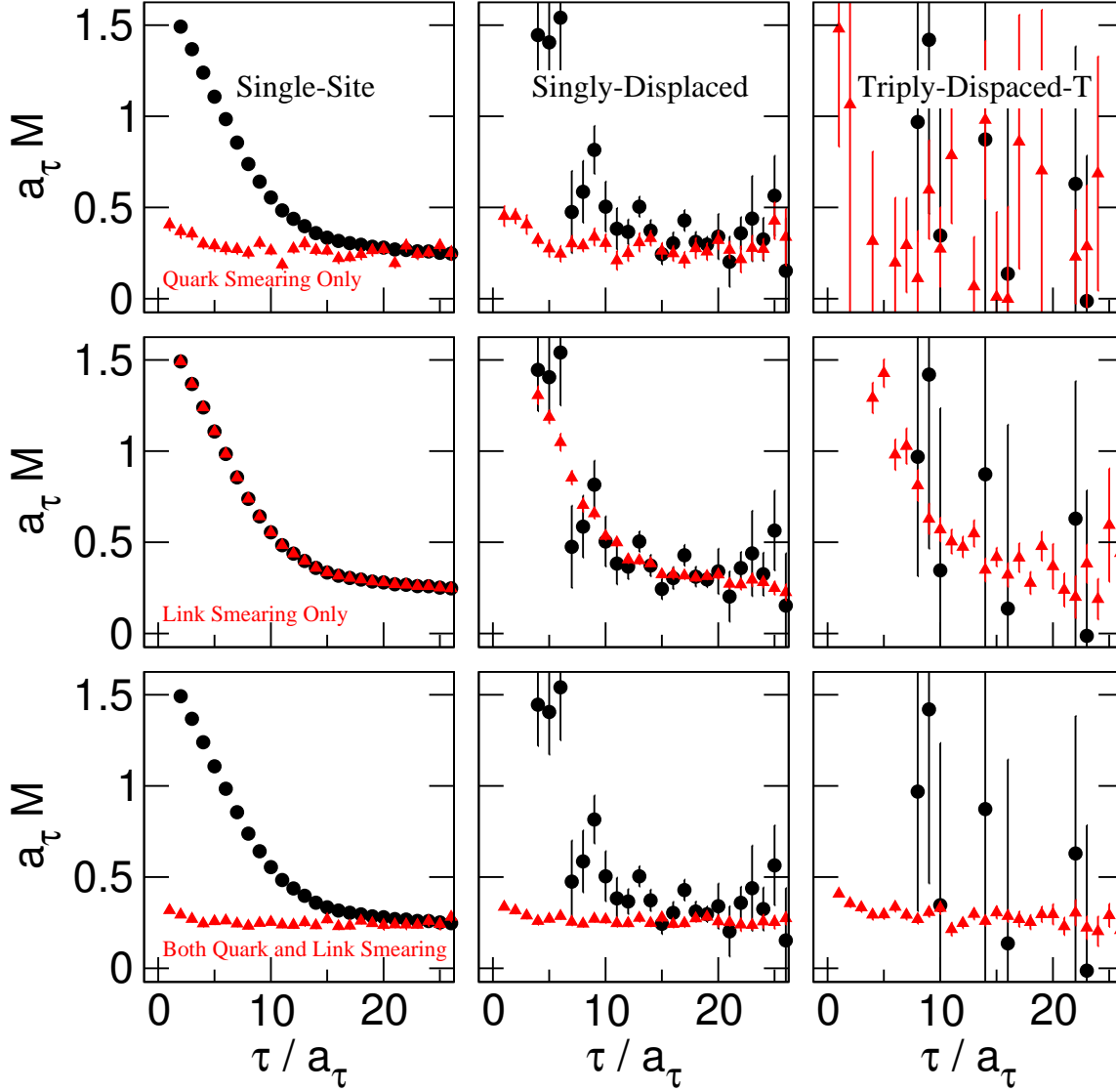


Figure 6.5: Effective masses $a_\tau M(\tau)$ for unsmeared (black circles) and smeared (red triangles) operators $\overline{\mathcal{O}}_{SS}$, $\overline{\mathcal{O}}_{SD}$, $\overline{\mathcal{O}}_{TDT}$. Top row: only quark field smearing $n_\sigma = 32$, $\sigma_s = 4.0$ is used. Middle row: only link-variable smearing $n_\rho = 16$, $n_\rho\rho = 2.5$ is applied. Bottom row: both quark and link smearing $n_\sigma = 32$, $\sigma_s = 4.0$, $n_\rho = 16$, $n_\rho\rho = 2.5$ are used, dramatically improving the signal for all three operators. Results are based on 50 quenched configurations on a $12^3 \times 48$ anisotropic lattice using the Wilson action with $a_s \sim 0.1$ fm, $a_s/a_\tau \sim 3.0$.

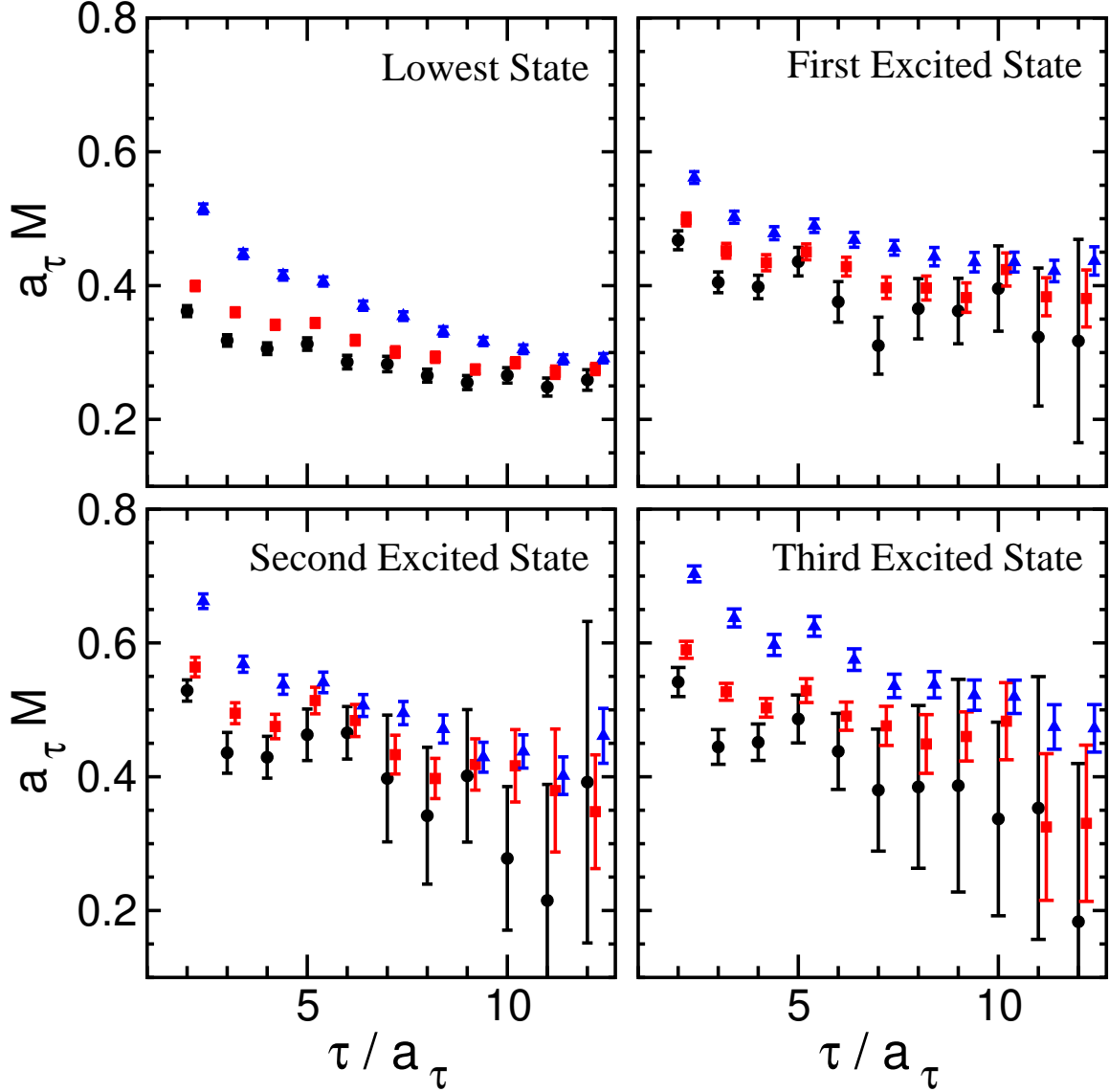


Figure 6.6: The effects of different values of the quark smearing radius σ_s on the excited states. Throughout, stout-link smearing is used with $n_\rho\rho = 2.5, n_\rho = 16$, and $n_\sigma = 32$ quark smearing interactions are used. The black circles have $\sigma_s = 4.0$, the red squares have $\sigma_s = 3.0$, and the blue triangles have $\sigma_s = 2.0$. A Gaussian radius of $\sigma_s = 3.0$ was chosen as a balance between high state contamination vs. stochastic noise in the excited states.

Chapter 7

Baryon operator pruning

At this point, we have constructed a set of gauge-invariant single-site and extended baryon operators endowed with specific momentum, flavor, and (lattice) spin quantum numbers. We have tuned the quark field and gauge link smearing parameters to reduce contamination from high-lying modes, and to reduce the noise in the extended operators. These efforts have rewarded us with a large set of candidate operators which can be used to extract the low-lying baryon spectrum. The numbers of baryon operators of each type which project into the different irreducible representations of O_h^D are given in Table 7.1.

For some set of candidate operators $\{\overline{\mathcal{O}}_i\}$, the Hermitian correlation matrix $C(\tau)$ is the fundamental quantity we estimate using the Monte Carlo method:

$$C_{ij}(\tau) = \langle \Omega | \mathcal{O}_i(\tau) \overline{\mathcal{O}}_j(0) | \Omega \rangle,$$

where we require $\tau > 0$ (c.f. Subsection 2.8.1) and once again assume a sufficiently large spatial extent $T \gg \tau$ and an action which satisfies reflection positivity. The variational

Operator type	Δ^{++}			Σ^+			N^+			Λ^0		
	G_{1g}	H_g	G_{2g}	G_{1g}	H_g	G_{2g}	G_{1g}	H_g	G_{2g}	G_{1g}	H_g	G_{2g}
Single-Site	1	2	0	4	3	0	3	1	0	4	1	0
Singly-Displaced	14	20	6	38	52	14	24	32	8	34	44	10
Doubly-Displaced-I	12	16	4	36	48	12	24	32	8	36	48	12
Doubly-Displaced-L	32	64	32	96	192	96	64	128	64	96	192	96
Triply-Displaced-T	32	64	32	96	192	96	64	128	64	96	192	96
Total	91	166	74	270	487	218	179	321	144	266	477	214

Table 7.1: The numbers of operators of each type which project into each row of the G_{1g} , H_g , and G_{2g} irreps for the Δ^{++} , Σ^+ , N^+ , and Λ^0 baryons. The numbers for the G_{1u} , H_u , and G_{2u} irreps are the same as for the G_{1g} , H_g , and G_{2g} irreps, respectively. The Ξ^0 operators are obtained from the Σ^+ operators by making the flavor exchange $u \leftrightarrow s$. The Ω^- operators are obtained from the Δ^{++} operators by making the flavor replacement $u \rightarrow s$.

method for extracting the excited states discussed in Chapter 2 requires us to solve:

$$C^{-1/2}(\tau_0)C(\tau)C^{-1/2}(\tau_0)u_i = \lambda_i u_i$$

for u_i and λ_i . In this study, we will attempt to extract the first eight excited levels in each irrep channel. If we were to construct a 179×179 correlation matrix for the N^+ (nucleon) G_{1g} channel, then we would have 179 principal correlation functions λ_i , of which we would only be interested in the first eight. Most of the other 171 principal correlation functions would have a negligible signal-to-noise ratio, suggesting that the matrix inversion step

$$C(\tau_0) \rightarrow C^{-1/2}(\tau_0)$$

would most likely fail before we could even solve the eigenvalue problem. Therefore it is infeasible to use all of the candidate operators to construct our correlation matrices. We chose instead to prune our set of candidate operators down to sixteen operators in each O_h^D irrep before attempting to extract the excited states in those channels using the variational method. We feel that this number provides a good balance between the need to use a large enough set of operators to reliably extract the states of interest, and the need to use a small enough set of operators such that the matrix inversions are not adversely affected by noise.

Additionally, for each irrep we used the same candidate operators for the even and odd-parity channels (G_{1g}/G_{1u} , H_g/H_u , G_{2g}/G_{2u}). This requirement allows us to improve our estimates of the correlation matrix elements by averaging with the backward propagating state information in the opposite-parity channel (discussed in Subsection 5.1.3). The two criteria we used to prune our operators were *signal quality* and *linear independence*. For this work, we focused on the N^+ (nucleon) channel.

7.1 Signal quality

We first calculated the effective mass function associated with each nucleon operator $\overline{\mathcal{O}}_i$ using 200 quenched configurations. These effective mass functions required Monte Carlo estimates of only the diagonal elements of the nucleon correlation matrices for each irrep:

- N^+ G_{1g}/G_{1u} matrices: 179 diagonal elements,
- N^+ H_g/H_u matrices: 321 diagonal elements,
- N^+ G_{2g}/G_{2u} matrices: 144 diagonal elements.

The 175 three-quark propagators we generated to construct these elements were saved for reuse in our subsequent pruning steps.

At this pruning stage, we wanted to select operators of each type which had a high quality signal. It is reasonable to assume that linear combinations of ‘quiet’ operators would yield

superior results over linear combinations of noisy operators. Examples of quiet vs. noisy operators are shown in Figure 7.1. Our measure of signal quality was the effective mass function’s jackknife error averaged over $\tau = 1, \dots, 16$. The consideration of average error rather than the signal-to-noise ratio facilitates a direct comparison between the different operators.

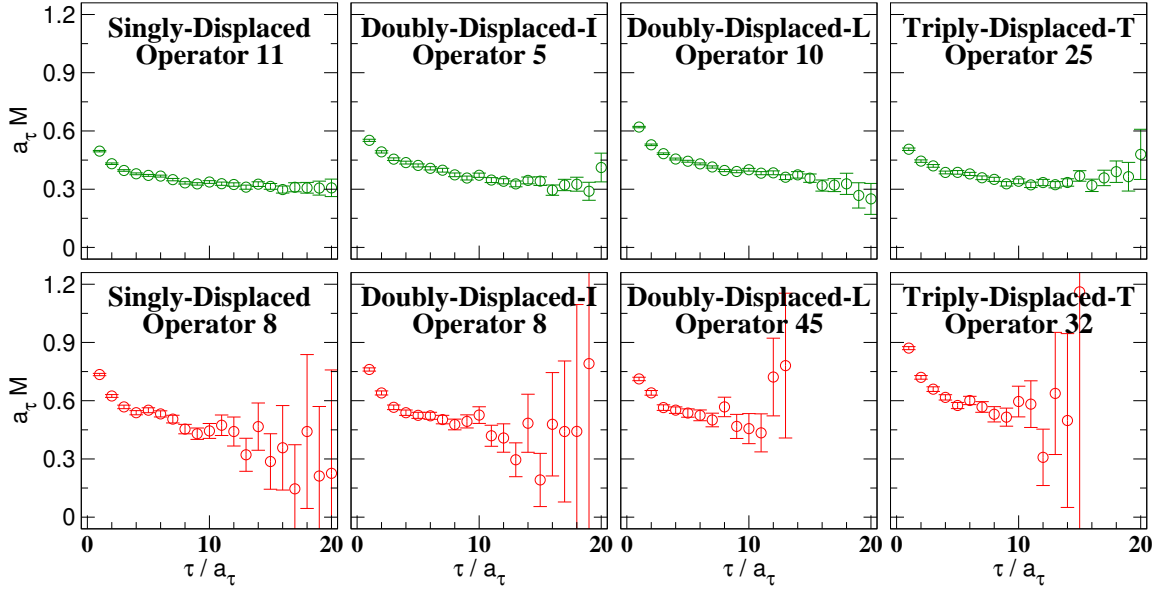


Figure 7.1: Effective mass plots for eight representative operators from the complete set of extended baryon operators in the G_{1u} channel. We chose up to ten candidate operators of each type (SD, DDI, DDL, TDT) based on the average jackknife error over the first sixteen time slices. This process helped us to identify ‘quiet’ operators (top row, in green) and remove some of the noisier operators (bottom row, in red).

Because there are three single-site type operators in the G_{1g}/G_{1u} channels, one in the H_g/H_u channels, and none in the G_{2g}/G_{2u} channels, we selected all single-site operators. Within each type of extended operator (singly-displaced, doubly-displaced-I, doubly-displaced-L, and triply-displaced-T), we sorted the operators in increasing order of the average jackknife error over the first sixteen non-zero time separations: $\tau = 1, \dots, 16$ and selected the first ten operators. At this point, we have selected all of the single-site operators and ten extended operators of each type in each irrep. For each operator selected in each even-parity channel, we also selected its opposite-parity partner in the odd-parity channel, and vice-versa. We performed the signal quality selection each extended operator type *separately* to ensure that we still had a representative set of operators of each type. We did not want noise to be the only factor in the selection process; we are primarily interested in the ability of an operator to interpolate for the excited states of interest.

7.2 Linear independence

We had eliminated our noisiest operators, but still had over forty candidate operators in each channel. We pruned our operators further by looking for subsets of operators which excited Hilbert states which were as distinct as possible. We considered such operators likely to perform well in the variational method because they would give a more nearly orthogonal trial state basis.

7.2.1 The normalized correlation matrix

We would like to select a subset of operators such that the corresponding states are as distinct as possible. To enable valid comparisons among our candidate operators $\{\overline{\mathcal{O}}_i\}$, we considered the *normalized*¹ Hermitian correlation matrix elements \hat{C}_{ij} defined in terms of $C_{ij}(\tau = a_\tau)$:

$$\begin{aligned}\hat{C}_{ij} &\equiv \frac{C_{ij}(a_\tau)}{\sqrt{C_{ii}(a_\tau)C_{jj}(a_\tau)}}, \\ &= \frac{\langle \Omega | \mathcal{O}_i e^{-Ha_\tau} \overline{\mathcal{O}}_j | \Omega \rangle}{\sqrt{\langle \Omega | \mathcal{O}_i e^{-Ha_\tau} \overline{\mathcal{O}}_i | \Omega \rangle \langle \Omega | \mathcal{O}_j e^{-Ha_\tau} \overline{\mathcal{O}}_j | \Omega \rangle}}\end{aligned}$$

remembering that the diagonal correlation matrix elements $C_{ii}(\tau)$ and $C_{jj}(\tau)$ are real and positive for $\tau \neq 0$. As in Subsection 2.8.1, we avoid expressions involving the correlation matrix evaluated at $\tau = 0$ due to the presence of Schwinger terms.

7.2.2 Pruning by condition number

For any set of n candidate operators $\{\overline{\mathcal{O}}_1, \overline{\mathcal{O}}_2, \dots, \overline{\mathcal{O}}_n\}$, we have $\hat{C}_{ii} = 1 \ \forall \ i$. In particular:

$$\text{Tr}(\hat{C}) = n.$$

If all of the states created by our candidate operators were orthogonal, then $\hat{C}_{ij} = \delta_{ij}$, which implies that all of the eigenvalues of \hat{C} are equal to one. In contrast, if two of the states were identical, then $\det(\hat{C}) = 0$, implying that at least one of the eigenvalues of \hat{C} is equal to zero. In order for maintain $\text{Tr}(\hat{C}) = n$, at least one of the other eigenvalues must therefore be greater than one.

Because our matrix is Hermitian, its eigenvalues are guaranteed to be real. We therefore choose as our measure of the degree of linear independence of our operators the *condition*

¹In this section we will use a hat to denote the normalized correlation matrix. This is not to be confused with the hat notation of Chapter 3.

number κ , the ratio of the largest to smallest eigenvalue of the normalized correlation matrix \hat{C} :

$$\kappa \equiv \lambda_{\max}/\lambda_{\min} \geq 1.$$

For perfectly orthogonal states $\kappa = 1$ and for completely degenerate states $\kappa \rightarrow \infty$. We therefore seek to find a subset of operators in each irrep such that the condition numbers of the associated even and odd correlation matrices satisfy some minimization condition. Selecting a correlation submatrix having a small condition number has another advantage: small condition numbers lead to the rapid convergence of matrix inversion algorithms [GL89].

7.2.3 Linear independence within each operator type

We proceeded by calculating all correlation matrix elements having the same type of extended operator at the source and sink. We reused the previously generated three-quark propagators for the diagonal elements, and generated the additional three-quark propagators needed for the off-diagonal elements.

For each correlation matrix, we calculated the condition numbers of all possible 5×5 submatrices using the singular value decomposition algorithm [PFTV92]. Because we wanted to select the same operators in both the even and odd-parity channels, we proceeded as follows for each irrep and operator type separately:

- Let x denote a subset of five extended operators of a specific type (i.e. all SD or all DDL):

$$x \equiv \{\overline{\mathcal{O}}_{i_1}, \overline{\mathcal{O}}_{i_2}, \dots, \overline{\mathcal{O}}_{i_5}\}.$$

- Let $\kappa^g(x)$ and $\kappa^u(x)$ be the condition numbers of the even and odd-parity correlation submatrices corresponding to the operator subset x , respectively².
- Let $\kappa_{>}(x) \equiv \max(\kappa^g(x), \kappa^u(x))$, the larger of the even and odd-parity condition numbers.
- We selected the operator set x^* which minimized $\kappa_{>}(x)$:

$$\kappa_{>}(x^*) = \min_x(\kappa_{>}(x)) = \min_x(\max(\kappa^g(x), \kappa^u(x))).$$

By minimizing the larger of the even and odd-parity condition numbers, we found a reasonably distinct set of operators across both the even and odd-parity channels. As a check of our results, we examined the smallest eigenvalue λ_{\min} of our selected submatrix to verify that it was much greater than its jackknife error, avoiding the possibility of signal-to-noise issues.

²Remember, we had selected the same operators for both the even and odd-parity channels during our signal quality pruning step.

A natural question which arises during the application of this method is: how much did we lose by requiring that the even and odd-parity channels of each irrep contain the same operators? In order to ensure that we were not sacrificing too much, we calculated the percent deviation of the condition number from the minimum possible condition number for the even and odd-parity channels separately:

$$\frac{\kappa^g(x^*) - \min_x(\kappa^g(x))}{\min_x(\kappa^g(x))}, \quad \frac{\kappa^u(x^*) - \min_x(\kappa^u(x))}{\min_x(\kappa^u(x))}.$$

We found that all of these percentages were below 20%, and most were below 5%. The extended operator results are shown in Table 7.2. Once again, we selected all single-site operators.

Operator type	G_{1g}	G_{1u}	H_g	H_u	G_{2g}	G_{2u}
Singly-Displaced	12.96(21) 3%	12.90(18) 10%	1.6972(58) 3%	1.6920(59) 0%	5.74(14) 0%	5.46(16) 0%
Doubly-Displaced-I	3.849(30) 1%	3.477(28) 7%	1.2956(32) 0%	1.2907(32) 0%	2.922(18) 1%	2.842(21) 0%
Doubly-Displaced-L	10.70(16) 18%	10.32(13) 12%	4.157(27) 16%	3.894(27) 0%	1.697(16) 0%	1.712(17) 0%
Triply-Displaced-T	4.209(42) 4%	4.048(48) 5%	1.7796(95) 0%	1.9163(89) 0%	1.744(12) 4%	1.856(13) 2%

Table 7.2: The condition numbers κ and for the 5×5 extended operator submatrices chosen. The percentages denote how much greater each condition number is than its minimum possible value.

7.2.4 Linear independence across operator types

In the previous pruning step, we selected all single-site operators and five extended operators of each type by considering correlation matrix elements between operators of the same type. We next considered correlation matrix elements between operators of *different* types. The total number of three-quark propagators needed was 671. Once again we reused previously generated three-quark propagators when possible, and generated the additional three-quark propagators needed.

After normalizing the correlation matrices, we took the best 16×16 submatrix according to the condition number minimization condition presented in the last subsection. Combining the five operators selected from each of the four types with the single-site operators gave the following correlation matrix sizes and submatrix numbers for each channel:

- N^+ G_{1g}/G_{1u} matrices: 23×23 elements and 245, 157 submatrices,
- N^+ H_g/H_u matrices: 21×21 elements and 20, 349 submatrices,

- N^+ G_{2g}/G_{2u} matrices: 20×20 elements and 4,845 submatrices,

where each submatrix has 16×16 elements.

The condition numbers corresponding to the final selected set of sixteen candidate operators are presented in Table 7.3, and the new operator number information for our final set of sixteen operators is presented in Table 7.4. The operator identification numbers used in our programs are given in Appendix 8.6. For completeness, the effective mass plots of the operators as calculated from the diagonal correlation matrix elements are shown in Figures 7.2, 7.3, 7.4, 7.5, 7.6, and 7.7. We also examined the principal effective plots to ensure that our selected operators interpolated well for the excited states (see Chapter 8).

Irrep	κ	$(\kappa - \kappa_{\min})/\kappa_{\min}$
G_{1g}	68.5(1.5)	0%
G_{1u}	63.85(68)	4%
H_g	53.57(84)	6%
H_u	50.09(67)	0%
G_{2g}	58.61(76)	0%
G_{2u}	56.5(2.3)	3%

Table 7.3: The condition numbers κ for the 16×16 final operator submatrices chosen. The percentages denote how much greater each condition number is than its minimum possible value. The operators in each odd-parity irrep are the opposite-parity partners of the operators in the corresponding even-parity irrep.

Operator type	N^+		
	G_{1g}/G_{1u}	H_g/H_u	G_{2g}/G_{2u}
Single-Site	1	0	0
Singly-Displaced	3	3	4
Doubly-Displaced-I	5	3	3
Doubly-Displaced-L	2	5	4
Triply-Displaced-T	5	5	5
Total	16	16	16

Table 7.4: The numbers of N^+ operators of each type which are used in each correlation matrix. The operators selected in the G_{1u} , H_u and G_{2u} irreps are the same as those selected for the G_{1g} , H_g , and G_{2g} irreps, respectively.

G_{1g} Effective Masses

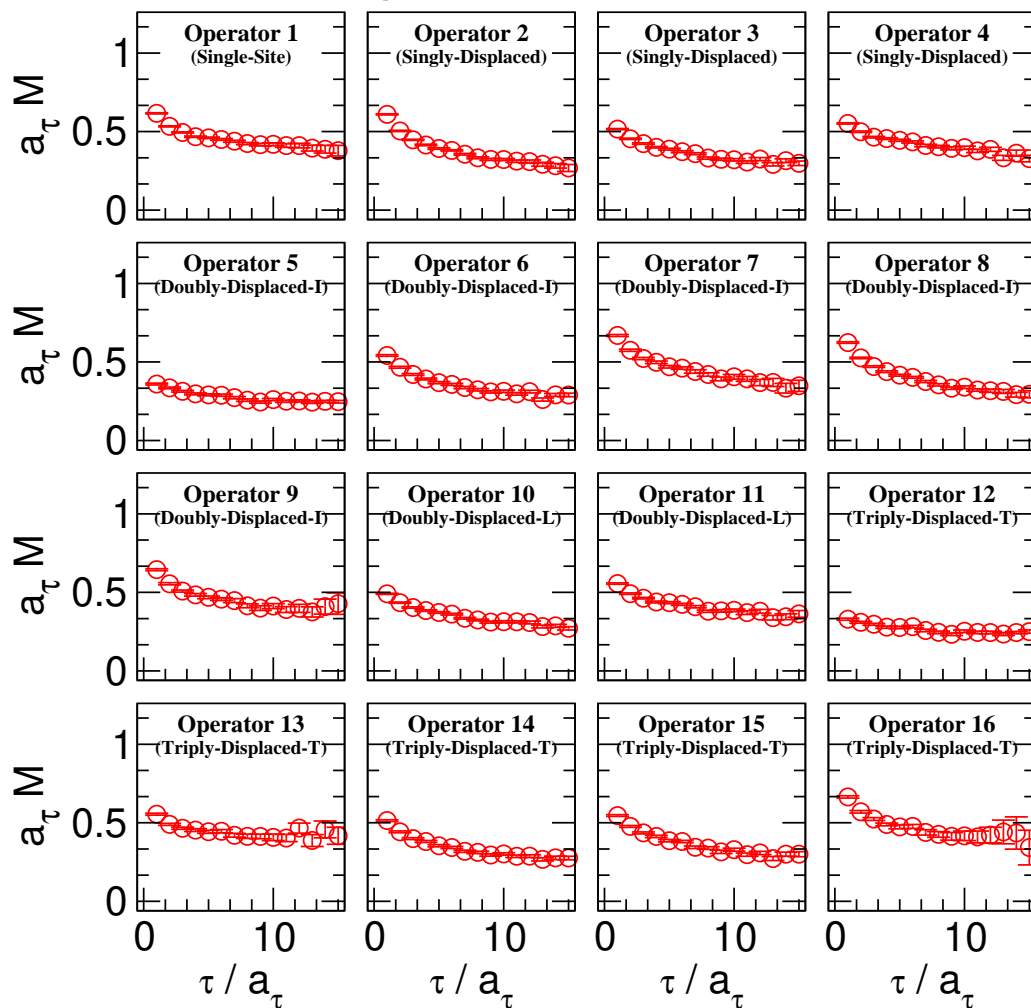


Figure 7.2: The effective masses for the final sixteen G_{1g} operators selected by our pruning process.

H_g Effective Masses

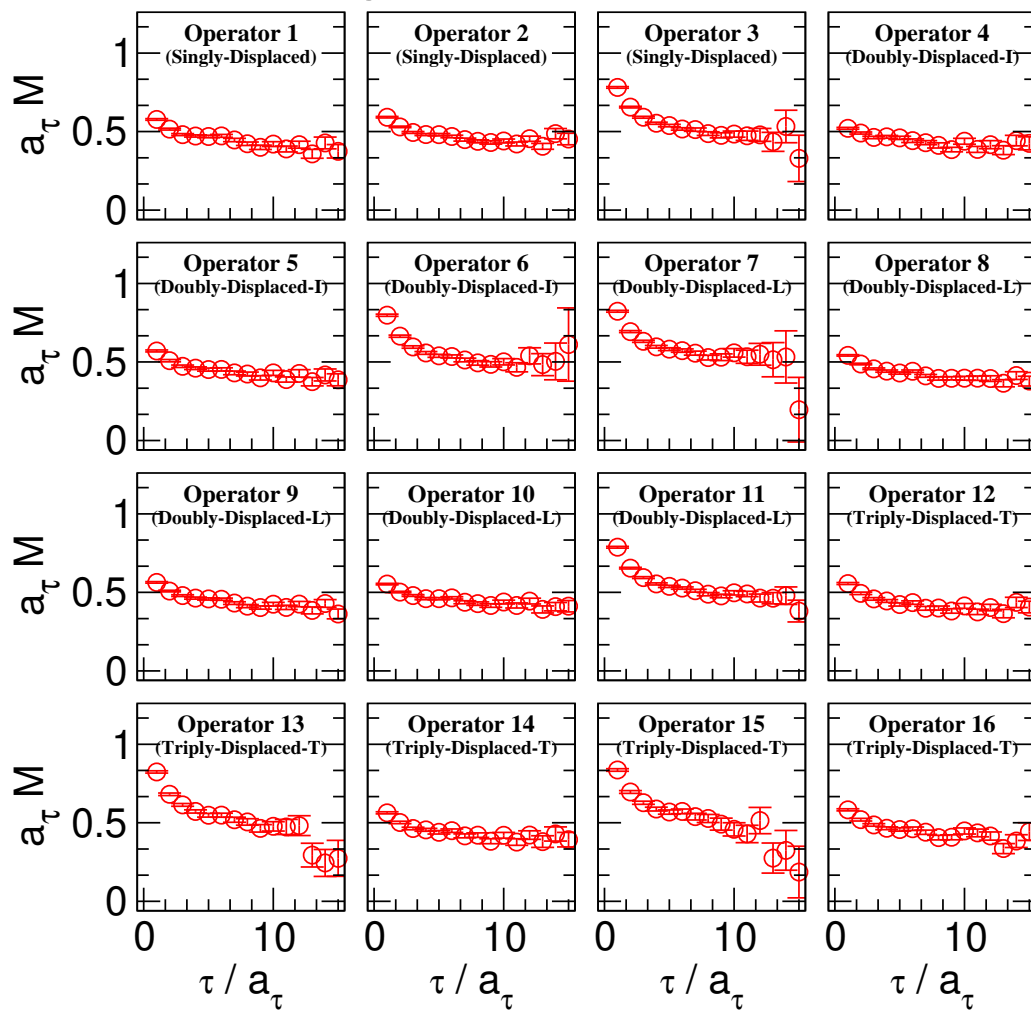


Figure 7.3: The effective masses for the final sixteen H_g operators selected by our pruning process.

G_{2g} Effective Masses

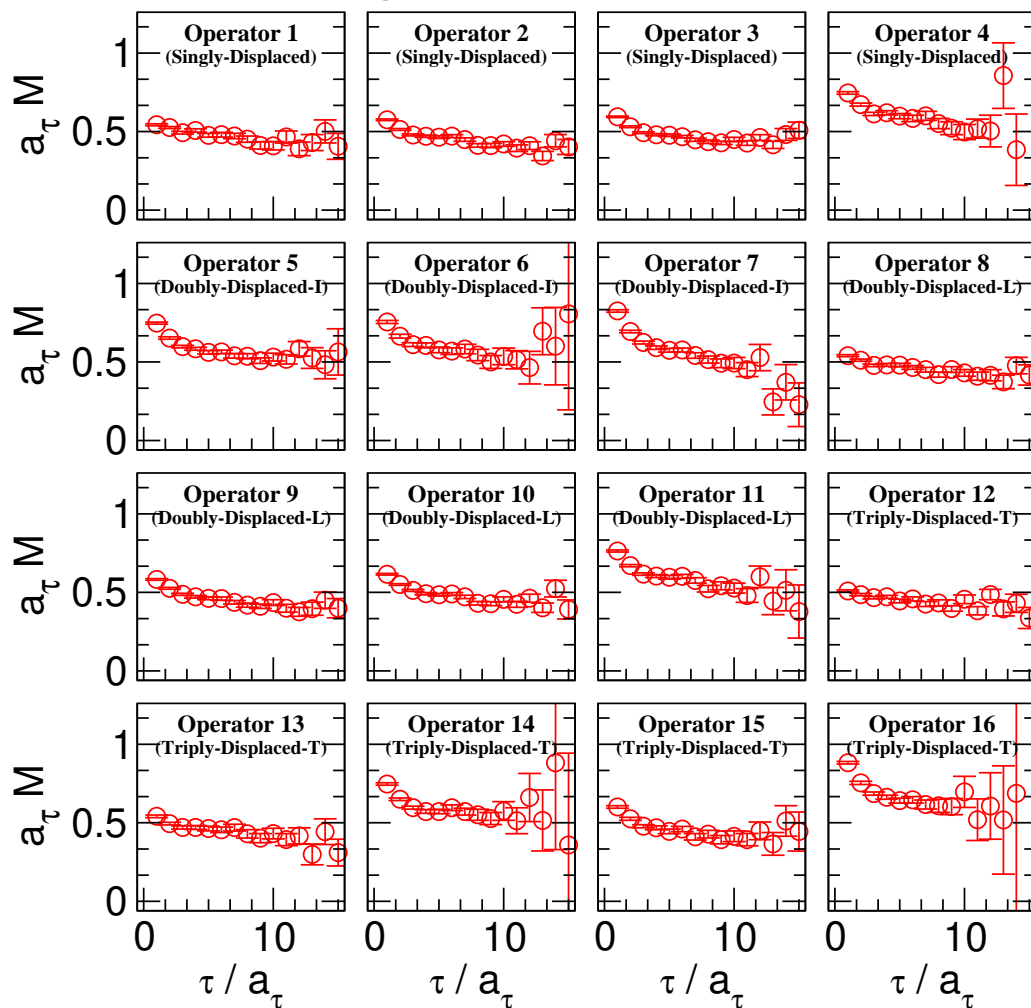


Figure 7.4: The effective masses for the final sixteen G_{2g} operators selected by our pruning process.

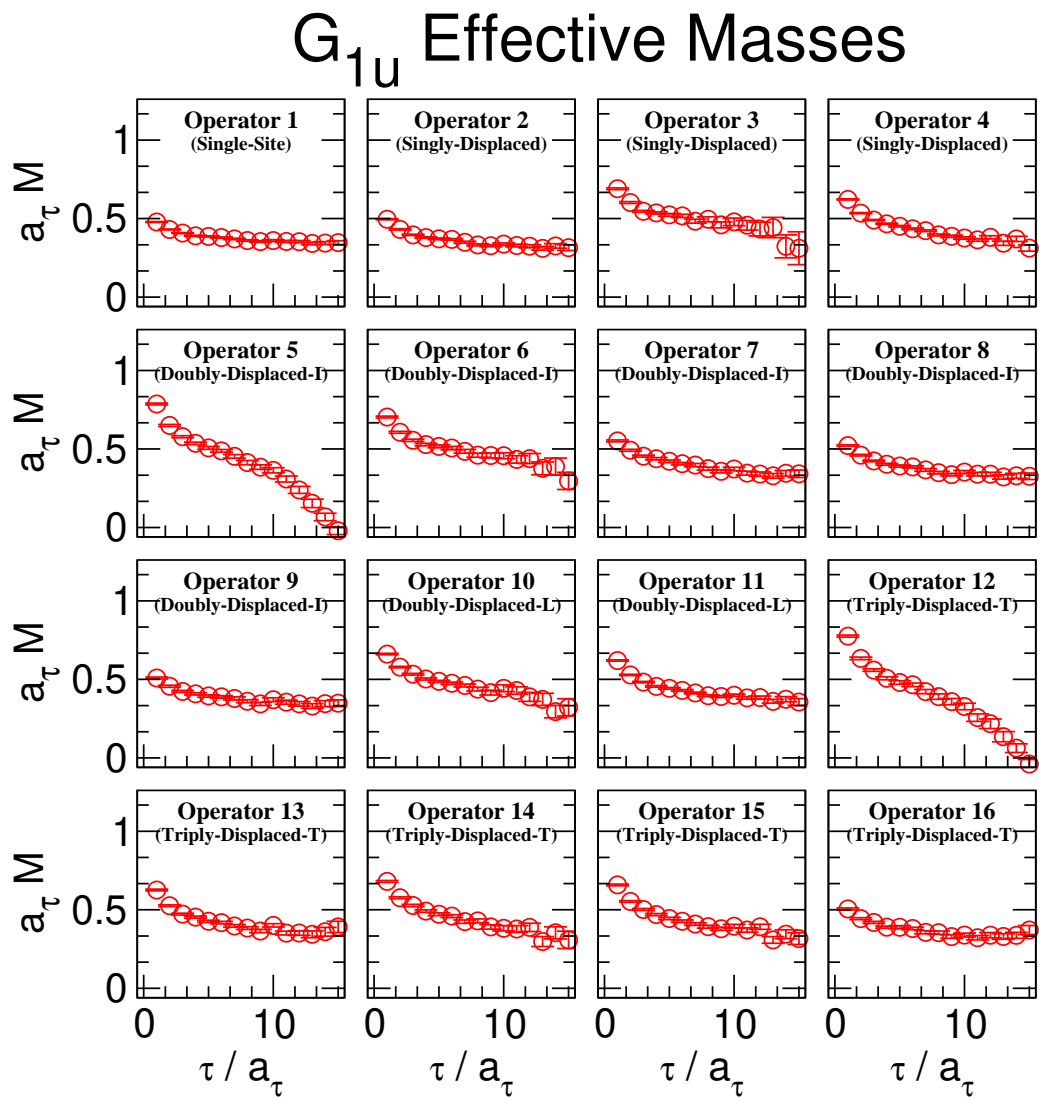


Figure 7.5: The effective masses for the final sixteen G_{1u} operators selected by our pruning process.

H_u Effective Masses

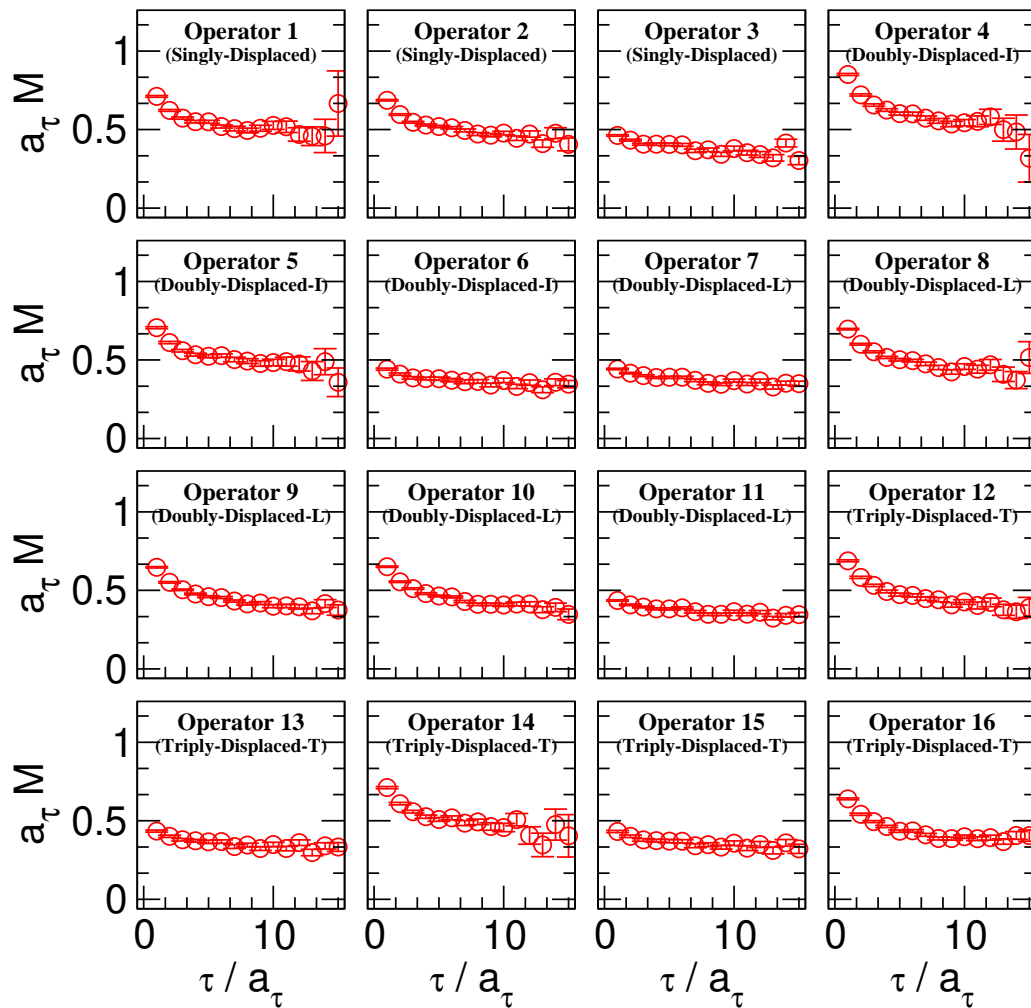


Figure 7.6: The effective masses for the final sixteen H_u operators selected by our pruning process.

G_{2u} Effective Masses

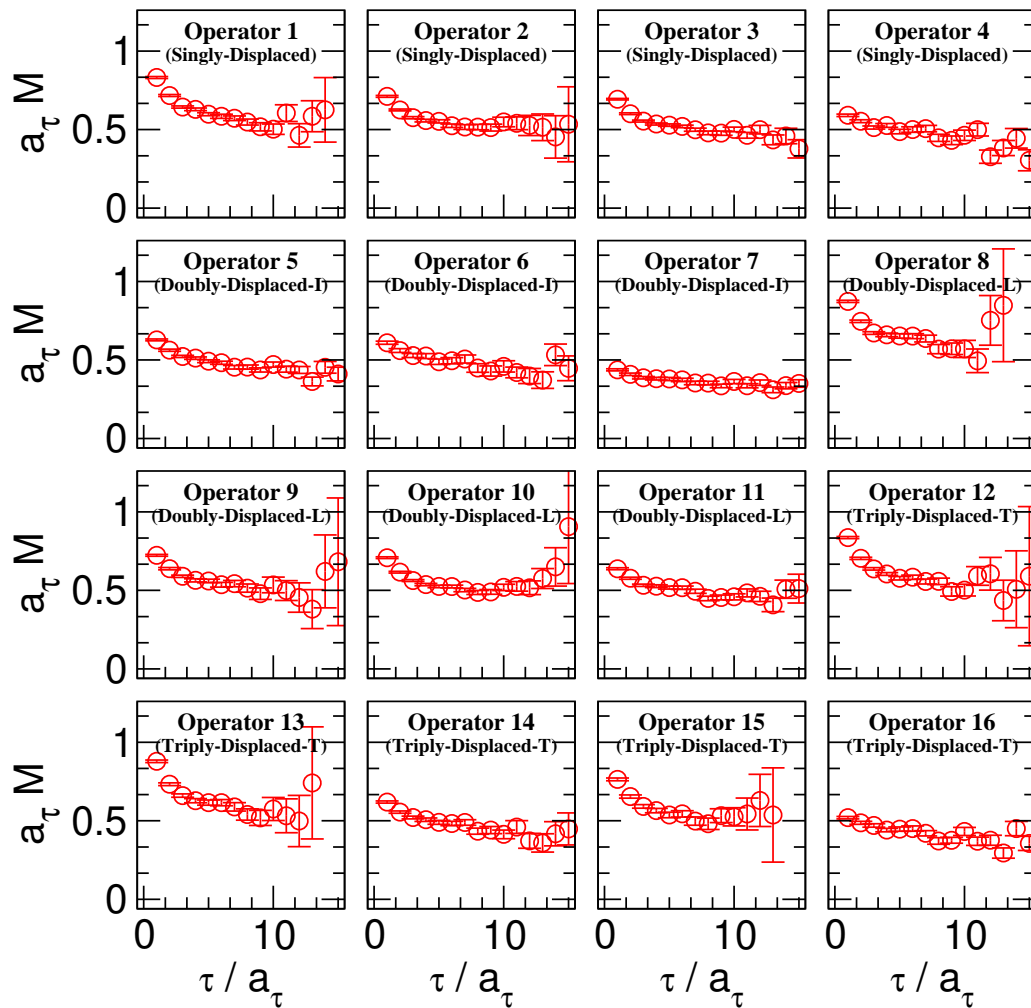


Figure 7.7: The effective masses for the final sixteen G_{2u} operators selected by our pruning process.

Chapter 8

Baryon operator results: The nucleon spectrum

Now that we have selected sixteen candidate nucleon operators $\{\bar{\mathcal{O}}_1, \bar{\mathcal{O}}_2, \dots, \bar{\mathcal{O}}_{16}\}$ in each O_h^D irreducible representation, we conclude this work by extracting the lowest eight energy levels in the $G_{1g}, H_g, G_{2g}, H_u,$ and G_{2u} nucleon channels, and the lowest seven energy levels in the G_{1u} nucleon channel¹.

8.1 Fixed-coefficient correlation functions

In each O_h^D irrep channel, we evaluated the elements of a 16×16 correlation matrix $C(\tau)$ on 200 quenched configurations. Our next step was to apply the variational method discussed in Subsection 2.8.1 to find linear combinations of operators

$$\bar{\Theta}_i \equiv \sum_{a=1}^{16} \bar{\mathcal{O}}_a v_{ai},$$

which couple strongly to single (distinct) states of interest and weakly to the other states. In other words, we are looking for fixed coefficient vectors v_i such that:

$$\begin{aligned} \langle \Theta_k(\tau) \bar{\Theta}_k(0) \rangle &= \sum_{a,b=1}^{16} v_{ak}^* C_{ab}(\tau) v_{bk} \equiv v_k^\dagger C(\tau) v_k, \\ &\approx |\langle k | \bar{\Theta}_k | \Omega \rangle|^2 e^{-E_k \tau}, \quad \tau_{\min} \leq \tau \leq \tau_{\max}, \end{aligned} \tag{8.1}$$

where $[\tau_{\min}, \tau_{\max}]$ specifies the range of τ values over which the single-exponential approximation is valid. It is not guaranteed that such a range exists, but this simple

¹We were unable to find a fit range which gave a satisfactory estimate for the 8th excited state in the G_{1u} channel

approach served us well in this exploratory study². A more sophisticated approach would attempt to take into account some of the exponential contamination terms neglected by this approximation.

If we solve

$$[C^{-1/2}(\tau_0)C(\tau)C^{-1/2}(\tau_0)] u_i(\tau, \tau_0) = \lambda_i(\tau, \tau_0)u_i(\tau, \tau_0),$$

for $u_i(\tau, \tau_0)$ and $\lambda_i(\tau, \tau_0)$, where τ_0 is a fixed reference time (we chose $\tau_0 = a_\tau$ in this work), then the principal correlation functions $\lambda_i(\tau, \tau_0)$ behave as:

$$\begin{aligned} \lim_{\tau \rightarrow \infty} \lambda_k(\tau, \tau_0) &= e^{-E_k(\tau - \tau_0)}(1 + O(e^{-\Delta_k(\tau - \tau_0)})), \\ \Delta_k &\equiv \min_{l \neq k} |E_l - E_k|, \end{aligned}$$

where the E_k are the energies of the first n states accessible from the vacuum by the action of our trial candidate operators $\{\bar{\mathcal{O}}_a\}$. The eigenvectors $u_i(\tau, \tau_0)$ may be chosen to be orthonormal, in which case we may write the principal correlation functions as:

$$\lambda_i(\tau, \tau_0) = u_i^\dagger(\tau, \tau_0) [C^{-1/2}(\tau_0)C(\tau)C^{-1/2}(\tau_0)] u_i(\tau, \tau_0). \quad (8.2)$$

Comparing Eqn. 8.2 to Eqn. 8.1, we see that a reasonable choice for the fixed coefficient vector v_i is:

$$v_i = C^{-1/2}(\tau_0)u(\tau^*, \tau_0),$$

where τ^* is some fixed time. We found that our estimates for v_i stabilized around $\tau^* = 3a_\tau$, which signaled the reduction of contamination coming from the higher-lying levels. The chosen value of $\tau^* = 3a_\tau$ was also small enough to ensure that our estimate for the fixed coefficient vectors v_i was based on data having a good signal-to-noise ratio³.

Our *fixed-coefficient* correlation functions were therefore given by the diagonal elements of the rotated correlation matrix, which is denoted by $\tilde{C}(\tau)$:

$$\begin{aligned} \tilde{C}_{kk}(\tau) &\equiv \langle \Theta_k(\tau) \bar{\Theta}_k(0) \rangle \\ &= v_k^\dagger C(\tau) v_k \\ &= u_k^\dagger(\tau = 3a_\tau, \tau_0 = a_\tau) [C^{-1/2}(a_\tau)C(3a_\tau)C^{-1/2}(a_\tau)] u_k(\tau = 3a_\tau, \tau_0 = a_\tau). \end{aligned}$$

These fixed-coefficient correlation functions can be used to define fixed-coefficient effective mass functions

$$a_\tau \tilde{M}_k(\tau) = \ln \left[\frac{\tilde{C}_{kk}(\tau)}{\tilde{C}_{kk}(\tau + a_\tau)} \right]$$

²We found that two-exponential fits to our rotated correlation matrix elements $v_i^\dagger C(\tau) v_j$ had inferior stability and errors when compared to our single-exponential fit results. The reason for this seems to be our effective removal of contamination from the correlation matrix (e.g. see Figure 8.3)

³The signal-to-noise ratio of Monte Carlo estimates of $C(\tau)$ decays exponentially with τ for baryon correlation functions [Lep]

8.2 Fitting range

Our next task was to find the range $[\tau_{\min}, \tau_{\max}]$ (if any) within which the fixed-coefficient correlation functions $\tilde{C}_{kk}(\tau) = v_k^\dagger C(\tau) v_k$ behave as single exponentials:

$$\tilde{C}_{kk}(\tau) \approx |\langle k | \bar{\Theta}_k | \Omega \rangle|^2 E^{-E_k \tau},$$

and within which the off-diagonal elements of the rotated correlation matrix $\tilde{C}_{ij}(\tau) = v_i^\dagger C(\tau) v_j$ are consistent with zero:

$$\tilde{C}_{ij}(\tau) \approx 0, \quad i \neq j.$$

The vanishing of the off-diagonal elements tells us that any plateaus we observe in our effective mass plots (within that range) correspond to orthogonal states.

8.2.1 Diagonal elements

In Chapter 5, we discussed the fact that correlation functions will receive contamination from the backward propagating states. Because chiral symmetry is spontaneously broken, the backward propagating states will have different masses than the forward propagating states:

$$\begin{aligned} \tilde{C}_{kk}^{(g)}(\tau) &= \tilde{C}_{kk}^{(u)}(T - \tau), \text{ but} \\ \tilde{C}_{kk}^{(g)}(\tau) &\neq \tilde{C}_{kk}^{(g)}(T - \tau), \end{aligned}$$

and similarly for the odd-parity correlation functions. $T = a_\tau N_\tau$ denotes the temporal extent of our lattice.

A sophisticated fitting approach would seek to fit the elements of $\tilde{C}(\tau)$ and $\tilde{C}(T - \tau)$ simultaneously using independent parameters. The collaboration is currently working to develop such a fitting package to use with the production run data. For this work, we performed single-exponential fits to the diagonal elements of the rotated correlation matrix, neglecting the backward propagating state effects.

In order to get a rough idea of when the backward propagating state contamination becomes significant, we can plot the effective mass function for a *trial* correlation function of the form:

$$C_{\text{trial}}(\tau) = e^{-m\tau} + e^{-m(T-\tau)}.$$

This simple form assumes the same mass for both the forward and backward propagating states, and a coefficient of one for both terms.

The associated effective mass is:

$$a_\tau M(\tau) = \ln \left[\frac{C_{\text{trial}}(\tau)}{C_{\text{trial}}(\tau + a_\tau)} \right], \quad (8.3)$$

$$= \ln \left[\frac{e^{-m\tau} + e^{-m(T-\tau)}}{e^{-m(\tau+a_\tau)} + e^{-m(T-(\tau+a_\tau))}} \right], \quad (8.4)$$

$$= a_\tau m + \ln \left[\frac{1 + e^{-a_\tau m(N_\tau - 2\tau/a_\tau)}}{1 + e^{-a_\tau m(N_\tau - 2(\tau/a_\tau + 1))}} \right], \quad (8.5)$$

and is plotted in Figure 8.1. For our lattice, $N_\tau = 48$ and the lowest level seen in our preliminary principal effective mass plots belonged to a G_{1g} state having $a_\tau m \approx 0.24$ (identified as the proton). From Figure 8.1 we conclude that in the (worst case) scenario in which our backward propagating state is the proton, we will begin to see backward propagating state contamination at

$$\tau_{\text{max}} \approx 20a_\tau,$$

a value which is comparable to the threshold at which our signal-to-noise ratio has degraded below acceptable levels for a fit (e.g. see Figure 8.3).

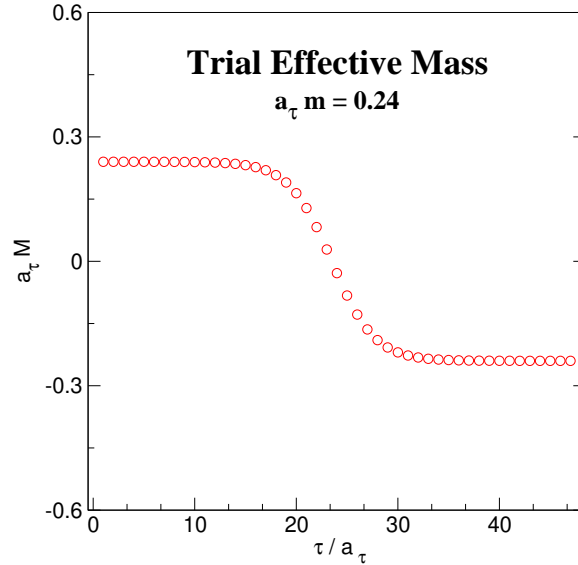


Figure 8.1: The effective mass function for the trial correlation function $C(\tau) = e^{-m\tau} + e^{-m(T-\tau)}$. The number of lattice sites in the temporal direction is $N_\tau = 48$, and the lowest baryon state is taken to be $a_\tau m = 0.24$. The backward propagating state significantly contaminates the effective mass function at times greater than $\tau \approx 20a_\tau$.

8.2.2 Off-diagonal elements

The fixed-coefficient correlation functions $\tilde{C}_{kk}(\tau)$ differ from the principal correlation functions $\lambda_k(\tau, \tau_0)$ because we are only solving the eigenvalue problem once, at $\tau^* = 3a_\tau$.

Thus, we are only guaranteed orthogonality at $\tau^* = 3a_\tau$:

$$\tilde{C}_{ij}(\tau^*) = 0 \quad \forall i \neq j.$$

The lack of orthogonality for $\tau > \tau^*$, no matter how small, means that our fixed-coefficient correlation functions will eventually relax to the lowest excited state

$$\tilde{C}_{kk}(\tau) \xrightarrow{\tau \gg \tau^*} |c_1|^2 \exp(-E_1 \tau).$$

Consequently, we seek a range of τ values over which

$$|\tilde{C}_{ij}(\tau)|^2 = 0 \quad \forall i \neq j$$

within errors. This would imply that the v_i coefficient vectors are good estimates for the coefficients of operators which excite orthogonal states, and would verify that we are not excluding too much information by ignoring the off-diagonal elements in our fits. We found that this is indeed the case for τ values less than $\tau \approx 30a_\tau$. An example of one such off-diagonal element is shown in Figure 8.2.

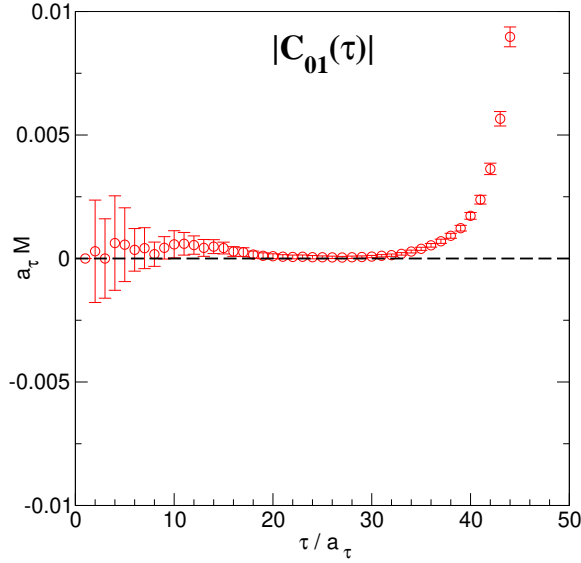


Figure 8.2: An example of an off-diagonal element of the rotated correlation matrix $\tilde{C}_{ij}(\tau) = v_i^\dagger C(\tau) v_j$ having $i = 0$ and $j = 1$. Because we are using fixed coefficients to rotate the matrix, we are unable to maintain the orthogonality of the states at all times τ . Here we see that we can safely work with the fixed-coefficient correlation functions until $\tau \approx 30a_\tau$. After that, they all relax to the lowest excited state: $\tilde{C}_{kk}(\tau) \rightarrow |c_1|^2 \exp(-E_1 \tau)$.

Considering the backward propagating state contamination along with the orthogonality of the fixed-coefficient correlation functions, we decided to require all of our fit ranges to lie within

$$\tau_{\min} = a_\tau, \quad \tau_{\max} = 20a_\tau.$$

In performing our fits (discussed below), we found that noise was the limiting factor for signal quality past $\tau \approx 17a_\tau$.

8.3 Fit method

To estimate the value of an energy level $a_\tau E_k$, we fit directly to the fixed-coefficient correlation function, not the principal correlation function or any effective mass function⁴. Fitting to correlation functions directly is simpler and introduces less noise into the process.

8.3.1 Correlated χ^2 fitting

In this study, we performed a single-exponential correlated χ^2 fit to the fixed-coefficient correlation functions. We fit each fixed-coefficient correlation function $\tilde{C}_{kk}(\tau)$ independently. For simplicity in notation, we consider one such fixed-coefficient correlation function and denote it by $C(\tau)$ for the remainder of this subsection. We note that $C(\tau)$ is a function in this subsection, not a matrix.

The particular form of our fitting function was

$$C_{\text{fit}}(\tau, A, a_\tau E_{\text{fit}}) = A \exp(-a_\tau E_{\text{fit}}(\tau/a_\tau)),$$

where A and $a_\tau E_{\text{fit}}$ are the two fit parameters. This simple form does not take into account the periodicity of the lattice; we required our fit ranges to lie within $\tau_{\text{min}} = a_\tau$ and $\tau_{\text{max}} = 20a_\tau$ to avoid the effects of backward propagating state contamination.

In our correlated χ^2 fit, χ^2 is given by

$$\chi^2(A, a_\tau E_{\text{fit}}) \equiv \sum_{\tau, \tau'} [C(\tau) - C_{\text{fit}}(\tau, A, a_\tau E_{\text{fit}})] \sigma_{\tau, \tau'}^{-1} [C(\tau') - C_{\text{fit}}(\tau', A, a_\tau E_{\text{fit}})] \quad (8.6)$$

where $\sigma_{\tau, \tau'}^{-1}$ is the inverse of the covariance matrix:

$$\sigma_{\tau, \tau'} \equiv \frac{1}{N(N-1)} \sum_{n=1}^{200} [C_n(\tau) - \bar{C}(\tau)][C_n(\tau') - \bar{C}(\tau')], \quad (8.7)$$

where $C_n(\tau)$ is the value of $C(\tau)$ evaluated the n^{th} configuration, and

$$\bar{C}(\tau) \equiv \frac{1}{200} \sum_{n=1}^{200} C_n(\tau).$$

The covariance matrix $\sigma_{\tau, \tau'}$ measures the amount of correlation between measurements at τ and τ' .

We used the Levenberg-Marquardt [PFTV92] non-linear fitting algorithm to find the values of A and $a_\tau E_{\text{fit}}$ which minimized our χ^2 . To estimate the uncertainty in our fit values, we

⁴We denote our energy levels by $a_\tau E_k$ because some may be multi-hadron states.

first generated 2048 bootstrap samples of size 200 by sampling randomly with replacement from the original set of 200 rotated correlation matrices. We repeated our single exponential fit (using the same fit range) on each bootstrap sample, and used the standard deviation of the resulting set of fit parameters as our uncertainty. We also calculated upper and lower limits for our plots using the percentile method [Efr82]. The upper limit of a fit parameter is chosen such that 84.1% of the bootstrap sample values lie below it. Similarly, the lower limit is chosen corresponding to a percentile of 15.9%. If the fit parameters are distributed normally across bootstrap samples, then the upper and lower limits correspond to the estimate plus and minus one standard deviation, respectively. We found no significant asymmetry in our fit error bars.

For each fixed-coefficient correlation function separately, we chose our fit range to make the χ^2 per degree of freedom close to 1.0, and to make the quality factor Q as large as possible (> 0.1 was desirable).

We examined the sensitivity of our fits as we increased or decreased the fit range as a check of the quality of our results. We also explored the possibility of adding a second exponential term to model some of the high-lying contamination, but those fits performed poorly compared to the single exponential method.

8.3.2 Fitting walk-through

In summary, the exact method we used to analyze our correlation matrices for each irrep in $G_{1g}, H_g, G_{2g}, G_{1u}, H_u, G_{2u}$ is as follows (using $\tau_0 = \tau_{\min} = a_\tau$, $\tau^* = 3a_\tau$, $\tau_{\max} = 20a_\tau$, $T = a_\tau N_\tau$, and $N_\tau = 48$):

1. Average the correlation matrix elements over all 200 configurations to form the best estimates for the elements of $C(\tau)$ using the improved estimation method discussed in Chapter 3:

$$C_{ab}^{(p)}(\tau) = \frac{1}{200} \sum_{n=1}^{200} \frac{1}{4} \left[C_{ab,n}^{(p)}(\tau) + C_{ba,n}^{(1-p)}(T - \tau) + C_{ba,n}^{(p)*}(\tau) + C_{ab,n}^{(1-p)*}(T - \tau) \right],$$

where $C_{ab,n}^{(p)}(\tau)$ is a correlation matrix element measured on the n^{th} configuration generated by the Markov chain (see Chapter 3), and $p = 0, 1$ for even and odd-parity, respectively.

2. Solve $C^{-1/2}(\tau_0)C(\tau^*)C^{-1/2}(\tau_0) u_i = \lambda_i u_i$ for the eigenvector u_i .
3. Calculate $v_i = C^{-1/2}(\tau_0)u_i$.
4. For each configuration $n = 1, \dots, 200$, store the elements of the rotated correlation matrix \tilde{C} for all τ values:

$$\tilde{C}_{ij,n}(\tau) \equiv \sum_{a,b=1}^{16} v_{ia}^* C_{ab,n}(\tau) v_{bj}.$$

5. Calculate the mean and jackknife error of the off-diagonal elements of the rotated correlation matrix $\tilde{C}(\tau)$ and verify that they are consistent with zero for $\tau_{\min} \leq \tau \leq \tau_{\max}$.
6. Perform single-exponential fits to each fixed-coefficient correlation function $\tilde{C}_{kk}(\tau)$. In these fits, the covariance matrix is calculated using Eqn. 8.7 on the sample of rotated correlation matrices and then inverted for use in the expression for χ^2 given in Eqn. 8.6. The fit parameters are varied until χ^2 is minimized. In each fit, choose a fit range such that the χ^2 per degree of freedom is near 1.0, the quality factor Q is as large as possible (> 0.1 is desirable), and the fit parameter $a_\tau E_{k,\text{fit}}$ is stable under small variations in the fit range. Store the value of $a_\tau E_{k,\text{fit}}$ as the estimate of the level value.
7. To estimate the uncertainty in each level estimate, generate a large number (we used 2048) of bootstrap samples of size 200 by sampling randomly with replacement from the original set of 200 rotated correlation matrices. Perform a single-exponential fit using the same fit range used for the fit on the original sample. Once again, the covariance matrix is estimated using Eqn. 8.7, this time on the members of the bootstrap sample. Each bootstrap sample yields an estimate of the level value $a_\tau E_{k,\text{fit}}$.
8. Store the standard deviation of the bootstrap estimates of $a_\tau E_{k,\text{fit}}$ as the uncertainty in the level estimate.
9. Examine the fixed-coefficient effective masses, the level estimates, and the principal effective masses to verify that the fits are reasonable and not adversely affected by outlying data.

8.4 Lattice nucleon spectrum results

This lattice study was performed using 200 quenched configurations on a $12^3 \times 48$ anisotropic lattice using the Wilson action with $a_s \sim 0.1$ fm and $a_s/a_\tau \sim 3.0$. The quark mass was such that the mass of the pion was approximately 700 MeV. We were able to perform satisfactory fits yielding the lowest-lying eight states in each lattice spin-parity channel, with the exception of the highest (eighth) G_{1u} level. Our spectrum fit results are tabulated in Tables 8.1 and 8.2, and plotted in Figures 8.3, 8.4, 8.5, 8.6, 8.7, and 8.8. The nucleon spectrum levels extracted from these fits are illustrated in Figure 8.9.

Level	τ_{\min}	τ_{\max}	$a_\tau E_{\text{fit}}$	$\chi^2/(\text{d.o.f.})$	Q
G_{1g} 1	9	17	0.2383(39)	0.89	0.51
G_{1g} 2	8	16	0.4030(78)	0.89	0.51
G_{1g} 3	8	16	0.4035(71)	1.20	0.30
G_{1g} 4	7	13	0.418(11)	1.58	0.16
G_{1g} 5	7	15	0.4250(81)	1.09	0.37
G_{1g} 6	6	11	0.475(14)	1.24	0.29
G_{1g} 7	6	15	0.521(13)	1.21	0.29
G_{1g} 8	6	15	0.548(21)	0.93	0.49
H_g 1	8	16	0.3961(53)	1.05	0.39
H_g 2	8	16	0.3996(71)	1.07	0.38
H_g 3	8	16	0.4063(64)	1.71	0.10
H_g 4	9	17	0.4089(83)	1.00	0.43
H_g 5	7	14	0.4366(61)	1.03	0.41
H_g 6	7	16	0.450(11)	1.75	0.08
H_g 7	7	14	0.482(15)	0.50	0.81
H_g 8	9	17	0.506(30)	1.01	0.42
G_{2g} 1	8	15	0.393(16)	0.71	0.65
G_{2g} 2	8	16	0.409(13)	0.63	0.74
G_{2g} 3	8	15	0.420(13)	1.04	0.40
G_{2g} 4	8	15	0.425(11)	0.99	0.43
G_{2g} 5	5	15	0.586(13)	1.10	0.36
G_{2g} 6	4	15	0.602(11)	0.66	0.76
G_{2g} 7	5	15	0.613(16)	0.47	0.89
G_{2g} 8	3	10	0.630(15)	0.95	0.46

Table 8.1: The final spectrum results for the even-parity channels. These results are based on 200 quenched configurations on a $12^3 \times 48$ anisotropic lattice using the Wilson action with $a_s \sim 0.1$ fm and $a_s/a_\tau \sim 3.0$. Our pion mass for this study was $a_\tau M_\pi = 0.1125(26)$ (see Figure 2.1), or approximately 700 MeV.

Level	τ_{\min}	τ_{\max}	$a_\tau E_{\text{fit}}$	$\chi^2/(\text{d.o.f.})$	Q
G_{1u} 1	8	15	0.3300(70)	0.69	0.66
G_{1u} 2	8	16	0.3325(50)	0.83	0.56
G_{1u} 3	8	16	0.463(15)	1.31	0.24
G_{1u} 4	9	17	0.466(14)	0.98	0.45
G_{1u} 5	7	15	0.468(19)	0.78	0.60
G_{1u} 6	8	15	0.479(13)	1.25	0.28
G_{1u} 7	7	15	0.499(16)	1.17	0.31
G_{1u} 8	—	—	—	—	—
H_u 1	7	15	0.3380(45)	1.11	0.35
H_u 2	7	14	0.3437(52)	1.02	0.41
H_u 3	9	17	0.3439(47)	1.38	0.21
H_u 4	7	15	0.458(18)	1.33	0.23
H_u 5	9	17	0.470(10)	1.17	0.32
H_u 6	6	15	0.4896(88)	1.09	0.37
H_u 7	7	13	0.492(16)	1.32	0.25
H_u 8	7	16	0.506(19)	0.95	0.47
G_{2u} 1	7	16	0.3422(53)	1.17	0.31
G_{2u} 2	8	16	0.460(18)	1.78	0.09
G_{2u} 3	7	16	0.486(17)	1.06	0.39
G_{2u} 4	5	13	0.496(11)	0.94	0.47
G_{2u} 5	8	13	0.506(23)	1.68	0.15
G_{2u} 6	7	14	0.514(19)	0.69	0.66
G_{2u} 7	7	16	0.523(18)	1.42	0.18
G_{2u} 8	5	13	0.529(16)	0.69	0.68

Table 8.2: The final spectrum results for the odd-parity channels. These results are based on 200 quenched configurations on a $12^3 \times 48$ anisotropic lattice using the Wilson action with $a_s \sim 0.1$ fm and $a_s/a_\tau \sim 3.0$. Our pion mass for this study was $a_\tau M_\pi = 0.1125(26)$ (see Figure 2.1), or approximately 700 MeV. We did not find a satisfactory fit range for the eighth level in the G_{1u} channel.

G_{1g} Nucleon Fit Results

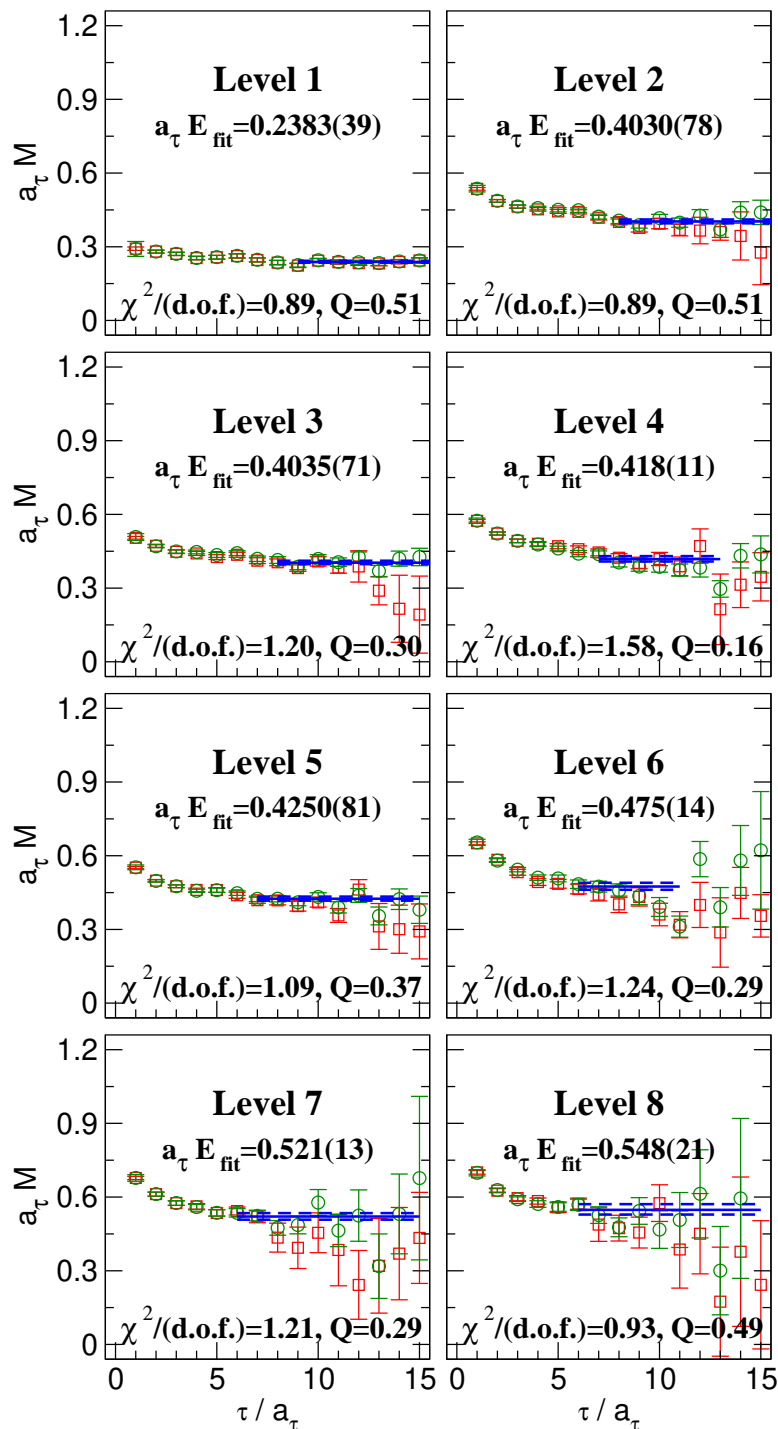


Figure 8.3: The lowest eight levels for the G_{1g} nucleon channel. The green circles are the fixed coefficient effective masses, and the red squares are the principal effective masses. The fits were made to the fixed coefficient correlation functions and are denoted by the blue lines.

H_g Nucleon Fit Results

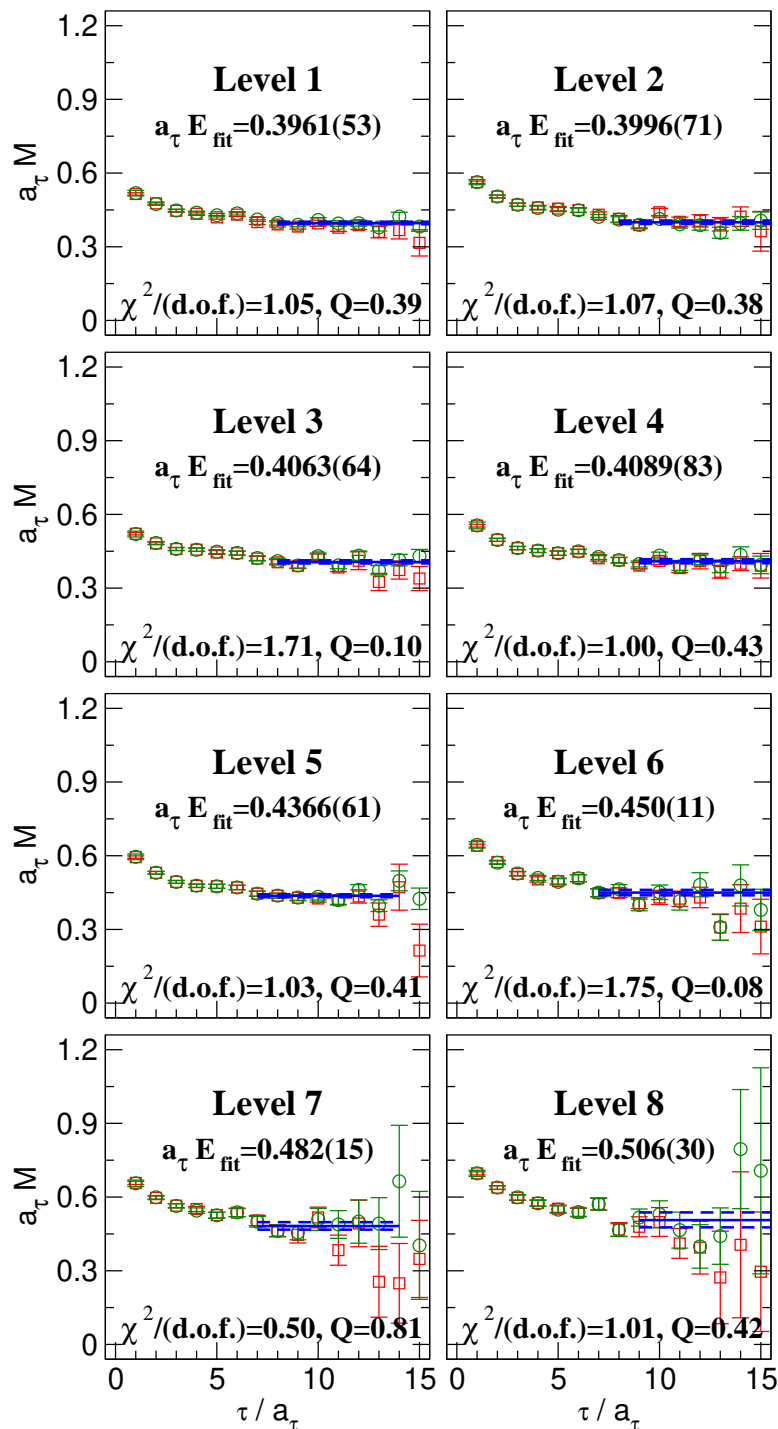


Figure 8.4: The lowest eight levels for the H_g nucleon channel. The green circles are the fixed coefficient effective masses, and the red squares are the principal effective masses. The fits were made to the fixed coefficient correlation functions and are denoted by the blue lines.

G_{2g} Nucleon Fit Results

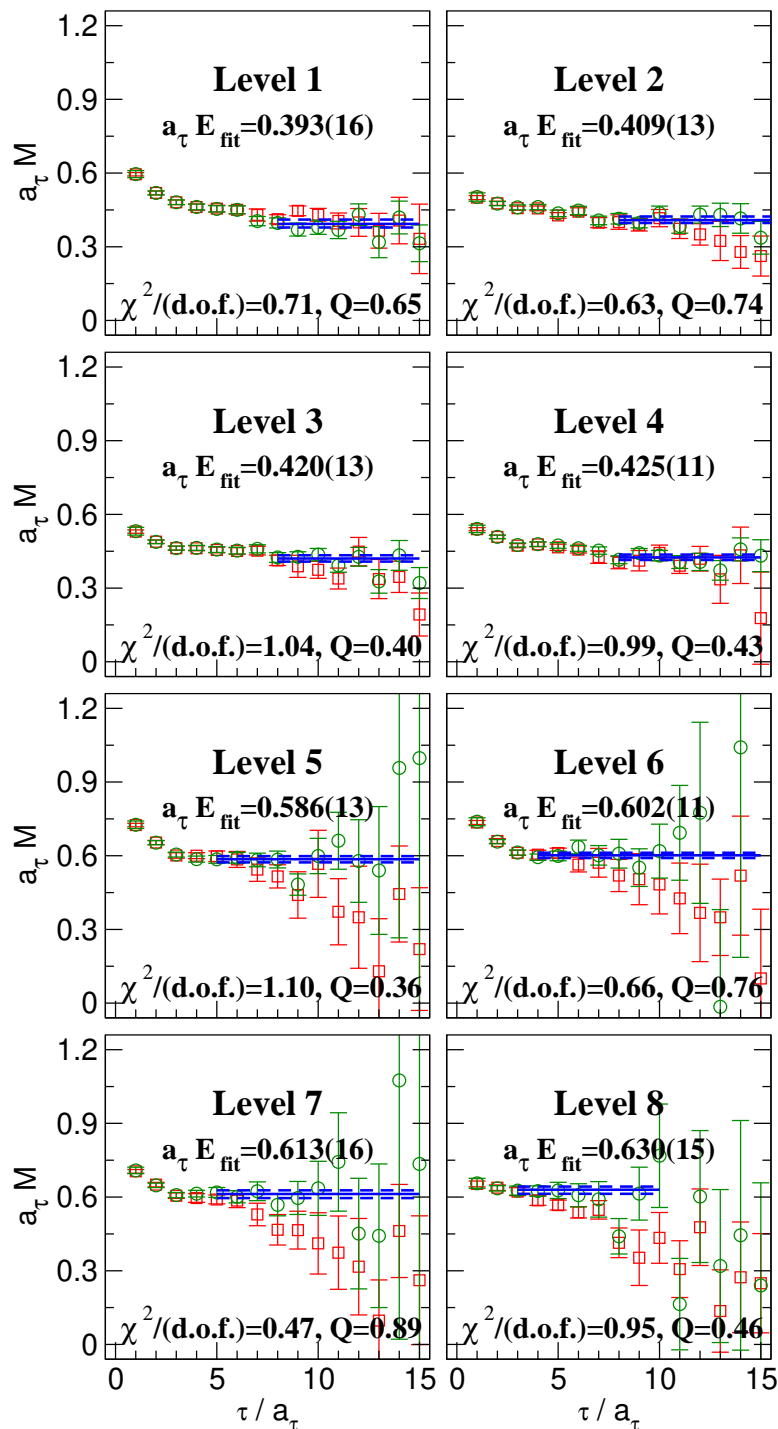


Figure 8.5: The lowest eight levels for the G_{2g} nucleon channel. The green circles are the fixed coefficient effective masses, and the red squares are the principal effective masses. The fits were made to the fixed coefficient correlation functions and are denoted by the blue lines.

G_{1u} Nucleon Fit Results

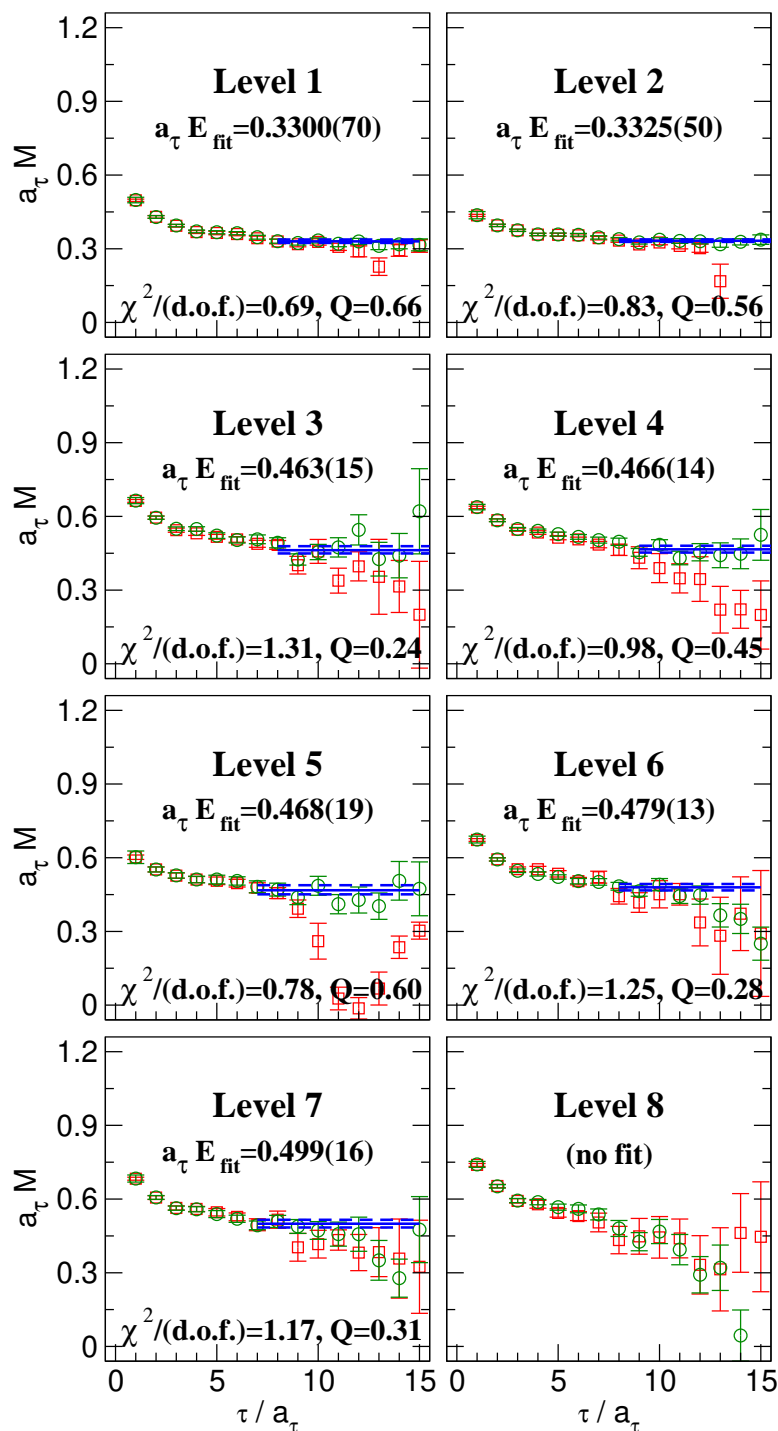


Figure 8.6: The lowest eight levels for the G_{1u} nucleon channel. The green circles are the fixed coefficient effective masses, and the red squares are the principal effective masses. The fits were made to the fixed coefficient correlation functions and are denoted by the blue lines.

H_u Nucleon Fit Results

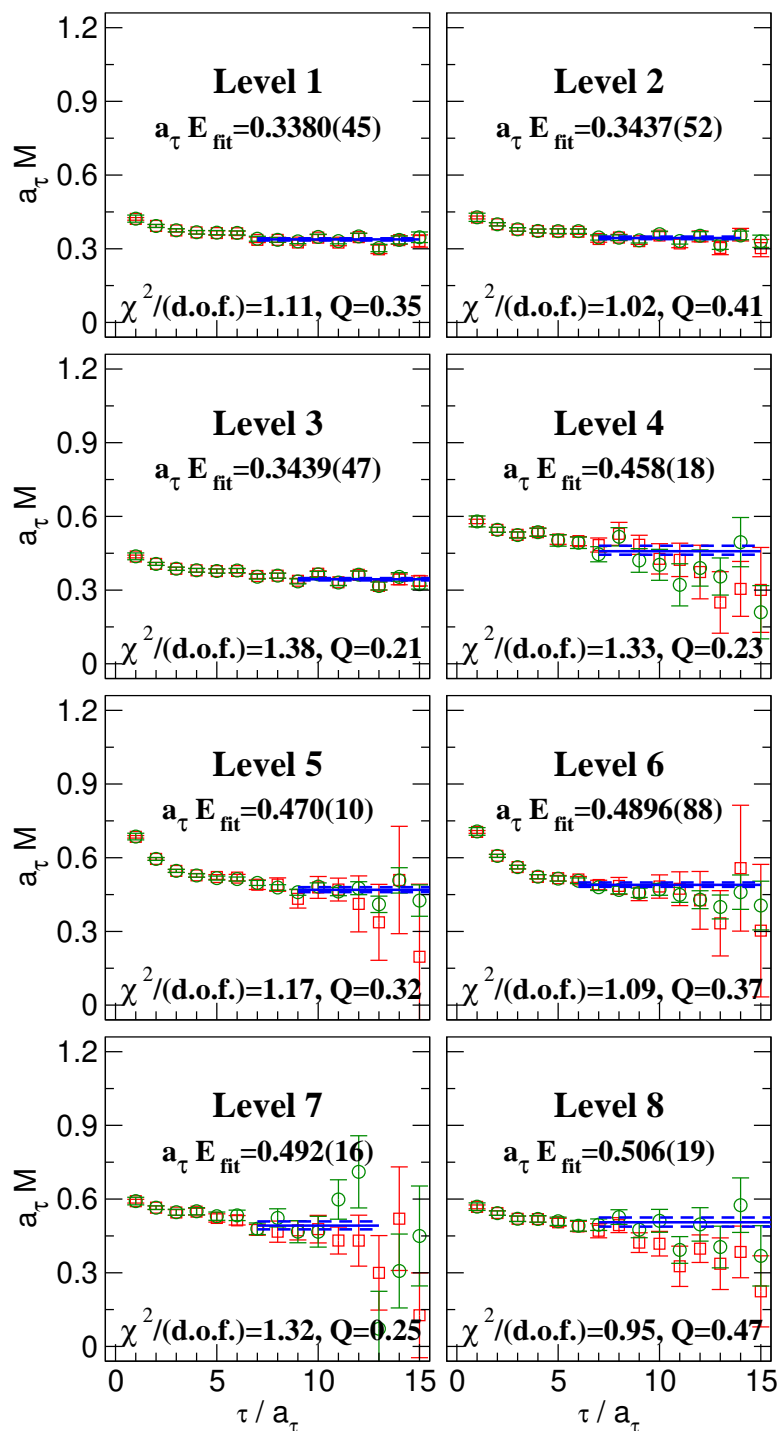


Figure 8.7: The lowest eight levels for the H_u nucleon channel. The green circles are the fixed coefficient effective masses, and the red squares are the principal effective masses. The fits were made to the fixed coefficient correlation functions and are denoted by the blue lines.

G_{2u} Nucleon Fit Results

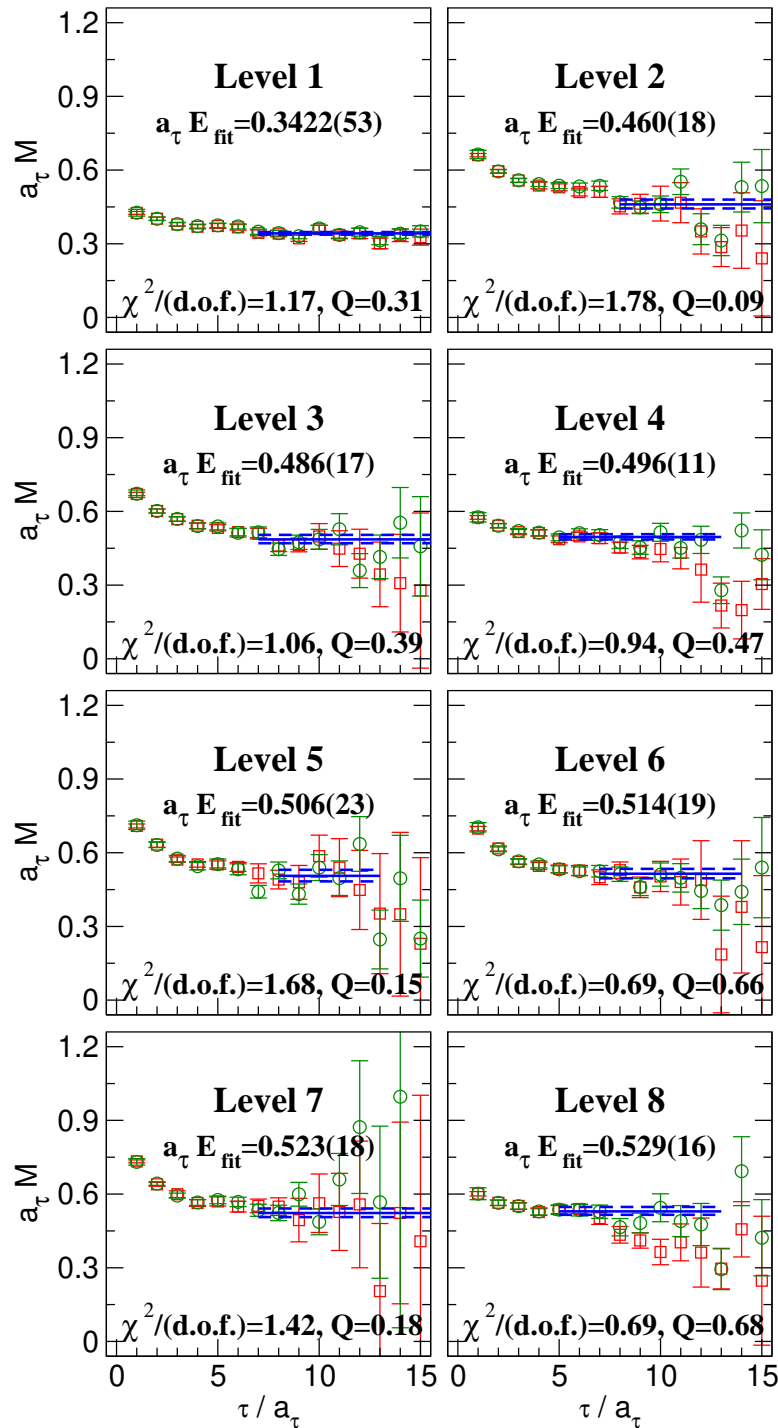


Figure 8.8: The lowest eight levels for the G_{2u} nucleon channel. The green circles are the fixed coefficient effective masses, and the red squares are the principal effective masses. The fits were made to the fixed coefficient correlation functions and are denoted by the blue lines.

Nucleon Mass Spectrum

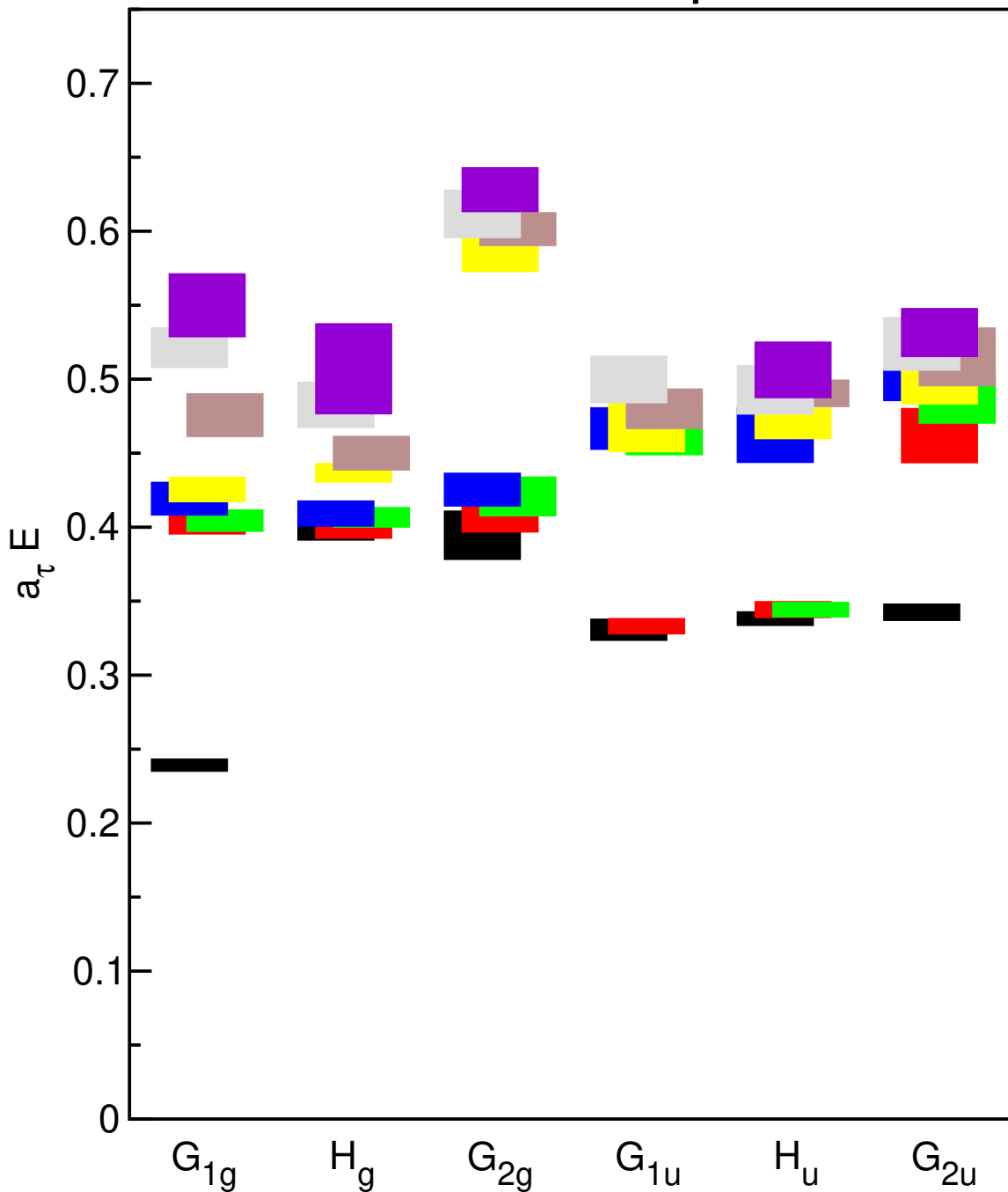


Figure 8.9: The low-lying $I=1/2$, $I_3=+1/2$ nucleon spectrum extracted from 200 quenched configurations on a $12^3 \times 48$ anisotropic lattice using the Wilson action with $a_s \sim 0.1$ fm and $a_s/a_\tau \sim 3.0$. The vertical height of each box indicates the statistical uncertainty in that estimate. Our pion mass for this study was $a_\tau M_\pi = 0.1125(26)$, or approximately 700 MeV. A different color was chosen for each level in a symmetry channel to help the reader discern among the different levels.

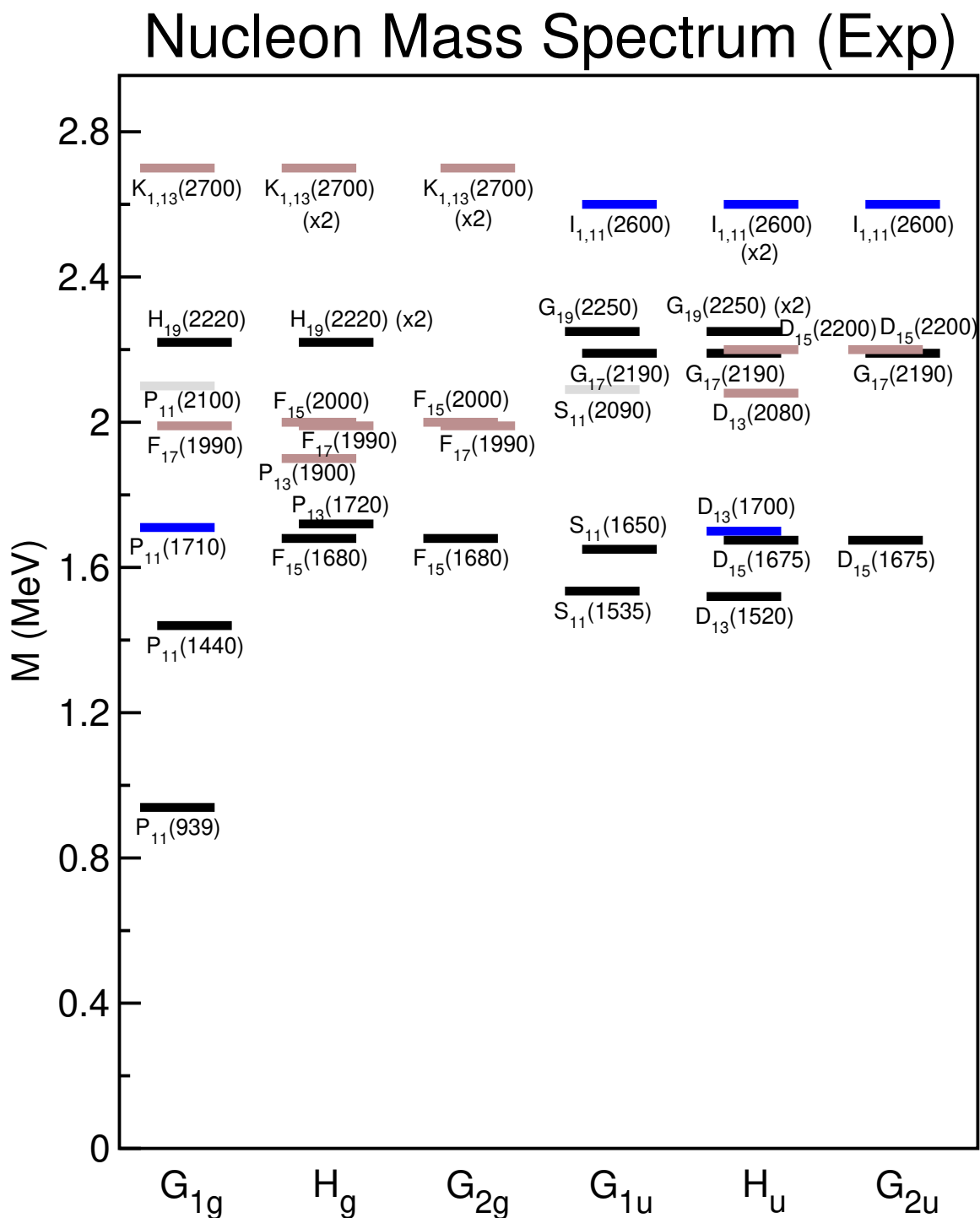


Figure 8.10: The $I=1/2, I_3=+1/2$ nucleon spectrum as determined by experiment [Y⁺06] and projected into the space of lattice spin-parity states. Black denotes a four-star state, blue denotes a three-star state, tan denotes a two-star state, and gray denotes a one-star state.

Nucleon Mass Spectrum (RQM)

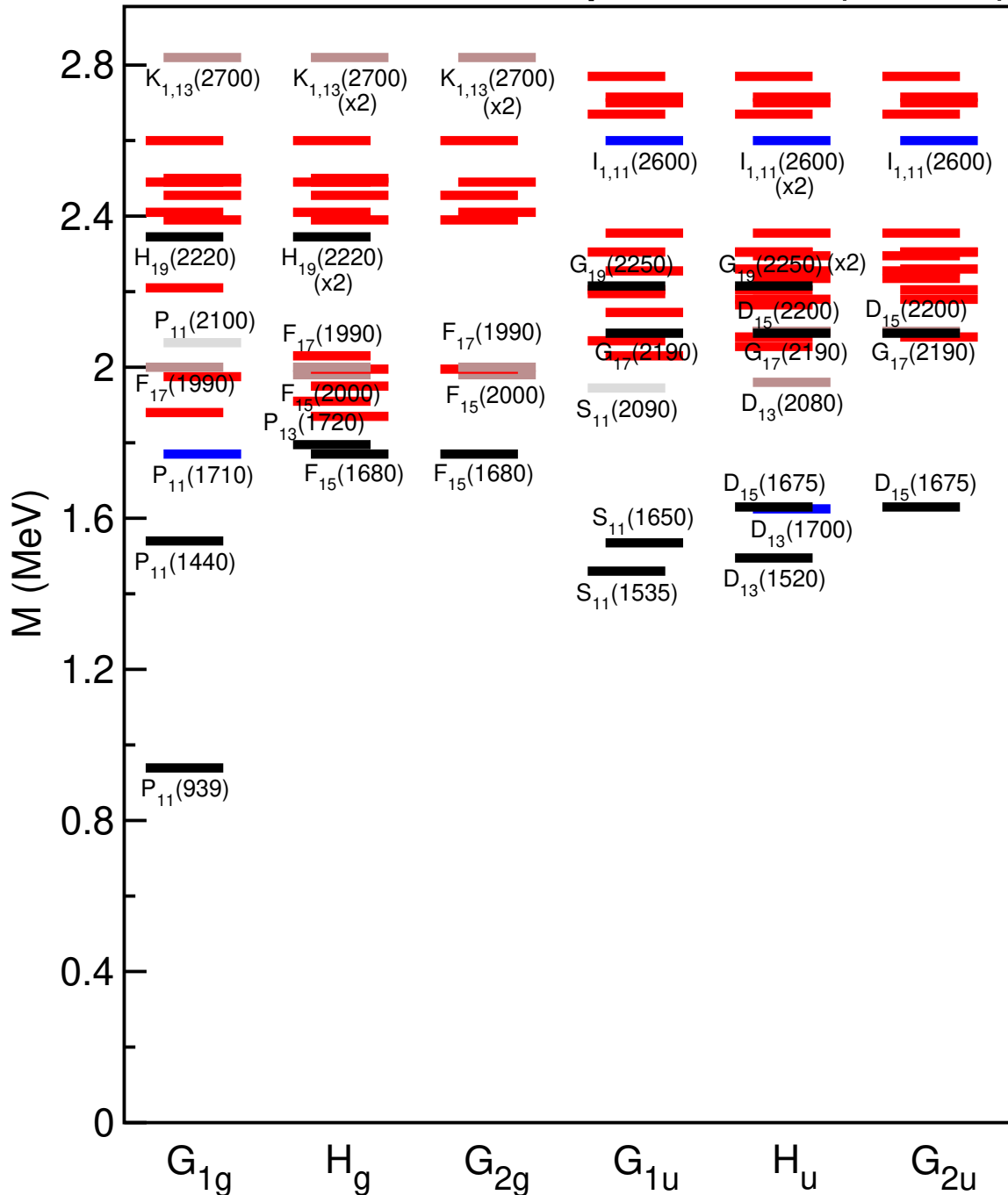


Figure 8.11: The low-lying $I=1/2$, $I_3=+1/2$ nucleon spectrum up to 2820 MeV as predicted by the relativistic quark model [CR93] and projected into the space of lattice spin-parity states. ‘Missing resonances’ are displayed in red, and observed resonances are labeled by their assigned state in the experimental spectrum. Note that the location of a labeled state is given by its predicted energy value, and the text of the label tells its experimentally measured energy value. For a labeled state black denotes a four-star state, blue denotes a three-star state, tan denotes a two-star state, and gray denotes a one-star state.

8.5 Discussion

Our final nucleon spectrum results for this study are tabulated in Tables 8.1 and 8.2, and illustrated in Figure 8.9. Comparison of these results with experiment is not justified because the quenched approximation was used, an unphysically large u, d quark mass was used, and the lattice volume was too small. Nevertheless, such a comparison is still interesting, so we discuss our results with an eye towards the experimentally observed spectrum, shown in Table 8.3 and Figure 8.10. It is also interesting to compare our results to the predictions of the relativistic constituent quark model [CI86, CR93, CR94], shown in Tables 8.4 and 8.5 and Figure 8.11.

We emphasize that most of the levels shown in Figure 8.9 have never before been calculated using first-principles QCD. Figure 8.9 is actually a first glimpse of the low-lying nucleon spectrum as predicted by QCD (with the caveats mentioned above).

First, the lightest nucleon state has a mass value around $0.24 a_\tau^{-1}$ and resides by itself in the G_{1g} channel, indicating a spin- $\frac{1}{2}$ state. This clearly corresponds to the proton at 939 MeV.

Second, there is a cluster or band of odd-parity states just below $0.35 a_\tau^{-1}$ and well separated from higher-lying states. In this band, there are two G_{1u} states, three H_u states, and one G_{2u} state. The G_{2u} level most likely corresponds to the $D_{15}(1675)$ spin- $\frac{5}{2}$ resonance⁵. This means that one of the H_u levels must correspond to this same state (see Table 8.3). The other two H_u states most likely correspond to the spin- $\frac{3}{2}$ $D_{13}(1520)$ and $D_{13}(1700)$ resonances. The two G_{1u} levels seem to correspond to the spin- $\frac{1}{2}$ $S_{11}(1535)$ and $S_{11}(1650)$ resonances. There are no other experimentally-observed odd-parity nucleon resonances below 2.0 GeV. So it appears that there is a one-to-one matching of the states in this band with experiment: every state that should be seen is seen, and there are no extra states. However, given that the mass of the pseudoscalar pion is about $0.11 a_\tau^{-1}$, we expect a two-particle N - π S -wave state in the odd-parity G_{1u} channel near this energy. We are either missing such a state, or are missing one of the $S_{11}(1535)$ or $S_{11}(1650)$ states. The most likely explanation is that the two-particle state is absent from our spectrum due to the quenched approximation combined with our use of single particle operators. Future unquenched calculations should resolve this question.

Third, we observe another band or cluster of states in the even-parity channels around $0.4 a_\tau^{-1}$. There are four states in each of the G_{1g}, H_g, G_{2g} channels, although two additional levels in H_g are only slightly higher. The most striking feature of this band is the lack of one G_{1g} state lying just below the previously discussed odd-parity band. Experiments clearly show a single resonance near 1440 MeV, known as the Roper resonance. The Roper resonance in our spectrum occurs at much too high of an energy compared with experiment. The most likely explanation for this is our use of unphysically large quark

⁵ Experimentalists refer to a baryon resonance having isospin I and total angular momentum J using the notation $L_{2I} 2J$, where $L = S, P, D, F, G, H, I, K \dots$ is the orbital angular momentum of an $N\pi$ system having the same J^P as the state.

masses. There is some evidence [MCD⁺05] from previous quenched lattice calculations that the Roper mass dramatically decreases when the u, d quark mass is decreased such that the pion mass falls below 300 MeV (our pion mass is around 700 MeV).

In the observed spectrum (Figure 8.10) between 1.6 GeV and 1.8 GeV, there are currently three well-established even-parity resonances: the $F_{15}(1680)$, the $P_{11}(1710)$, and the $P_{13}(1720)$. A second band of four more even-parity resonances has been tentatively identified near 2.0 GeV containing the $P_{13}(1900)$, the $F_{17}(1990)$, the $F_{15}(2000)$, and the $P_{11}(2100)$ states. Our results do not reproduce this two-band pattern. Rather, we find a single band of four states in the each of the G_{1g} , H_G , and G_{2g} channels around $0.4 a_\tau^{-1}$.

One possibility is that our calculations have identified resonances in the 1.6 to 1.8 GeV range which have not yet been observed in experiments. These states would correspond to some of the ‘missing resonances’ predicted by the relativistic constituent quark model (see below and Figure 8.11).

However, if the mass splittings among the experimentally observed levels are particularly sensitive to the u, d quark mass, one may speculate that all of those levels, including the Roper, might merge to a single band at large u, d mass. If so, one would observe four nearly degenerate levels in the G_{1g} channel, five levels in the H_g channel, and three in the G_{2g} channel. Such a pattern would more closely resemble the results of our calculation (see Figure 8.9).

Additionally, the single-band structure observed in the even-parity channels may split when we add a clover ($\sigma \cdot F$) improvement term⁶ to our action [SW85, EHK98b, EHR03]. Such a term not only compensates for the $O(a)$ discretization errors introduced by the chiral-symmetry-breaking Wilson term, but may also restore level splitting behavior disrupted by the Wilson term at $O(a)$.

Increased statistics and a finite lattice spacing study (involving data from several different lattice spacings a_s) are needed in order to deduce the spin content in this even-parity band. Note that we also expect two-particle π - $S_{11}(1535)$ and π - $D_{13}(1520)$ states to occur in the even-parity spectrum just slightly above this band’s energy, but the quenched approximation might again make such states inaccessible to the operators used in this study. Whether or not all of these levels merge into a single band at large u, d mass will be eventually answered; in future calculations we will determine the mass spectrum for various values of the u, d quark mass to resolve this issue.

Although our odd-parity results agree qualitatively with the quark model [CR93], the quark model predicts more even-parity states around 2 GeV than we found. Quark model calculations [CR93] predict a rather dense spectrum of four $\frac{1}{2}^+$ states, five $\frac{3}{2}^+$ states, three $\frac{5}{2}^+$ states, and one $\frac{7}{2}^+$ state in the 1.65 to 2.15 GeV energy region. If this were correct, then our lattice spectrum would contain a low-lying band of five states in the G_{1g} irrep, nine states in the H_g irrep, and four states in the G_{2g} irrep (see Figure 8.11). The number

⁶The σ matrices are given by $\sigma_{\mu\nu} = -\frac{i}{2}[\gamma_\mu, \gamma_\nu]$, and F is a discretization of the gauge field strength.

State and Mass (MeV)	J^P	Experimental Status	Appearance in O_h^D Irrep					
			G_{1g}	H_g	G_{2g}	G_{1u}	H_u	G_{2u}
$P_{11}(939)$	$\frac{1}{2}^+$	***	1	0	0	0	0	0
$P_{11}(1440)$	$\frac{1}{2}^+$	***	1	0	0	0	0	0
$D_{13}(1520)$	$\frac{3}{2}^-$	***	0	0	0	0	1	0
$S_{11}(1535)$	$\frac{1}{2}^-$	***	0	0	0	1	0	0
$S_{11}(1650)$	$\frac{1}{2}^-$	***	0	0	0	1	0	0
$D_{15}(1675)$	$\frac{5}{2}^-$	***	0	0	0	0	1	1
$F_{15}(1680)$	$\frac{5}{2}^+$	***	0	1	1	0	0	0
$D_{13}(1700)$	$\frac{3}{2}^-$	**	0	0	0	0	1	0
$P_{11}(1710)$	$\frac{1}{2}^+$	**	1	0	0	0	0	0
$P_{13}(1720)$	$\frac{3}{2}^+$	***	0	1	0	0	0	0
$P_{13}(1900)$	$\frac{3}{2}^+$	**	0	1	0	0	0	0
$F_{17}(1990)$	$\frac{7}{2}^+$	**	1	1	1	0	0	0
$F_{15}(2000)$	$\frac{5}{2}^+$	**	0	1	1	0	0	0
$D_{13}(2080)$	$\frac{3}{2}^-$	**	0	0	0	0	1	0
$S_{11}(2090)$	$\frac{1}{2}^-$	*	0	0	0	1	0	0
$P_{11}(2100)$	$\frac{1}{2}^+$	*	1	0	0	0	0	0
$G_{17}(2190)$	$\frac{7}{2}^-$	***	0	0	0	1	1	1
$D_{15}(2200)$	$\frac{5}{2}^-$	**	0	0	0	0	1	1
$H_{19}(2220)$	$\frac{9}{2}^+$	***	1	2	0	0	0	0
$G_{19}(2250)$	$\frac{9}{2}^-$	***	0	0	0	1	2	0
$I_{1,11}(2600)$	$\frac{11}{2}^-$	**	0	0	0	1	2	1
$K_{1,13}(2700)$	$\frac{13}{2}^+$	**	1	2	2	0	0	0

Table 8.3: The current experimental values [Y⁺06] for all known nucleon resonances. The state names are given in spectroscopic notation: $L_{2I\ 2J}$, where $L = S, P, D, F, \dots$ is the orbital angular momentum of an $N\pi$ system having the same J^P as the state, I is the isospin, and J is the total angular momentum. A four-star experimental status implies that existence is certain and that the properties are fairly well explored. A three-star status implies that existence ranges from very likely to certain, but further confirmation is desirable. Two stars implies that the evidence for existence is only fair, and one star implies that the evidence is poor. The number of times each state is expected to appear in each lattice O_h^D irrep (obtained from subduction) is also shown. The experimental uncertainties are at the 5% level or less.

Model State	J^P	$N\pi$ State Assignment	Experimental Status	Appearance in O_h^D Irrep					
				G_{1g}	H_g	G_{2g}	G_{1u}	H_u	G_{2u}
$S_{11}^1(1460)$	$\frac{1}{2}^-$	$S_{11}(1535)$	***	0	0	0	1	0	0
$D_{13}^1(1495)$	$\frac{3}{2}^-$	$D_{13}(1520)$	***	0	0	0	0	1	0
$S_{11}^2(1535)$	$\frac{1}{2}^-$	$S_{11}(1650)$	***	0	0	0	1	0	0
$P_{11}^2(1540)$	$\frac{1}{2}^+$	$P_{11}(1440)$	***	1	0	0	0	0	0
$D_{13}^2(1625)$	$\frac{3}{2}^-$	$D_{13}(1700)$	**	0	0	0	0	1	0
$D_{15}^1(1630)$	$\frac{5}{2}^-$	$D_{15}(1675)$	***	0	0	0	0	1	1
$F_{15}^1(1770)$	$\frac{5}{2}^+$	$F_{15}(1680)$	***	0	1	1	0	0	0
$P_{11}^3(1770)$	$\frac{1}{2}^+$	$P_{11}(1710)$	**	1	0	0	0	0	0
$P_{13}^1(1795)$	$\frac{3}{2}^+$	$P_{13}(1720)$	***	0	1	0	0	0	0
$P_{13}^2(1870)$	$\frac{3}{2}^+$	—	—	0	1	0	0	0	0
$P_{11}^4(1880)$	$\frac{1}{2}^+$	—	—	1	0	0	0	0	0
$P_{13}^3(1910)$	$\frac{3}{2}^+$	—	—	0	1	0	0	0	0
$S_{11}^3(1945)$	$\frac{1}{2}^-$	$S_{11}(2090)$	*	0	0	0	1	0	0
$P_{13}^4(1950)$	$\frac{3}{2}^+$	—	—	0	1	0	0	0	0
$D_{13}^3(1960)$	$\frac{3}{2}^-$	$D_{13}(2080)$	**	0	0	0	0	1	0
$P_{11}^5(1975)$	$\frac{1}{2}^+$	—	—	1	0	0	0	0	0
$F_{15}^2(1980)$	$\frac{5}{2}^+$	$F_{15}(2000)$	**	0	1	1	0	0	0
$F_{15}^3(1995)$	$\frac{5}{2}^+$	—	—	0	1	1	0	0	0
$F_{17}^1(2000)$	$\frac{7}{2}^+$	$F_{17}(1990)$	**	1	1	1	0	0	0
$P_{13}^5(2030)$	$\frac{3}{2}^+$	—	—	0	1	0	0	0	0
$S_{11}^4(2030)$	$\frac{1}{2}^-$	—	—	0	0	0	1	0	0
$D_{13}^4(2055)$	$\frac{3}{2}^-$	—	—	0	0	0	0	1	0
$P_{11}^6(2065)$	$\frac{1}{2}^+$	$P_{11}(2100)$	*	1	0	0	0	0	0
$S_{11}^5(2070)$	$\frac{1}{2}^-$	—	—	0	0	0	1	0	0
$D_{15}^2(2080)$	$\frac{5}{2}^-$	—	—	0	0	0	0	1	1
$G_{17}^1(2090)$	$\frac{7}{2}^-$	$G_{17}(2190)$	***	0	0	0	1	1	1
$D_{13}^5(2095)$	$\frac{3}{2}^-$	—	—	0	0	0	0	1	0
$D_{15}^3(2095)$	$\frac{5}{2}^-$	$D_{15}(2200)$	**	0	0	0	0	1	1

Table 8.4: The quark model predictions [CR93] for the excited nucleon spectrum below 2100 MeV. The proton is used to set the parameters of the model. The state names are given in spectroscopic notation: $L_{2I} 2J$, where $L = S, P, D, F, \dots$ is the orbital angular momentum of an $N\pi$ system having the same J^P as the state, I is the isospin, and J is the total angular momentum. The superscripted integer on the model state name denotes the principal quantum number in the quark model (see [CR93]). The number of times each state is expected to appear in each lattice O_h^D irrep is also shown. Dashes indicate ‘missing resonances.’

Model State	J^P	$N\pi$ State Assignment	Experimental Status	Appearance in O_h^D Irrep					
				G_{1g}	H_g	G_{2g}	G_{1u}	H_u	G_{2u}
$S_{11}^6(2145)$	$\frac{1}{2}^-$	—	—	0	0	0	1	0	0
$D_{13}^6(2165)$	$\frac{3}{2}^-$	—	—	0	0	0	0	1	0
$D_{13}^7(2180)$	$\frac{3}{2}^-$	—	—	0	0	0	0	1	0
$D_{15}^4(2180)$	$\frac{5}{2}^-$	—	—	0	0	0	0	1	1
$S_{11}^7(2195)$	$\frac{1}{2}^-$	—	—	0	0	0	1	0	0
$G_{17}^2(2205)$	$\frac{7}{2}^-$	—	—	0	0	0	1	1	1
$P_{11}^7(2210)$	$\frac{1}{2}^+$	—	—	1	0	0	0	0	0
$G_{19}^1(2215)$	$\frac{9}{2}^-$	$G_{19}(2250)$	***	0	0	0	1	2	0
$D_{15}^5(2235)$	$\frac{5}{2}^-$	—	—	0	0	0	0	1	1
$G_{17}^3(2255)$	$\frac{7}{2}^-$	—	—	0	0	0	1	1	1
$D_{15}^6(2260)$	$\frac{5}{2}^-$	—	—	0	0	0	0	1	1
$D_{15}^7(2295)$	$\frac{5}{2}^-$	—	—	0	0	0	0	1	1
$D_{15}^8(2305)$	$\frac{5}{2}^-$	—	—	0	0	0	0	1	1
$G_{17}^4(2305)$	$\frac{7}{2}^-$	—	—	0	0	0	1	1	1
$H_{19}^1(2345)$	$\frac{9}{2}^+$	$H_{19}(2220)$	***	1	2	0	0	0	0
$G_{17}^5(2355)$	$\frac{7}{2}^-$	—	—	0	0	0	1	1	1
$F_{17}^2(2390)$	$\frac{7}{2}^+$	—	—	1	1	1	0	0	0
$F_{17}^3(2410)$	$\frac{7}{2}^+$	—	—	1	1	1	0	0	0
$F_{17}^4(2455)$	$\frac{7}{2}^+$	—	—	1	1	1	0	0	0
$H_{1,11}^1(2490)$	$\frac{11}{2}^+$	—	—	1	2	1	0	0	0
$H_{19}^3(2490)$	$\frac{9}{2}^+$	—	—	1	2	0	0	0	0
$H_{19}^2(2500)$	$\frac{9}{2}^+$	—	—	1	2	0	0	0	0
$H_{1,11}^2(2600)$	$\frac{11}{2}^+$	—	—	1	2	1	0	0	0
$I_{1,11}^1(2600)$	$\frac{11}{2}^-$	$I_{1,11}(2600)$	***	0	0	0	1	2	1
$I_{1,11}^2(2670)$	$\frac{11}{2}^-$	—	—	0	0	0	1	2	1
$I_{1,11}^3(2700)$	$\frac{11}{2}^-$	—	—	0	0	0	1	2	1
$I_{1,13}^1(2715)$	$\frac{13}{2}^-$	—	—	0	0	0	1	2	2
$I_{1,11}^4(2770)$	$\frac{11}{2}^-$	—	—	0	0	0	1	2	1
$K_{1,13}^1(2820)$	$\frac{13}{2}^+$	$K_{1,13}(2700)$	**	1	2	2	0	0	0

Table 8.5: The quark model predictions [CR93] for the excited nucleon spectrum from 2100 MeV to 2820 MeV. Dashes indicate ‘missing resonances.’

of states appearing in the lowest H_g band is too small to support this. Future studies will extract more levels in the H_g channel to shed more light on this issue.

With statistics based on only 200 configurations, the interpretation of the states above $0.45 a_\tau^{-1}$ is somewhat problematic. However, the absence of states between $0.45 a_\tau^{-1}$ and $0.55 a_\tau^{-1}$ in the G_{2g} channel is an interesting feature of the spectrum and does appear to tentatively agree with experiment. The quark model does not predict such a large gap (see Figure 8.11). On the other hand, our calculation also shows a large clustering of levels around $0.5 a_\tau^{-1}$ in the G_{2u} channel, which agrees more with the predictions of the quark model than with the experimental data.

8.6 Conclusion and outlook

In this work, we have presented a systematic approach to baryon operator design for use in lattice QCD baryon spectrum calculations. We described the formalism for extracting excited states from correlation matrix elements between quantum operators, and emphasized the importance of using operators which couple strongly to the states of interest and weakly to the high-lying contaminating modes.

We discussed the evaluation of correlation matrix elements using the Monte Carlo method on an anisotropic space-time lattice. The anisotropy allows both a fine temporal resolution for the examination of exponentially decaying correlation functions, and a coarse spatial resolution enabling the use of a larger spatial volume. The signal quality associated with the diagonal correlation matrix elements was defined in terms of the effective mass function, which provided not only a quantitative measure of the contamination and noise, but also a method of visualizing the presence of stationary energy states as plateaus in effective mass plots.

The baryon operators used in this study were composed of gauge-covariantly-displaced three-quark operators. The covariant quark displacements allowed us to incorporate radial structure resulting in operators which better interpolated for excited baryon states. We found it essential to use smeared gauge links in our extended operators to suppress the noise introduced by using gauge links to covariantly displace the quarks. Additionally, we found that while quark field smearing had little effect on the noise, it dramatically reduced the coupling to high-lying contaminating modes. By systematically exploring the smearing parameter space while monitoring the behavior of the effective mass plots associated with three trial operators, we found values of the smearing parameters which reduced the noise and contamination in the correlation matrix elements while preserving the integrity of the excited state signals.

We then used group theory to construct operators which transformed irreducibly under the symmetry group of the cubic spatial lattice. This resulted in operators with well-defined lattice quantum numbers, allowing us to identify the J^P quantum numbers of the corresponding continuum states. The good quantum numbers on our lattice were the linear momentum (chosen to be zero for our spectrum calculations), color (our operators were gauge-invariant, or colorless), isospin (e.g. nucleon operators only excited nucleon states), and the lattice spin-parity irreducible representation label corresponding to the spinorial representations of O_h^D , the double-valued octahedral point group of rotations and reflections on the cubic spatial lattice. This last label, which took the values $G_{1g}, H_g, G_{2g}, G_{1u}, H_u,$ and G_{2u} , provided a way to identify the continuum J^P quantum numbers of the spectral states.

The group-theoretical approach led to an unmanageably large number of extended baryon operators. We developed a method to select sixteen operators in each lattice spin-parity channel to be used for the final extraction of the spectrum. This pruning method was based on three crucial requirements: low noise, maximal independence, and good overlap with the excited states as judged by principal effective mass quality. We evaluated the

diagonal elements of the operator correlation matrix to remove noisy operators, and then selected the sixteen operators whose renormalized correlation matrix at a fixed small time separation had a low condition number for both the even- and odd-parity channels.

We then applied a variational method to rotate our basis set of operators into a new set which could be used to extract the lowest seven or eight levels of the spectrum in each channel. We found a range of τ values over which the temporal correlation function for each of these new operators could be fit to a single exponential. After performing the fits, we interpreted the results in terms of both experimental data and quark model predictions.

Although comparison with experiment is not justified, the pattern of levels obtained qualitatively agrees with the observed spectrum. We also compared our spectrum to relativistic quark model predictions; the quark model predicts more low-lying even-parity states than this study found, but both the quark model and this study predict more odd-parity states near 2 GeV than currently observed in experiments. These results are not only interesting, but also serve as a powerful validation of the operator design methodology described in this work and provide a preview of what we expect to achieve in this long-term effort.

We focused on the nucleon channel in this work, but the methodology used here is readily applied to the other baryon channels (Δ , Σ , Ξ , Λ , and Ω). Our approach to building operators and extracting the spectrum is also expected to be equally effective when adapted for the construction of meson operators, an important next step.

An important improvement to our calculation technique will be the use of all-to-all propagators [FJO⁺05], rather than one-to-all propagators, when evaluating correlation matrix elements. All-to-all propagators will allow us to treat the source and sink operators separately, an improvement over the current method in which we are forced to express correlation matrix elements in terms of thousands of three-quark propagator terms. It will be computationally feasible to spatially average over the source as well as the sink to improve our statistics, and to evaluate correlation matrix elements between multi-hadron operators.

This research was carried out as part of the ongoing Lattice Hadron Physics Collaboration QCD spectroscopy project. The LHPC has recently been awarded over ten million CPU hours on the QCDOC at Brookhaven National Laboratory, a massively parallel ASIC ⁷ supercomputer [BCC⁺04]. We are currently generating 1,000 large-volume unquenched gauge configurations. Because this unquenched run includes the fermion determinant, we are correctly including quark loop effects in the calculation of our propagators. Using clover-improved Wilson fermions, an improved gauge action, and a pion mass around 300 MeV, we expect this production run data to resolve many of the questions raised by the preliminary spectrum results presented here, and to provide us with a first *ab initio* look into the baryon spectrum as predicted by QCD.

⁷QCDOC stands for “QCD On a Chip” and ASIC stands for “Application-Specific Integrated Circuit.”

Appendix: Final operator selection

The number of nucleon operators of each type is shown in Table 6. For future studies, we record here the corresponding identification numbers for the final sixteen nucleon operators selected from each O_h^D irreducible representation in Tables 7, 8, and 9. These identification numbers are used to index the different operators in our `projection_coefficients` data files.

N^+ Operator type	G_{1g}	H_g	G_{2g}
Single-Site	3	1	0
Singly-Displaced	24	32	8
Doubly-Displaced-I	24	32	8
Doubly-Displaced-L	64	128	64
Triply-Displaced-T	64	128	64
Total	179	321	144

Table 6: The numbers of operators of each type which project into each row of the G_{1g} , H_g , and G_{2g} irreps for the N^+ baryons. The numbers for the G_{1u} , H_u , and G_{2u} irreps are the same as for the G_{1g} , H_g , and G_{2g} irreps, respectively.

$$G_{1g}/G_{1u} \text{ Operators}$$

Operator Number	Operator Type	Operator ID
1	Single-Site	2
2	Singly-Displaced	11
3	Singly-Displaced	17
4	Singly-Displaced	20
5	Doubly-Displaced-I	0
6	Doubly-Displaced-I	4
7	Doubly-Displaced-I	5
8	Doubly-Displaced-I	9
9	Doubly-Displaced-I	12
10	Doubly-Displaced-L	4
11	Doubly-Displaced-L	10
12	Triply-Displaced-T	3
13	Triply-Displaced-T	5
14	Triply-Displaced-T	9
15	Triply-Displaced-T	11
16	Triply-Displaced-T	25

Table 7: The identification numbers for the final sixteen nucleon operators selected from the G_{1g}/G_{1u} channels. The ID number corresponds to the operator number within each type (see Table 6) as indexed in our `projection_coefficients` data files.

H_g/H_u Operators

Operator Number	Operator Type	Operator ID
1	Singly-Displaced	9
2	Singly-Displaced	10
3	Singly-Displaced	31
4	Doubly-Displaced-I	8
5	Doubly-Displaced-I	17
6	Doubly-Displaced-I	31
7	Doubly-Displaced-L	47
8	Doubly-Displaced-L	54
9	Doubly-Displaced-L	84
10	Doubly-Displaced-L	113
11	Doubly-Displaced-L	124
12	Triply-Displaced-T	35
13	Triply-Displaced-T	71
14	Triply-Displaced-T	86
15	Triply-Displaced-T	95
16	Triply-Displaced-T	104

Table 8: The identification numbers for the final sixteen nucleon operators selected from the H_g/H_u channels. The ID number corresponds to the operator number within each type (see Table 6) as indexed in our `projection_coefficients` data files.

G_{2g}/G_{2u} Operators		
Operator Number	Operator Type	Operator ID
1	Singly-Displaced	0
2	Singly-Displaced	1
3	Singly-Displaced	2
4	Singly-Displaced	6
5	Doubly-Displaced-I	5
6	Doubly-Displaced-I	6
7	Doubly-Displaced-I	7
8	Doubly-Displaced-L	32
9	Doubly-Displaced-L	37
10	Doubly-Displaced-L	41
11	Doubly-Displaced-L	52
12	Triply-Displaced-T	1
13	Triply-Displaced-T	33
14	Triply-Displaced-T	45
15	Triply-Displaced-T	51
16	Triply-Displaced-T	61

Table 9: The identification numbers for the final sixteen nucleon operators selected from the G_{2g}/G_{2u} channels. The ID number corresponds to the operator number within each type (see Table 6) as indexed in our `projection_coefficients` data files.

Bibliography

- [A⁺87] M. Albanese et al., *Glueball masses and string tension in lattice QCD*, Phys. Lett. **B** (1987), no. 192, 163.
- [A⁺98] G. S. Adams et al., *Observation of a new $J(PC) = 1-+$ exotic state in the reaction $\pi^- p \rightarrow \pi^+ \pi^- \pi^- p$ at 18-GeV/c*, Phys. Rev. Lett. **81** (1998), 5760.
- [ADL⁺95] M. G. Alford, W. Dimm, G. P. Lepage, G. Hockney, and P. B. Mackenzie, *Lattice QCD on small computers*, Phys. Lett. **B361** (1995), 87.
- [AKL96] M. Alford, T. Klassen, and P. Lepage, *The D234 action for light quarks*, Nucl. Phys. **B (Proc. Suppl)** (1996), no. 47, 370.
- [AKL97] M. G. Alford, T. R. Klassen, and G. P. Lepage, *Improving lattice quark actions*, Nucl. Phys. **B496** (1997), 377.
- [ASB⁺93] C.R. Allton, C.T. Sachrajda, R.M. Baxter, S.P. Booth, K.C. Bowler, S. Collins, D.S. Henty, R.D. Kenway, B.J. Pendleton, D.G. Richards, J.N. Simone, A.D. Simpson, B.E. Wilkes, and C. Michael, *Gauge-invariant smearing and matrix correlators using Wilson fermions at $\beta = 6.2$* , Phys. Rev. **D** (1993), no. 47, 5128.
- [B⁺64] V. E. Barnes et al., *Observation of a hyperon with strangeness -3*, Phys. Rev. Lett. **12** (1964), 204–206.
- [BCC⁺04] P. A. Boyle, D. Chen, N.H. Christ, M. Clark, S.D. Cohen, C. Cristian, Z. Dong, A. Gara, B. Joo, C. Jung, C. Kim, L. Levkova, X. Liao, G. Liu, R.D. Mawhinney, S. Ohta, K. Petrov, T. Wettig, and A. Yamaguchi, *Hardware and software status of QCDOC*, Nucl. Phys. Proc. Suppl. **129** (2004), 838.
- [BCP36] G. Breit, E.U. Condon, and R.D. Present, *Theory of scattering of protons by protons*, Phys. Rev. **50** (1936), 825.
- [BEF⁺05a] S. Basak, R. Edwards, G.T. Fleming, U.M. Heller, C. Morningstar, D.G. Richards, I. Sato, and S.J. Wallace, *Clebsch-Gordan construction of lattice interpolating fields for excited baryons*, Phys. Rev. **D72** (2005), 074501.

-
- [BEF⁺05b] S. Basak, R. Edwards, G.T. Fleming, U.M. Heller, C. Morningstar, D.G. Richards, I. Sato, and S.J. Wallace, *Group-theoretical construction of extended baryon operators in lattice QCD*, Phys. Rev. **D72** (2005), 094506.
- [Bil86] P. Billingsley, *Probability and Measure*, second ed., John Wiley and Sons, Inc., 1986.
- [BMK73] K. Binder and Müller-Krumbhaar, *Dynamic properties of the Monte Carlo method in statistical mechanics*, J. Stat. Phys. **8** (1973), no. 1, 1.
- [Bro92] L. Brown, *Quantum Field Theory*, Cambridge University Press, 1992.
- [C⁺99] S. U. Chung et al., *Evidence for exotic $J(PC) = 1^{-+}$ meson production in the reaction $\pi^{-} p \rightarrow \eta \pi^{-} p$ at 18-GeV/c*, Phys. Rev. **D60** (1999), 092001.
- [CG89] R. Cahn and G. Goldhaber, *The Experimental Foundations of Particle Physics*, Cambridge University Press, 1989.
- [Cha32] J. Chadwick, *Possible existence of a neutron*, Nature **129** (1932), 312.
- [CI86] S. Capstick and N. Isgur, *Baryons in a relativized quark model with chromodynamics*, Phys. Rev. **D34** (1986), 2809.
- [CJR79] M. Creutz, L. Jacobs, and C. Rebbi, *Monte Carlo study of Abelian lattice gauge theories*, Phys. Rev. **D20** (1979), 1915.
- [CM82] N. Cabibbo and E. Marinari, *A new method for updating $SU(N)$ matrices in computer simulations of gauge theories*, Phys. Lett. **B119** (1982), 387.
- [Col01] CLEO Collaboration, *The CLEO-c page*, <http://www.lns.cornell.edu/public/CLEO/spoke/CLEOc>, October 2001.
- [Col02] CLEO Collaboration, *The CLEO II central detector drift chambers*, <http://www.lepp.cornell.edu/public/lab-info/cd.html>, August 2002.
- [CR93] S. Capstick and W. Roberts, *$N \pi$ decays of baryons in a relativized model*, Phys. Rev. **D47** (1993), 1994.
- [CR94] S. Capstick and W. Roberts, *Quasi two-body decays of nonstrange baryons*, Phys. Rev. **D49** (1994), 4570.
- [Cre85] M. Creutz, *Quarks, Gluons and Lattices*, Cambridge University Press, 1985.
- [Cre87] M. Creutz, *Overrelaxation and Monte Carlo simulation*, Phys. Rev. **D36** (1987), 515.
- [CT77] G. Cohen-Tannoudji, *Quantum Mechanics*, vol. II, John Wiley and Sons, Inc., 1977.
- [Dir27] P. A. M. Dirac, *Quantum theory of emission and absorption of radiation*, Proc. Roy. Soc. Lond. **A114** (1927), 243.

-
- [Edw05] R.G. Edwards, *QDP++ data parallel interface for QCD*, SciDAC Software Coordinating Committee, 1.15.0 ed., August 2005.
- [Efr82] B. Efron, *The Jackknife, the Bootstrap and Other Resampling Plans*, Society for Industrial and Applied Mathematics, 1982.
- [EHK98a] R. G. Edwards, U. M. Heller, and T. R. Klassen, *Accurate scale determinations for the Wilson gauge action*, Nucl. Phys. **B517** (1998), 377.
- [EHK98b] R. G. Edwards, Urs M. Heller, and T. R. Klassen, *The effectiveness of non-perturbative $O(a)$ improvement in lattice QCD*, Phys. Rev. Lett. **80** (1998), 3448.
- [EHR03] R. G. Edwards, U. M. Heller, and D. G. Richards, *Spectroscopy using the anisotropic clover action*, Nucl. Phys. Proc. Suppl. **119** (2003), 305.
- [ER85] R. Eisberg and R. Resnick, *Quantum Physics of Atoms, Molecules, Solids, Nuclei, and Particles*, second ed., John Wiley and Sons, Inc., 1985.
- [Fey48] R. P. Feynman, *Space-time approach to nonrelativistic quantum mechanics*, Rev. Mod. Phys. **20** (1948), 367.
- [FGM72] H. Fritzsch and M. Gell-Mann, *Current algebra: Quarks and what else?*, Proc. XVI Int. Conf. on High Energy Physics (Fermilab) **2** (1972), 135.
- [FGML73] H. Fritzsch, M. Gell-Mann, and H. Leutwyler, *Advantages of the color octet gluon picture*, Phys. Lett. **B47** (1973), 365.
- [FJO⁺05] J. Foley, J.K. Juge, A. O’Cais, M. Peardon, S.M. Ryan, and J. I. Skullerud, *Practical all-to-all propagators for lattice QCD*, Comput. Phys. Commun. **172** (2005), 145.
- [GL89] G. H. Golub and C. F. Van Loan, *Matrix Computations*, second ed., The Johns Hopkins University Press, 1989.
- [Gla61] S. L. Glashow, *Partial symmetries of weak interactions*, Nucl. Phys. **22** (1961), 579.
- [GLM⁺89] S. Gusken, U. Low, K.H. Mutter, R. Sommer, A Patel, and K. Schilling, *Nonsinglet axial vector couplings of the baryon octet in lattice QCD*, Phys. Lett. **B** (1989), no. 227, 266.
- [GM09] H. Geiger and E. Marsden, *On a diffuse reflection of the α -particles*, Proceedings of the Royal Society **A** (1909), no. 82, 495.
- [GMN00] M. Gell-Mann and Y. Ne’eman, *The Eightfold Way*, Perseus Publishing, 2000.
- [Gre64] O. W. Greenberg, *Spin and unitary spin dependence in a paraquark model of baryons and mesons*, Phys. Rev. Lett. **13** (1964), 598.

-
- [Gri87] D. Griffiths (ed.), *Introduction to Elementary Particles*, John Wiley and Sons, Inc., 1987.
- [H⁺02] K. Hagiwara et al., *Review of particle physics*, Phys. Rev. **D** (2002), no. 66, 010001.
- [Ham62] M. Hamermesh, *Group Theory and its Application to Physical Problems*, Dover Publications, Inc., 1962.
- [HM84] F. Halzen and A. Martin, *Quarks and Leptons: An Introductory Course in Modern Particle Physics*, John Wiley and Sons, Inc., 1984.
- [I⁺00] N. Isgur et al., *Nuclear theory with lattice QCD*, U.S. Department of Energy Proposal, March 2000.
- [Ken06] A.D. Kennedy, *Simulation algorithms for lattice QCD*, ECT* 2006 Doctoral Training Programme lecture, April 2006.
- [Kla98a] T. R. Klassen, *The anisotropic Wilson gauge action*, Nucl. Phys. **B533** (1998), 557.
- [Kla98b] T. R. Klassen, *The Schroedinger functional for improved gluon and quark actions*, Nucl. Phys. **B509** (1998), 391.
- [Kla99] T. R. Klassen, *Non-perturbative improvement of the anisotropic Wilson QCD action*, Nucl. Phys. Proc. Suppl. **73** (1999), 918.
- [KP85] A. D. Kennedy and B. J. Pendleton, *Improved heat bath method for Monte Carlo calculations in lattice gauge theories*, Phys. Lett. **B156** (1985), 393.
- [Lep] G. P. Lepage, *The analysis of algorithms for lattice field theory*, Invited lectures given at TASI'89 Summer School, Boulder, CO, Jun 4-30, 1989.
- [LM93] G. P. Lepage and P. B. Mackenzie, *On the viability of lattice perturbation theory*, Phys. Rev. **D48** (1993), 2250.
- [LMB⁺06] A. Lichtl, C. Morningstar, S. Basak, I. Sato, S. Wallace, R.G. Edwards, D.G. Richards, G.T. Fleming, and U.M. Heller, *Combining quark and link smearing to improve extended baryon operators*, PoS **LAT2005** (2006), 076.
- [Lus86] M. Luscher, *Volume dependence of the energy spectrum in massive quantum field theories II: Scattering states*, Commun. Math. Phys. **105** (1986), 153.
- [Lus91a] M. Luscher, *Signatures of unstable particles in finite volume*, Nucl. Phys. **B364** (1991), 237.
- [Lus91b] M. Luscher, *Two particle states on a torus and their relation to the scattering matrix*, Nucl. Phys. **B354** (1991), 531.

-
- [LW90] M. Lüscher and U. Wolff, *How to calculate the elastic scattering matrix in two-dimensional quantum field theories by numerical simulation*, Nucl. Phys. **B** (1990), no. 339, 222.
- [Man05] D. M. Manley, *Status of baryon spectroscopy*, J. Phys. Conf. Ser. **9** (2005), 230.
- [MCD⁺05] N. Mathur, Y. Chen, S.J. Dong, T. Draper, I. Horvath, F.X. Lee, K.F. Liu, and J.B. Zhang, *Roper resonance and $S(11)(1535)$ from lattice QCD*, Phys. Lett. **B605** (2005), 137.
- [MEF⁺04] C. Morningstar, R.G. Edwards, R. Fiebig, G.T. Fleming, U.M. Heller, D.G. Richards, I. Sato, and S.J. Wallace, *Baryonic operators for lattice simulations*, Nucl. Phys. Proc. Suppl. **129** (2004), 236.
- [Mer98] E. Merzbacher, *Quantum Mechanics*, third ed., John Wiley and Sons, Inc., 1998.
- [MM94] I. Montvay and G. Münster, *Quantum Fields on a Lattice*, Cambridge University Press, 1994.
- [Mor83] K. Moriyasu, *An Elementary Primer for Gauge Theory*, World Scientific Publishing Company, 1983.
- [MP99] C. J. Morningstar and M. J. Peardon, *The glueball spectrum from an anisotropic lattice study*, Phys. Rev. **D60** (1999), 034509.
- [MP04] C. Morningstar and M. Peardon, *Analytic smearing of $SU(3)$ link variables in lattice QCD*, Phys. Rev. **D** (2004), no. 69, 054501.
- [Mut98] T. Muta, *Foundations of Quantum Chromodynamics*, second ed., World Scientific Publishing Company, 1998.
- [NNMS04] Y. Nemoto, N. Nakajima, H. Matsufuru, and H. Suganuma, *Lambda(1405) and negative-parity baryons in lattice QCD*, hep-lat/0404012 (2004).
- [OS73a] K. Osterwalder and R. Schrader, *Axioms for Euclidean Green's functions*, Comm. Math. Phys. **31** (1973), 83.
- [OS73b] K. Osterwalder and R. Schrader, *Euclidean Fermi fields and a Feynman-Kac formula for boson-fermion models*, Helv. Phys. Acta **46** (1973), 277.
- [OS75] K. Osterwalder and R. Schrader, *Axioms for Euclidean Green's functions II*, Comm. Math. Phys. **42** (1975), 281.
- [Per47] D.H. Perkins, *Nuclear disintegration by meson capture*, Nature **159** (1947), 126.
- [Per00] D.H. Perkins, *Introduction to High Energy Physics*, fourth ed., Cambridge University Press, 2000.

-
- [PFTV92] W.H. Press, B.P. Flannery, S.A. Teukolsky, and W.T. Vetterling, *Numerical Recipes in C*, second ed., Cambridge University Press, 1992.
- [PRSZ99] B. Povh, K. Rith, C. Scholz, and F. Zetsche, *Particles and Nuclei: An Introduction to the Physical Concepts*, second ed., Springer-Verlag, 1999.
- [PS95] M. Peskin and D. Schroeder, *An Introduction to Quantum Field Theory*, Perseus Books, 1995.
- [Ram90] P. Ramond, *Field Theory: A Modern Primer*, second ed., Perseus Publishing, 1990.
- [Rot97] H.J. Rothe, *Lattice Gauge Theories: An Introduction*, second ed., World Scientific Publishing Company, 1997.
- [Rut11] E. Rutherford, *The scattering of α and β particles by matter and the structure of the atom*, Philosophical Magazine, Series 6 **21** (1911).
- [Sal68] A. Salam, *Elementary Particle Theory*, Almquist and Wiksell, 1968.
- [Sch59] J. Schwinger, *Field theory commutators*, Phys. Rev. Lett. **3** (1959), 296.
- [Sch85] B.F. Schutz, *A First Course in General Relativity*, Cambridge University Press, 1985.
- [SLLL06] S. Su, L. Liu, X. Li, and C. Liu, *A numerical study of improved quark actions on anisotropic lattices*, Int. J. Mod. Phys. **A21** (2006), 1015.
- [SW85] B. Sheikholeslami and R. Wohlert, *Improved continuum limit lattice action for QCD with Wilson fermions*, Nucl. Phys. **B259** (1985), 572.
- [tH71] G. 't Hooft, *Renormalizable Lagrangians for massive Yang-Mills fields*, Nucl. Phys. **B35** (1971), 167.
- [Wei67] S. Weinberg, *A model of leptons*, Phys. Rev. Lett. **19** (1967), 1264.
- [Wei85] D. Weingarten, *Algorithms for Monte Carlo calculations with fermions*, Nucl. Phys. **B257** (1985), 629.
- [Wei95] S. Weinberg, *The Quantum Theory of Fields*, vol. I, Cambridge University Press, 1995.
- [Wil74a] D. N. Williams, *Euclidean Fermi fields with a Hermitean Feynman-Kac-Nelson formula I*, Commun. Math. Phys. **38** (1974), 65.
- [Wil74b] K.G. Wilson, *Confinement of quarks*, Phys. Rev. **D10** (1974), 2445.
- [Y+06] W. M. Yao et al., *Review of particle physics*, J. Phys. **G33** (2006), 1–1232.